DESIGN OF CATALYTIC AND FUNCTIONAL CARBON NANOREACTORS

Mehtap Aygün, MRes

Thesis submitted to the University of Nottingham
for the degree of Doctor of Philosophy

October 2017

I declare that this thesis is an original report of my research, has been written by me and has not been submitted for any other degree or professional qualification. The experimental work is almost entirely my own work; the collaborative contributions have been indicated clearly and acknowledged. Due references have been provided on all supporting literatures and resources.

Mehtap Aygün

Abstract

The work presented in this thesis describes the development and applications of hollow carbon nanostructures both as the catalytically active, magnetically separable carbon nanoreactors, and electrodes for electrocatalytic reactions. The work is separated into three distinct parts, the formation of carbon nanoreactors of different diameters and shapes in which the effect of confinement imposed by the nanotube is probed in exploratory hydrogenation reactions, the functionalisation of carbon nanoreactors with magnetic nanoparticles for magnetically separable catalyst supports, and the development of new hybrid metal-carbon nanoreactors as efficient electrocatalysts for hydrogen fuel cell applications.

In the first part of the thesis, a $Ru_3(CO)_{12}$ precursor was successfully inserted into carbon nanoreactors of different diameters – very narrow single walled carbon nanotubes (SWNTs, d_{SWNT} ~1.5 nm) and much wider hollow graphitised carbon nanofibers (GNFs, internal d_{GNF} ~50 nm) using sublimation followed by the formation of uncoated metallic Ru nanoparticles via thermal decomposition. The resultant RuNPs@SWNT and RuNPs@GNF nanoreactors were then tested in hydrogenation reactions using a high pressure $scCO_2$ batch reactor, where the excellent diffusivity and mass transfer properties of $scCO_2$ as solvent enabled the efficient delivery of the reagents to the catalyst surface within the narrow nanoreactors. RuNPs confined in the narrowest channels of SWNT was observed to be highly active and selective in competitive hydrogenation reaction of alkenes, but concurrently reduce the accessible volume of the SWNTs by 30-40 % resulting in lower overall turnover numbers (TONs). In contrast, RuNPs confined in wider GNFs were entirely accessible and indicated outstanding activity in comparison to unconfined RuNPs on the outer surface of SWNTs or carbon black.

In the second part of the work, GNFs sidewalls were functionalised by non-covalent attachment of commercial graphene-like carbon coated magnetic Co nanomagnets ($Co@C_n$) exploiting van der Waals forces via dispersion in an organic solvent using ultrasonic treatment, and by the in situ formation of carbon coated iron nanomagnets ($Fe@C_n$). A number of experiments were carried out to find the minimum amount of nanomagnets required to enable complete separation of the nanotubes from the solution with an external magnetic field. Characterisation of this composite material by high resolution transmission electron microscopy (HRTEM) showed that $Co@C_n$ and $Fe@C_n$ successfully attached to the GNFs. Magnetic functionalisation steps were then combined with uncoated, palladium and platinum nanoparticle catalyst formation and the resultant catalytically active and magnetically separable hybrid materials were investigated in the reduction of nitrobenzene. The recyclability and stability of these magnetic and catalytic nanoreactors were studied in the reduction of nitrobenzene using magnetic recovery, and only negligible catalyst loss (< 0.5% by wt.) was observed over 5 cycles in comparison to that of filtration based catalyst recovery (>10% catalyst loss by wt.).

In the third part, GNFs were shortened by ball milling and combined with palladium catalyst to form (PdNPs/-PdNPs@)s-GNF using a novel procedure and the resultant activity and stability towards hydrogen evolution and hydrogen oxidation reactions (HER/HOR) in acid media was studied. (PdNPs/-PdNPs@)s-GNF exhibited enhanced activity and excellent durability during 30000 electro-catalytic cycles in HER compared to that of state-art commercial Pt/C which exhibited decreasing activity and poor durability during the cycling in acid. Moreover, s-GNF demonstrated an enhanced HER activity and stability during 5000 cycles. HRTEM revealed some chemical transformations at the step edges within GNF during the electrochemical cycling contributing to durability of the electrocatalyst. Overall, the superior HER/HOR activity

and durability was attributed to the corrugated morphology of s-GNF, and therefore the ability to stabilise the Pd nanoparticles at the graphitic step-edges effectively through strong bonding and synergetic effects between the Pd and s-GNF support.

These results clearly indicate that carbon nanoreactors as catalyst supports and electrocatalystd show significant promise for a variety of chemical reactions.

Publications

(1) M. Aygun, C. T. Stoppiello, M. A. Lebedeva, E. F. Smith, M. del Carmen Gimenez-Lopez, A. N. Khlobystov and T. W. Chamberlain, Comparison of alkene hydrogenation in carbon nanoreactors of different diameters: probing the effects of nanoscale confinement on ruthenium nanoparticle catalysis, *J. Mater. Chem. A*, 2017, DOI: 10.1039/C7TA03691D.

(2) M. Aygun, M. del Carmen Gimenez-Lopez, T. W. Chamberlain and, A. N. Khlobystov, Magnetic and catalytic carbon nanoreactors, *manuscript in preparation*.

Acknowledgements

There are a number of people who I would like to express my thanks towards for their support and guidance during the course of my doctoral studies. I would firstly and most importantly my supervisors Prof. Andrei N. Khlobystov and Dr. Maria Del Carmen Gimenez-Lopez for providing me such a great opportunity, for their support, continued guidance and encouragement throughout the course. I also would like to thank to Dr. Maria Del Carmen Gimenez-Lopez as she devoted her time for analysing the magnetic measurement data performed in the University of Valencia, Spain.

Secondly, and equally as importantly, I would like to express my deepest gratitute to Dr. Thomas W. Chamberlain for his support on a daily basis and guidance during my course. His knowledge, enthusiasm, invaluable patience, understanding, encouragement and friendship has driven my doctoral studies and served as an inspriation. I am eternally indebted to Tom, as he has continued to help and support me despite moving to a different university. Without him, this thesis would not have been possible.

I would like to thank Maria Lebedeva for her continued help, support, and practical expertise in carrying out hydrogenation experiments and characterisation studies, in particular, ^{1}H NMR analysis in the first year of my course.

I would like to thank all of the other current and past members of the Nottingham Nanocarbon Group, specially, Rhys Lodge and Dr. Alessandro La Torre for transmission electron microscopy imaging. I would like to thank Dr. Craig Stoppiello for his day-to-day help and transmission electron microscopy imaging. I would also like to thank Graham, Abdullah, Carlos, Arran, Bradley, Scott, Robert, Julie, Nityananda, Rossella and Kate for all of their support and providing a great working atmosphere.

My thanks also go to Mark Guyler and Ben Pointer-Gleadhill for helping with ICP-OES measurements, Helena Matabosch Coromina and Abdulsalam Ajumayli for helping in use of the BET equipment and Dr Emily Smith for XPS measurements. I would like to thank Glen Murry for helping to perform the electrochemistry experiments.

I would like to extend my acknowledgement to Republic of Turkey Ministry of National Education for the financial support during my PhD studies.

I would like to thank my dearest friends Hilal, Fulya, Sena, Rahmet, Helena, Saddam, Abdullah, Feyza, Yadigar, Hüsna, Furkan, Nurdan, Kübra, Şeyda, Neslihan, Carlos, Aslı, Havazen, Rasha, Özlem, Pelin, Hatice, Ayşe, Sarah, Sean, Fiona, Marco and Josh. I am glad to have them for the valued friendship.

Last but not least, I would like to express the deepest thanks to parents, my dearest mum (Gülinaz), dad (Cengiz) and brother (Akın) and my dearest sister Funda Çatan. They have provided me with love and support on a daily basis. Without them, I could not have achieved this.

List of Acronyms, abbreviations and symbols

Acronym, abbreviation or symbol	**Definition**
CNT	Carbon nanotube(s)
SWNT	Single-walled carbon nanotube(s)
DWNT	Double-walled carbon nanotube(s)
MWNT	Multi-walled carbon nanotube(s)
GNF	Graphitised carbon nanofibre(s)
CNS	Carbon nanostructure(s)
NP	Nanoparticle(s)
C_{60}	Buckminster fullerene
RuNP	Ruthenium nanoparticle(s)
$Ru_3(CO)_{12}$	Triruthenium dodecacarbonyl
^1H NMR	Proton nuclear magnetic resonance spectroscopy
$CDCl_3$	Deuterated chloroform
d	Diameter
L	Length
E_A	Activation energy
$Co@C_n$	Graphene-like carbon coated cobalt nanomagnet(s)
$Fe@C_n$	Graphene-like carbon coated iron nanomagnet(s)
FeNP	Iron nanoparticle(s)
PdNP	Palladium nanoparticle(s)
PtNP	Platinum nanoparticle(s)
dba	Dibenzylideneacetone
T	Tesla
PTFE	Poly(tetrafluoroethylene)
nm	Nanometre
wt	Weight
HRTEM	High resolution transmission electron microscopy
XPS	X-Ray photoelectron spectroscopy
TGA	Thermo-gravimetric analysis

EDX	Energy-dispersive X-ray
ICP-OES	Inductively coupled plasma optical emission spectrometry
XRD	The powder X-ray diffraction
UV-vis	Ultraviolet-visible thesisspectroscopy
s-GNF	Shortened graphitised nanofiber(s)
PEMFC	Proton exchange membrane fuel cell
GC	Glassy carbon
RDE	Rotating disk electrode
RHE	Reversible hydrogen electrode
E	Potential
η	Overpotential
H*	Adsorbed hydrogen species on electrode surface
H_{ad}	Adsorbed hydrogen
HER	Hydrogen evolution reaction
HOR	Hydrogen oxidation reaction
OER	Oxygen evolution reaction
ORR	Oxygen reduction reaction
LSV	Linear sweep voltammetry
GCE	Glassy carbon electrode
CV	Cyclic voltammetry
Hupd	Hydrogen under potential deposition
F	Faraday constant
I	Current
I_{lim}	Diffusion-limiting current
Ik	Mass-transport free kinetic current
J	Current density
J_0	Exchange current density
Dec	Decade
V	Volt
A	Amper

s	Second
geo	Geometric surface area of glassy carbon
$HClO_4$	Perchloric acid
M	Molar
R	Solution resistance (ohm)

Table of Contents

1 TOWARDS CATALYTIC CARBON NANOREACTORS

1.1 INTRODUCTION

Catalysis is essential in the synthesis of molecules where the participation of a catalyst increases the rate of the chemical reaction by decreasing the activation energy without being consumed during the process.[1-4] It has been recently reported that more than 85% of all chemical products are synthesised in the presence of catalyst, costing ~14 billion US$ per year for the use in different sectors such as polymer industry, manufacturing of chemicals, coal, oil and gas refining.[5] Therefore, it is crucial for the industrial companies and universities to take part in research to create new catalysts which are cheaper, efficient, long lasting, re-useable and environmentally friendly, as well as improving existing catalysts which will lead to a decrease in costs, thus saving time and energy in large-scale industrial processes.

Catalysts can be classified very basically by considering solely whether they are in the same (homogeneous catalyst) or different (heterogeneous catalyst) phase to the reactants. A homogeneous catalyst is typically dissolved, along with the reactants in a solvent, enabling the catalysis to occur in the same phase with the reactants. An intimate and fluid interaction with the catalyst and the reactants limits the diffusion problems leading to great activity and selectivity. However, homogeneous catalysts suffer from a number of disadvantages, including poor thermal stability, difficult and expensive catalyst recovery. Extraction and distillation are mostly used processes which are highly energy-consuming and can cause the catalyst and/or products to decompose at high temperatures. All these disadvantages make the homogeneous catalyst industrially less relevant. Heterogeneous catalysts are typically solids and catalyse reactions of reactants in either liquid or gas phases. As a result, heterogeneous catalysts can be separated from reactants and thus

recovered after the reaction reasonably easily and in a cheap way such as by filtration. They are also generally robust, stable to high temperatures and not easily deactivated, and thus, have high industrial relevance. However, only surface atoms of the heterogeneous catalyst participate in chemical reaction which can limit the activity and selectivity of the catalyst.

1.2 SUPPORTED METAL NANOPARTICLE CATALYSTS

This thesis is mainly focused on the investigation of heterogeneous catalysis, specifically studying the effects of metal nanoparticles supported on carbon support materials such as carbon nanotubes (CNTs) and graphitised carbon nanofibers (GNFs), and exploring their use in a number of field such as industrial and energy related applications. Metal catalysts with nanoscale dimensions are very promising heterogeneous catalyst for chemical reactions as they have a high surface area with a large proportion of surface atoms. However, they are thermodynamically metastable and nanoparticles (NPs) have a high tendency to agglomerate due to van der Waals forces, which leads to a loss of active surface area and a decrease in the activity of the catalyst.[6-7] Therefore supporting them is essential to stabilise the particles to prevent agglomeration and sintering and to allow the optimisation of the properties of nanoparticles for a particular process.[8-9] Metal particles can be supported using a number of different highly porous support materials such as metal oxides, zeolites, metal-organic frameworks (MOF), molecular cage compounds and carbon nanomaterials.[9-23] Reactant molecules can therefore adsorb onto the active catalyst both on the exterior of the support structure, and also diffuse through the support material by entering the pores. This results in a large increase in the available active surface of the catalyst for reactions to occur, and thus a faster overall rate of reaction. As well as stabilising the NPs the support can also influence the reaction in a number of other

ways, the shape and structure of the support, *i.e.* the nanoporous scaffolds enable their use as a nanoscale reaction container, imparting confinement for catalyst particles and reactants and influencing reaction pathways. Furthermore, the support material can alter the electronic state of catalyst particles and thus influence the reduction/oxidation behaviour of metal catalyst.[20,32]

1.2.1 Hollow 1D carbon nanomaterials as catalyst support and nanoreactors

In this project hollow carbon nanotubes (CNT) and graphitised nanofibres (GNF), collectively known as carbon nanoreactors, which have recently been demonstrated to be suitable support materials due to their thermal stability and low chemical reactivity, will be used.[20-26] Unlike classical graphite, activated carbon, alumina, silica or zeolite supported metal catalysts, metal catalysts deposited both on the exterior and interior of CNT or GNF show different behaviour depending on the curvature of the carbon nanostructure.[27-28]

Carbon nanotubes are axially aligned hollow cylindrical tubes and can be divided into two categories, single-walled carbon nanotubes (SWNTs) and multi-walled carbon nanotubes (MWNTs).[29-31] A SWNT consists of a single sheet of sp^2 hybridised carbon rolled into a cylindrical tube and as a result possesses an extremely high surface area (all atoms are surface atoms). The structure of a SWNT is very narrow with diameters ranging from 0.4 to 2 nm, whilst, MWNTs consist of a number of aligned or concentric cylindrical tubes (Figure 1.1a and b).[32] MWNTs have larger internal diameters, typically 4-20 nm, compared to SWNTs. All carbon nanotubes are mechanically robust, thermally stable and chemically very inert since they have very few open edges and dangling carbon bonds, as a result molecules and nanoparticles tend to physically adsorb onto the nanotube walls rather than chemically react with them.[30-34]Another important feature of carbon

nanoreactors is the curved structure, which makes the concave structure of the interior suitable for catalytic reactions as the nanoparticles are held tightly in the interior of nanoreactor due to the greater van der Waals interactions.

This is a result of the energy of encapsulation being considerably higher for species located on the inner surface (E_{enc}) compared to species adsorbed (E_{ads}) on the convex outer surface ($E_{enc} > E_{ads}$) (Figure 1.1).[32]

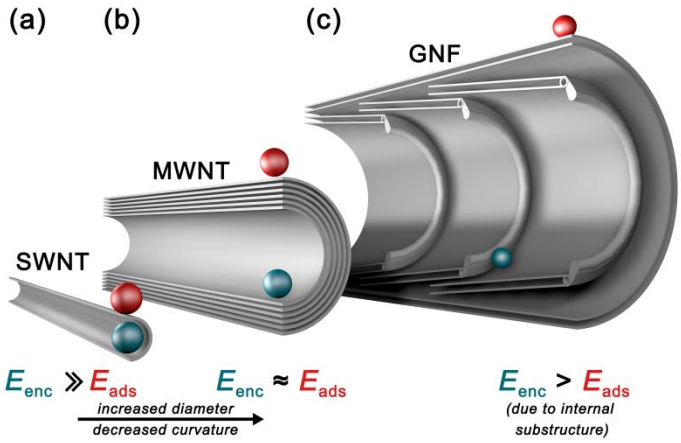

Figure 1.1. Schematics of (a) SWNT, (b) MWNT and (c) GNF (not to scale) showing encapsulated (blue) and externally adsorbed (red) species. The difference between energy of encapsulation (E_{enc}, blue) and energy of external adsorption (E_{ads}, red) often exhibits a general trend depending on the curvature of the graphitic surface and thus, carbon nanotube. Adapted from Miners *et al.* [32]

The narrow internal volume of SWNTs enables strong interactions with the guest molecules and enhances the effect of the confinement on the resultant reaction. Miners, *et al*. has recently studied the effect of nanoreactor diameter on the selectivity of bromination of *N*-phenylacetamide within SWNTs and showed that the inner cavity of the nanoreactor changed the regioselectivity and the activity of the bromination reaction as illustrated in Figure 1.2.[35]

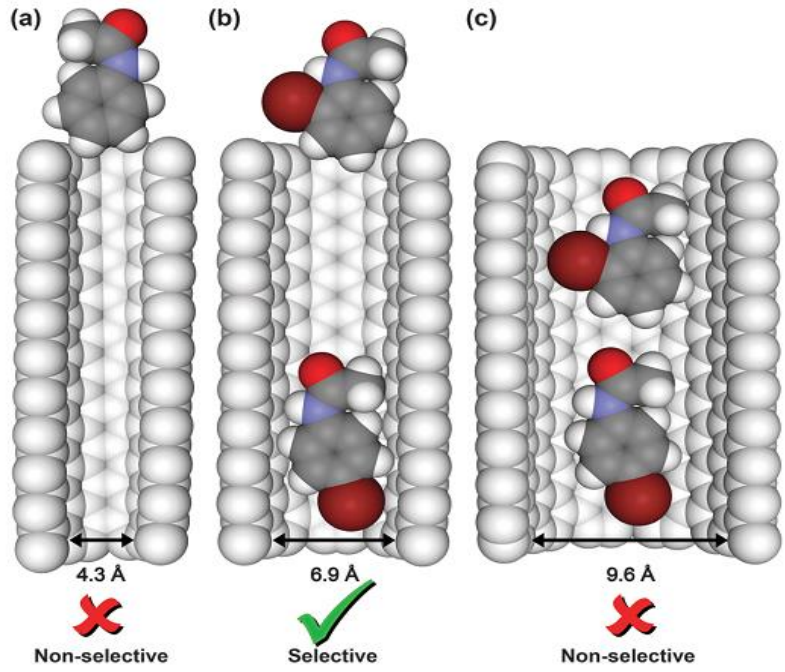

Figure 1.2. Comparison of the van der Waals diameter of the internal cavity (d_{NT}) of three types of nanotubes to the critical van der Waals diameter ($d_{critical}$) of reactant and product molecules. (a) SWNT (d_{NT} = 4.3 Å), too narrow allowing the confinement of the reactant, (b) SWNT (d_{NT} = 6.9 Å), allowing the formation of para- but not ortho-product and (c) wider SWNT (d_{NT} = 9.6 Å) freely allowing the formation of both products. Adapted from Miners *et al.*[35]

In contrast to CNTs, hollow GNFs consist of stacked truncated cones of graphene layers arranged at an angle along the main axis and have an internal diameter ranging from 50 nm to more than 100 nm (Figure 1c).[22, 25,32,34] The interior and exterior surfaces of GNF are relatively different from each other. The internal surface has a succession of step edges while the exterior surfaces are atomically flat consisting of sp^2 hybridised carbon enveloping the stacked carbon cones. The wide GNFs cavity constitutes an almost unrestricted internal channel and is expected to have little or no confinement effect for the guest molecules, however, the nanostructured step edges are around 3 nm high and can act as anchoring points for both catalysts and guest molecules and impart significant local confinement effects.[6,32,50]

1.2.1.1 Carbon nanoreactor supported metal NPs

Carbon nanotubes and nanofibers are therefore of great interest for use as nanoreactors in a variety of different catalytic chemical reactions, since they can be used as a nanocontainer and template for the formation of catalytically active metallic nanoparticles.[20-29,32,36-54] Their commensurate structure enhances the stability and selectivity of the catalyst confined within the nanotube allowing strict control of the nanoparticle size, functionality and reactivity by providing stabilisation of the metal nanoparticles preventing aggregation into larger particles and bulk material. As a result, extremely small and stable nanoparticles can be formed, which display high chemical and catalytic activity as the surface of the nanoparticles are not coated by a capping agent (surfactant).[8,55] Most of the studies in the literature involve metal nanoparticles (MNPs) on the exterior of the CNTs as this provides an open and highly accessible surface for chemical reactions. For example, Li *et al.* demonstrated that Pt nanoparticles supported on carbon nanotubes (NPs/CNT) exhibited greater activity than the nanoparticles supported on activated carbon as a result of the increased surface area of the smaller nanoparticles when supported on the nanotubes.[47] However, confinement of nanoparticles inside CNTs (MNPs@CNT) can preferentially improve the stability of catalytic centres and may change the reaction mechanism leading to entirely different products.[32,35-37,45-50] The commensurate shape of carbon nanoreactors also enables extreme confinement for the guest molecules and enhances interactions between the guest species leading to altered thermodynamic parameters and new reaction pathways inside the carbon nanotubes. Lebedeva *et al.* synthesized fullerene containing and fullerene free Pd(II)Salen complexes encapsulated on the step edges within GNF and both catalysts confined within GNF indicated significantly higher activity and selectivity in several Heck reaction compared to the bulk solution.[50]

1.2.1.1.1 Hydrogenation reactions

Hydrogenation reactions in the presence of a catalyst have great importance in industry, in particular for the generation of oils from foods, and manufacturing gasoline and other petrochemical products from hydrocarbons.[56-58] Hydrogenation reactions in the presence of a carbon nanotube supported metal catalyst such as ruthenium, palladium and platinum have been recently studied in the development of efficient hydrogenation catalysts.

Zhang *et al*. studied the hydrogenation of benzene catalysed by palladium nanoparticles confined within MWNT and reported increased catalytic activity compared to PdNPs both on the activated carbon and Y-type zeolite which directly confirms the influence of confinement and intimate interactions between benzene molecules and carbon nanotubes.[52] NiNPs located on GNFs (NiNPs/GNF) were investigated in the liquid phase hydrogenation reactions of benzene to produce cyclohexene.[59] NiNPs/GNF indicated a higher catalytic activity compared to Ni/alpha-Al2O3 because of intrinsic properties of the GNF support such as higher surface area, conductive structure enabled an efficient electron transfer and spillover of hydrogen during the reaction.

Li and co-workers reported that Co-B nanoparticles confined inside carbon nanotubes strikingly enhanced the conversion of *m*-chloronitrobenzene (*m*-CNB) to *m*-chloroaniline (*m*-CAN) due to the presence of the smaller, more homogeneous, and the thermally more stable nanoparticles within nanotubes compared to that of Co-B nanoparticles located outside of the nanotubes (Figure 1.3).[60]

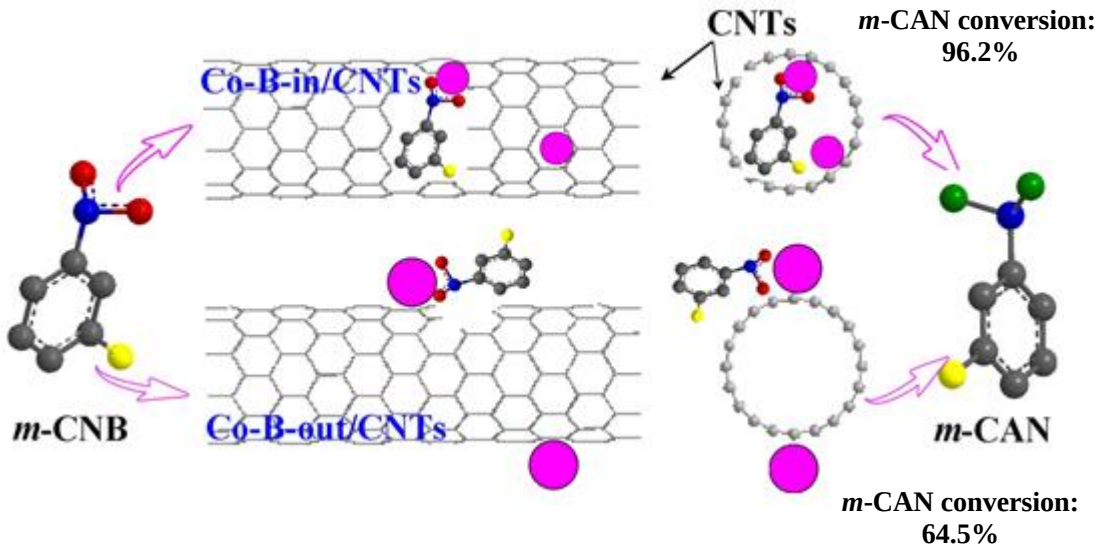

Figure 1.3. Schematic diagram of hydrogenation of *m*-CNB to *m*-chloroaniline over Co-B supported either inside or outside of the carbon nanotube container. Reproduced from Li *et al*.[60]

Guan *et al.* studied the asymmetric hydrogenation of α,β-unsaturated carboxylic acids, and found that confinement of palladium nanoparticles within MWNT enhanced the catalytic activity and enantioselectivity (92%) of PdNPs in comparison to PdNPs supported on the outside of MWNT (Figure 1.4).[41]

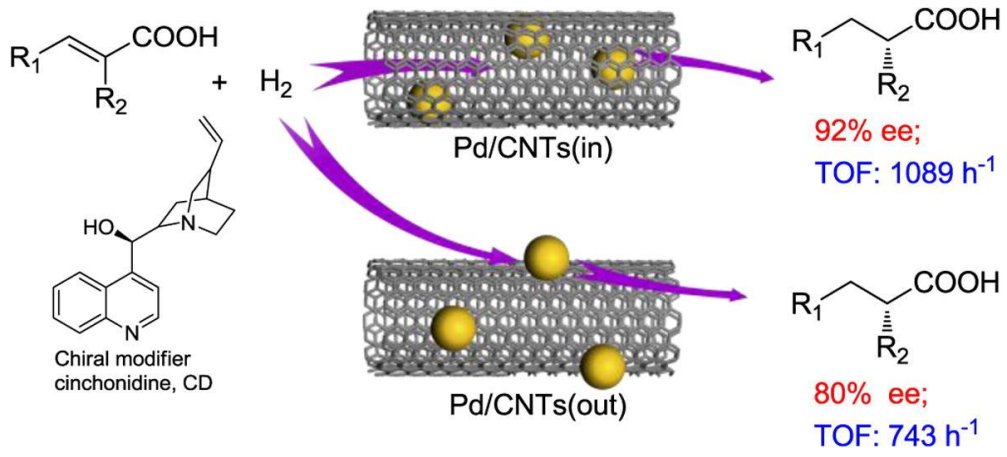

Figure 1.4. Asymmetric hydrogenation of α,β-unsaturated carboxylic in the presence of PdNPs encapsulated within MWNT and PdNPs adsorbed on the exterior of MWNT. Reproduced from Guan *et al*.[41]

The majority of hydrogenation reactions discussed so far has been investigated within the accessible cavities of MWNTs and GNFs while the narrower SWNTs (~ an internal diameter of 1-1.5 nm) are expected to impart greater confinement on typical organic molecules such as benzene due to the strong van der Waals interactions that should occur between the similarly sized reactant molecules and nanotube interior (N.B. critical van der Waals diameter of benzene ~ 0.7 nm).[32] However, using such a narrow nanoreactor can limit efficiency of the catalysis due to slow molecular transport in the very narrow space which means that a suitable solvent is required to ensure effective delivery of reactants and product to and from the catalyst centres. In general, the use of hydrogen (gas) in hydrogenation reactions with a conventional liquid solvent in the presence of metal catalysts supported by a porous material, such as carbon nanotubes, leads to mass transfer resistance problems due to the formation of a liquid-like layer over the catalyst which does not allow uniform delivery of the hydrogen and can deactivate the catalyst.[61-63] However, working in a supercritical regime can eliminate these issues due to the formation of a homogeneous reaction solution of hydrogen gas, and by reducing the viscosity and increasing the diffusion rates relative to the liquid phase hydrogenation reactions. For example, CO_2 behaves as a supercritical fluid above its critical temperature (31.1 °C) and critical pressure (73.8 bar), where it expands to fill a container like a gas but with a density like that of a liquid in equilibrium. This property of $scCO_2$ enables hydrogen, which is readily dissolved and miscible in $scCO_2$, and other reagents to diffuse into the porous supports, helping the transport of them to the catalyst surface (Figure 1.5).[61-65]

Poliakoff *et al.*[66] demonstrated that a wide range of organic feedstocks could be hydrogenated using $scCO_2$ as a solvent in hydrogenation reactions. High product selectivity was achieved following on from this study as the tunability of $scCO_2$ allowed

changes in fluid properties and thus, $scCO_2$ can now be used in large-scale industrial processes as an economically viable solvent.[67] Therefore, using a supercritical solvent such as $scCO_2$ in hydrogenation reactions can eliminate gas-liquid mass and heat transfer limitations in the narrow SWNT channels and improves the reaction rates and selectivity.

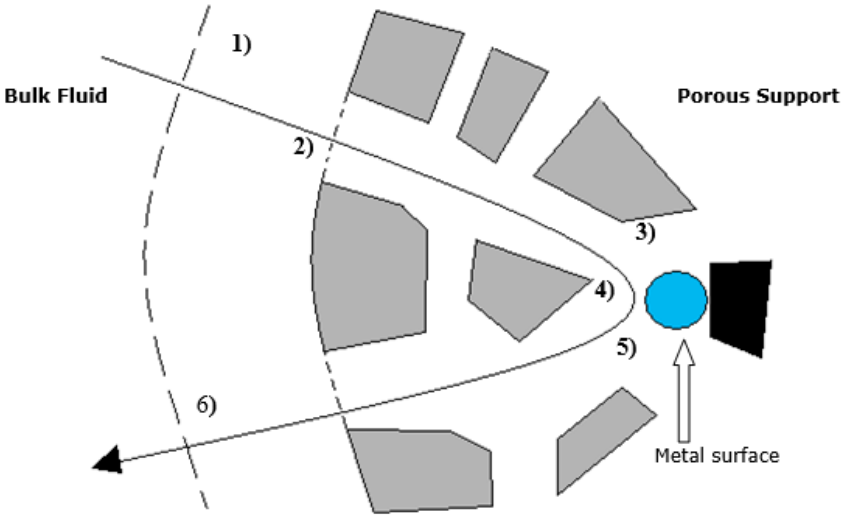

Figure 1.5. Diffusion of H_2 from the bulk gas to the catalyst surface in a porous support. 1) H_2 diffuses through liquid film to the porous support; 2) H_2 diffuses through the pore; 3) Adsorption of H_2 onto metal surface; 4) dissociation of H_2 to hydrogen atoms on the metal surface and surface reaction to form product; 5) desorption of the products from surface; 6) diffusion of the products from the surface into bulk gas.[61]

Chamberlain *at al*. carried out hydrogenation reactions of alkenes over Ru nanoparticles confined within SWNT using $scCO_2$ as a solvent and observed very high yield of the products due to dramatic confinement effects and enhancement of reactant concentration inside the narrow SWNT. The channel of the SWNT imposed a significant stabilising effect on the RuNPs and enabled RuNPs to remain active and unchanged in comparison to RuNPs supported on commercial, non-porous carbon (see Figure 1.6).[37]

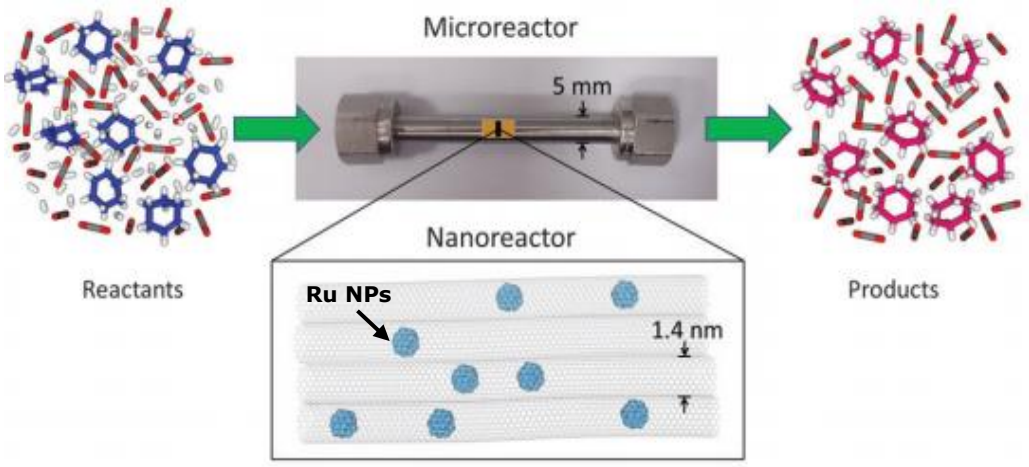

Figure 1.6. Diagram of the hydrogenation of cyclohexene (blue) to cyclohexane (pink) using bundles of RuNPs@SWNT catalytic nanoreactor (shown in the expanded box) in a continuous flow $scCO_2$ milli-scale reactor. Adapted from Chamberlain *et al.*[37]

1.2.2 Magnetic Nanomaterials for Magnetic Separation of Catalyst

The difficulties and the high costs associated with catalyst recovery have increased environmental concerns with respect to metal pollution problems.[68-70] These issues have led to a significant interest in preparation of new catalytic systems which are environmentally friendly, enabling facile and quick separation of the heterogeneous catalyst from the products in liquid phase catalytic reactions. A number of conventional separation methods including filtration and centrifugation have been used in academic studies and industry for the separation and recycling of the heterogeneous catalyst.[70-73] However, each one of these methods comes with important limitations such as cost, time, efficiency and the requirement of secondary processes. In order to minimize the costs and challenges in conventional catalyst separation and facilitate the recycling of the catalyst, intense research efforts have been focused on the development of magnetic heterogeneous metal catalysts. This approach is based on the selective separation of

magnetic metallic material supported catalyst from the reaction mixture containing the products (non-magnetic species) by magnetic means.

In general, magnetic metal nanoparticles such as Fe, Ni and Co are not stable in air and are easily oxidized in acid media giving rise to a change or loss of their magnetization, resulting in their use in synthetic applications being compromised.[70,74] One way to avoid this issue is to fully protect the magnetic nanoparticles with an appropriate inert material such as silica, polymers or carbon before using them as supports for the attachment of additional, active, non-magnetic catalytic metal nanoparticles. This dual nanoparticle system can then be utilised as an effective heterogeneous magnetic metal catalysts which can be separated from products efficiently.[68-75]

Preparation of carbon coated magnetic nanoparticles has recently received increasing attention as carbon nanomaterials are chemically and thermally stable, and robust to most reaction conditions. These materials are based on an approach where the magnetic cobalt nanoparticles are covered by a graphene like shell which ensure the magnetic core is retained and makes the material chemically inert.[76-82] The shell also protects the magnetic nanoparticles against oxidation and erosion by strong acids or bases allowing their use under harsh conditions in organic synthesis applications. The carbon shell of these particles can be suitably functionalised allowing both covalent and non-covalent attachment of metal catalyst to create magnetically recoverable catalysts suitable for a variety of catalytic applications.

Lu *et al*., developed a synthetic procedure for magnetic Co particles on ordered mesoporous carbons (Co-OMC) in which cobalt was deposited on a carbon/silica composite prior to the carbonisation process and combined with cobalt following of the dissolution of silica to create mesoporous carbon-coated Co nanoparticles with a 1 nm thick carbon shells (Figure 1.7).[80]

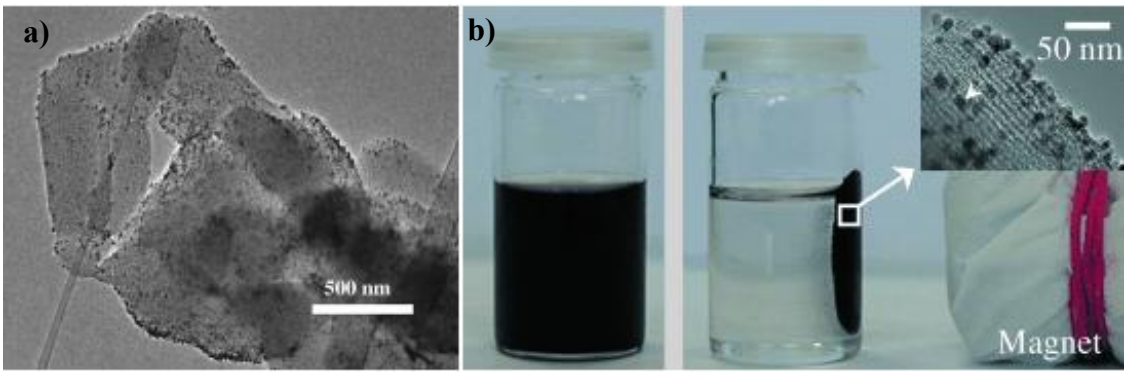

Figure 1.7. a) TEM image of Co–OMC, and b) separation of Co-OMC from the solution by a magnetic field (with a high magnefication TEM image of Co-OMC inset). Reproduced from Lu *et al.*[80]

The Co-OMC was then loaded with palladium and the catalytic activity of Pd-loaded Co-OMC was tested in the hydrogenation of octene to octane. It was reported that the reaction rate of the catalyst which had been recovered by applying a magnetic field was almost identical to the rate off the original material.

Kong *et al*. fabricated novel carbon coated hybrid microspheres (Fe_3O_4@C) using a polyethylene glycol (PEG) surfactant as the connecting agent between the Fe_3O_4 and glucose as the carbon source (Figure 1.8a).[81] Palladium was then deposited on the Fe_3O_4@C support and the catalytic ability and stability of the Fe_3O_4@C/Pd composite was investigated in the reduction of methyl orange (MO). To enable comparison, the renewable activity of Fe_3O_4@C/Pd recovered by applying a magnetic field, was compared with that of Pd/C recovered by centrifugation, in five successive catalyst

cycles. The recovered catalysts were treated with 1M HNO_3 and ultrasonic waves to remove the residual reactants and products after the reaction.

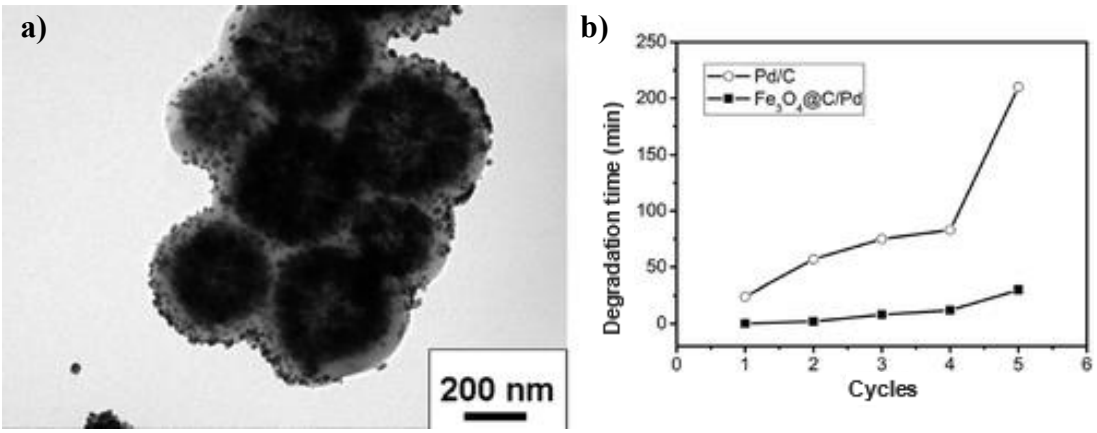

Figure 1.8. a) TEM image of Fe_3O_4@C/Pd b) Reduction time of MO in five successive cycles in the presence of Fe_3O_4@C/Pd and Pd/C catalysts. Reproduced from Kong *et al.*[81]

It was demonstrated that the trend in the increase of the reduction time of MO in the presence of Fe_3O_4@C/Pd was significantly shorter than that of the Pd/C after each cycle (Figure 1.13b). These results reveal that the catalytic activity of Fe_3O_4@C/Pd was better preserved than that of Pd/C which was attributed to reduced catalyst loss using magnetic recovery, and the strong interaction between the PdNPs and the Fe_3O_4@C. This was confirmed by TEM, which showed that after the fifth cycle significantly less leaching had occurred, compared to Pd/C, as a result of the greater resistance of the Fe_3O_4@C support to the repeated HNO_3 treatments.

Wittmann *et al*. reported the preparation of a palladium complex non-covalently attached to the graphene-layer of magnetic Co nanoparticles (Co/C) based on strong π-π stacking interactions between pyrene units and outer-most graphene layer.[82] The highly magnetic properties of the resultant Co/C and palladium complex powder permitted its efficient separation and recycling.

The authors used this immobilized catalyst in the hydroxycarbonylation reaction of 4-iodophenol with CO in water and observed moderately high conversions even after ten cycles by recycling the catalyst using an applied magnetic field (Figure 1.9).

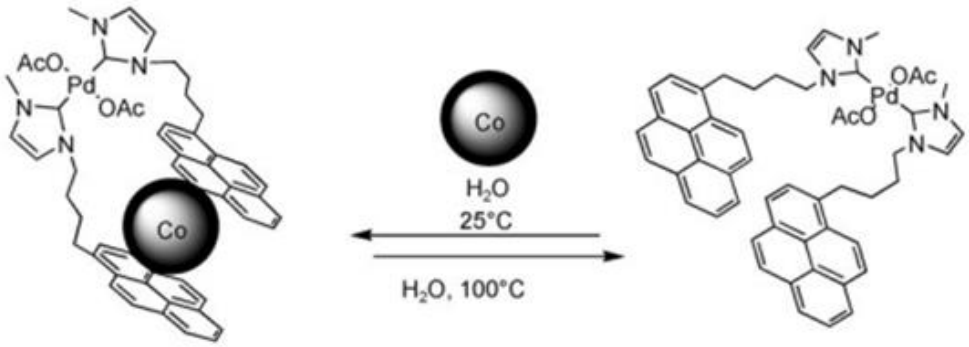

Figure 1.9. Preparation of a pyrene-tagged palladium NHC complex and reversible immobilization on carbon coated Co nanomagnets. Adapted from Wittmann *et al*.[82]

Overall, the studies based on the use of carbon coated metal particles as metal catalyst supports indicate that these materials can serve as a promising and versatile support for magnetically separable heterogeneous metal catalysts. Furthermore, the graphene-like outermost shell in magnetic nanoparticles, which is similar to the walls of carbon nanotubes, can facilitate their combination with carbon nanoreactors by non-covalent functionalisation to make the nanoreactors magnetically separable.

To summarize, the coupling of carbon nanoreactor systems with carbon coated magnetic nanoparticles using non-covalent interactions could potentially allow the separation of carbon nanoreactors and any catalytically active centres embedded in them from reaction mixtures in a fast, non-destructive and efficient way, simply by applying a magnetic field.

1.2.3 Carbon Nanomaterials in Electro-Catalytic Chemical Reactions

Carbon nanomaterials have been used in energy related applications such as energy storage devices, sensors and electrodes due to their excellent electrical conductivity.[81-84] One dimensional (1D) hollow carbon nanoreactors, such as CNT and GNF, have recently been exploited as nanostructured electrodes in a range of electrochemical reactions such as water splitting, *i.e.* hydrogen evolution (HER)[89,95,98] and oxygen evolution reactions (OER)[93,99], oxygen reduction (ORR)[98-100] and hydrogen oxidation reactions (HOR)[105-106]. A number of electrochemical studies has been carried out to date using either metal-free carbon nanoreactors or metal nanoparticles containing carbon nanoreactors.[87-104] Cui *et al.* reported for the first time in 2014 that MWNT can be utilised as a metal-free, highly active and stable electrocatalyst, stable over 4000 cycles, in HER in acidic electrolyte.[89]

Lu *et al.* studied surface-oxidized MWNT, post-treated by hydrothermal and electrochemical activation treatments and showed unprecedented OER activity even in the absence of surface metal oxide catalysts.[93] They observed that an overpotential of 350 mV is required to obtain a current density of 10 mA/cm^2 in 0.1 M KOH which was comparable with state-of-the-art transition metal OER catalysts based on metal oxides composites in basic media.

PtNPs confined within MWNT has been studied in the electrocatalytic oxidation of methanol in fuel cell applications and indicated improved activity and stability after 600 cycles as a result of confinement effects in comparison to PtNPs both externally adsorbed on MWNT and on commercial activated carbon (AC) supports.[94]

Youn *et al*. investigated the HER activity of Mo_2C, Mo_2N, and MoS_2 supported by carbon nanotube-graphene (CNT- GR) composite in 0.5 M H_2SO_4. Pt/C revealed the highest activity for HER with nearly zero onset overpotential and the highest current density of 0.541 mA/cm^2.[95] However, Mo_2C/CNT-GR exhibited very high activity and durability for HER with one of the best performances among the recently reported Mo-based catalysts with an onset potential of 62 mV, Tafel slope of 58 and an exchange current density of 0.062 mA/cm^2. Furthermore, each catalyst showed excellent electrochemical stability after 1000 repeated potential cycles. They suggested that the CNT-graphene hybrid support enhances the activity of molybdenum compounds by reducing the aggregation of the nanocrystals, enabling a large area and facilitating efficient electron transfer.

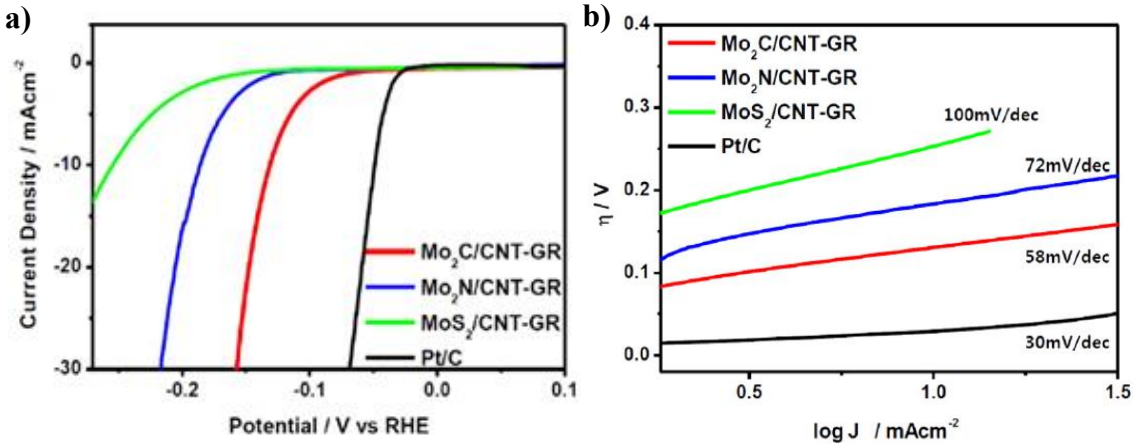

Figure 1.10. a) HER polarization curves and b) Tafel plots of Mo_2C/CNT-GR, Mo_2N/CNT-GR, and MoS_2/CNT-GR in acid media using a commercial Pt/C as a benchmark catalyst in HER. Reproduced from Yuan *et al.* [95]

Huang *et al.* studied the electrocatalytic performance of cobalt-based CNTs doped with palladium nanoparticles with different Pd content (Pd-CoCNTs) in the HER and ORR in comparison to commercial Pt/C, Pd/C, free-standing PdNPs and CoCNTs catalysts.[98]

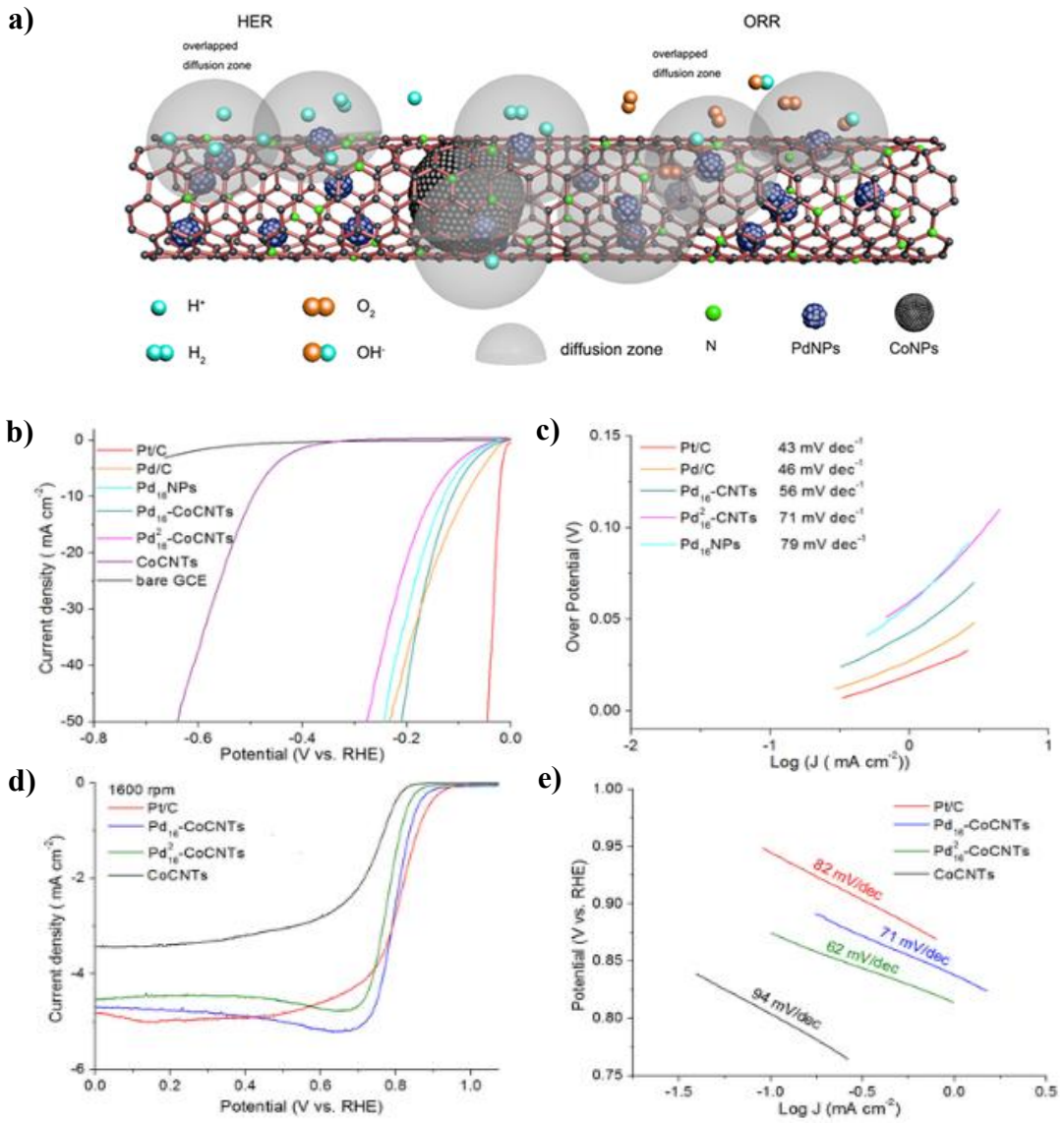

Figure 1.11. a) Schematic illustration of HER and ORR in the presence of Pd-CoCNTs. Polarization curves and Tafel slopes of Pd-CoCNTs in different Pd content (b-c) in HER compared to the Pd/C, Pt/C, free standing PdNPs and CoCNTs in H_2 saturated 0.5 M H_2SO_4 solution at a scan rate of 5 mV/s (d-e) in ORR compared to the Pt/C and CoCNTs recorded on a RDE at 1600 rpm in O_2 saturated 0.1 M KOH solution. Reproduced from Huang *et al.*[98]

They observed the best HER catalytic activity for the Pt/C in 0.5 M H_2SO_4. The HER activity of Pd-CoCNTs was not as good as that of Pt/C but comparable to that of commercial Pd/C (Figure1.8b-c). They also showed that the HER activity of Pd-CoCNTs was highly dependent on the Pd content, with an increase in the Pd content of Pd-CoCNTs enhancing the HER activity due to the presence of the highly active centres of the PdNPs on the surface of the CoCNTs, while the CoCNTs in the absence of Pd exhibited very poor performance. The durability of Pd-CoCNTs after 3000 cycles showed a negligible decrease in the current density and thus, it was a highly stable catalyst. Further to HER measurements, the authors studied the ORR activity of Pd-CoCNTs in 0.1 M KOH and observed a Pt/C like ORR activity at 1600 rpm rotating speed using a rotating disc electrode (RDE) (Figure 1.11d-e).

Ma *et al.*, investigated the OER and ORR activity of cubic cobalt–manganese oxide spinel (CMO) supported on non-oxidized carbon nanotubes (CMO@CNTs) under alkaline conditions.[99] They also studied the effect of other supports such as reduced graphene oxide, carbon black (Vulcan X-72R) and oxidized CNTs on the ORR and OER activity of CMO and compared them with commercial Pt/C. It was demonstrated that CMO@CNTs had the highest catalytic performance for both OER and ORR with a considerably lower OER onset potential of 1.49 V and the smallest Tafel slopes of 81.1 mV/decade and a much more positive ORR onset potential and higher cathodic currents among the other supports following an order of CMO@CNTs > CMO@rGO > CMO@oxCNTs > CMO@Vulcan (Figure 1.12).

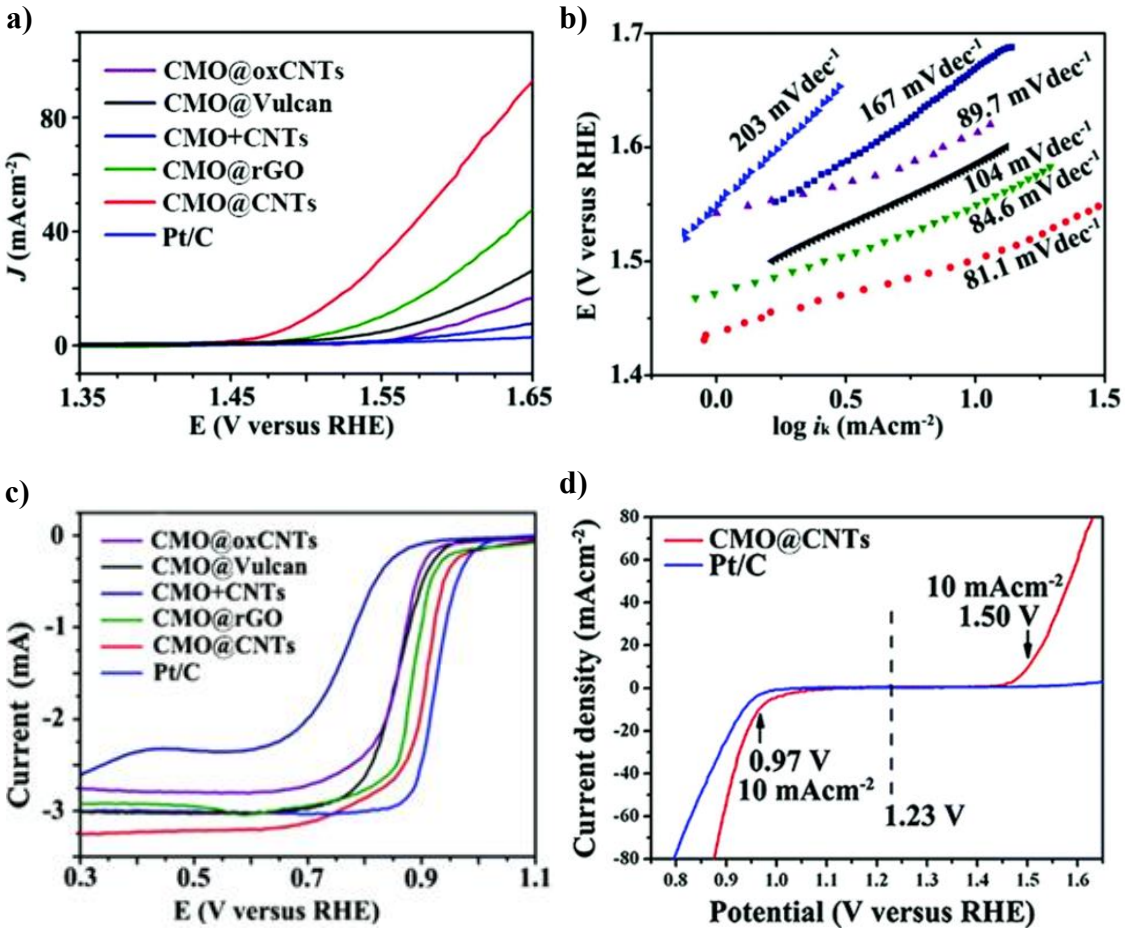

Figure 1.12. a) OER polarisation curves b) Tafel plots and c) ORR polarisation curves of CMO@CNTs, CMO@rGO, CMO@oxCNTs, CMO@Vulcan, CMO + CNTs, and Pt/C in oxygen saturated 1 M KOH at a potential sweeping rate of 5 mV s^{-1} and rotation speed of 1600 rpm. d) electro-catalytic activities of CMO@CNTs and Pt/C within the ORR and OER potential window. Reproduced from Ma *et al.*[99]

The outstanding ORR/OER activity of CMO@CNTs in an alkaline electrolyte was attributed to a combination of CMO and non-oxidized CNTs nanocomposite with high electrical conductivity, and a large electrochemically active surface area.

PtNPs confined within shortened GNF (S-GNF) were investigated in ORR by Gimenez-Lopez *et al*. and are observed to be incredibly stabile to extensive cycling in comparison to commercial PtNPs on carbon black due to the stabilised of the PtNPs at the step edges in GNF during the cycling (50000 cycles were performed, Figure 1.13).[100]

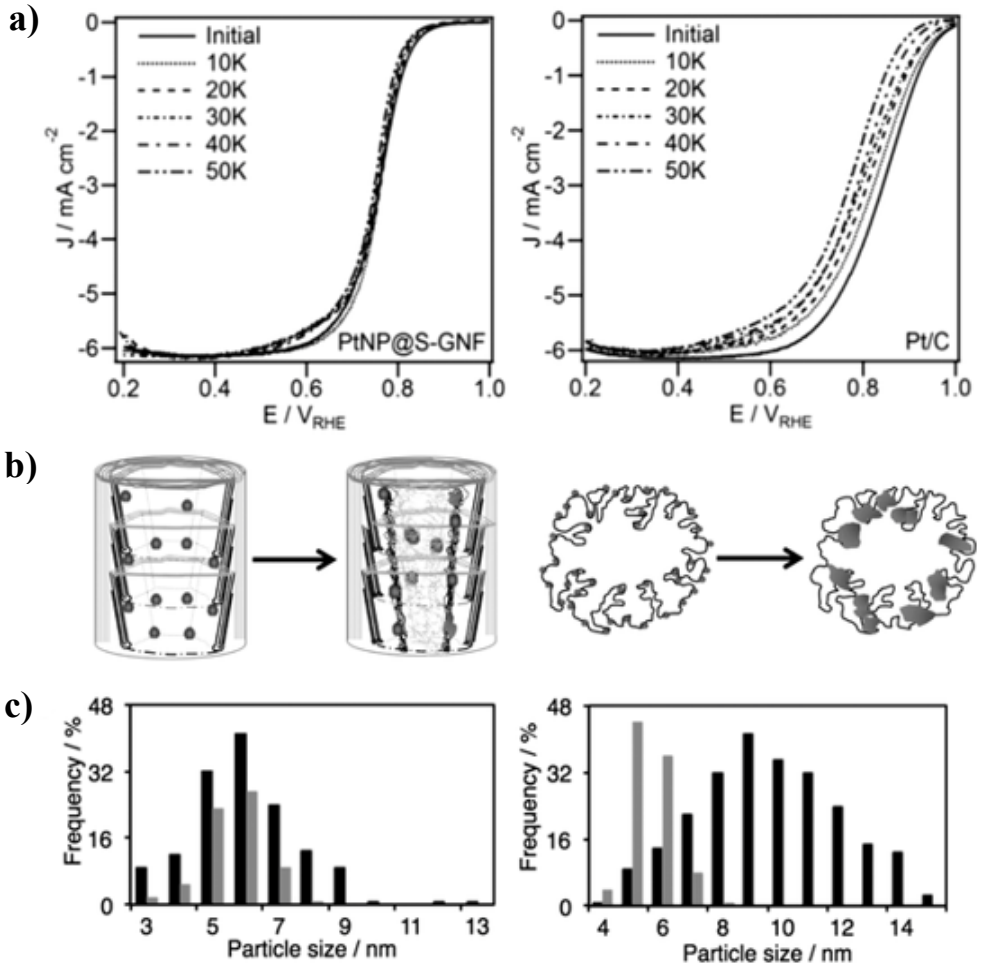

Figure 1.13. Comparison of the PtNPs@S-GNF and Pt/C electrocatalysts over 50000 potential cycles. a) ORR polarization curves, showing superior durability of PtNPs@S-GNF. b) Schematic diagrams and c) nanoparticle size distribution before (grey data bars) and after (black data bars) 50000 cycles of ORR of PtNPs@S-GNF and Pt/C, respectively. Reproduced from Gimenez-Lopez *et al.*[100]

Davodi *et al*. studied the OER and HER activity of nitrogen doped multi-walled carbon nanotubes (NMWNTs) in alkaline media.[101] They reported that 20-NMWNT ('20' refers to the NMWNTs prepared with a sonication time of 20 h) exhibited superior electrocatalytic activity as bifunctional metal-free catalysts in OER with an onset potential of 1.54 V and 78 mV/dec Tafel slope in 0.1 M NaOH and thus, were the most active electrocatalysts for OER so far, while the pristine MWNT showed very poor catalytic activity compared to it (Figure 1.14a). The authors also observed that the 20-NMWNT indicated a significant improvement in HER activity compared to that of pristine MWNTs which was comparable to that of Pt/C (Figure 1.14b). The stability of the catalyst was also investigated in 1000 potential cycles, and an excellent stability in both OER and HER was observed, with no significant degradation. The excellent OER/HER activity and stability of 20-NMWNT was assigned to the high conductivity and large surface area of NMWNTs and the presence of pyridinic N serving as the highest active site, compared to other nitrogen types, toward both OER and HER.

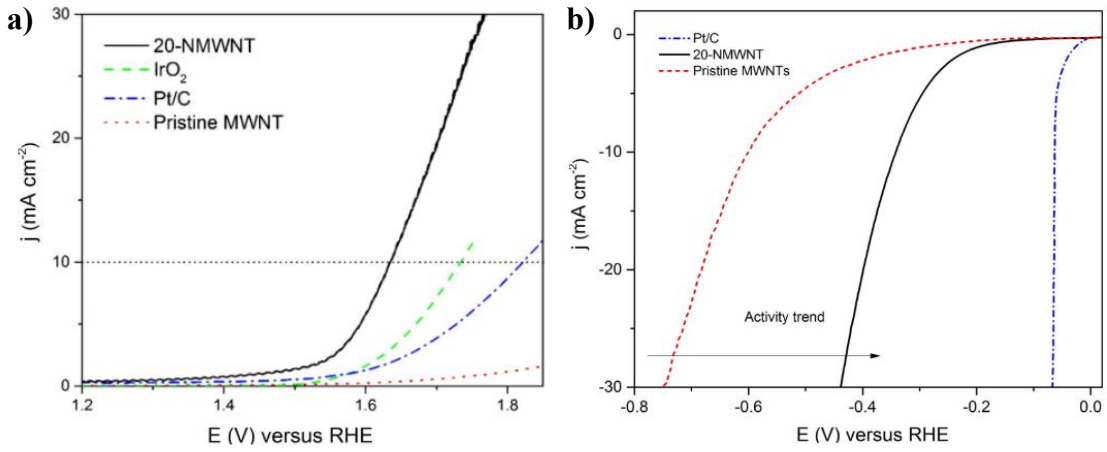

Figure 1.14. a) The RDE polarization curves obtained with 20-NMWNT, IrO2, Pt/C (20 wt%), and pristine MWNT in 0.1 M NaOH solution. The polarization curves have been reported with iR compensation at a scan rate of 5 mV/s and a rotation of 1600 rpm. b) The HER polarization curves of pristine MWNT (blue dash dotted line), 20-NMWNT (black solid line), and Pt/C (red dashed line). The polarization curves have been reported with iR compensation at a scan rate of 5 mV/s. Reproduced from Davodi *et al.* [101]

All of these studies demonstrate the potential advantages of metal-free carbon nanoreactors or metal nanoparticles supported by carbon nanoreactors for improved electro-catalytic efficiency and stability in a number of electrochemical applications.

1.3 SUMMARY

This chapter surveys a number of studies on the catalytic ability of the metal nanoparticles confined inside 1D carbon nanoreactors in industrially important catalytic reactions and electrochemical applications.

Carbon nanoreactor supported metal nanoparticles have shown a wide variety of promising properties in chemical reactions. Firstly, the restricted nanoscale environment of carbon nanoreactors ranging from 1 to 100 nm enables control of the nanoparticle growth and stability. The environment can also accommodate a number of different catalytic reaction types, as the internal cavity of nanoreactors can host molecules of different shapes and sizes and can influence the way in which products are formed. Secondly, reactions performed in the confined space of nanoreactors benefit from changes in the local concentration of reactant molecules, which can result in enhanced interactions between the reactants and catalyst and thus influence the activity of the catalyst significantly. Thirdly, the conductive nature of carbon nanoreactors can be exploited to control the electron transfer interactions between the molecules, metal nanoparticles and nanoreactors in catalytic reactions, in particularly in electrocatalysis.

Furthermore, the addition of magnetic nanoparticles to carbon nanoreactors is an exciting area, currently being investigated to enable the facile recovery of catalysis from reaction mixtures. A number of studies outlined above based on the use of carbon-coated metal particles as metal catalyst supports indicate that these materials may serve as a promising and versatile alternative for magnetically separable heterogeneous metal catalysts. The

coupling of carbon nanoreactor systems with magnetic nanomaterials could potetnially allow the separation of carbon nanoreactors from reaction mixtures in a fast, easy and efficient way by simply applying a magnetic field.

However, we believe the synthetic routes to such exciting materials are still yet to be fully developed or understood. Therefore, the investigation of a methodology to synthesise catalytically active and magnetically separable carbon nanoreactors containing metal nanoparticle catalyst and the subsequent testing of both the catalytic activity and recyclability of magnetic heterogeneous catalyst is crucial if the full industrial application of such catalysts is to be achieved.

1.4 REFERENCES

1. J. R. H. Ross, Heterogeneous Catalysis Fundamentals and Applications, Elsevier, Amsterdam, 2012.
2. G. Rothenberg, The Basics of Catalysis, in Catalysis: Concepts and Green Applications, Wiley-VCH Verlag GmbH & Co. KGaA, Weinheim, Germany, 2008.
3. S. S. B. Viswanathan, A. V. Ramaswamy, S. Sivasanker, Catalysis: Principles and Applications, CRC Press, Boca Raton, FL, 2002.
4. A. Zecchina, S. Bordiga, E. Groppo, Selective nanocatalysts and nanoscience: concepts for heterogeneous and homogeneous catalysis. Wiley-VCH Germany, 2011.
5. J. Heveling, *J. Chem. Educ.*, 2012, 89, 1530−1536.
6. G. A. Rance, D. H. Marsh, S. J. Bourne, T. J. Reade, A. N. Khlobystov, *ACS Nano*, 2010, 4, 4920-4928.

7. J. L. Contreras and G. A. Fuentes, *Sintering - Methods and Products, Sintering of Supported Metal Catalysts*, ISBN: 978-953-51-0371-4, InTechOpen, Rijeka, 2012.
8. T. W. Chamberlain, T. Zoberbier, J. Biskupek, A. Botos, U. Kaiser, A. N. Khlobystov, *Chem. Sci*., 2012, 3, 1919-1924.
9. G. J. K. Acres, A. J. Bird, J. W. Jenkins and F. King, *The Design and Preparation of Supported Catalysts*, The Royal Society of Chemistry, Oxford, 1981.
10. R. B. N. Baig, R. S. Varma, *ACS Sustainable Chem. Eng.* 2013, 1, 805.
11. T. Chatterjee, R. Dey, B. C. Ranu, *J. Org. Chem.* 2014, 79, 5875.
12. A. Mandal, D. Roy, R. V. Chaudhari, M. Sastry, *Chem. Mater.* 2004, 16, 3714-3724.
13. P. S. F. Mendesa, G. Lapisardi, C. Bouchy , M.Rivallan, J. M. Silvaa, M. F. Ribeiro, *Appl. Catal., A*, 2015, 504, 17-28.
14. A. H. Chughtai, N.Ahmad, H. A. Younus, A. Laypkovc, F. Verpoort, Chem. Soc. Rev., 2015, 44, 6804
15. C. Wu, M. Zhao, *Adv. Mater.* 2017, 29, 1605446.
16. B. Mondal, K. Acharyya, P. Howlader, P. S. Mukherjee, *J. Am. Chem. Soc.* 2016, 138, 1709−1716.
17. Z. Y. Zhang, F. Xiao, J. B. Xi, T. Sun, S. Xiao, H. R. Wang, S. Wang, Y.Q. Liu *Sci. Rep*., 2014, 4, 4053.
18. T. Harada, S. Ikeda, F. Hashimoto, T. Sakata, K. Ikeue, T. Torimoto, M. Matsumura, *Langmuir*, 2010, 26, 17720-17725.
19. A. H. Labulo, B. S. Martincigh, B. Omondi, V. O. Nyamori, *J.Mat. Sci.*, 2017, 52 (16), 9225-9248.
20. P. Serp, J. L. Figueiredo, Carbon materials for catalysis, *Wiley*, 2009, 56.

21. P. Serp, B. Machado, Nanostructured Carbon Materials for Catalysis, Royal Society of Chemistry, Cambridge, U.K., 2015, 570.

22. P. Serp, M. Corrias, P. Kalck, *Appl. Catal. A*, 2003, 253, 337–358.

23. G. G. Wildgoose, C. E. Banks, R. G. Compton, *Small*, 2006, 2, 182-193.

24. P. Serp, E. Castillejos, *Chem. Cat. Chem*., 2010, 2, 41–47.

25. M. J. Ledoux, R. Vieira, C. Pham-Huu, N. Keller, *J. Catal.* 2003, *216*, 333.

26. J. K. Chinthaginjala, K. Seshan, L. Lefferts, *Ind. Eng. Chem. Res*. 2007, 46, 3968−3978.

27. M. Menon, A. N. Andriotis, G. E. Froudakis, *Chem. Phys. Lett.*, 2000, 320, 425-434.

28. G. Chen, Y. Kawazoe, *Phys. Rev. B*, 2006, 73, 125410.

29. S. Iijima, *Nature*, 1991, 354.

30. M. S. Dresselhaus, G. Dresselhaus, A. Jorio, *Annu. Rev. Mater. Res*., *2004*, *34*, *247*–278.

31. S. A., Hodge, M. K., Bayazit, K. S., Coleman, M.; Schaffer, *Chem. Soc. Rev.*, 2012, 41, 4409-4429.

32. S. A. Miner, G. A. Rance, A. N. Khlobystov, *Chem. Soc. Rev.*, 2016, 45**,** 4727-4746.

33. M. M. Daenen, R. D. De Fouw, B. Hamers, P. G. A. Janssen, K. Schouteden, M. A. J. Veld, The Wondrous World of Carbon Nanotubes 'a review of current carbon nanotube technologies'. Eindhoven University of Technology, 2003, 1-96.

34. B. K. T. Kenneth, *C.* Singh, *M.* Chhowalla, W. *I.* Milne, *Encyclopedia of Nanoscience and Nanotechnology,* 2004, 1, 665-686.

35. S. A. Miners, G. A. Rance, A. N. Khlobystov, *Chem. Commun.*, 2013, 49, 5586-5588.

36. X. Pan, and X. Bao, *Acc. Chem. Res.* 2011, 44, 553-562.

37. T. W. Chamberlain, J. H. Earley, D. P. Anderson, A. N. Khlobystov and R. A. Bourne, *Chem. Commun.* 2014, 50**,** 5200-5202.

38. J.-P. Tessonnier, L. Pesant, G. Ehret, M. J. Ledoux and C. Pham-Huu, *Appl. Catal., A*, 2005, 288, 203-210.

39. C. Pham-Huu, N.Keller, G. Ehret, L.J. Charbonniere, R. Ziessel, M. J. Ledoux, *J. Mol.Catal. A Chem.*, 2001, 170, 155–163.

40. Z. sun, Y. Zhao, Y. Xie, R. Tao, H. Zhang, C. Huang, Z. Liu, *Green Chem*., 2010, 12, 1007–1011.

41. Z. Guan, S. Lu and C. Li, *J. Catal.*, 2014, 311, 1-5.

42. J. L. Figueiredo and M. F. R. Pereira, Carbon materials for catalysis, Carbon as Catalyst, in Carbon Materials for Catalysis (eds P. Serp and J. L. Figueiredo), John Wiley & Sons, Inc., Hoboken, NJ, USA, 2008.

43. J. Zhu, A. Holmen and D. Chen, *Chem. Cat. Chem.* 2013, 5, 378-401.

44. A. N. Khlobystov, *ACS Nano* 2011, 5, 9306-9312.

45. X. Pan, and X. Bao, *Chem. Commun*. 2008, 6271-6281.

46. E. Castillejos, P. J. Debouttiere, L. Roiban, A. Solhy, V. Martinez, Y. Kihn, O. Ersen, K. Philippot, B. Chaudret and P. Serp, *Angew. Chem., Int. Ed.* 2009, 48, 2529-2533.

47. C. H. Li, Z. X. Yu, K. F. Yao, S. F. Ji, J. Liang, *J. Mol. Catal. A*, 2005, 226, 101-105.

48. W. A. Solomonsz, G. A. Rance, M. Suyetin, A. La Torre, E. Bichoutskaia and A. N. Khlobystov, *Chem. Eur. J.* 2012, 18, 13180-13187.

49. X. Pan, Z. Fan, W. Chen, Y. Ding, H. Luo and X. Bao, *Nature Mater.* 2007, 7, 507-511.

50. M. A. Lebedeva, T. W. Chamberlain. A. Thomas B. E. Thomas, C. T. Stoppiello, E. Volkova, M. Suyetin, A. N. Khlobystov, *Nanoscale* 2016, 8, 11727-11737.

51. E. Castillejos, M. Jahjah, I. Favier, A. Orejón, C. Pradel, E. Teuma, A. M. Masdeu-Bultó, P. Serp and M. Gómez, *ChemCatChem*, 2012, 4, 118-122.

52. A. M. Zhang, J. L. Dong, Q. H. Xu, H. K. Rhee and X. L. Li, *Catal. Today*, 2004, 93-95, 347-352.

53. J. Deng, P. Ren, D. Deng, L. Yu, F. Yang and X. Bao, *Energy Environ. Sci*. 2014, 7, 1919.

54. X. Li, T. Hungria C. G. Marcelot, M. R. Axet, P. -F. Fazzini, R. Tan, P. Serp, and K. Soulantica, *Chem. Commun.* 2016, 52, 2362-2365.

55. G. G. Wildgoose, C. E. Banks, R. G. Compton, *Small*, 2006, 2, 182-193.

56. I. Karamé, Hydrogenation, *InTech*, 2012, DOI: 10.5772/3208.

57. I. Kubičková, D. Kubička, *Waste Biomass Valor*,2010, 1, 293-308.

58. D. Kubička, P. Šimáček, N. Žilková, *Top Catal*, 2009, 52, 161-168.

59. P. Liu, H. Xie, S. Tan, K. You, N. Wang, H., Luo, *React. Kinet. Catal. Lett.*, 2009, 97, 101−108.

60. F. Li, R. Ma, B. Cao, J. Liang, Q. Ren, H. Song, *Appl. Catal., A.*, 2016, 514, 248–252.

61. A. Baiker, *Chem. Rev.*, 1999, 99, 453−473.

62. M. Burgener, D. Ferri, J. Grunwaldt, T. Mallat, A. Baiker, *Phys. Chem. B*, 2005, 109, 16794-16800.

63. M. A. McHugh, V. J. Krukonis, Supercritical fluid extraction: principles and practice. Butterworth-Heinemann, Boston, MA, 1994, 2nd edition.

64. M. Türk, *J. Supercrit. Fluids*, 1999, 15, 78-89.

65. L. T. Taylor, Supercritical Fluid Extraction. John Wiley &Sons: New York, 1996.

66. M. G. Hitzler, M. Poliakoff, *Chem. Commun*., 1997, 1667-1668.

67. M. G. Hitzler, F. R. Smail, S. K. Ross, M. Poliakoff, *Organic Process Research & Development*, 1998, 2, 137-46.

68. L. Alaerts, J. P. Wahlen, A. Jacobs, D.E. De Vos, *Chem Commun*. 2008, 15, 1727-1737.

69. A. Corma, H. Garcia, *Adv. Synth.Catal*., 2006, 348, 1391-1412.

70. L. M. Rossi, N. J. S. Costa, F. P. Silva, R. Wojcieszak, *Green Chem.*, 2014,

71. A. Hutten, D. Sudfeld, I. Ennen, G. Reiss, W. Hachmann, U. Heinzmann, K. Wojczykowaki, P. Jutzi, W. Saikaly, G.J. Thomas. *Biotechnol.*, 2004, 112, 47.

72. A. H. Lu, W. Schmidt, N. Matoussevitch, H. Bönnemann, B. Spliethoff, B. Tesche, E. Bill, W. Kiefer, F. Schüth, *Angew. Chem.*, 2004, 116, 4403.

73. H. Jia, Y. Lian, M. Ishitsuka, T. Nakahodo, Y. Maeda, T. Tsuchiya, T. Wakahara, T. Akasaka, *Sci. Technol. Adv. Mater.*, 2005, 6, 571-581.

74. A-H. Lu, E. L. Salabas, F. Schüth, *Angew. Chem. Int. Ed.*, 2007, 46, 1222 – 1244.

75. L, Zhang, Li. Pinhua, L. Hongji, L. Wang, *Catal. Sci. Technol*., 2012, 2, 1859-1864.

76. R. N. Grass, W. J. Stark, *J. Mater. Chem.* 2006, 16, 1825-1830.

77. R. Fuhrer, E. K. Athanassiou, N. A, Luechinger, W.J. Stark, S*mall*, 2009, 5, 383–388.

78. R. N. Grass, E. K. Athanassiou, W. J. Stark, *Angew. Chem. Int. Ed*., 2007, 46, 4909-4912.

79. I.K. Herrmann, R. N. Grass, D. Mazunin, W. J. Stark, *Chem. Mater*., 2009, 21, 3275-3281.

80. A-H. Lu, W. Schmidt, N. Matoussevitch, H. Bönnemann, B. Spliethoff, B. Tesche, E. Bill, W. Kiefer, F. Schüth, Angew. *Chem. Int. Ed.*, 2004, 43, 4303 –4306.

81. L. Kong, X. Lu, X. Bian, W. Zhang, C. Wang, *ACS Appl. Mater. Interfaces* , 2011, 3, 35–42.

82. S. Wittmann, A. Schätz, R. N. Grass, W. J. Stark, O. Reiser, *Angew. Chem. Int. Ed.*, 2010, 49, 1867-1870.

83. K. Balasubramanian, T. Kurkina, A. Ahmad, M. Burghard, K. Kern, *J. Mater. Res.*, 27 (2) (2012), 391-402

84. M. Pumera,*Chem. Eur. J.* 2009, 15, 4970 – 4978.

85. S. A. Hodge, S. Fogden, C. A. Howard, N. T. Skipper and M. S. P. Shaffer, *ACS Nano*, 2013, **7**, 1769.

86. I. Dumitrescu, P.R. Unwin, J. V. Macpherson, *Chem. Commun.*, 2009, 6886–6901.

87. J. Wang, Z. Dong, J. Huang, J. Li, X. Jin, J. Niu, J. Sun, J. Jin and J. Ma, *Appl. Surf. Sci.*, 2013, 270, 128-132.

88. D. Deng, L. Yu, X. Chen, G. Wang, L. Jin, X. Pan, J. Deng, G. Sun and X. Bao, *Angew. Chem., Int. Ed.*, 2013, 52, 371-375.

89. W. Cui, Q. Liu, N. Cheng, A. M. Asiri, X. Sun, *Chem. Comm.* 2014, 50, 940.

90. S. Pal, M. Sahoo, V. T. Veettil, K. K. Tadi, A. Ghosh, P. Satyam, R. K. Biroju, P. M. Ajayan, S. K. Nayak, T. N. Narayanan, *ACS Catal.*, 2017, 7, 2676−2684.

91. M. Gong, W. Zhou, M. C. Tsai, J. Zhou, M. Guan, M. C. Lin, B. Zhang, Y. Hu, D. Y. Wang, J. Yang, S. J. Pennycook, B. J. Hwang, H. Dai, *Nat. Commun.* 2014, *5*, 4695.

92. S. Li, Z. Lu, Y. Yang, Y. Liu, H. Zou, H. Yang, J. Jin, J. Ma, *J. Mat. Chem. A*, 2017, 5, 6405–6410

93. X. Lu, W, Yim, B. H. R. Suryanto, C. Zhao, *J. Am. Chem. Soc.*, 2015, 137, 2901−2907.

94. J. Zhang, S. Guo, J. Wei, Q. Xu, W. Yan, J. Fu, S. Wang, M. Cao and Z. Chen, *Chem.-Eur. J.*, 2013, 19, 16087-16092

95. D. Y. Youn, S. Han, J. Y. Kim, J. Y. Kim, H. Park, S. H. Choi, J. S. Lee, *ACS Nano*, 2014, *8*, 5164–5173.

96. R. L. McSweeney, T. W. Chamberlain, E. S. Davies and A. N. Khlobystov, *Chem. Commun.*, 2014, 50, 14338-14340.

97. E. Heydari-Bafrooei, S. Askari, *Int. J. of Hydrogen Energy*, 2017, 42, 2961-2969.

98. B. Huang, L. Chen, Y. Wang, L. Quyang, J. Ye,*Chem.Eur.J*., 2017, 23,7710–7718.

99. T. Ma, C. Li, X. Chen, F. Cheng, J. Chen, *Inorg. Chem. Front*., 2017, DOI: 10.1039/c7qi00367f.

100. M. D. C. Gimenez-Lopez, A. Kurtoglu, D. A. Walsh, A. N. Khlobystov, *Adv. Mat.*, 2016, 28, 9103-9108.

101. F .Davodi, M. Tavakkoli, J. Lahtinen, T. Kallio, *J. Catal.*, 2017, 353, 19-27.

102. H. Han, S. Chao, X. Yang, X. Wang, K. Wang, Z. Bai, L. Yang, *Int. J. of Hydrogen Energy*, 2017, 42, 16149-16156.

103. M. Beltrán-Gastéluma, M. I. Salazar-Gastéluma, R. M. Félix-NavarroaS.Pérez-Sicairosa, E. A. Reynoso-Sotoa, S. W. Lina, J. R. Flores-Hernández, T. Romero-Castañón, I. L. Albarrán-Sánchez, F. Paraguay-Delgadoc, *Energy*, 2016, 109, 446-455.

104. J. Guo, J. Wang, C, Xuan, Z. Wu, W. Lei, J. Zhu, W. Xiao, D. Wang, *J. Electroanal. Chem.*, 2017, 801, 7–13.

105. R. K. Das, Y. wang, S. V. Vasilyeva, E. Donoghue, I. Pucher, G. Kamenov, H-P. Cheng, A. G. Rinzler, *ACS Nano*, 2014, *8*, 8447–8456.

106. Z. Zhuang, S. A. Giles, J. Zheng, G. R. Jenness, S. Caratzoulas, D. G. Vlachos, Y. Yan, *Nat. Commun*. 2016, 7, 10141.

2 COMPARISON OF ALKENE HYDROGENATION IN CARBON NANOREACTORS OF DIFFERENT DIAMETERS: PROBING THE EFFECTS OF NANOSCALE CONFINEMENT ON RUTHENIUM NANOPARTICLE CATALYSIS

2.1 INTRODUCTION

Gaining control of chemical reactions in order to improve the yield of a particular product and/or change the reaction pathway is a great challenge in chemical synthesis. One method commonly used to achieve this is to perform reactions in sterically confined environments using materials such as zeolites, porous silica or alumina, molecular cages and carbon nanomaterials to act as nanoscale reaction vessels or nanoreactors.[1-9] All of these systems have nanosized pores, holes or channels of different geometries and diameters which are capable of accommodating reactants and affecting the distribution of products by imparting some form of steric effect on the transition states or intermediates of reactions.

Carbon nanostructures (CNS) have recently become of great interest for use as nanoreactors in a variety of different catalytic chemical reactions as they are robust, chemically inert, and available in a large range of well-defined pore shapes and sizes. Most importantly, due to recent advances in production, CNS are now readily available in large quantities at low cost which opens up the potential for application in large-scale preparative syntheses for the first time.[10-12] In addition to acting as reaction vessels and templates to the formation of specific products, CNS also make the ideal support materials for metal nanoparticle (MNP) catalysts. By immobilizing catalytic NPs inside CNS it is possible to combine all of the advantages of nanoreactors, offering control of the size and shape of the reaction volume, with the inherent advantages of heterogeneous catalysis, *i.e.* enhanced stability and recyclability of metal nanoparticles.[13-17] As a result a significant number of studies have reported the application of MWNTs and hollow

GNFs, with internal channels ranging from 5-50 nm, as nanoscale reaction vessels and flow reactors for catalytic chemical reactions. In which their commensurate hollow structure facilitates encapsulation of the metal nanoparticles inside the nanotube and provides the perfect environment for reactions to occur within a strictly controlled nanoscale volume.[9, 17-22] Serp *et al.* performed the selective hydrogenation of cinnamaldehyde to cinnamyl alcohol over a bimetallic Pt–Ru catalyst confined inside MWNTs and compared the metal catalyst activity with both the same sized free standing MNPs and MNPs supported on the outside surface of MWNTs.[17] A significant increase in catalytic performance with higher turnover frequency and selectivity for cinnamyl alcohol was observed for the catalyst inserted in MWNTs as a result of the confinement and enrichment of reactant concentration inside the nanotubes due to stronger interactions between the molecules and the internal surface of the carbon nanostructures. Pan *et al.* reported that Rh nanoparticles confined inside carbon nanotubes substantially enhanced ethanol conversion compared with the same catalyst located outside of the nanotubes.[9] Moreover, platinum nanoparticles both inserted into GNFs and adsorbed on to the outside surface were probed in the competitive hydrosilylation reaction of phenylacetylene by Solomonsz *et al.,* demonstrating significant changes in the selectivity of reactions of aromatic and aliphatic molecules within the nanoreactor.[18]

The latest studies reveal that the size and shape of the nanotube channel enhances the stability and selectivity of the confined NP catalysts allowing strict control of the nanoparticle size, functionality and reactivity by providing stabilization to the NPs, preventing aggregation into larger particles and bulk metal.[23-26] Less is known about the use of narrower SWNTs and DWNTs, with an internal mean diameter of ~1-2 nm, however it has been shown that they enable the formation of small, highly stable metal nanoparticles.[25] The advantageous nature of MNPs@SWNT catalysts, in which the cavity

dimensions are commensurate with the size of small organic reactant molecules, is that they impart significant steric influence on reaction pathways thus exhibiting greater effects on the products of reactions than wider MWNTs. Recently other researchers in the group reported the hydrogenation reaction of alkenes catalyzed by RuNPs confined within extremely narrow SWNTs and observed very high yields of the products as a result of an enrichment of reactant species inside the nanonoreactor due to confinement effects.[27] Narrow DWNTs (nanotube diameter of 1-1.5 nm) were utilised to stabilise Pd-V bimetallic nanoparticles and the resultant catalyst was shown to be more active for benzene hydroxylation than the same NPs in wider, and hence less confined MWNT (nanotube diameter = 4-8 nm).[28] Similar enhancements in activity as a result of extreme nanotube confinement have also been reported for sub-nanometre titania NPs in DWNTs for propylene epoxidation[29] and Re NPs in DWNT for benzene hydroxylation.[30]

There are also a few examples of non-catalysed chemical reactions within SWNT, such as a study by Miners *et al*. who reported the effect of SWNT diameter on the selectivity of *N*-phenylacetamide bromination within SWNT and showed that the inner cavity of the nanotube changed the regioselectivity and activity of a bromination reaction.[10, 31-32] These studies demonstrate that the extreme confinement imposed by the unique reaction environment of SWNT-based nanoreactors can significantly alter the selectively and rate of chemical reactions. In addition, the SWNT support changes the chemical and physical properties of the NP catalyst, allowing strict control of the NP functionality and reactivity as well as NP size.[27] Thus, confinement of catalytic processes in very narrow carbon nanoreactors has been shown to control the size and shape selectivity of hydrogenation reactions.

In this chapter the effects of such extreme confinement on the mass transport of reactants and products into and out of SWNT-based catalytic nanoreactors are explored and

compared to GNFs, which are wider, and therefore more accessible to reactants and crucially, in contrast to MWNTS, have structured internal channels which can also influence chemical reactions. With this aim, a number of RuNPs@carbon nanoreactor catalyst were created and the catalytic properties of these materials were probed in selective hydrogenation reactions of norbornene and benzonorbornadiene using scCO2 as the solvent in a high pressure batch reactor system. Consequently, RuNPs confined within SWNTs and GNFs resulted in dramatic changes to reactions compared to unconfined RuNPs on the outer surface of SWNTs or on carbon black.

2.2 RESULTS AND DISCUSSIONS

In this study, a simple and efficient approach for catalyst synthesis in the inner cavity of carbon nanotubes is used to create very active Ru nanoparticles within an extremely constrained carbon nanoreactor environment.[35] In this approach, $Ru_3(CO)_{12}$ molecules inserted from the vapour phase into the freshly opened SWNTs are decomposed to form Ru nanoparticles within the nanotube (RuNPs@SWNT). High resolution transmission electron microscopy (HRTEM) imaging of the resultant hybrid nanomaterial RuNPs@SWNT reveals the shape, size and location of Ru nanoparticles inside the nanoreactor (Figure 2.1). HRTEM confirmed that the RuNPs were located mostly inside the SWNTs, where the nanotube sidewall stabilises and templates the formation of NPs resulting in small, well defined particles with a narrow size distribution, (d_{NP} = 0.74 ± 0.18 nm, Table 1).

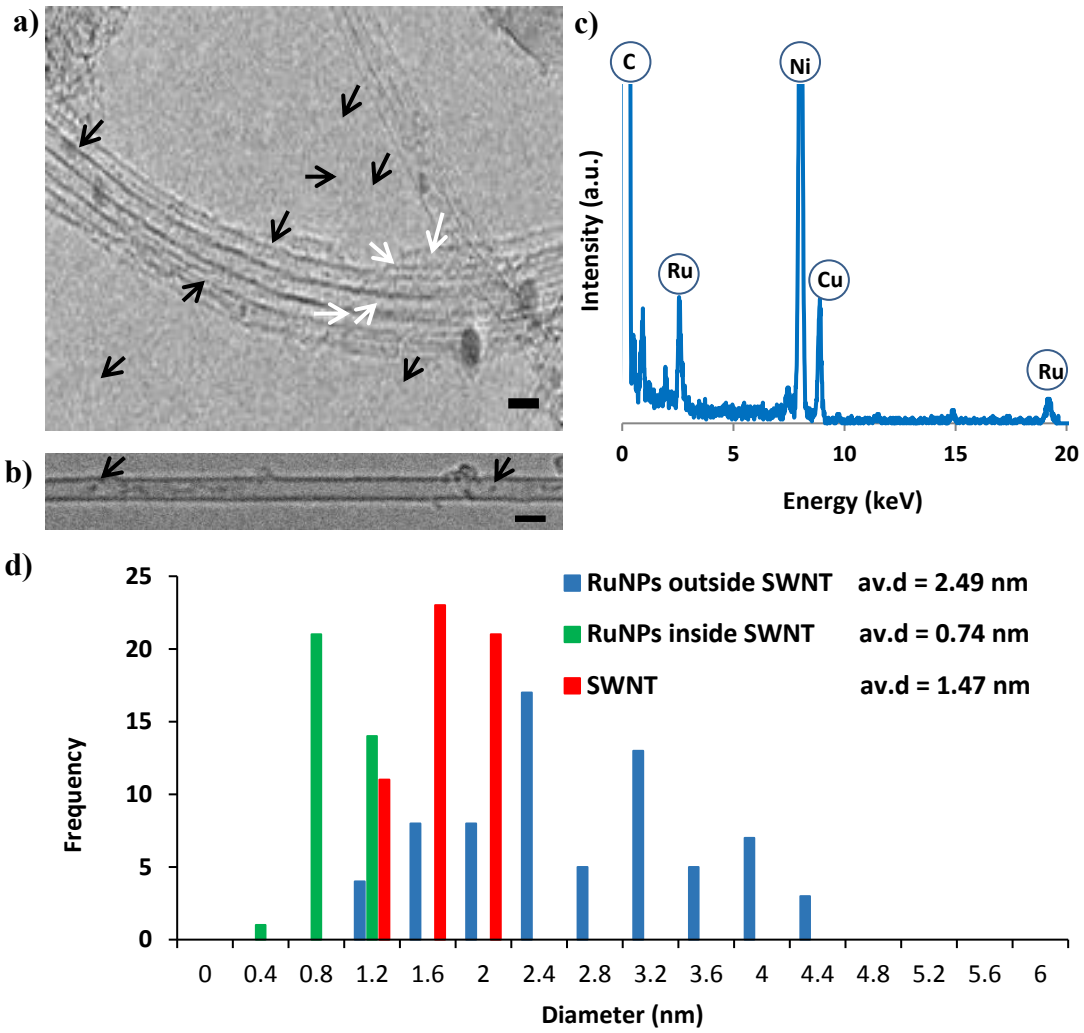

Figure 2.1. (a-b) HRTEM image of RuNPs@SWNT loaded with 3.1% of Ru by wt., black and white arrows indicate RuNPs inside and outside of the SWNT respectively. **c)** EDX spectrum showing the composition of RuNP@SWNT. Ni peaks are from the synthetic process of SWNT manufacture and the Cu from the TEM grid, respectively. d) A histogram showing the size distribution of SWNT (red), RuNPs located inside the SWNT (green) and RuNPs located outside the SWNT (blue). Scale bar: 2 nm.Scale bars: 2 nm in all images.

A combination of thermogravimetric analysis (TGA) and inductively coupled plasma optical emission spectrometry (ICP-OES) was used to determine the precise loading of Ru in RuNPs@SWNT showing the material to be 1.6 % Ru by weight (Experimental section 2.4.2). This represents the maximum loading of Ru nanoparticles into SWNT with the remaining Ru material deposited and subsequently washed from the outer walls

of the nanotubes prior to nanoparticle formation, an essential step to ensure no unconfined nanoparticles are present to take part in the reaction (Figures 2.15 and Table 2.5 in Experimental section 2.4.2,). However, TEM reveals a small portion (<10 %) of NPs are located on the outside of the nanotubes where they do not benefit from the same templating effect and therefore are larger and less uniform (d_{NP} = 2.49 ± 0.85 nm) (Figure 2.1a).

Energy dispersive X-ray spectroscopy (EDX), X-Ray photoelectron spectroscopy (XPS), and lattice spacing analysis of HRTEM images and powder XRD are consistent with a hexagonally close packed structure of metallic the RuNPs (Figures 2.1a-c, 2.2a, 2.4b and 2.8).[36]

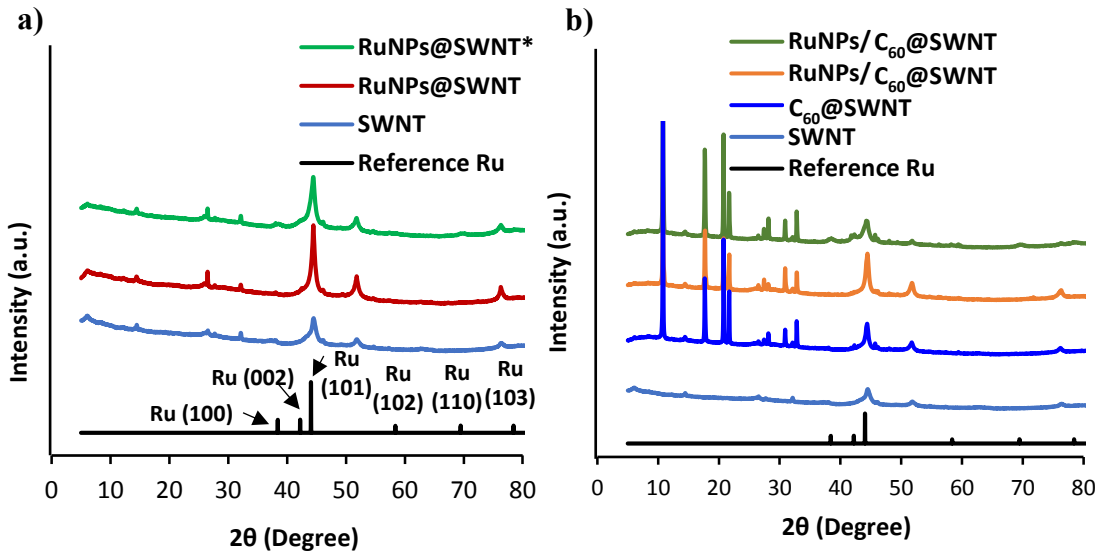

Figure 2.2. Powder XRD patterns of a) RuNPs@SWNT (1.6 % Ru by wt.) and RuNPs@SWNT* (10 % Ru by wt.) and, b) C_{60}@SWNT and RuNPs/C_{60}@SWNT (3.1 % Ru by wt.) and RuNPs/C_{60}@SWNT * (10 % Ru by wt.) together with SWNT and reference patterns for Ru.[37] (**SWNT was annealed at 380 °C for 20 min prior to use).

Table 2.1. Nanoparticle sizing data and theoretical active Ru surface area for all carbon nanoreactor supported RuNP catalysts.

Catalyst	Average size of RuNPs (nm)	Theoretical active Ru surface area (m^2/g of catalyst)[a]
RuNPs@SWNT	0.74 ± 0.18	7.46
RuNPs/C_{60}@SWNT	2.56 ± 0.62	4.31
RuNPs@GNF	3.58 ± 1.14	1.00
Ru/C[c]	6.63 ± 2.45	2.69

[a] The active Ru surface area of the RuNPs catalysts was calculated assuming all of the NPs to be the average diameter measured by TEM (see Experimental 2.4.7 for full details).

The RuNPs@SWNT catalyst was then investigated using exploratory alkene hydrogenation reactions and as the RuNPs are located predominantly within the nanotube channel all reactions are assumed to be performed under the effects of extreme confinement. When selecting an appropriate reactant it is important that the van der Waals size of the reactant molecules is smaller than the 1.5 nm diameter of the SWNT channel. As the hydrogenation of cycloalkenes and butanal in continuous flow reactors has recently been demonstrated in nanotubes, in this study bicyclic alkene norbornene (**1a**) and a tricyclic alkene benzonorbornadiene (**2a**) were selected as both have non-planar angular shapes, and in the case of **2a** an additional aromatic ring increasing the steric bulk as compared to **1a** (Scheme 2.1).[27]

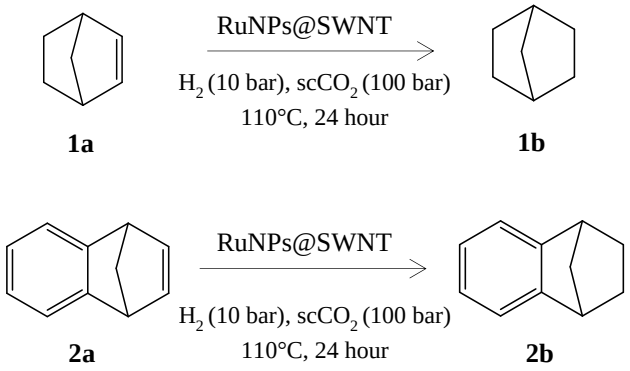

Scheme 2.1. Hydrogenation of norbornene and benzonorbornadiene in the presence of RuNPs@SWNT.

The RuNPs@SWNT catalyst was initially tested in the hydrogenation reaction of norbornene using molecular hydrogen in a conventional organic solvent, cyclooctane, at atmospheric pressure using laboratory glassware (Experimental section 2.4.5). Very low catalytic activity was observed for RuNP@SWNT under these conditions (a 10 % yield of norbornane in 24 h), and is attributed to the restricted space in the narrow nanotube channels hindering access of the solvent/reactants to the confined metal catalyst. Typically, the use of supercritical CO_2 can eliminate such mass transfer problems in nano- or microporous structures,[27] therefore, a high pressure $scCO_2$ batch reactor system was utilized in which the excellent diffusivity and mass transfer properties of $scCO_2$ are exploited to efficiently deliver the reagents to the RuNP catalyst surface within the narrow nanoreactors (Figure 2.3).

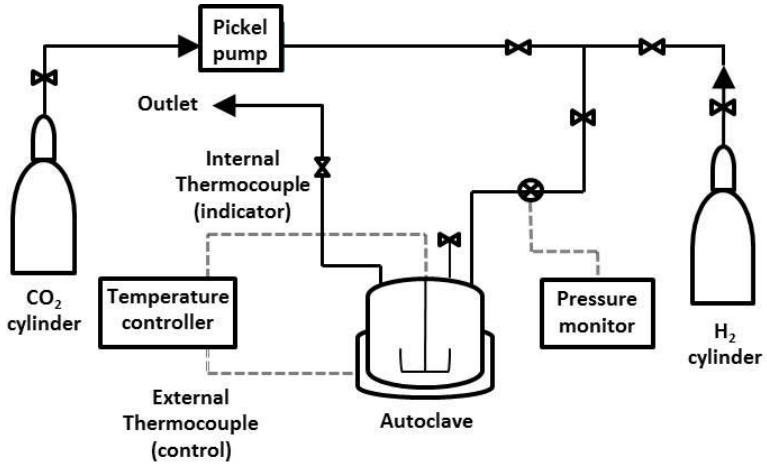

Figure 2.3. A schematic diagram of the $scCO_2$ hydrogenation batch reactor.

Test hydrogenation reactions were performed using the $scCO_2$ batch reactor in the presence of RuNPs@SWNT, and norbornene showed a higher TON (total number of product molecules formed per available Ru active site, see Experimental section 2.4.6 for details of how this was calculated),[27] than the larger benzonorbornadiene under identical reaction conditions (Scheme 2.1 and Table 2.2). Control reactions using as-received SWNTs showed no reactivity despite EDX and TEM (Figure 2.1c) showing the presence of residual Ni/Y catalyst from nanotube synthesis implying that all of the nickel is completely passivated by layers of graphitic carbon shells (Table 2.2).

Table 2.2. Hydrogenation reactions of norbornene and benzonorbornadiene in the presence of RuNPs@SWNT, RuNPs/C_{60}@SWNT, RuNPs@GNF and commercial Ru/C using a high pressure $scCO_2$ batch reactor.

Catalyst	Yield[c] of Products (%) / **TON[d]**		Ratio of TONs for **1b**:**2b**
	1b	**2b**	
SWNT[a]	0	N/A	N/A
RuNPs@SWNT	91 / **2959**	61 / **1983**	1.5:1
C_{60}@SWNT	0	N/A	N/A
RuNPs/C_{60}@SWNT	12 / **675**	7 / **393**	1.7:1
GNF[b]	0	N/A	N/A
RuNPs@GNF	46 / **11216**	17 / **4145**	2.7:1
Ru/C	51 / **7428**	21 / **3058**	2.4:1

Reaction conditions: alkene (1 mmol), catalyst (equivalent of 0.0017 mmol of ruthenium in the reaction mixture), H_2 (10 bar), $scCO_2$ (100 bar), 24 h, 110 °C. [a]SWNT was annealed at 380 °C for 20 minutes to open their termini prior to use. [b]GNF was annealed at 450 °C for 1 hour prior to use. [c]Yield determined by ^{1}H NMR with an error of ± 2 % (see Figure 2.16 in Experimental section 2.4.5) . [d]The turnover number (TON) was calculated as the ratio of the number of molecules of substrate consumed in the reaction per number of available Ru active sites in catalyst used in the reaction (see Experimental section 2.4.7 for details of the calculation of the theoretical number of active Ru sites in each catalyst).

Crucially, to verify the precise location of the reaction it was important to investigate the effect of the small portion of larger RuNPs located on the outside of the SWNT which were more readily accessible than the RuNPs confined within the nanotube channel. A control material was therefore synthesised, in which RuNPs are located solely on the outside of SWNT, RuNPs/C_{60}@SWNT. This material was prepared by filling of the internal cavities of the SWNT support material with C_{60} to block the channels prior to exposure to the RuNP precursor, Ru_3CO_{12} vapour (Figure 2.4). HRTEM (Figure 2.10) and gas absorption measurements, which reveal an absence of 1-2 nm pores in the C_{60}@SWNT support, agree with the fact that the C_{60} molecules completely block the inner channels of the SWNTs, such that the Ru_3CO_{12} can only deposit on the outside of the nanotubes and subsequent thermal treatment causes decomposition of the precursor resulting in RuNPs formation exclusively on the outer surface of the SWNT (Figure 2.4). Removal of the templating effect of the inner nanotube cavity during NP formation resulted in the Ru nanoparticles of diameter 2.56 ± 0.66 nm on the nanotube surface exhibiting a wider size distribution significantly larger as compared to nanoparticles formed inside, but comparable to the NPs located on the outside of, nanotubes in RuNPs@SWNT (c.f. average NP sizes of 0.74 ± 0.18 nm and 2.49 ± 0.85 nm for NPs inside and outside respectively) (Table 2.1). This allowed comparison of the catalytic activity of RuNPs located on the outside of the SWNT (RuNPs/C_{60}@SWNT) with RuNPs located inside the nanotube (RuNPs@SWNT). For reference C_{60}@SWNT exhibited no catalytic activity when tested in $scCO_2$ hydrogenation reactions, (Table 2.2).

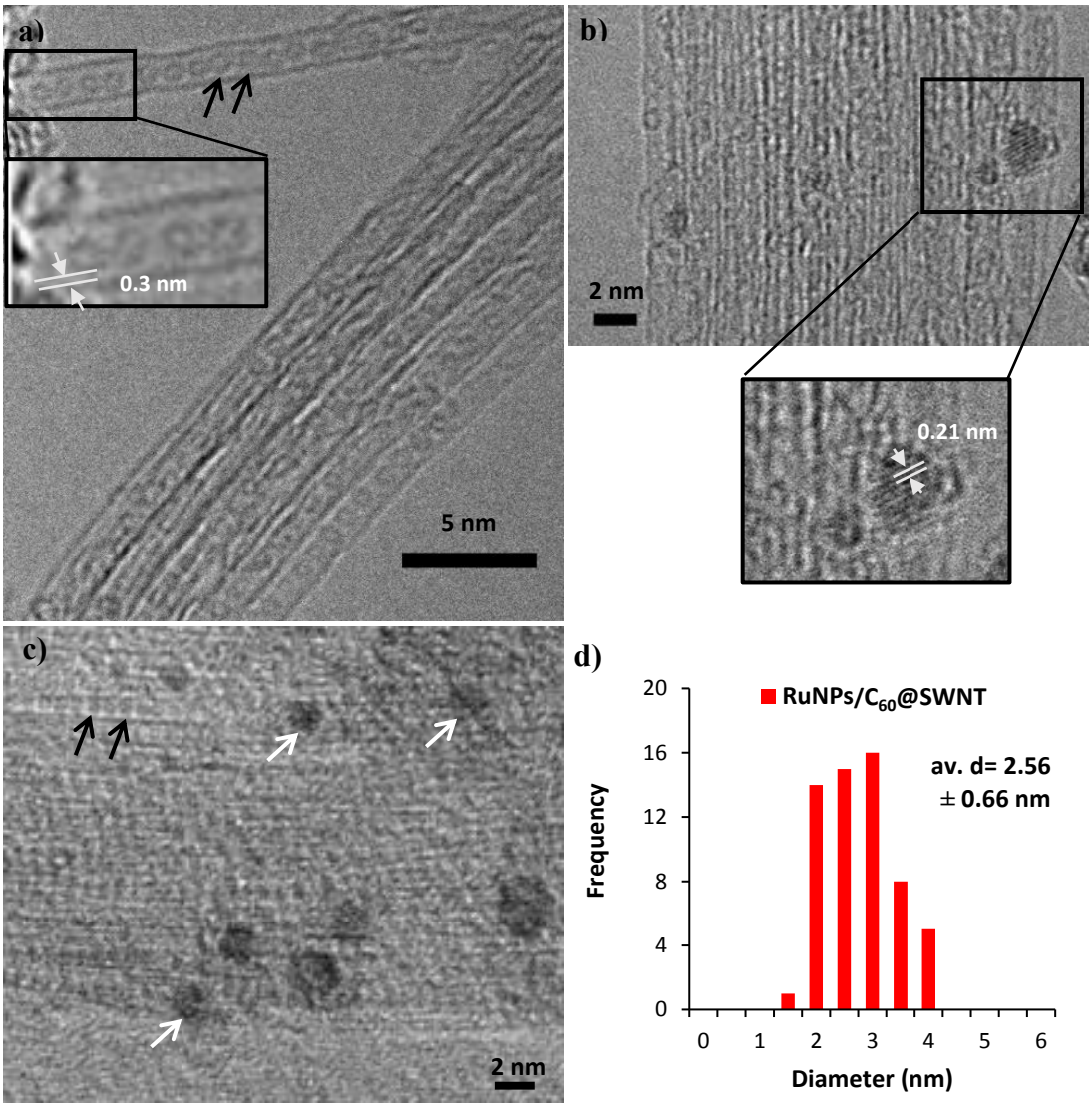

Figure 2.4. a) HRTEM image of the C_{60}@SWNT support material showing the internal channels of the SWNT are completely full of C_{60}. Enlarged region (inset) shows only single C_{60}@SWNT structure in which a 0.3 nm van der Waals gap can be observed between C_{60} molecules and the SWNT wall confirming that there is no space for reactants or Ru NP precursors to fit. (b) HRTEM image showing the Ru [002] lattice spacing (d = 0.21 nm) of an individual, hcp structured, metallic NP which corresponds to the 2θ peak centred at 42.2° in the XRD (Figure 2.3). c) HRTEM image of RuNPs/C_{60}@SWNT loaded with 3.1 % of Ru by wt. after filling the SWNT with C_{60}, and d) the size distribution of RuNPs on the outside of the SWNT (red) in RuNPs/C_{60}@SWNT is observed to be greater than the confined NPs inside and comparable to the NPs located on the outside of the SWNT in RuNPs@SWNT.

To fully understand the impact of the restricted reaction space within the SWNT,[27] hydrogenation of norbornene and benzonorbornadiene was performed with catalysts which provide lower (RuNPs@GNF) and no confinement (RuNPs/carbon black) of reactants around the catalytic nanoparticles. To achieve this, GNFs were used, which have an inner diameter of 52 ± 13 nm and an outer diameter of 99 ± 25 nm, and are, like MWNTs, significantly wider than SWNTs, allowing reactants in (and products out) more readily and thus can be considered as providing a lower level of confinement. In addition, unlike the entirely smooth MWNTs, GNFs have a unique step-edge internal structure, which stabilises the RuNPs and has the capacity to impart additional confinement effects on reactions which will be probed in this study. RuNPs within the GNF (RuNPs@GNF) were formed using similar conditions to RuNPs@SWNT, however due to the significantly lower surface area of the GNFs only 1% Ru by weight was used, to ensure that RuNPs were only formed in the cavity of the GNFs.[18] In identical fashion to SWNT, it is the internal structure of the GNF which templates the formation of the RuNPs, stabilising the NPs and controlling their size and shape. HRTEM imaging confirms that RuNPs are located solely inside the GNF, at the step-edges formed by rolled-up graphitic sheets, with a mean nanoparticle diameter of 3.58 ± 1.14 nm (Figure 2.5a, Table 2.1). HRTEM and XRD analyses confirm the metallic nature of the RuNPs and STEM, (Figures 2.5a-b and 2.6a), approximates the amount of RuNP material on the outer surface to be ~7 %.

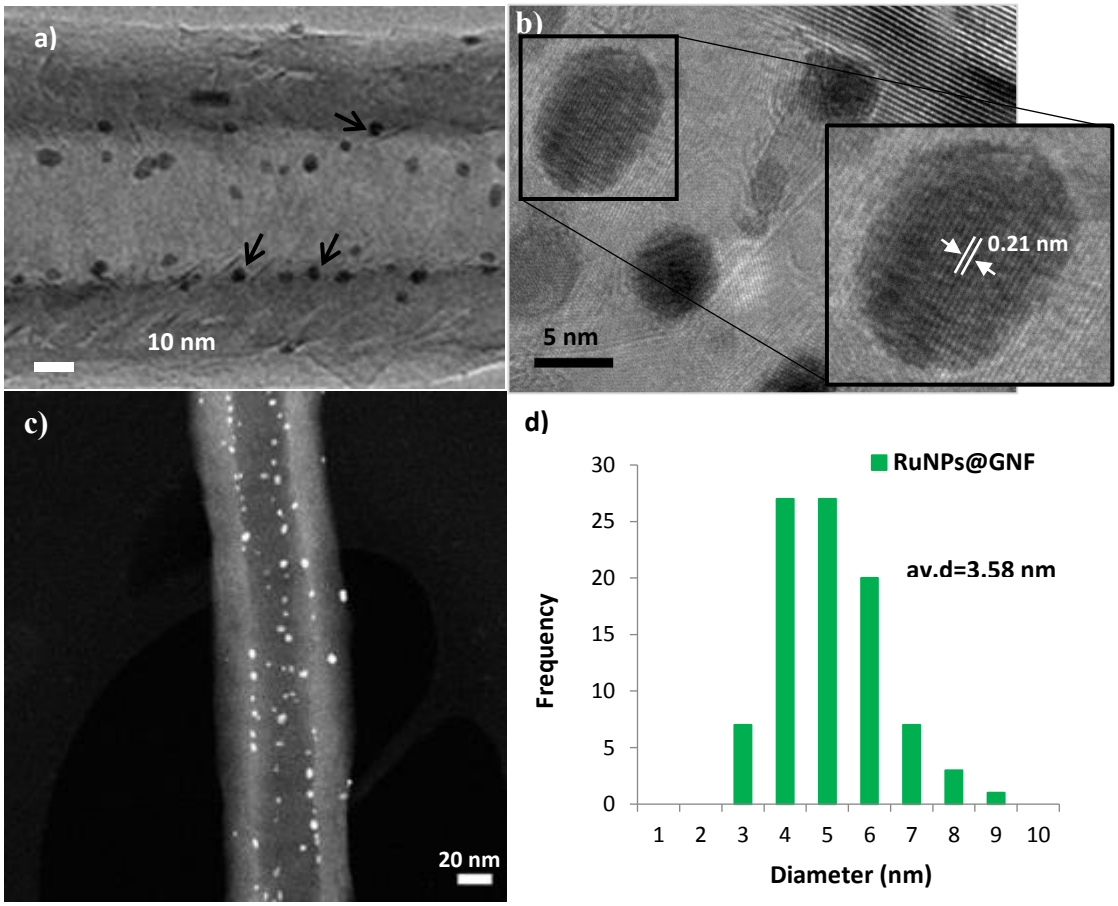

Figure 2.5. a-b) HRTEM images of RuNPs@GNF loaded with RuNPs (1 % by wt), with enlarged region (b) showing the Ru [002] lattice spacing (d = 0.21 nm) of an individual, hcp structured, metallic NP which corresponds to the 2θ peak centred at 42.2° in the XRD (see Figure 2.6). Black arrows show RuNPs on the step edges inside the GNF. c) Dark-field scanning TEM image of RuNPs@GNF loaded with RuNPs. Only a very small amount of Ru material (~7 % approximated by TEM analysis), is located on the outer surface of the GNF so all conversion is assumed to be a result of reactions catalysed by RuNPs on the inside of the GNF.

TGA was used to measure the content of Ru metal within the RuNPs@GNF catalyst. As pure GNFs do not contain additional residual metal species it is possible to equate the residual weight after oxidation of the carbon in RuNPs@GNF samples to the loading of Ru metal (Figure 2.6b). In addition, commercially available Ru/C, containing 5% Ru by weight, was used as a control material in which the RuNPs are located on the surface of carbon black which imparts no confinement effects. HRTEM confirmed that the metal nanoparticles are

distributed throughout the carbon support in Ru/C and showed a wide distribution of NP sizes, with a mean diameter of 6.63 ± 2.45 nm (Figure 2.7, Table 2.1).

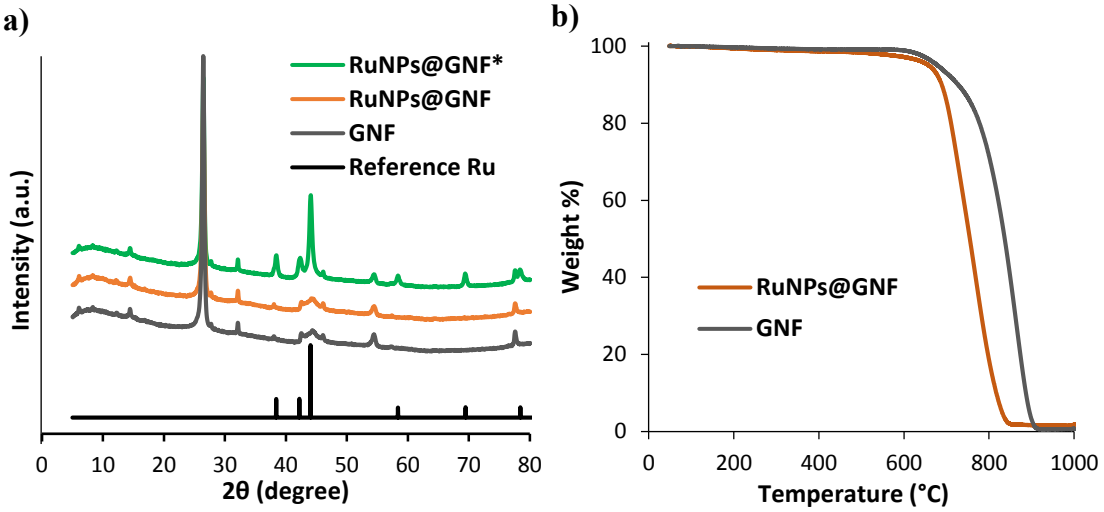

Figure 2.6. a) Powder XRD patterns of RuNPs@GNF (1 % Ru by wt.) and RuNPs@GNF* (10 % Ru by wt.) and GNF (**GNF was was annealed at 450 °C for 1 h prior to use) together with reference patterns for Ru.[37] b) TGA curves of GNF (grey) with 0.62% residual weight, and RuNPs@GNF (orange) with 1.6 % residual weight, which corresponds to 1 % wt. ± 0.1 of Ru in the carbon supported RuNP catalyst**.** Both measurements were carried out between 25-1000 °C in air at a heating rate of 10 °C/min.

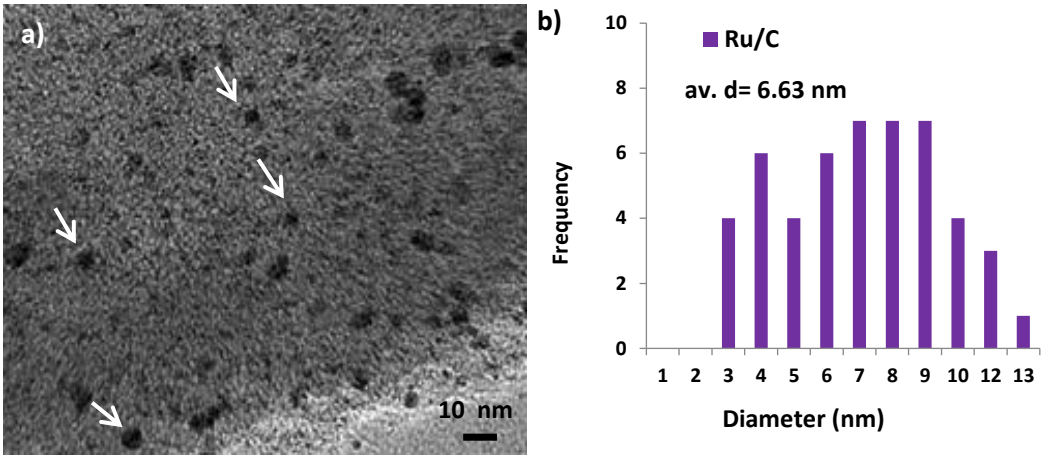

Figure 2.7. a) HRTEM image of commercial Ru/C loaded with RuNPs (5 % by wt.). White arrows show RuNPs located on the carbon support. b) The size distribution of RuNPs on the carbon (purple) shows the wide distribution of diameters of the RuNPs in the material.

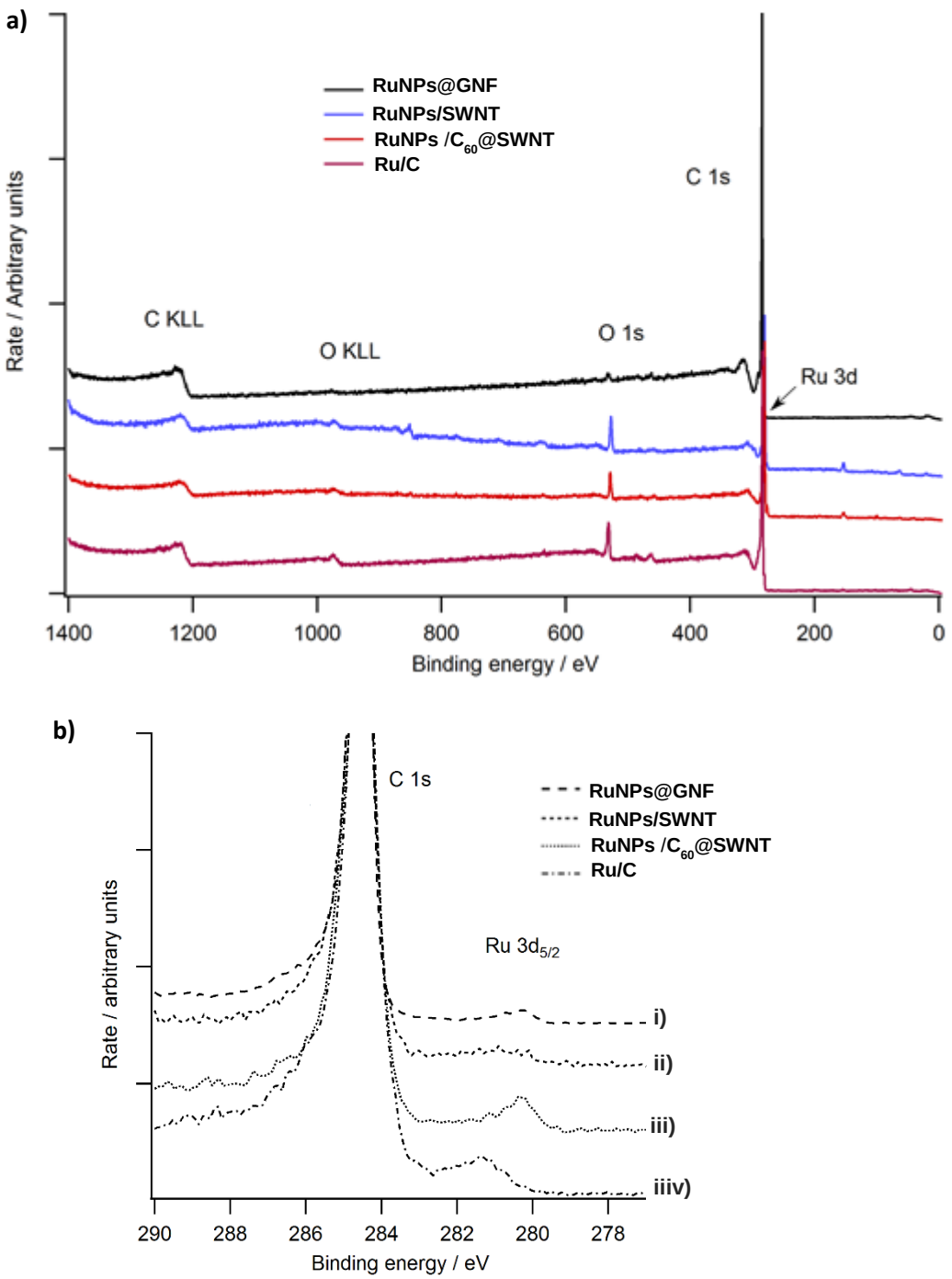

Figure 2.8. a) XPS data for RuNPs@GNF (black), RuNPs@SWNT (blue), RuNPs/C_{60}@SWNT (red) and Ru/C (purple) collected with a monochromated Al Kα X-ray source (1486.6 eV) operated at 10 mA emission current and 12 kV anode potential (120 W). Oxygen peak is associated with defects in the carbon supports. b) Enlarged regions of the XPS data for i) RuNPs@GNF, ii), RuNPs@SWNT, iii) RuNPs/C_{60}@SWNT, and iv) Ru/C control showing the characteristic Ru 3d 5/2 peak at 280.2 eV for the all carbon nanostructure supported catalysts which is consistent with the binding energy for metallic Ru reported previously.[38]

XPS reveals an overlapped Ru 3d and C 1s region at ~283.5-286.5 eV, therefore a characteristic Ru 3d 5/2 peak at 280.2 eV was used for all three carbon nanostructure supported RuNPs materials which is consistent with the previously reported literature for metallic ruthenium (Figure 2.8).[38]

In comparison with RuNPs@SWNT, RuNPs/C_{60}@SWNT showed very low catalytic performance in $scCO_2$ reactions implying that the larger NPs on the outer walls of the nanoreactor are less active than the smaller RuNPs confined within the nanoreactor.[39-40] Interestingly, the RuNPs on the outside of the C_{60}@SWNT support (d_{NP} = 2.56 nm) are similar in size to the RuNPs inside the GNF in the RuNPs@GNFs catalyst (d_{NP} = 3.58 nm), see below for details, but give significantly lower reaction yields, (Table 2.2). It is hypothesised, therefore, that the lack of activity of the RuNPs/C_{60}@SWNT catalyst is most likely a result of the lack of confinement for the reactions, which cannot create a similarly high local concentration of the reactant molecules around the catalyst nanoparticles in RuNPs/C_{60}@SWNT as in RuNPs@SWNT (and RuNPs@GNF) leading to a lower yield of the products in the case of the former material. This is consistent with the previously reported examples of enhanced local concentration of reactants inside nanotubes resulting in higher yields and is consistent with our observation of low norbornene conversion (~10 %) in the reaction catalyzed by RuNPs@SWNT performed in cyclooctane solvent in which the reaction only takes place on the accessible Ru nanoparticles located on the outside surface of SWNT in the absence of high pressure $scCO_2$ (c.f. RuNPs/C_{60}@SWNT showed 6% norbornene conversion to norbornane using the same conditions).[18-19, 26, 31-32] It is therefore concluded that the RuNPs located inside the carbon nanoreactor are significantly more active and are responsible for the majority of product formation, and thus, the contribution of the minority of RuNPs on the outside of the SWNT (~10% by HRTEM) and GNF (~7% by STEM, Figure 2.6c) for

RuNPs@SWNT and RuNPs@GNF catalysts respectively, is negligible (Figure 2.1). The general observed trend of higher TONs for norbornene, compared to benzonorbornadiene, is most likely due to the steric bulk of the additional benzyl group hindering adsorption of benzonorbornadiene on the Ru NP surface, as well as potentially an electron withdrawing effect of the additional benzene ring compared to norbornene.[41] Interestingly, however, there is a significant difference in the relative TONs of reactions of **1b** and **2b** for each of the SWNT catalysts, highlighted by considering the ratio of TONs, Table 2, implying the shape of the catalyst affects the reactions in an appreciable way. The extremely confined RuNPs@SWNT system, where the ratio of TONs of **1b**:**2b** is dramatically lower than for the unconfined RuNPs/C_{60}@SWNT system, appears to have a higher affinity for **2b**, potentially due to favourable π-π interactions between the aromatic group and the nanotube sidewall. Cleary understanding the nature and extent of the confinement in these systems is crucial to selecting the correct environment for a specific reaction.

It is important to note that as the RuNPs are not identical sizes across the catalysts in this study, it is not possible to unambiguously assign all differences in reactivity solely to the effect of confinement. However, as the shape and size of the NPs in each material is a direct result of the confinement experienced during formation, and the differences in reactivity cannot be explained solely by considering the size of the NPs, vital information can be obtained by comparing the reactivity of the catalysts.

In similar fashion to the SWNT nanoreactors, the catalytic activities of RuNPs@GNF and Ru/C, along with the as-supplied GNFs as a control, were investigated in hydrogenation of norbornene and benzonorbornadiene (Table 2.2). The empty GNFs displayed no catalytic activity at all. Interestingly, the RuNPs@GNF catalyst exhibited turnover numbers for norbornene (11216) and benzonorbornadiene (4145) conversion,

which are significantly higher when compared to RuNPs@SWNT (c.f. (2959) and (1983) respectively), and the unconfined Ru nanoparticles in commercial Ru/C or in RuNPs/C_{60}@SWNT. This is possibly due to the RuNPs inside of the much wider GNF cavity being more accessible for the reactant molecules coupled with the formation of favourable π-π interactions with both **1a** and **2a** at the step-edge enhancing the local concentration of the reactants near the RuNPs, and therefore the rate of reaction.[42]

Previous studies have revealed that both the size and crystal structure of RuNPs have important effects on the catalytic activity of RuNPs in hydrogentation.[43-46] Li *et al*. reported that the size and loading of hcp RuNPs supported on MWNTs for the hydrogenation of long-chain alkenes was optimum for 1.3 nm NPs and and metal loadings of 1% by wt., while in solution 3.1 nm RuNPs were observed to be the most active.[43-44] Dupont *et al*. reported that 2.6 ± 0.4 nm RuNPs were the most active for the partial hydrogenation of benzene, with TON of up to 165 for supported RuNPs catalysts.[45] It is also observed that distortions to the lattice planes of hcp RuNPs[46] or changes in crystal packing to face-centred cubic Ru[36] results in significant effects to both the activity and selectivity of RuNP catalysed reactions.

Our hydrogenation results, in which all RuNPs catalysts have the same hcp structure (confirmed by HRTEM), show an interesting trend in activity, consistent for indivudal reactions with both alkene starting materials with TONs in the order of RuNPs@GNF>Ru/C>RuNPs@SWNT>RuNPs/C_{60}@SWNT. It is important to highlight that the mass of catalyst in each reaction was scaled so the same molar percent of of Ru was present in all our reactions (0.0017 mmol% of Ru), and the trend in activity cannot be rationalised by simply considering the average NP size or total NP surface area for each sample, (for our series, the total surface area of RuNPs@SWNT>RuNPs/C_{60}@SWNT>RuNPs@GNF>Ru/C), nor the extent of

confinement, where the confinement in RuNPs@SWNT> RuNPs@GNF >RuNPs/C_{60}@SWNT >Ru/C. Therefore, the enhancement in activity observed upon confinement inside GNF must be a result of a balance of surface area of RuNP, confinement of the reaction and accessibility of the catalytic centres. Indeed, GNF provides an optimum balance of RuNP confinement, leading to stabilisation and enhancement of local concentrations of reactants around the nanoparticles, and the ease of accessibility of the reactants to catalytic centres (hindered in the case of RuNP@SWNT). Recently, similar effects were observed in the oxygen reduction reaction catalysed by PtNP@GNF.[47]

In addition, the RuNPs@GNFs catalyst shows a marked enhancement in reactivity for the production of **1b** (**1b**:**2b** ratio = 2.7:1) compared to the unconfined Ru/C catalyst (ratio = 2.4:1) (Table 2) implying remarkable TON for **1b**, rationalised as a result of faster diffusion of the non-aromatic molecules to and from the step-edge compared to the aromatic benzonorbornadiene which may interact more strongly with the sp^2 carbon of the step-edge and therefore diffuse to and from the RuNPs less rapidly. In contrast RuNPs@SWNT shows the opposite effect exhibiting an enhanced reactivity for the production of **2b** (**1b**:**2b** ratio = 1.5:1), potentially due to strong interactions between the aromatic core of **2a** and the narrow inner channel of the SWNT.

In summary, these results reveal that the confinement imposed by the carbon nanoreactor can not only increase the activity of the Ru catalyst by both templating the formation of small, very active and stable RuNPs and potentially by increasing the local concentration of reactant molecules in the vicinity of the Ru catalyst but can also dramatically affect the efficiency of individual reactions depending on the size and shape of the reactant molecules. This is highlighted by the RuNPs@SWNT catalyst which shows that RuNPs confined in narrow SWNT are particularly efficient at converting aromatic **2a** whilst the

less constrained GNF catalyst are highly active and show enhanced relative conversion of **1a** compared to the unconstrained (carbon black) reaction environment. Understanding the accessibility of the different catalysts is essential in order to fully appreciate the role that confinement plays in the performance of these materials.

These results are in agreement with previous observations that performing reactions in confinement has a number of important effects on catalysis and alters the outcome of reactions in a complex fashion;[15] by enhancing the activity of nanoparticle cataltysts,[48] increasing the local concentration of reagents and thus increasing the rate of reactions,[49] and by imposing restrictions on both the transition states of intermediates[42] and the flow of reactants in and products out of the nanoreactor.[27]

2.2.1 Evaluating the surface area of Ru@CNS

To investigate the 3D structure of the materials the experimentally measured active surface area of RuNPs@SWNT, RuNPs@GNF and commercial Ru/C catalysts were compared with theoretically calculated surface areas based on ideal models of the materials, *i.e.* assuming the entire catalyst is perfectly formed and accessible to reagents (Experimental section 2.4.7). Brunauer-Emmett-Teller (BET) measurements based on isothermal N_2 gas adsorption at -196 °C (77 K) were performed for RuNPs@SWNT, RuNPs@GNF and commercial Ru/C catalysts along with control measurements of the support materials, *i.e.* SWNT, GNF and amorphous carbon materials to quantify both surface area (Table 2.3) and pore volume and size distribution (Figures 2.9-12 and Tables 2.3-4). This provided a reasonable gauge of how much of the internal volume of the catalysts were accessible to gaseous N_2, and comparison to the theoretical maximum values, revealed the portion of the internal volume which is either blocked by Ru nanoparticles large enough to completely fill the channels or other inherent material such as amorphous carbon and residual Ni/Y catalyst present following the initial nanotube

synthesis. BET measurements showed that the commercial Ru/C (929 m^2/g) has the largest surface compared to that of RuNPs@SWNT (352 m^2/g) and RuNPs@GNF (29 m^2/g) (Table 2.3).

Table 2.3. Theoretical and BET surface area calculations for SWNT, GNF, RuNPs@SWNT, RuNPs@GNF and commercial Ru/C.

Catalyst	**Theoretical Surface Area (m^2/g)**	**BET Surface Area (m^2/g)**
SWNT[a]	2630.00	507.90
RuNPs@SWNT	2637.46	351.94
C_{60}@SWNT	1315.00	120.99
RuNPs/C_{60}@SWNT	1319.31	164.82
GNF[b]	35.00	12.08
RuNPs@GNF	35.99	28.53
Carbon Black	N/A	900.00
Ru/C[c]	N/A	929.41

[a] SWNT was annealed at 380 °C for 20 min prior to use. [b] GNF was annealed at 450 °C for 1 hour prior to use. [c] BET surface area value for the carbon black used to synthesize the Ru/C was obtained from the manufacturer (Sigma-Aldrich).

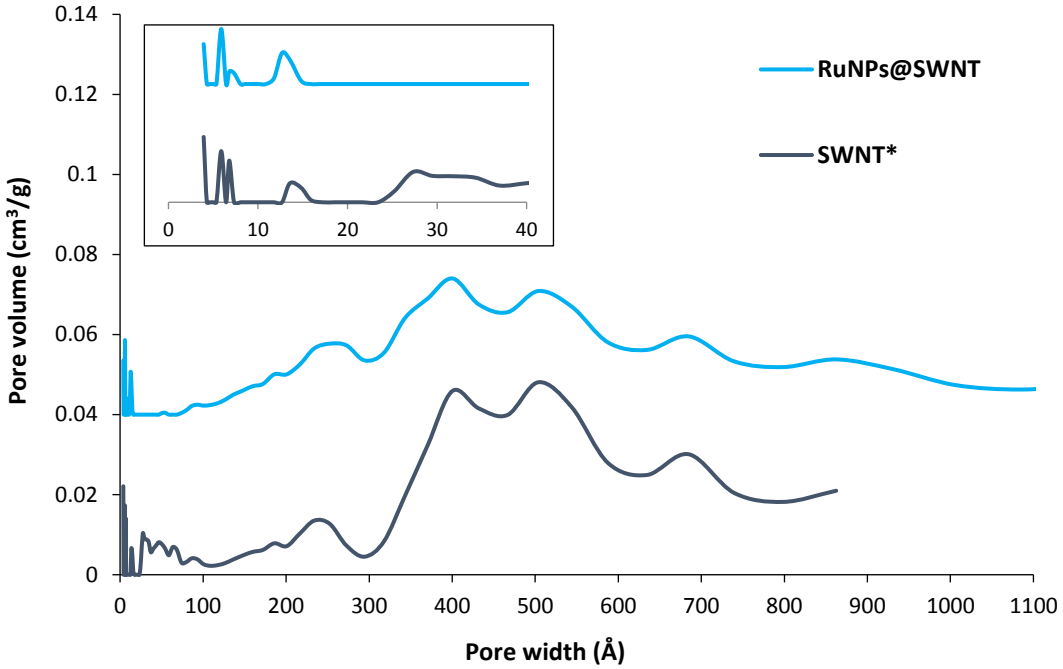

Figure 2.9. Pore size distribution curves of SWNT (*SWNT was annealed at 380 °C for 20 min prior to use) and RuNPs@SWNT.

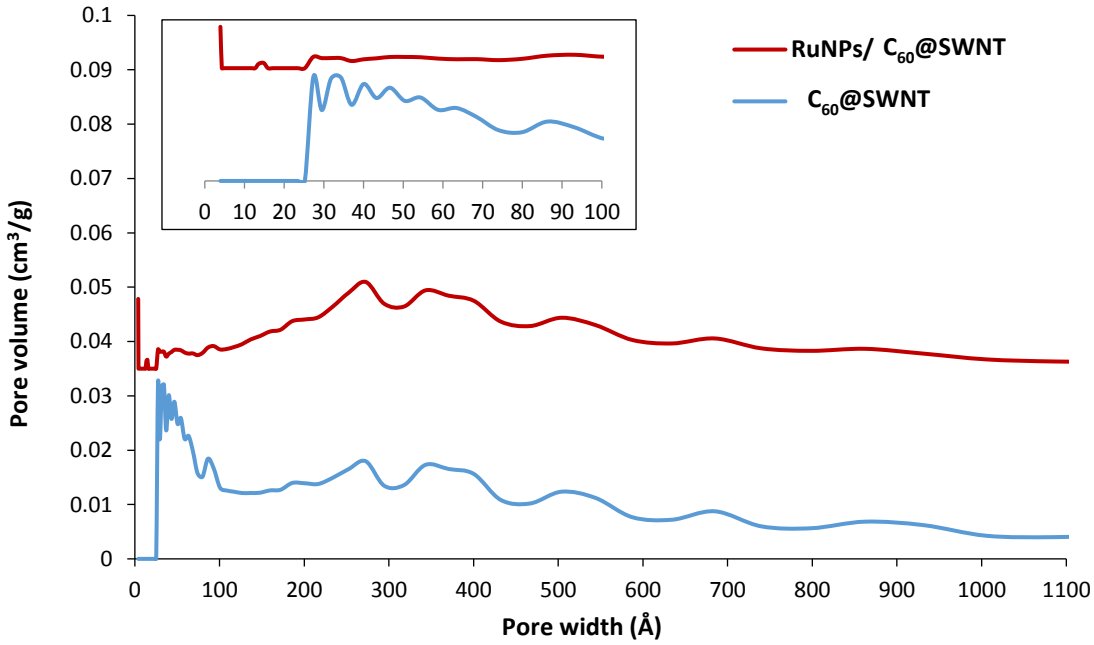

Figure 2.10. Pore size distribution curves of C_{60}@SWNT and RuNPs/C_{60}@SWNT.

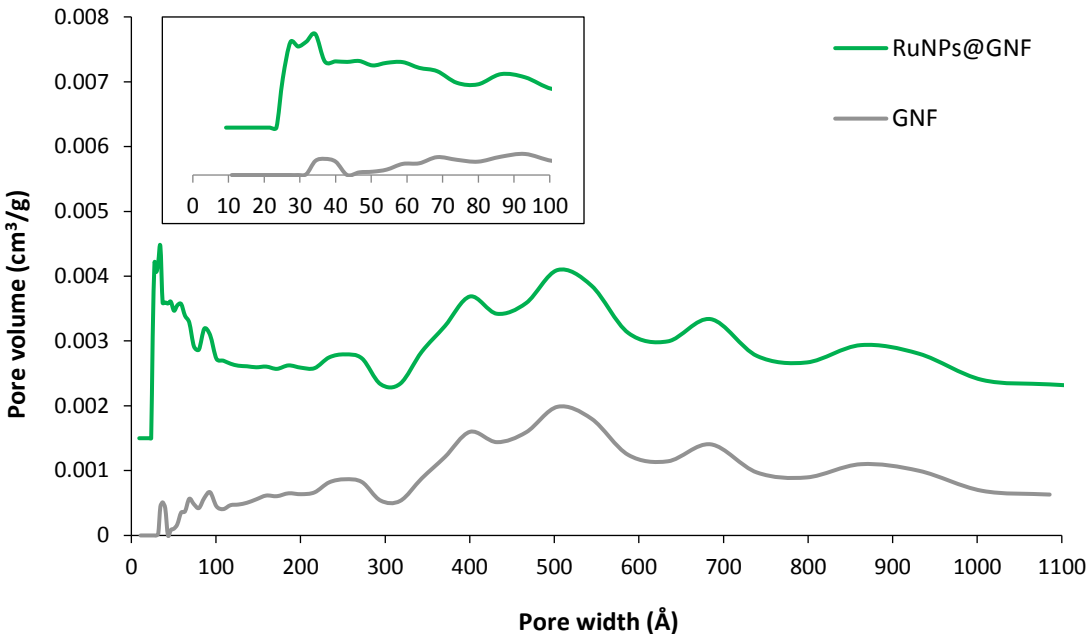

Figure 2.11. Pore size distribution curves of GNF (*GNF was annealed at 450 °C for 1 h prior to use) and RuNPs@GNF.

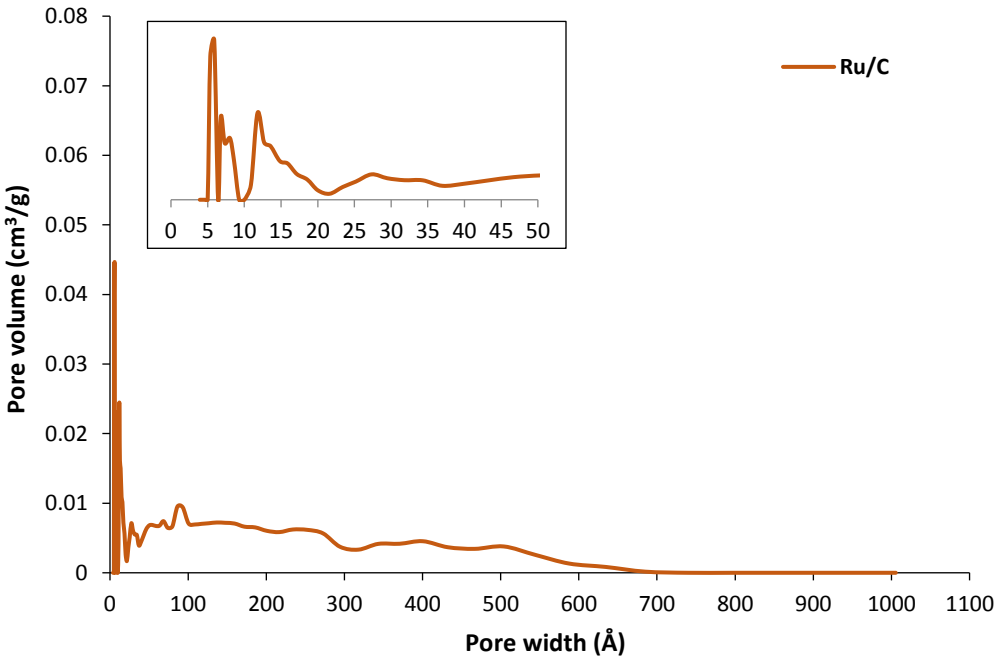

Figure 2.12. Pore size distribution curves of commercial Ru/C

The increased BET surface area of Ru/C and RuNPs@GNF compared to the background carbon and empty GNF supports respectively is attributed to the presence of the RuNPs. In contrast RuNPs@SWNT (352 m^2/g) exhibited a lower BET surface area than that of the background SWNT (508 m^2/g). This is rationalised as a consequence of a small number of large (>1.2 nm) RuNPs blocking a significant percentage (c.a. 30-40 %) of the entrances and/or channels/pores of the narrow nanotubes and not allowing N_2 to access the full internal volume of the material.

Typically, carbon nanomaterials have very large surface areas due to their nanometer scale features; see theoretical specific surface calculated for each sample (see Table 2.7 in Experimental 2.4.7). Peigney *et. al.* investigated the theoretical surface area of CNT and reported that the specific surface area of SWNT, independent of its diameter and length, is the same as that of both sides of a graphene sheet, *i.e.* 2630 m^2/g.[50] As we opened the ends of the nanotubes prior to use, *i.e.* both internal and external walls of the nanotubes can be assumed to be accessible, the theoretical surface area for the SWNT sample is 2630 m^2/g. However, in reality the majority of SWNT form bundles and therefore it is difficult to approximate an accurate number for the theoretical surface area for nanotubes as the outer surface of most single nanotubes are not available as they are contained within the bundles. Clearly the experimental value for SWNT, 508 m^2/g, is dramatically lower and can be considered as the effect of bundling.

When considering the accessibility of GNFs it is important to understand that their structure is different to the concentric tubes of traditionally MWNTs and consists of stacked truncated cones of graphite layers arranged at an angle along the main axis.[51] The internal surface has a succession of step edges which can act as anchoring points for guest molecules while the exterior surfaces are atomically flat. Therefore there is no reported framework for calculating a theoretical value for the surface area of GNFs. In this

approach the internal surfaces of a GNF are approximated to be flat and the sidewalls to consist of ~75 graphene layers (using an average thickness value of a GNF as 25 nm). Therefore, utilizing the same mathematical approach used by Peigney *et al*. for MWNTs, we calculated as theoretical surface area of 35 m^2/g, which is significantly higher that of the BET measurement (12 m^2/g). This is rationalized as the effect of the overlapping of the truncated cones in the internal channels decreasing the internal surface area compared to our theoretical model, but could also be a result of the presence of a number of GNFs in the sample with thicker sidewalls. Therefore, though it is difficult to comment on the RuNPs@SWNT sample, as a significant portion of the material appears to be blocked and inaccessible, c.f. an observed surface area of >4 times lower than predicted. This comparison does reveal that even though the Ru/C catalyst has a higher surface area than RuNPs@GNF, both in terms of total catalyst and the RuNPs, it is significantly less active. This must be due to the size and shape of the pores, *i.e.* the nature of the confinement imposed.

2.2.2 Competitive hydrogenation towards RuNPs@CNS

To probe these effects of confinement further competitive reactions were investigated in which equimolar amounts of norbornene and benzonorbornadiene were simultaneously reduced within the nanoreactor catalyst (Scheme 2.2 and Figure 2.13). Competitive reactions reveal that the confined space of carbon nanoreactors considerably affects the selectivity of the reactions compared to reactions performed in the absence of confinement (Ru/C) (Table 2.4).

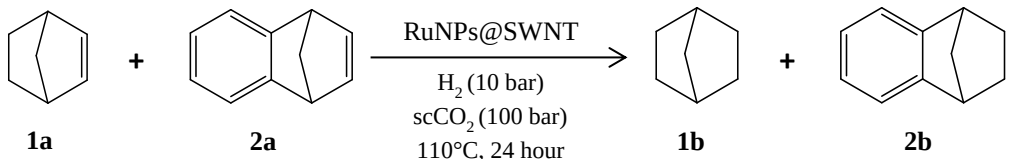

Scheme 2.2. Competitive reactions of norbornene and benzonorbornadiene in the presence RuNPs@SWNT using a $scCO_2$ high pressure rig.

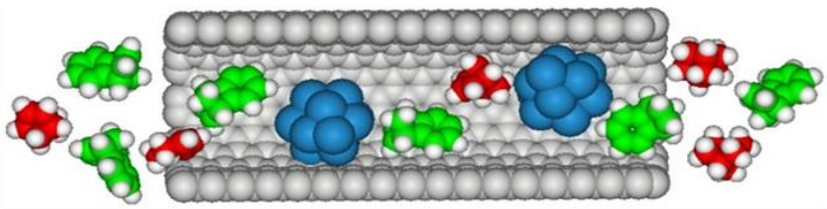

Figure 2.13. a) Schematic representation of the competitive hydrogenation of norbornene (red) and benzonorbornadiene (green) over RuNPs (blue) within SWNT. This shows how the extremely confined space within the nanotube channel traps the reactants close to the catalytic nanoparticles, effectively increasing the local concentration of reagents and increasing the rate of reaction.

Table 2.4. Competitive hydrogenation reactions of norbornene and benzonorbornadiene in the presence of RuNPs@SWNT, RuNPs/C_{60}@SWNT, RuNPs@GNF and commercial Ru/C using a high pressure $scCO_2$ batch reactor.

Catalyst	Yield[a] of Products (%) / **TON**[b]		Ratio of TONs for
	1b	2b	1b:2b
RuNPs@SWNT	70 / **1138**	89 / **1447**	0.79:1
RuNPs/C_{60}@SWNT	7 / **197**	13 / **366**	0.54:1
RuNPs@GNF	21 / **2560**	42 / **5120**	0.5:1
Ru/C	52 / **3787**	53 / **3860**	0.98:1

Reaction conditions; substrates (0.5 mmol of each alkene), catalyst (0.0017 m mol% of Ru in each reaction system), H_2 (10 bar), $scCO_2$ (100 bar), 24 h, 110 °C. [a] Yield determined by ^{1}H NMR with an error ± 2 % (See Figure 2.16 in Experimental 2.4.5). [b]The turnover number (TON) was calculated as the ratio of the number of molecules of substrate consumed in the reaction per theoretical number of true active Ru sites in catalyst used in the reaction.

For all reactions in carbon nanoreactors benzonorbornadiene was preferentially reduced over norbornene in the presence of carbon nanoreactors due to the strong aromatic character of the **2b**. In fact the TONs of **2b i**n the competitive reactions are larger than the individual reactions for RuNPs@GNF and Ru/C despite a reduction in the starting concentration (Table 2.2), indicating that the presence of equimolar quantities of **1a** may have an effect on π-π interactions of the aromatic ring of **2a** and the sp^2 hybridized carbon network of the interior of the nanoreactors being amplified in the presence of the non-aromatic **1a** leading to an increased local concentration of the aromatic reactant in proximity to RuNPs catalyst thus promoting reduction of **2a**.[42]

RuNPs@GNF exhibited both the highest activity (total TON = 7680) and the greatest selectivity towards **2b** formation (ratio **1b**:**2b** = 0.5:1) compared to RuNPs@SWNT (ratio of 0.79:1) (Table 2.4). This can be explained by considering the nature of the confinement imposed by the step-edges of the internal channel of the GNF. Any increase in the local concentration of the reactants at the step-edges compared to the local concentration inside the nanotube cavity and bulk would result in a much higher rate of reaction.[49] As shown in Figure 2.5a, the step-edges enable a very well-ordered distribution of RuNPs. The height of the step-edges, ~3 nm, provides a controlled space, which forms favourable π-π interactions between the aromatic **2a** and the sp^2 hybridized carbon step-edges and thus increases the concentration of **2a** in the vicinity of the RuNPs and consequently increases the observed conversion of the aromatic compound. The same effect is observed for SWNT, with the formation of **2b** observed to be enhanced compared to **1b** in the individual reactions (see ratio of TONs in Table 2.2), however, the physical size of the aromatic compound means that there will be a significant steric barrier to the movement of the molecules into the narrow SWNT channels compared to the relatively larger space at the step edges in GNF which explains the lower observed TON for the SWNT catalyst.

2.3 CONCLUSIONS

In conclusion, a series of RuNPs@carbon nanoreactor catalysts have been synthesized and the catalytic properties of these materials have been assessed and the role of confinement explored. Overall, the confinement imposed by RuNPs@SWNT and RuNPs@GNF results in dramatic changes to reactions compared to commercially used Ru/C which exhibits no confinement. The affinity of aromatic groups for the interior channels of carbon nanoreactors results in enhanced conversion of aromatic reagents in

competitive hydrogenation reactions providing the ability to alter the selectivity of chemical reactions using support/reactant interactions.

Interestingly the extreme confinement imposed by the shape of the SWNT nanoreactors is found to be a double-edged sword, as though they exhibit enhanced selectivity towards aromatic substrates, as a result of strong interactions between the aromatic species and nanotube sidewall, the constricted space inside the SWNT lowers TONs in general. Remarkably it is the wider, structured interiors of GNF which have a greater effect on reactions, enhancing the activity and resulting in much higher TONs than the extremely narrow SWNT and thus offer the best of both worlds, in that they are wide enough not to limit diffusion of reactants but structured enough to impart the positive effects of reaction confinement.

2.4 EXPERIMENTAL

SWNTs, GNFs and C_{60} were purchased from Helix Material Solutions (Arc-discharge, USA), Pyrograf Products Inc (PR19, chemical vapor deposition, USA) and SES Research (USA), respectively. All other reagents and solvents were purchased from Sigma-Aldrich (UK) and used without further purification. All of the glassware required to perform the experiments was thoroughly cleaned with 'aqua regia' (concentrated hydrochloric and nitric acids (3:1)) and rinsed with deionized water prior to use.

HRTEM analysis was performed on a JEOL 2100 Field emission gun microscope with an information limit of 0.12 nm at 100 kV or 200 kV. High resolution scanning transmission microscopy (HRSTEM) images were acquired using the JEOL digital STEM system. Samples (RuNPs@SWNT, RuNPs/C_{60}@SWNT, RuNPs@GNF and Ru/C) were prepared for TEM analysis by dispersing the materials in HPLC grade iso-

propanol using ultra-sonication, then drop casting the resultant suspension onto a lacey carbon film coated copper grid.

^{1}H NMR spectra were recorded using a Bruker DPX300 NMR spectrometer. ^{1}H NMR spectra were taken in $CDCl_3$ and were referenced to residual trimethysilane (TMS) (0 ppm) and reported as follows: chemical shift, multiplicity (s = singlet, d = doublet, t = triplet, dd = doublet of doublet, m = multiplet).

TGA analysis was performed on a TA Instruments TGA-SDTQ600 analyser. Samples for TGA analyses were heated in an inert atmosphere up to 1000 °C with a heating rate of 10 °C/min.

The powder X-ray diffraction (XRD) patterns were obtained using a PANanalytical X'Pert PRO diffractometer equipped with a Cu-Ka radiation source operating at 40 kV and 40 mA, with 0.05252° step size and 5925.18 second step time.

Samples were analysed by XPS using the Kratos AXIS ULTRA with a mono-chromated Al kα X-ray source (1486.6 eV) operated at 10 mA emission current and 12 kV anode potential (120 W.) A charge neutralizer filament was used to prevent surface charging. Hybrid –slot mode was used measuring a sample area of approximately 0.5 mm^2. The analysis chamber pressure was better than 5 x 10^{-9} mbar. Three areas per sample were analysed. A wide scan spectra at low resolution (at 1400 - -5 eV binding energy range, pass energy of 80 eV, step 0.5 eV, sweep times of 20 minutes) and high resolution spectra (at pass energy of 20 eV with step of 0.1 eV, sweep times of 10 minutes) were acquired for photoelectron peaks from the detected elements. The high resolution spectra were charge corrected to the C 1s peak set to 284.5 eV. CasaXPS (version 2.3.18dev1.0x) software was used for quantification and spectral modelling.

Surface area analysis was performed using the Brunauer–Emmett–Teller (BET) method based on adsorption data in the relative pressure (P/Po) range 0.02 to 0.22 by measuring nitrogen sorption isotherms of the samples (50 mg) at -196 °C on a Micromeritics ASAP 2020 sorptometer. Before analysis, the samples were evacuated for 12 hr at 200 °C under vacuum. The pore size distributions were obtained from a Non-Local Density Functional Theory (NLDFT) method using nitrogen-sorption data.

2.4.1 Catalyst preparation

SWNTs were annealed at 380 °C for 20 minutes to open their termini and remove any residual amorphous carbon from the internal cavities; a 20-30 % weight loss was observed prior to use. Average SWNT length after thermal treatment was reported previously to be 2.43 ± 0.85 μm.[33] GNFs were thermally annealed at 450 °C for 1 hour prior to use. The average length after thermal treatment was measured by TEM to be 15.34 ± 12.10 μm (Figure 2.14)

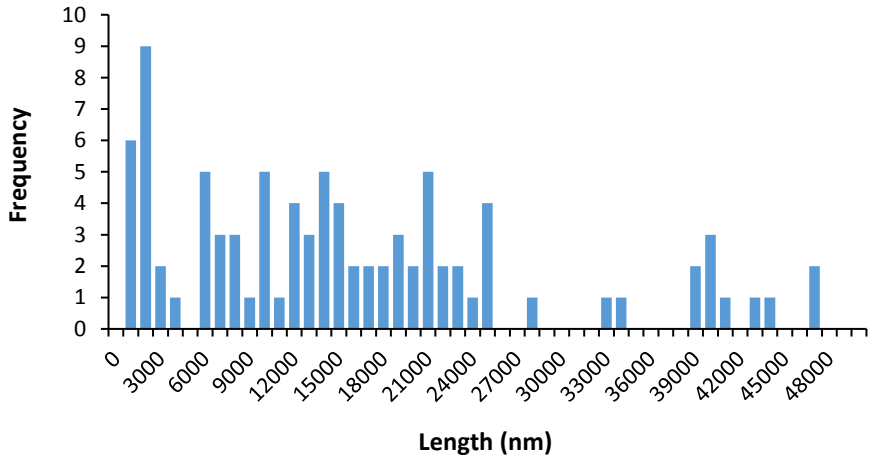

Figure 2.14. A histogram showing the size distribution of GNF used to fabricate RuNPs@GNF, L_{GNF} = 15340 ± 12099 nm.

2.4.1.1 Synthesis of RuNPs@CNS

RuNPs@SWNT and RuNPs@GNF - The metal carbonyl precursor, $Ru_3(CO)_{12}$ (1.05 mg/0.21 mg, masses equivalent to the wt.% of Ru metal required for SWNT and GNF respectively) were combined with freshly opened SWNTs (10 mg) or GNFs (10 mg) in a quartz ampoule, and sealed under vacuum (10^{-6} bar) heated at 140 °C for 3 days. After 3 days, the sample inside the quartz ampoule was cooled by immersing in an ice bath. The sample was then removed from the ampoule, sonicated in tetrahydrofuran (10 mL) for 15 minutes, then filtered through a PTFE membrane filter (pore size 0.2 μm) and repetitively washed with tetrahydrofuran (3 x 10 mL). After washing, the sample was sealed in a quartz ampoule under an argon atmosphere and heated at 600 °C for 2 hours to decompose the metal carbonyl into the desired pure metal nanoparticles.

RuNPs/(C_{60}@SWNT) - Freshly opened SWNT (10 mg) and C_{60} (20 mg) were sealed under vacuum (10^{-6} bar) in a quartz ampoule and heated at 500 °C for 2 days. After 2 days, the sample was removed from the ampoule and sonicated in toluene (10 mL) for 15 minutes. The sample was then filtered through a nylon membrane filter (pore size 0.2 μm) and repetitively washed with toluene (3 x 10 mL). After washing, the C_{60}@SWNT (10 mg) and $Ru_3(CO)_{12}$ (0.65 mg, a mass equivalent to the wt.% of Ru metal required) were combined in a quartz ampoule and sealed under an argon atmosphere and heated at 600 °C for 2 hours decompose the metal carbonyl into the desired pure metal nanoparticles.

2.4.2 ICP-OES experiments

As the method of SWNT production results in the unavoidable presence of significant and inhomogeneous amounts of large, inert Ni/Y nanoparticles in the pure support (~40 %) this makes quantification of the amount of Ru present solely by TGA difficult. In

addition, SWNT do not completely digest in strong acids making ICP-OES of NT samples problematic. To address this the RuNPs@SWNT material was initially oxidised by TGA to remove the carbon material and the remaining residual metal was then digested in acid and analysed by ICP-OES using the following general method:

RuNPs@SWNT (3 x 2 mg) were heated to 1000 °C in air in a TA Instruments TGA-SDTQ600 analyser to oxidise and remove all of the carbon material and leave just the ruthenium metal in the alumina crucible (Figure 2.15).

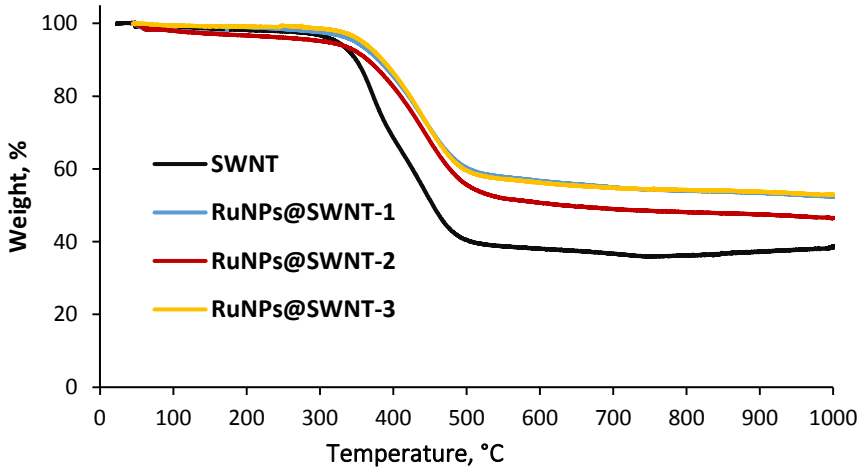

Figure 2.15. TGA curves of SWNT and three 5 mg samples of RuNPs@SWNT (labelled 1, 2 and 3). All measurements were carried out between 25-1000 °C in air at a heating rate of 10 °C/min.

The residual material was then dissolved in HNO_3 (2 mL, 69 % HNO_3) with heating and stirring at 50 °C for 6 hours and the resultant solution was diluted with ultrapure water to make a dilute HNO_3 solution (10% by volume in water). ICP-OES was used to determine the Ru content of the solution using a Perkin Elmer, Optima 2000 DV ICP-OES with S10 autosampler with an axial detection method at wavelengths of 240.272 and 349.894 nm. Calibration Ru solutions (0.005, 0.01, 0.05 and 0.1 mg mL^{-1}) were prepared using a Ru standard (VWR Chemicals) and 10% HNO_3, and gave a linear plot with an R coefficient of 0.999999. Blanks showed 0.00 mg L^{-1} of Ru. Corrected concentrations were measured

as 0.9, 1.2 and 1.2 mg of Ru per litre for each sample, which correlates to Ru loadings of 1.33, 1.58 and 1.76 % Ru respectively for the three RuNPs@SWNT sample (average = 1.55 % Ru by wt.), see Table 2.5.

Table 2.5. Data showing the precise loading of Ru metal in RuNPs@SWNT catalyst calculated by TGA and ICP-OES.

	Amount of material before TGA / mg	**Amount of Ru by ICP-OES / mg.L^{-1}**	**Amount of Ru by TGA And ICP-OES / wt. %**	**Average amount of Ru by TGA and ICP-OES / wt. %**
RuNPs@SWNT-1	1.345	0.9	1.36	
RuNPs@SWNT-2	1.502	1.2	1.58	
RuNPs@SWNT-3	1.36	1.2	1.76	**1.55**

2.4.3 Benzonorbornadiene (2a) synthesis by Diels Alder reaction

Benzonorbornadiene was synthesized according to the previously reported procedure.[34] 1,2-Dibromobenzene (5.00 g, 21.45 mmol) and cyclopentadiene (1.42 g, 21.45 mmol) were stirred in toluene (13 mL) at 0 ^{o}C under Ar. *n*-BuLi (12 mL, 1.78 M in hexanes, 21.45 mmol) was added to this solution dropwise over 30 min during which the reaction solution became first yellow then cloudy white. After an additional 10 min at 0 ^{o}C the mixture was allowed to warm to room temperature, stirred overnight and treated with H_2O (20 mL) and extracted with hexanes (3 × 30 mL). The organic layer was dried over

$MgSO_4$, filtered, and concentrated to obtain yellow oil. The product was purified by chromatography on silica gel eluting with hexanes to provide a clear and colourless oil (1.60 g, 0.11 mmol, 65 %).

2.4.4 Hydrogenation reactions using lab glassware

All reactions were performed in a pyrex pressure tube (10 bar) with a stirring bar. RuNPs@carbon nanoreactor (in each case an amount equivalent 0.0017 mmol% of Ru in the reaction mixture) was suspended in cyclooctane (1 mL) in the bottom of the tube and the resulting mixture was saturated with H_2 by bubbling a mixture of 10 % H_2 and 90 % Argon gas (1 bar) through the solution at 25 °C for 30 minutes. The alkene (0.05 mL) was then added to the resulting H_2 saturated solution. The tube was sealed and the resultant suspension was heated at 110 °C for 24 hour. After this, the reaction was stopped and the mixture was cooled down to room temperature. The resultant material was analysed by ^{1}H NMR spectroscopy.

2.4.5 Hydrogenation reactions using a high pressure $scCO_2$ batch reactor

In general, RuNPs@carbon nanoreactor (0.0017 mmol% of Ru) and alkene substrate (1 mmol) were put into a high pressure reactor (10 mL) and an O-ring was placed to seal the reactor. The reactor volume was degassed thoroughly with H_2 for 30 min by opening the outlet valve. Then, the reactor was sealed and pressurized with H_2 (10 bar) and heated initially to 40 °C in order to add the CO_2 (50 bar) as a supercritical phase using a Pickel pump and then heated slowly to 110 °C to make sure that overall pressure is 100 bar by adding more $scCO_2$ at this temperature. The reaction was then left for 24 hour and cooled under room temperature to depressurize slowly by opening outlet valve.The resultant material was analysed by ^{1}H NMR spectroscopy (Figure 2.16). All catalytic reactions were performed in duplicate, and the yields given are averages of the two experiments.

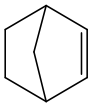

Norbornene (**1a**); ^{1}H NMR (300 MHz, 297 K, $CDCl_3$, δ, ppm): 6.01 (m, 2H), 2.85-2.9 (m, 2 H), 1.58-1.66 (m, 2H), 1.30-1.35 (m, 1H), 1.07-1.10 (m, 1H), 0.93-0.98 (m, 2H).

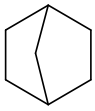

Norbornane (**1b**); ^{1}H NMR (300 MHz, 297 K, $CDCl_3$, δ, ppm): 2.21 (m, 2 H), 1.50 (m, 4H), 1.18 (m, 6 H).

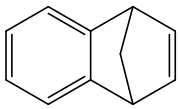

Benzonorbornadiene (1,4-dihydro-1,4-methano-naphthalene) (**2a**); ^{1}H NMR (300 MHz, 297 K, $CDCl_3$, δ, ppm): 7.24-7.21 (m, 2 H), 6.95-6.92 (m, 2H), 6.80 (m, 2 H), 3.90 (m, 2 H), 2.34-2.30 (m, 1H), 2.26-2.23 (m, 1H).

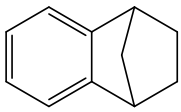

1,4-Methano-1,2,3,4-tetrahydronaphthalene (**2b**); ^{1}H NMR (300 MHz, 297 K, $CDCl_3$, δ, ppm): 7.30-7.10 (m, 4 H, ArH), 3.50-3.35 (m, 2H, CH), 2.10-1.50 and 1.50-1.10 (m, 6H, CH_2).

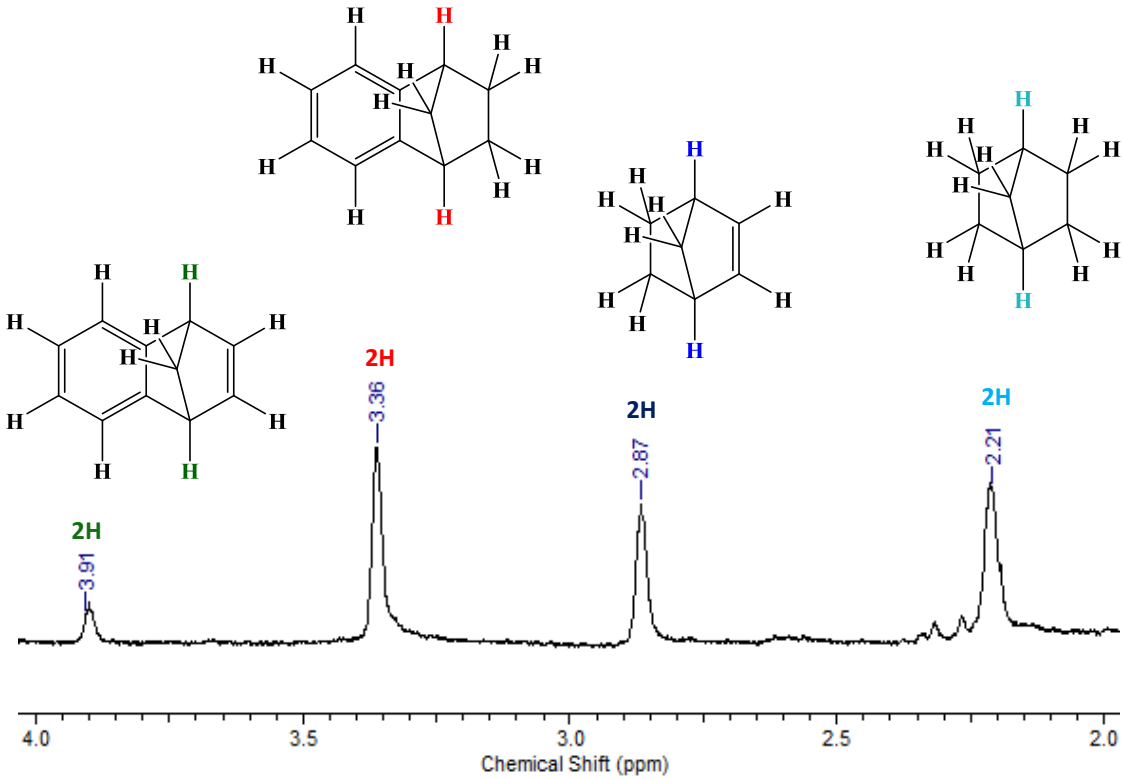

Figure 2.16. [1]H NMR of spectrum of the reaction mixture of catalytic hydrogenation of norbornene vs. benzonorbornadiene, where bridge hydrogens of the starting material of norbornene gives a multiplet at 2.87 ppm (green) was compared in the product of norbornane giving three multiplets at 2.21 ppm (red) and bridge hydrogens of the starting material of benzonorbornadiene gives a multiplet at 3.91 ppm (dark blue) was compared in the product of 1,4-methano-1,2,3,4-tetrahydronaphthalene giving a multiplet at 3.36 (blue).

2.4.6 TON Calculations

Turnover numbers (TONs) in molecules per active site were calculated using the previously reported method[27]as follows;

Table 2.6. Experimentally determined and theoretically calculated values used to approximate the TON of product molecules per active site for all carbon supported ruthenium catalysts.

Catalyst	RuNPs@SWNT	RuNPs/C_{60}@SWNT	RuNPs@GNF	Ru/C
Average RuNP size[a] / nm	0.74 ± 0.18	2.56 ± 0.62	3.58 ± 1.14	6.63 ± 2.45
Surface area of 1 RuNP[b] / nm^2	1.72	20.60	40.28	138.15
Number of Ru NPs in the catalyst (equiv. to 0.0017 mmol% of Ru per reaction)[c]	3.28×10^{16}	1.59×10^{15}	1.87×10^{14}	9.13×10^{13}
Active Ru surface area of the catalyst / $m^2\ g^{-1}$	7.46	4.31	1.00	2.69
Surface area of the Ru NPs used in the reaction / m^2	0.04	0.02	0.006	0.009
Number of Ru active sites in the catalyst used in the reaction[d]	1.85×10^{17}	1.07×10^{17}	2.46×10^{16}	4.13×10^{16}
Norbornene molecules produced[e]	5.48×10^{20}	7.22×10^{19}	2.77×10^{20}	3.07×10^{20}
TON / molecules of product per active site	2959	675	11216	7428

[a] Determined experimentally by HRTEM. [b] The active Ru surface area of the RuNPs catalysts was calculated assuming all of the NPs to be the average diameter measured by TEM, see Table 1. [c] By treating the nanoparticles as perfect spheres and knowing the mass of Ru metal in the sample enabled the number of NPs to be calculated. The surface area occupied by an individual Ru atom on the nanoparticle surface was approximated to be 0.89 nm^2 and assumes that the surface of the Ru nanoparticles is a 1:1 mix of 001 and 100 crystallographic planes.[52] [d] Calculated using the true active surface areas, details of how this was calculated are shown below. [e] Calculated from the single hydrogenation of norbornene in which RuNPs@carbon nanoreactor (0.0017 mmol of Ru) and alkene substrate (1 mmol) with H_2 (10 bar) and CO_2 (100 bar) and heated to 110 °C for 24 hour and the resultant material was analyzed by ^{1}H NMR spectroscopy.

2.4.7 Calculations of theoretical surface areas and comparison with BET surface area values

RuNPs in all samples was assumed to be perfectly spherical in shape and have a diameter equal to the mean diameter measured experimentally by HRTEM.

For RuNPs@SWNT;

Atomic radius of a Ru atom= 0.134 nm

Surface area of a Ru atom = 4*(22/7)*(0.134^2)= 0.226 nm2 = 2.226*10^^-19 m^2

An average diameter of RuNP in SWNT= 0.74 nm (measured from HRTEM).

Volume of a RuNP = (4/3)*22/7*(0.74/2) ^{3}= 0.212 nm^3= 2.12*10^{-22} cm^3.

Density of Ru = 12.45 g/cm^3.

Mass of a RuNP = 2.12*10^{-22} *12.45 =~ 2.64*10^{-21} g.

Mass of RuNPs@SWNT =0.0056 g.

Mass of Ru in RuNPs@SWNT (1.55 % Ru by wt.) =0.0000868 g.

Number of all RuNPs = 0.0000868/2.64*10^{-21} = ~3.28*10^{16}.

Atomic surface area of a RuNP = 4*22/7*(0.74/2) ^{2} = 1.72 nm^2=1.72*10^{-18} m^2.

Total surface area of all RuNPs = 3.28*10^{16}*1.72*10^{-18}= 0.057 m^2.

Active surface area of all RuNPs (only 73.93% of surface atoms are active[532]) = 0.057*0.7393= 0.0418 m^2.

Number of active Ru sites in RuNPs@SWNT used in the reaction

= Active surface area of all RuNPs / Surface area of a Ru atom

= 0.0418/ 2.226*10^^-19= 1.85*10^^17.

Active surface area of Ru atoms per gr RuNPs@SWNT = 0.04179 m^2 / 0.0056 g = ~7.46 m^2/g.

Theoretical surface area of SWNT (both internal and external surface) = 1315*2 =2630 m^2/g.[51]

Theoretical surface area of RuNPs@SWNT = 7.46 + 2630 = 2637.46 m^2/g.

The theoretical surface area of C_{60}@SWNT, RuNPs/C_{60}@SWNT, GNF, RuNPs@GNF and Ru/C were also calculated using the same calculations showed above (Table 2.7).

Table 2.7. Theoretical and BET surface area calculations for SWNT, RuNPs@SWNT, C_{60}@SWNT. RuNPS/C_{60}@SWNT, GNF, RuNPs@GNF and commercial Ru/C.

Material	Theoretical Surface Area / m^2/g	BET Surface Area / m^2/g
SWNT	2630	507.90
RuNPs@SWNT	2637.46	351.94
RuNPs in RuNPs@SWNT	7.46	N/A
C_{60}@SWNT	1315	120.99
RuNPs/C_{60}@SWNT	1319.31	164.82
RuNPs in RuNPs/C_{60}@SWNT	4.31	44.17
GNF	35	12.08
RuNPs@GNF	35.99	28.53
RuNPs in RuNPs@GNF	35.99	16.45
Carbon Black	N/A	900*
Ru/C	2.69	929.41
RuNPs in Ru/C	N/A	29.41

2.5 REFERENCES

1. D. K. Mishra, A. A. Dabbawala and J. S. Hwang, *J. Mol. Catal. A: Chemical* 2013, 376, 63–70.
2. Q. Lin, G. Yang, Q. Chen, R. Fan, Y. Yoneyama, H. Wan and N. Tsubaki, *Chem. Cat. Chem.* 2015, 7, 682-689.
3. I. Lee, M. A. Albiter, Q. Zhang, J. P. Ge, Y. D. Yin and F. Zaera, *Phys. Chem. Chem. Phys*. 2011, 13, 2449-2456.
4. K. Okitsu, A. Yue, S. Tanabe and H. Matsumoto, *Chem. Mater*. 2000, 12, 3006-3011.
5. M. Yoshizawa, J. K. Klosterman, and M. Fujita, *Angew. Chem., Int. Ed.* 2009, 48, 3418.
6. N. A. Dhas, H. Cohen, and A. Gedanken, *J. Phys. Chem. B* 1997, 101, 6834-6838.
7. B. S. Kong, J. X. Geng and H. T. Jung, *Chem. Commun.* 2009, 274-2176.
8. G. M. Scheuermann, L. Rumi, P. Steurer, W. Bannwarth, and R. Mulhaupt, *J. Am. Chem. Soc*. 2009, 131, 8262-8270.
9. X. Pan, and X. Bao, *Acc. Chem. Res.* 2011, 44, 553-562.
10. D. A. Britz, A. N. Khlobystov, K. Porfyrakis, A. Ardavan and G. A. D. Briggs, *Chem. Commun.* 2005, 37-39.
11. S. Iijima, *Nature*, 1991, 354.
12. S. M. Dresselhaus, G. Dresselhaus and A. Jorio, *Annu. Rev. Mater. Res*. *2004, 34, 247*-278.
13. J. L. Figueiredo and M. F. R. Pereira, Carbon materials for catalysis, Carbon as Catalyst, in Carbon Materials for Catalysis (eds P. Serp and J. L. Figueiredo), John Wiley & Sons, Inc., Hoboken, NJ, USA, 2008.
14. J. Zhu, A. Holmen and D. Chen, *Chem. Cat. Chem.* 2013, 5, 378-401.

15. A. N. Khlobystov, *ACS Nano* 2011, 5, 9306-9312.

16. X. Pan, and X. Bao, *Chem. Commun*. 2008, 6271-6281.

17. E. Castillejos, P. J. Debouttiere, L. Roiban, A. Solhy, V. Martinez, Y. Kihn, O. Ersen, K. Philippot, B. Chaudret and P. Serp, *Angew. Chem., Int. Ed.* 2009, 48, 2529-2533

18. W. A. Solomonsz, G. A. Rance, M. Suyetin, A. La Torre, E. Bichoutskaia and A. N. Khlobystov, *Chem. Eur. J*. 2012, 18, 13180-13187.

19. B. Cornelio, A. R. Saunders, W. A. Solomonsz, M. Laronze-Cochard, A. Fontana, J. Sapi, A. N. Khlobystov and G. A. Rance, *J. Mater. Chem. A.* 2015, 3, 3918-3927.

20. D. Wang, G. Yang, O. Ma, M. Wu, Y. Tan, Y. Yoneyama and N. Tsubaki, *ACS Catal.* 2012, 2, 1958-1966.

21. A. Benyounes, M. Kacimi, M. Ziyad and P. Serp, *Chin. J. Catal*. 2014, 35, 970-978.

22. X. Pan, Z. Fan, W. Chen, Y. Ding, H. Luo and X. Bao, *Nature Mater.* 2007, 7, 507-511.

23. J. Deng, P. Ren, D. Deng, L. Yu, F. Yang and X. Bao, *Energy Environ. Sci*. 2014, 7, 1919.

24. T. W. Chamberlain, T. Zoberbier, J. Biskupek, A. Botos, U. Kaiser and A. N. Khlobystov, *Chem. Sci*. 2012, 3, 1919-1924.

25. X. Li, T. Hungria C. G. Marcelot, M. R. Axet, P. -F. Fazzini, R. Tan, P. Serp, and K. Soulantica, *Chem. Commun.* 2016, 52, 2362-2365.

26. I. Such-Basánez, M. C. Roman-Martínez and P. Serp, *Microporous Mesoporous Mat.*, 2016, 225, 378-384.

27. T. W. Chamberlain, J. H. Earley, D. P. Anderson, A. N. Khlobystov and R. A. Bourne, *Chem. Commun.* 2014, 50, 5200-5202.

28. H. Zhang, X. Pan and X. Bao, *Journal of Energy Chemistry* 2013, 22, 251-256.

29. H. Zhang, X. Pan, J. Liu, W. Qian, F. Wei, Y. Huang and X. Bao, *ChemSusChem* 2011, 4, 975-980.

30. H. Zhang, X. Pan, X. Han. X. Liu, X. Wang, W. Shenand X. Bao, *Chem.l Sci.*, 2013, 4, 1075-1078.

31. H. Shiozawa, T. Pichler, A. Grüneis, R. Pfeiffer, H. Kuzmany, Z. Liu, K. Suenaga and H. Kataura, *Adv. Mater.* 2008, 20, 1443-449.

32. S. A. Miners, G. A. Rance and A. N. Khlobystov, *Chem. Commun.* 2013, 49, 5586-5588.

33. S. A. Miners, G. A. Rance, A. La Torre, S. M. Kenny, A. N. Khlobystov, *J. Mater. Chem. C*, 2014, 2, 8357-8363.

34. J. W. Coe, M. C. Wirtz, C. G. Bashore and J. Candler, *Org. Lett*. 2004, 6(10), 1589-92

35. E. Castillejos, P. J. Debouttiere, L. Roiban, A. Solhy, V. Martinez, Y. Kihn, O. Ersen, K. Philippot, B. Chaudret, P. Serp, *Angew. Chem., Int. Ed.* 2009, 48, 2529-2533.

36. K. Kusada, H. Kobayashi, T. Yamamoto, S. Matsumura, N. Sumi, K. Sato, K. Nagaoka, Y. Kubota, H. Kitagawa, *J. Am. Chem. Soc.* 2013, 135, 5493−5496.

37. H. E. Swanson, R. K. Fuyat and G. M. Ugrinic, *National Bureau of Standards (U.S.), Circular*, 1955, 5, 539.

38. J. F. Moulder, W. F. Stickle, P. E. Sobol and K. D. Bomben, 1992 Handbook of X-ray Photoelectron Spectroscopy (Perkin-Elmer, Minnesota) pp. 44 and 114.

39. W. Chen and S. W. Chen, *Angew. Chem. Int., Ed.* 2009, 48, 4386–4389.

40. R. S. Oosthuizen and V. O. Nyamori, *Platinum Metals Rev.* 2011, 55, 154-169.

41. Z. -Q. Feng, X. -L. Yang, Y. -F. Ye and L. -Y. Hao, *Bull. Korean Chem. Soc.* 2014, 35, No. 4.

42. M. A. Lebedeva, T. W. Chamberlain. A. Thomas B. E. Thomas, C. T. Stoppiello, E. Volkova, M. Suyetin, A. N. Khlobystov, *Nanoscale* 2016, 8, 11727-11737.

43. S. Guo, K. Y. Liew, J. Li, *J Am Oil Chem Soc* 2009, 86, 1141–1147.

44. B. Xu, K. Y. Liew, J. Li, *J Am Oil Chem Soc* 2007, 84, 117–122.

45. E. T.Silveira, A. P.Umpierre, L. M. Rossi, G. Machado, J. Morais, G. V. Soares, I. J. R. Baumvol, S. R. Teixeira, P. F.P. Fichtner, J. Dupont, *Chem. Eur. J.* 2004, 10, 3734-3740.

46. J. Mao, W. Chen, W. Sun, Z. Chen, J. Pei, D. He, C. Lv, D. Wang, Y. Li *Angew. Chem., Int. Ed.*, 2017, 56, 1-6.

47. M. C. Gimenez-Lopez, A. Kurtoglu, D. A. Walsh, A. N. Khlobystov *Adv. Mat.* 2016, 28, 9103-9108.

48. S. Guo, X. Pan, H. Gao, Z. Yang, J. Zhao, X. Bao, *Chem Eur J* 2010, 6, 5379–5384.

49. M. J. Ledoux, R. Vieira, C. Pham-Huu, N. Keller, *J. Catal.* 2003, 216, 333–342.

50. A. Peigney, C. Laurent, E. Flahaut, R. Bacsa and A. Rousset, *Carbon*, *Elsevier* 2001, 39, 507-514

51. A. La Torre, M. C. Gimenez-Lopez, M. W. Fay, G. A. Rance, W. A. Solomonsz, T. W. Chamberlain, P. D. Brown and A. N. Khlobystov, *ACS Nano* 2012, 6, 2000-2007.

52. R. A. D. Betta, *Journal of Catalysis*, 1974, 34, 57-60.

53. S. Agarwal, J. N. Ganguli, RSC Adv., 2014, 11893-11898.

3 MAGNETICALLY RECYCLABLE CATALYTIC CARBON NANOREACTORS

3.1 INTRODUCTION

Carbon nanotubes are mechanically robust, thermally and chemically stable cylindrical tubes that can be used to immobilise both molecules and nanoparticles which efficiently physically adsorb onto the nanotube walls and/or are encapsulated within the internal cavity of the nanotube via non-covalent forces such as van der Waals interactions.[1-8] Once the catalyst is immobilized in the hollow structure catalytic chemical reactions which occur within the accessible confined space of the nanoreactor interior can benefit from increases in the rate of reactions and changes in product selectivity.[9-13] Therefore carbon nanotubes are of great interest for use as nanoreactors in a variety of different catalytic chemical reactions as they not only template the formation of catalytically active metallic nanoparticles but also influence the subsequent catalytic reaction.[11,14-22] However, despite the fact that carbon nanotubes are great supports for heterogenous catalyst systems, the inherent properties of carbon nanotubes, including their low density and hydrophobicity, makes separation of them from the reaction solution using conventional separation techniques such as filration and centrifugation challenging, meaning that currently expensive equipment and secondary processes are required.[23-25] In order to minimize the costs and challenges in conventional catalyst separation and facilitate the recycling of the catalyst, intense research efforts have been focused on the development of magnetic supported metal nanoparticle catalysts which show a response to an applied magnetic field.[26-30] This enables the implementation of an approach based on the selective separation of

magnetic material supporting catalysts from the reaction mixture containing the products (non-magnetic species) by appliaction of a magnetic field (Scheme 3.1).

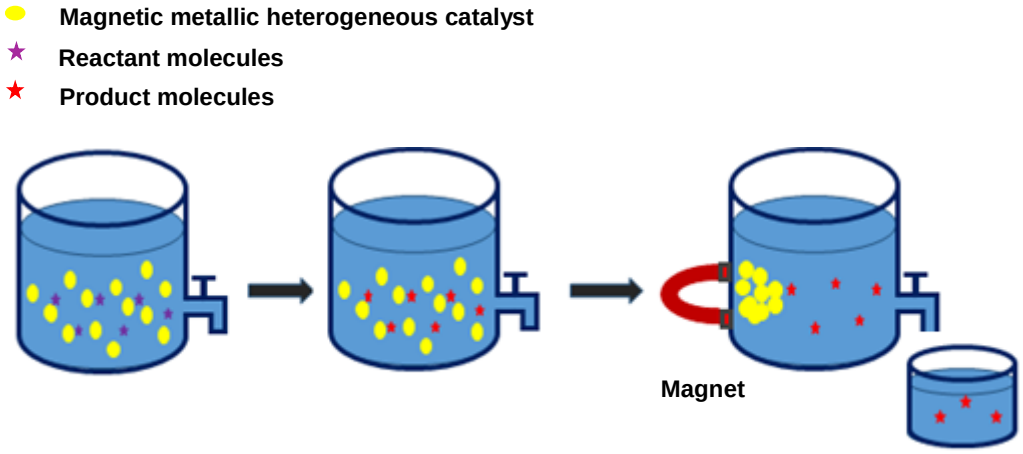

Scheme 3.1. A schematic illustration of catalyst recovery by magnetic means from a liquid solution after a chemical reaction. Reproduced from Rossi *et al.*[28]

Ferromagnetic metal nanoparticles such as Fe, Ni and Co combine high catalytic activity with a non-zero magnetic moment at room temperature due to unpaired electrons, which is interesting for many catalytic reactions.[29-30] However, as these magnetic metal nanoparticles are not stable in air and easily oxidized in acid media, resulting in a change or loss of their magnetization, their use in synthetic applications has been limited.[24] Therefore, an alternative route is to combine a fully protected magnetic nanoparticle component, coated with an appropriate inert material such as silica, polymers or carbon, with a second, non-magnetic but catalytically active metal nanoparticle component to perform the catalysis on a suitable support material.[31-34]

Preparation of carbon coated magnetic nanoparticles has recently received increasing attention as carbon nanomaterials have been proven to be both chemically and thermally more stable and robust than silica and polymer coatings.[35] These materials consist of magnetic nanoparticles, providing a magnetic core, and a graphene like outer shell which

ensures that the material is completely coated and protected against oxidation and erosion by strong acids or bases allowing their use under harsh conditions in organic synthesis applications. A number of methods have been applied to prepare carbon coated magnetic nanoparticles, especially in the metallic phase which have higher magnetic moments compared to metal oxides, using chemical vapour deposition and the sequential spraying and controlled pyrolysis of carbon sources at elevated temperatures.[31,36-37] Recently Grass *et al*. developed a method to synthesise carbon coated Co nanomagnets ($Co@C_n$) using reducing flame spray pyrolysis under an inert atmosphere.[31] This method allowed the production of nearly spherical magnetic particles with an onion-like graphene based carbon coating of 2-3 nm and a mean particle size of about 4-100 nm (Figure 3.1).

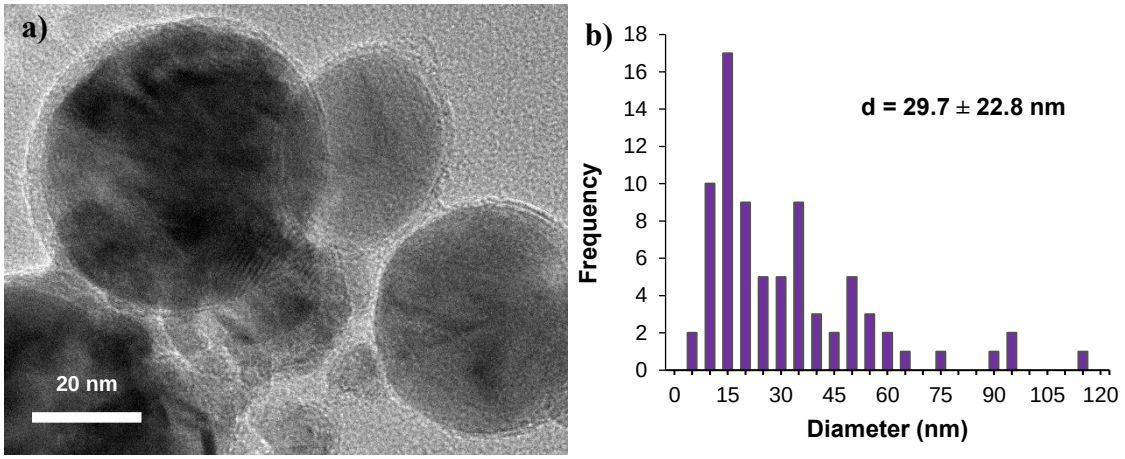

Figure 3.1. a) HRTEM image of the graphene like carbon covered cobalt nanomagnets in ($Co@C_n$)/GNF where the graphene layers can be seen in the close-up of the particle, b) particle size distribution of $Co@C_n$ (the combined diameter of the Co NP and graphitic shell were measured for more than 80 particles).

It was subsequently demonstrated that it is possible to modify the carbon coating using both covalent and non-covalent sidewall functionalisation and this has been exploited to attach catalytic nanoparticles to the surface of the nanomagnets, creating magnetically

recoverable heterogeneous catalysts for a variety of catalytic applications.[38-43] On the other hand, Wittmann *et al*. demonstrated the preparation of a palladium complex non-covalently attached to Co@C_n based on strong π-π stacking interactions between pyrene units and the outer-most graphene layer enabling efficient catalyst recovery.[39] Furthermore, the graphene-like outermost shell of carbon coated magnetic nanoparticles is very similar to the sp^2 hybridised carbon surface of carbon nanotubes which enables combination of the two materials via non-covalent adsorption of the nanoparticles onto the exterior sidewalls or into the internal channel of the nanotubes using van der Waals forces.[40] The combination of catalytic carbon nanoreactors with magnetic Co@C_n nanoparticles using non-covalent interactions (van der Waals forces) could potentially allow the separation of the carbon nanoreactors from reaction mixtures in a fast, easy and efficient way by simply applying a magnetic field. In this study, this idea of creating magnetically separable carbon nanoreactors which contain catalytically active metal nanoparticle catalysts in their interiors is explored and both the catalytic activity and the magnetically induced separation of the resultant hybrid materials is investigated.

Graphitised carbon nanofibers (GNF) were chosen as the carbon nanoreactor support as they, unlike carbon nanotubes, have negligible residual metal content making analysis of the metal nanoparticle nanocarbon hybrids easier to deconvolute.[44] Furthermore, GNF have different structures of their internal and external surfaces and large, continuous internal channels, with an average diameter of ~50 nm. Finally, unlike carbon nanotubes, the internal surface has a succession of step edges which can act as anchoring points for guest species which makes GNF a great candidate to immobilize catalytic particles and perform catalytic reactions in a nano-confined environment.[7, 18-19] With this aim, two different procedures to create magnetically recyclable GNF based carbon nanoreactors were developed; 1, simple attachment of commercially available Co@C_n to GNF through

non-covalent interactions, and 2, *in situ* formation of Fe@C_n on the GNF. In addition, two different methodologies were then developed to combine active palladium and platinum nanoparticle catalyst formation and magnetic functionalisation steps. As a result, catalytically active and magnetically separable hybrid materials were successfully produced and the activity of these materials were probed using the industrially important reaction of the reduction of nitrobenzene.

3.2 RESULTS AND DISCUSSION

3.2.1 Making magnetic nanoreactors by non-covalent attachment of commercial cobalt Co@C_n to GNF ((Co@C_n)/GNF)

Commercially available magnetic Co@C_n were attached to individual GNFs using non-covalent interactions. As GNFs mostly exist aligned to each other in bundles, held together by van der Waal forces (0.5 eV/Mm), a good solvent was required to obtain well-dispersed and separated tubes.[45] Therefore, GNFs were initially dispersed using ultrasonic treatment in hexane. Co@C_n were also dispersed using the same method, and then added to the hexane/GNF dispersion very slowly whilst being continuously treated with ultrasonic waves to create a material in which the Co@C_n nanoparticles are non-covalently attached to the outside of the GNF, (Co@C_n)/GNF (Scheme 3.2 and

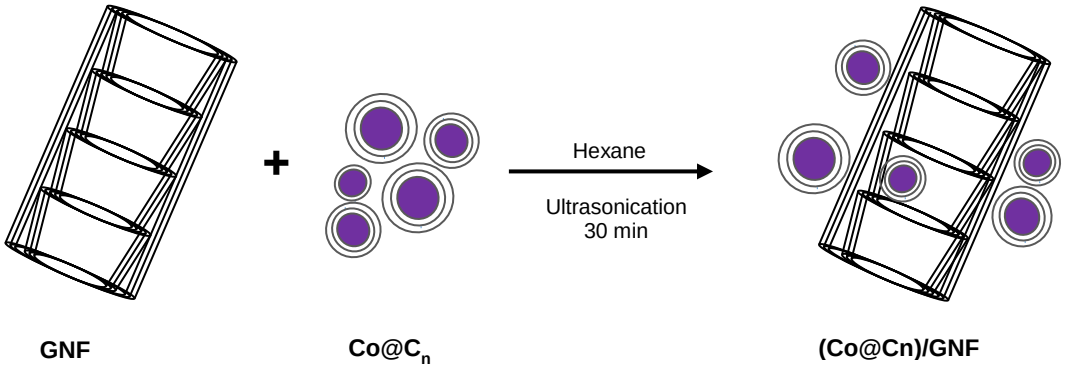

Scheme 3.2. Schematic illustration of the experimental procedure to synthesise carbon coated CoNPs attached to GNF.

Experimental 3.4.2). Experiments were preformed to find the minimum loading of $Co@C_n$ required that would still allow complete separation of the composite material from solution. This was evaluated by simply changing the amount of magnetic $Co@C_n$ in the $(Co@C_n)$/GNF material and exposing each sample, suspended in hexane, to an external magnet and evaluating the resulting solution by eye. $(Co@C_n)$/GNF was prepared in 1, 5 and 10 % by wt. of $Co@C_n$ in GNF and the resultant functionalised GNF composites were separated from the solvent by applying an external magnetic field using a commonly available neodymium magnet with a magnetic strength of ~0. 1 Tesla (T, $V.s/m^2$ in unit). Complete separation for $(Co@C_n)$/GNF containing 10 % of $Co@C_n$ was achieved (Experimental section 3.4.2). Lower $Co@C_n$ loadings, however resulted in incomplete separation compromising the recovery of all the catalyst material that is strictly required when pursuing recyclable catalytic reactions (Figure 3.2).

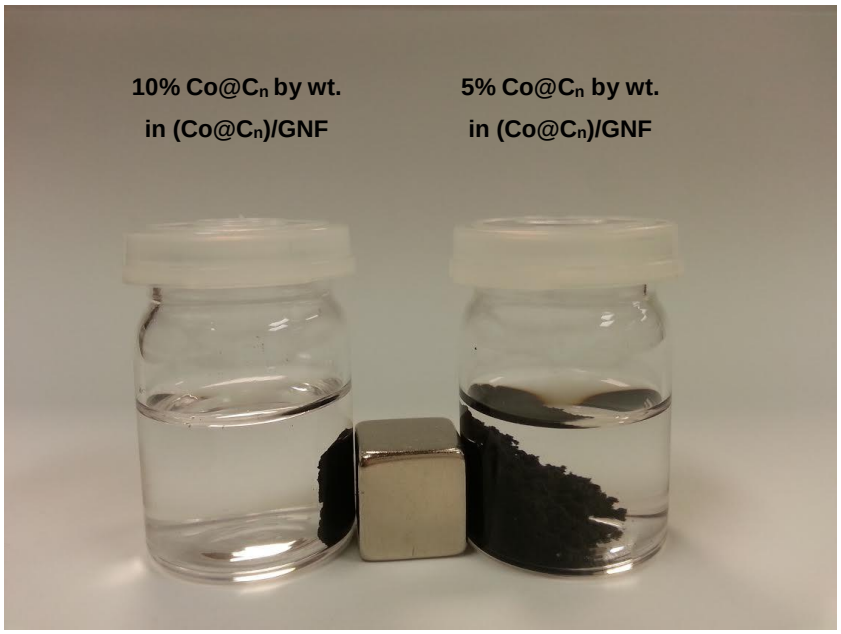

Figure 3.2. Comparison of the effectiveness of the magnetic separation for $(Co@C_n)$/GNF with a 10 % (wt) (left) and a 5 % (wt) (right) $Co@C_n$ loading where $(Co@C_n)$/GNF was dispersed in hexane by ultrasonication and exposed to a magnet (0.1 T).

The ($Co@C_n$)/GNF sample with 10 % by wt. loading was then characterised by HRTEM, TGA and powder XRD. HRTEM confirmed the presence of very-well distributed $Co@C_n$ on both the inside and outside GNF sidewalls with an average diameter of 29.7 ± 22.8 nm (Figure 3.3).

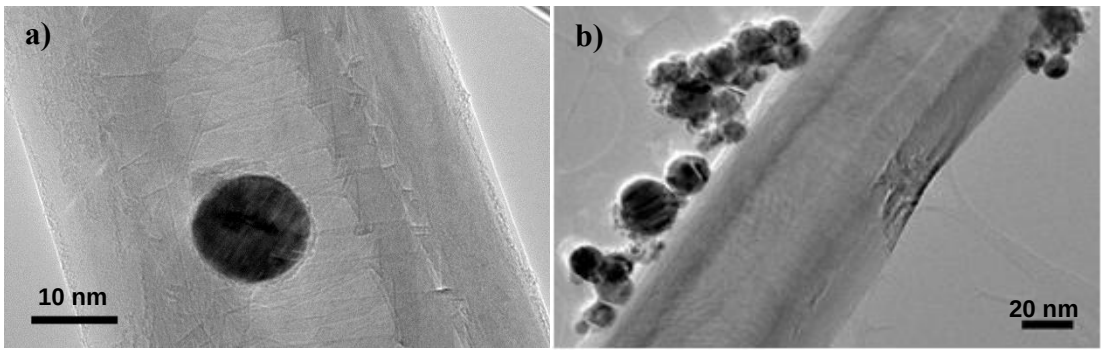

Figure 3.3 HRTEM images of $Co@C_n$/GNF material (10 % by wt.) showing the $Co_n@C$ non-covalently attached to the inner (a) and outer (b) GNF sidewalls.

As expected the majority of the $Co@C_n$ nanomagnets (>90 %) are adhered to the GNF outer walls, presumably due to the more readily accessible surface and aromatic character of the GNF results in a better affinity for $Co@C_n$ than the corrugated, step-edge containing internal channel. The smooth graphitic shell of the $Co@C_n$ is presumably engaged in π-π stacking interactions with the smooth exterior of GNF and thus results in stronger van der Waals forces between the $Co@C_n$ and the GNF outer surface. There is also possibly an energetic barrier to diffusion of the larger $Co_n@C$ nanoparticles diffusing down the internal channel of the GNF.

The composition of the ($Co@C_n$)/GNF was determined by powder XRD showing the presence of a metallic cobalt phase which is in good agreement with the reference fcc-Co metal pattern (Figure 3.4a).[46]

TGA was used to identify the degree of magnetic metal loading in ($Co@C_n$)/GNF after heating in air up to 1000 °C at a heating rate of 10 °C per minute (Figure 3.4b). TGA

studies of (Co@C_n)/GNF showed that the presence of Co led to a significant decrease in the oxidation temperature of the GNF from ~700 °C to 500 °C. The carbon content of the material completely burned at ~800 °C, before this temperature no weight gain was observed, which means that the carbon shell around the Co and GNF provided an effective barrier against the oxidation of Co enabling long term stability of the magnetic material which is consistent with the literature.[47-48] The weight gain observed due to oxidation of the residual Co after the carbon shells have been removed, observed between ~800 °C and 1000 °C, was negligible, however, to ensure this was accounted for the residual weight was recorded as an average value between 800-850 °C and revealed the material to be 8.5 ± 0.5 % by wt. Co.

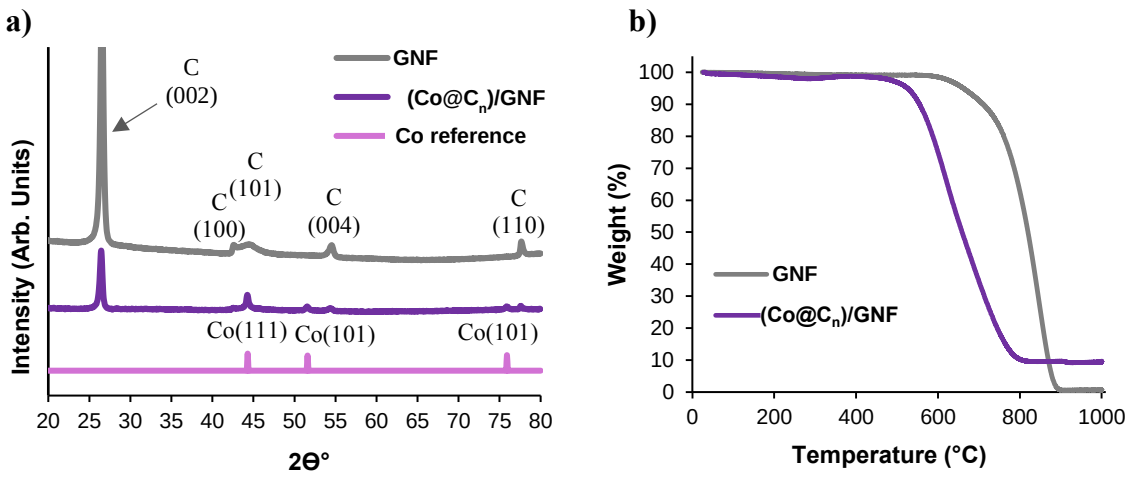

Figure 3.4. a) Powder XRD patterns of (Co@C_n)/GNF (purple), metallic cobalt (pink) and GNF (grey) for comparison, b) TGA measurements of (Co@C_n)/GNF (purple) and GNF (grey) showing residual weights (wt.%) of 8.5 ± 0.5 and ~0.5, respectively, at 1000 °C.

3.2.2 Making magnetic nanoreactors via *in situ* formation of carbon coated Fe nanoparticles on GNF ((Fe@C_n)/GNF)

An experimental method was developed to make carbon coated Fe nanoparticles directly on GNF, (Fe@C_n)/GNF. Importantly, the same number of moles of Fe as the amount of Co that is present in the (Co@C_n)/GNF system was used to allow direct comparison of the two magnetic systems. In this novel experimental method, ferrocene was inserted from the vapour phase into GNF at 350 °C under vacuum and subsequently heated in inert environment to 500 °C to decompose the ferrocene into Fe NPs coated in graphitic shells in/on the GNF (N.B. the carbon is a result of ligand decomposition) (Scheme 3.3 and Experimental section 3.4.3).

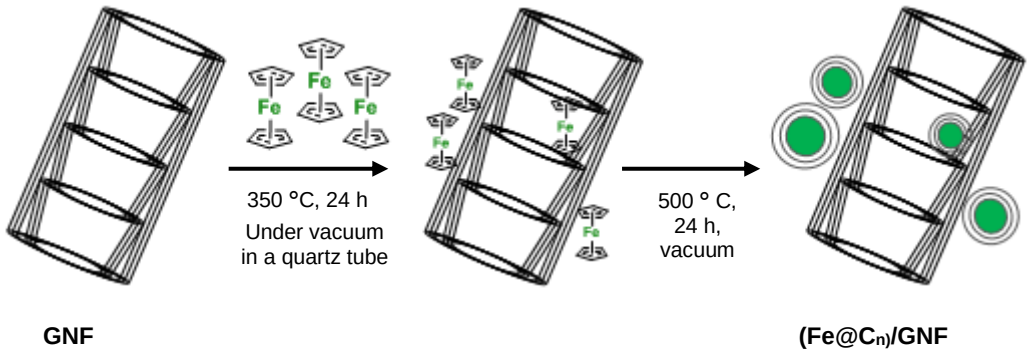

Scheme 3.3 Schematic illustration of the experimental procedure for synthesis of carbon coated FeNPs attached to GNF ((Fe@C_n)/GNF).

HRTEM measurements confirmed the presence of FeNPs coated by a graphitic like shell in which the interplanar distance was measured to be 0.34 nm which is comparable to that of the interlayer spacing in graphite. The Fe@C_n nanoparticles are distributed both inside and mostly outside of the GNF sidewalls with an average diameter of 23.9 ±14.9 nm (Figure 3.5).

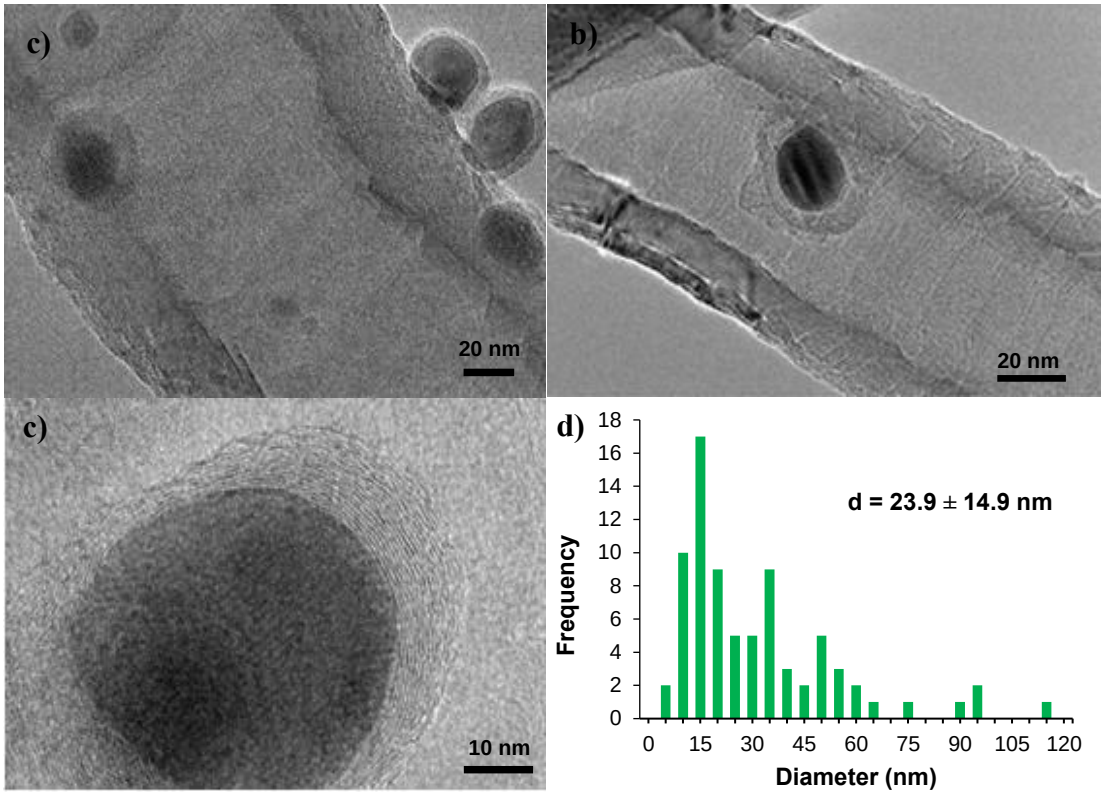

Figure 3.5. a) HRTEM image of a graphene like carbon coated iron nanomagnet in (Fe@C_n)/GNF where the graphene layers can be seen in the close-up of the particle, b) particle size distribution of Fe@C_n (the size of Fe and graphitic shell were measured together using more than 80 particles c-d) HRTEM images of Fe@C_n non-covalently attached to the GNF.

In contrast to the Co@C_n/GNF system, where the majority of nanomagnets are deposited and thus located on the outer surface of the GNF, the majority (>60 %) of the Fe nanomagnets are adhered to the internal channels of the GNF structure. This could be a results of the step edges providing better adsorption sites for individual ferrocene molecules during the decomposition process. Thus, as the iron material is already inside the channel, upon rapid thermal decomposition the resultant carbon coated Fe nanomagnets are formed, and therefore located, primarily inside the GNF channel. In addition to this, the conjugated surface is probably a good for nucleation of Fe@C_n. It is proposed that the small percentage of iron nanomagnets located on the outside of the GNF are either a result of the small portion of ferrocene molecules which were initially

adsorbed on outer of the GNF and/or a result of ferrocene molecule from the inside which rapidly desorbed from the step edges into the gas phase before they have time to decompose during the decomposition step and therefore deposit on the outside of the GNF when formed.

The structure of the FeNPs was also analysed by powder XRD, revealing the presence of a metallic Fe phase which is in good agreement with the diffraction pattern of α-FeNPs reported previosuly (Figure 3.6a).[49] The residual Fe loading (wt.%) in the (Fe@C_n)/GNF was quantified using TGA (Figure 3.6b).

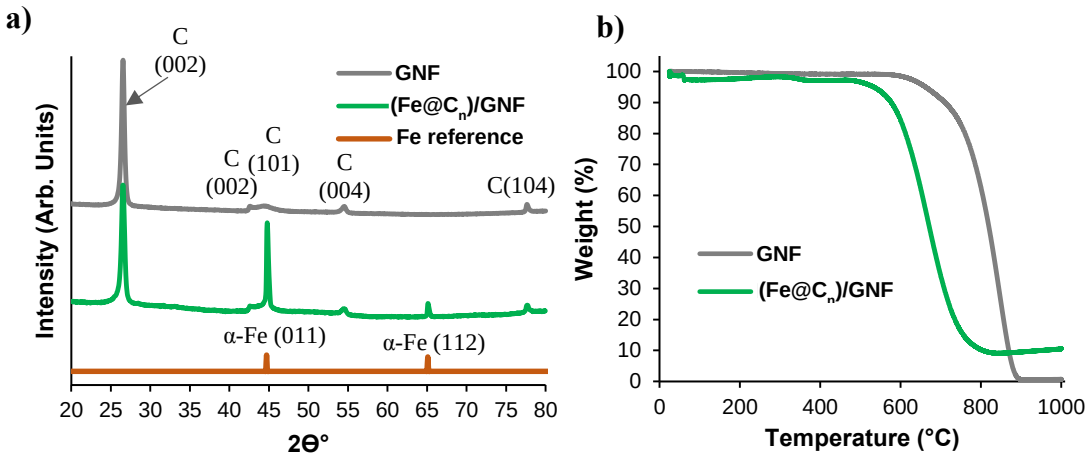

Figure 3.6. a) Powder XRD patterns of (Fe@C_n)/GNF, metallic iron and GNF for comparison, b) TGA measurements of (Fe@C_n)/GNF (green) and GNF (grey) showing residual weights (wt.%) of 8.5 ± 0.6 and ~0.5, respectively, at 1000 °C.

Similar to (Co@C_n)/GNF, TGA study showed that the presence of Fe in (Fe@C_n)/GNF led to a significant decrease in the oxidation temperature of the GNF from ~700 °C to ~500 °C. The carbon content of the material completely burned at ~820 °C and up to this temperature no weight gain was observed as a result of oxidation of the Fe due to the protection of the FeNPs by the carbon shell and GNF. The mass of residual Fe observed between 820-850 °C from the material was essentially constant, however, after 850 °C a

small weight gain, presumably oxidation of the Fe, was observed. Therefore, the residual Fe content (wt.%) was recorded as the average mass between 820-850 °C, and was observed to be 8.5 ± 0.6 wt.%, (Figure 3.6b), *i.e.* a very similar metal loading to the (Co@C_n)/GNF material.

3.2.3 Evaluating the efficiency of the magnetic separation of (Co@C_n)/GNF and (Fe@C_n)/GNF

Separation of the resultant functionalised GNF composite suspensions from the solvent was achieved by placing a magnet (0.1T) on the external wall of the sample tube for a short period of time (90 s) (Figure 3.7a). The effect of varying the extent of loading of both Co@C_n and Fe@C_n on the separation of the GNFs was evaluated using an ultraviolet–visible (UV-Vis) spectroscopy in which (Co@C_n)/GNF and (Fe@C_n)/GNF samples were suspended separately in hexane by stirring and exposed to an external magnet for different lengths of time (see Experimental section 3.4.14 for full details). UV-Vis spectroscopy was used to evaluate the concentration of Co@C_n/GNF and Fe@C_n/GNF remaining suspended in the hexane after application of the magnet. We used the intensity of absorbance measured by UV-Vis spectroscopy to determine the concentration of GNF-magnetic material composite remaining as a suspension after magnetic separation at the visible wavelength range, 350-700 nm. We approximate that the visible light passing through the GNF suspension is absorbed and/or scattered by the GNF present and the extent of this, i.e. the absorbance observed, is directly proportional to the concentration of GNF present, in accordance with the Beer-Lambert law.[50-51] Excellent separation for both materials was achieved after exposure to the magnetic field for very short time periods of ~ 90 s (Figure 3.7).

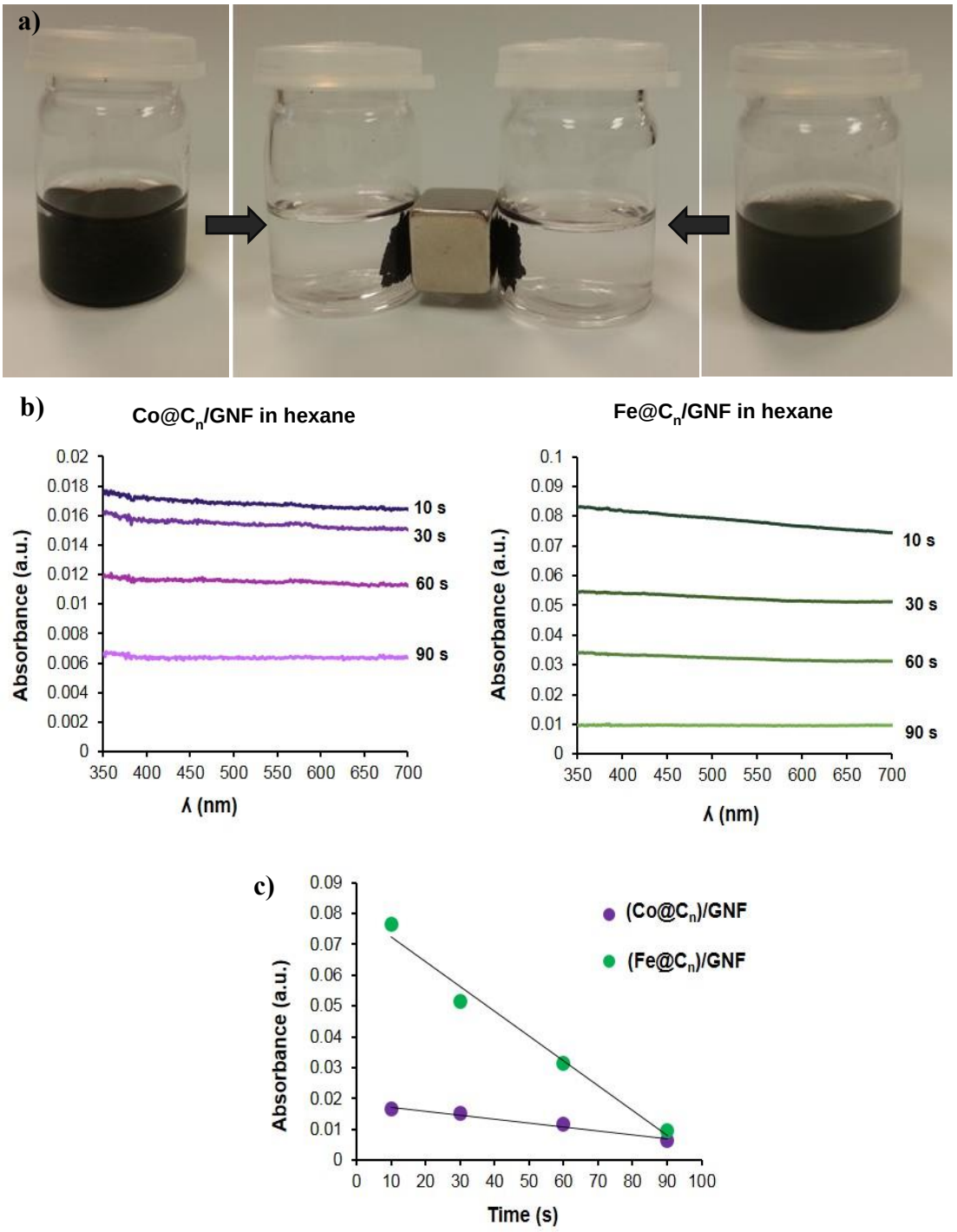

Figure 3.7. a) Suspensions of (Co@C$_n$)/GNF (left) and (Fe@C$_n$)/GNF (right) after applying a magnetic field for 90 s. b) UV-Vis measurements for the solutions of Co@C$_n$)/GNF (left) and (Fe@C$_n$)/GNF (right) after magnetic separation at various times. c) Plot of optical density at 500 nm of the solutions from (Co@C$_n$)/GNF and (Fe@C$_n$)/GNF separations in hexane versus the length of time that the magnetic field (0.1 T) was applied for.

UV-Vis spectroscopy measurements for the separation of each material follow a linear trend over time at a single wavelength (500 nm) as shown in Figure 7c. The absorbance is observed to decrease over time upon application of the magnetic field for each material, however, (Co@C_n)/GNF is observed to reach lower absorbances faster than (Fe@C_n)/GNF, which shows a slower decrease in absorbance, *i.e.* (Co@C_n)/GNF is separated from hexane more quickly. The magnetic properties of iron, nickel and cobalt nanoparticles have been investigated previously and it is reported that ferromagnetism is stronger for bigger magnetic nanoparticles.[52] Though the magnetic Co and Fe nanoparticles in our materials both have a broad distribution of sizes, the average diameter of the cobalt nanoparticles (29 nm) is slightly larger than the iron nanoparticles (23 nm) which could explain the slightly faster separation of the (Co@C_n)/GNF system.

With the principal aim of developing high performance magnetically recyclable nanoreactors, the magnetic behaviour of (Co@C_n)/GNF and (Fe@C_n)/GNF was studied in depth (Experimental section 3.4.13). The magnetic response of both systems under an external applied magnetic field displayed the hysteresis loops shown in Figure 3.8 and exhibited the magnetic parameters summarised in Table 3.1. While at 5 T (Fe@C_n)/GNF reaches higher magnetic saturation values than (Co@C_n)/GNF at both 2 K and 300 K, at low magnetic fields (below 0.1 T) the magnetisation values observed for (Co@C_n)/GNF are slightly higher than that of the Fe analogue. These observations are also in agreement with the thermal variation measurements of the magnetisation performed for both materials at 0.1 T. As shown in Figure 3.8.c, (Co@C_n)/GNF showed higher magnetisation values than that of (Fe@C_n)/GNF for all of the temperature range studied (2-300 K).

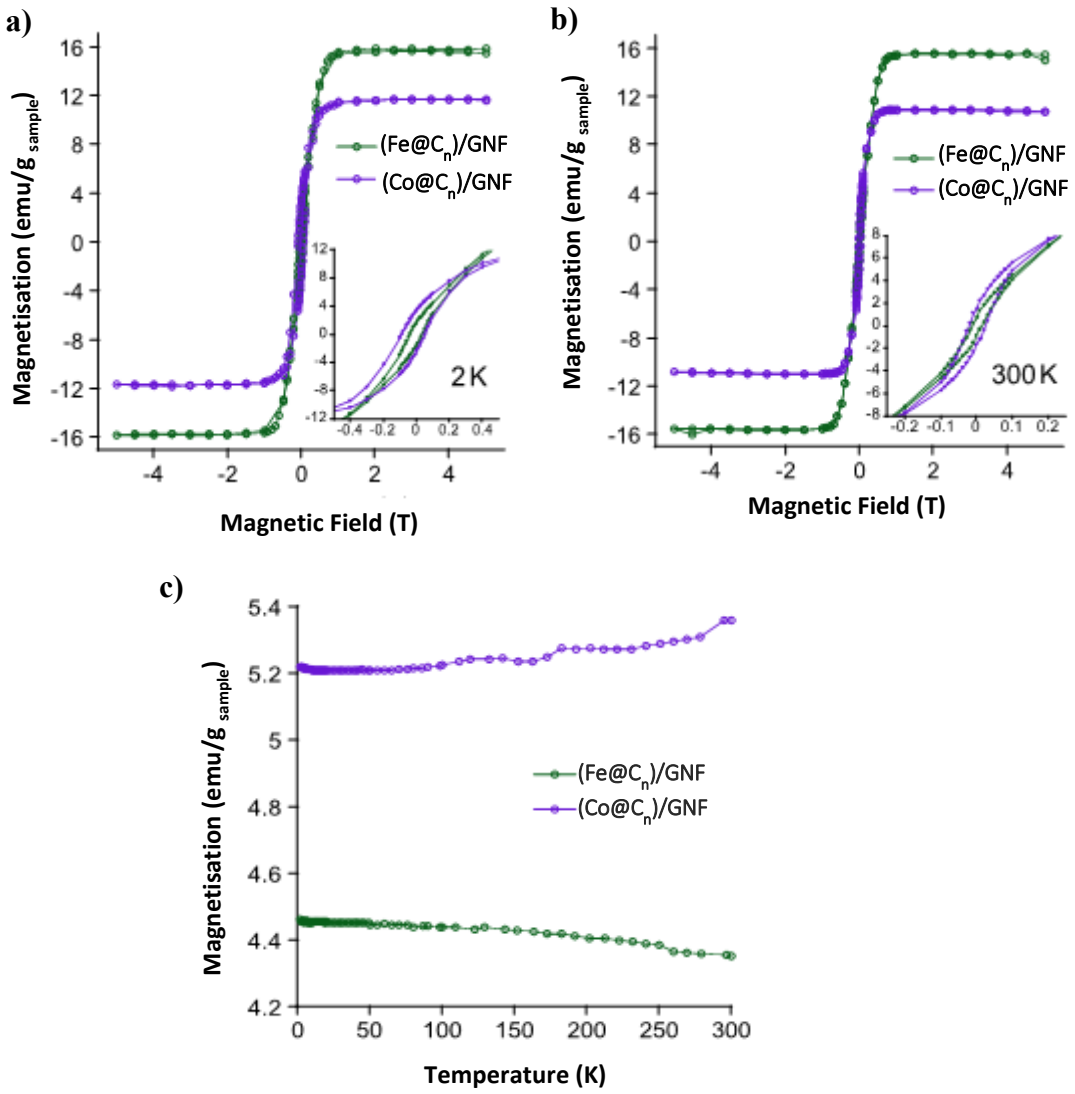

Figure 3.8. Magnetic hysteresis loops for (Co@C_n)/GNF and (Fe@C_n)/GNF recored at; a) 2 K and b) 300 K (inset: expanded region at low magnetic fields between -0.5 and 0.5 T) c) Thermal variation of magnetization under an applied magnetic field of 0.1 T for (Co@C_n)/GNF and (Fe@C_n)/GNF at 300 K.

These results are consistent with our UV-vis measurements for which we observed a better separation with (Co@C_n)/GNF in comparison to (Fe@C_n)/GNF when a small magnetic field (<0.1 T) was applied for the separation at room temperature.

Table 3.1. Magnetisation, remanent and coercivity magnetic fields for (Co@C_n)/GNF and (Fe@C_n)/GNF at 2 K and 300 K.

	Magnetisation at 5T (emu/g_{sample})	**Remanent magnetisation (emu/g_{sample})**	**Coercivity magnetic field (T)**	**Magnetisation at 0.1 T (emu/g_{sample})**
(Co@C_n)/GNF at 2K	11.65	6.91	0.14	5.22
(Co@C_n)/GNF at 300 K	10.76	1.56	0.045	5.36
(Fe@C_n)/GNF at 2 K	15.84	1.59	0.04	4.45
(Fe@C_n)/GNF at 300 K	15.58	1.42	0.026	4.35

3.2.4 Catalytic chemical reactions within magnetically recoverable carbon nanoreactors

3.2.4.1 Catalytic carbon nanoreactors

After successful demonstration of the magnetic separation of ($Co@C_n$)/GNF and ($Fe@C_n$)/GNF nanoreactors the next step was to confine catalytically active metal nanoparticles within the nanoreactors in order to utilise these materials in a suitable catalytic reaction. The reduction of nitrobenzene was chosen as it is a very important reaction both in industry and academia, with aniline used as a precursor in the synthesis of chemicals, dyes and pharmaceuticals.[53] Palladium (PdNPs) and platinum nanoparticles (PtNPs) were selected as they have been demonstrated as highly active catalysts for the solution phase reduction of nitrocompounds previously.[54-62] In addition, they are both paramagnetic metals, so no competing magnetic effects are expected in the final composite materials. The formation of Pd and Pt nanoparticles supported by the GNF nanoreactor (MNPs@GNF; MNPs stands for metal nanoparticles) was initially investigated in the absence of the magnetic nanoparticles so that suitable formation conditions could be found. The Pd and PtNPs@GNF were synthesized using suitable metal procursors, (see Experimental section 3.4.4 for details), and then tested in the reduction of nitrobenzene using a high pressure H_2 glass vessel (Scheme 3.4).

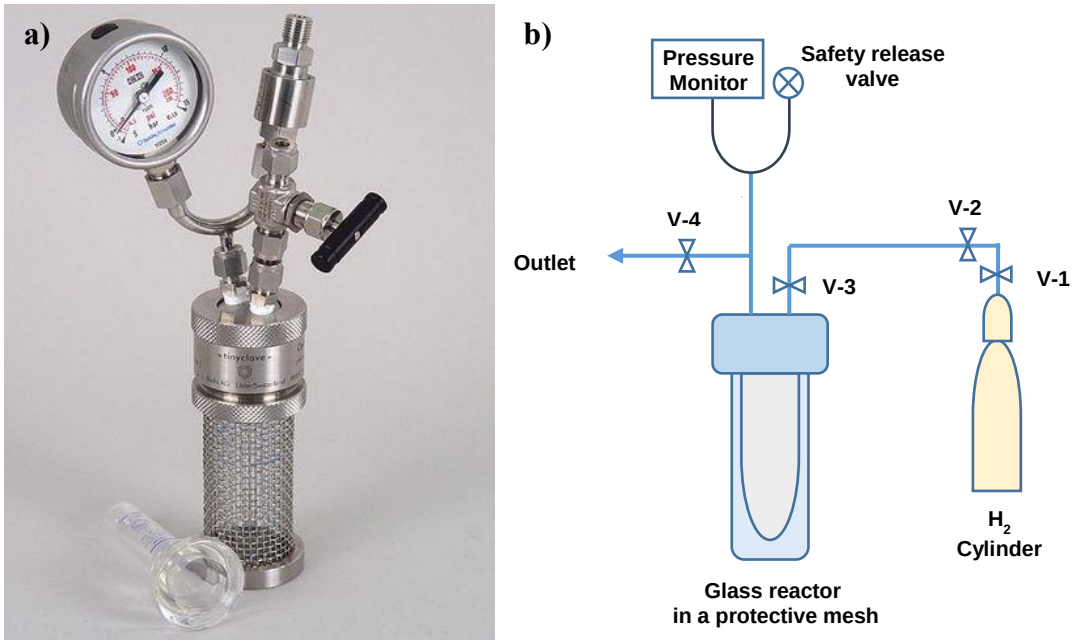

Scheme 3.4. a) The high-pressure glass reactor, and b) a schematic of the high-pressure glass hydrogenation batch system (right).

Two different Pd metal precursors were utilised to form palladium nanoparticles in GNF (PdNPs@GNF) to find the optimal system. PdNPs@GNF-1 was produced by the thermal decompostion of $Pd(acac)_2$ to form Pd nanoparticles inside the GNF and HRTEM confirmed the formation of PdNPs with an average particle size of 10.79 ± 3.86 nm (see Experimental section 3.4.4 and Figure 3.9a-b). PdNPs@GNF-2 was synthesised using an adapted method based on work reported by Pentsak *et al.* in which nanoparticle palladium species are generated in a chloroform solution of Pd_2dba_3 in the presence of GNFs and the resultant PdNPs preferentially attach to the step edges of the GNF (see Experimental section 3.4.4).[63] This resulted in the formation of very small and well distributed PdNPs, observed mostly inside the GNF by HRTEM with an average diameter of 2.26 ± 0.56 nm (Figure 3.9a and 9b).

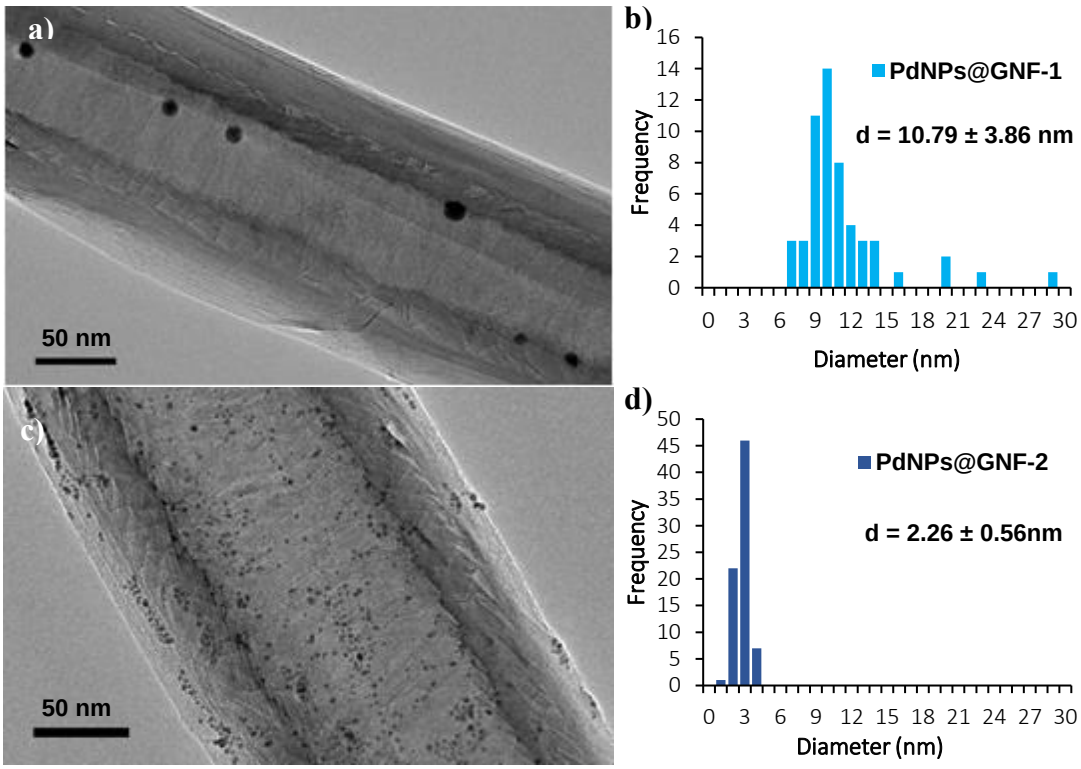

Figure 3.9. Representative HRTEM images of a) PdNPs@GNF-1, and c) PdNPs@GNF-2 loaded with PdNPs (0.5 % by wt. Pd), and b) and d) the histograms showing the size distribution of the PdNPs in their respectively composites.

The powder XRD patterns for PdNPs@GNF-1 and PdNPs@GNF-2 were studied and the presence of metallic Pd phases for PdNPs@GNF-1 was confirmed via comparison to the Pd reference patterns (Figure 3.10a).[64] However, XRD measurement of PdNPs@GNF-2 did not exhibit clear Pd diffraction patterns due to the presence of only very small Pd nanoparticles. Therefore, we re-synthesised a new PdNPs@GNF-2* material with a higher metal loading (15 % Pd by wt.) using the same procedure to synthesis PdNPs@GNF-2 and observed distinctive Pd diffraction patterns by XRD (Figure 3.10b).

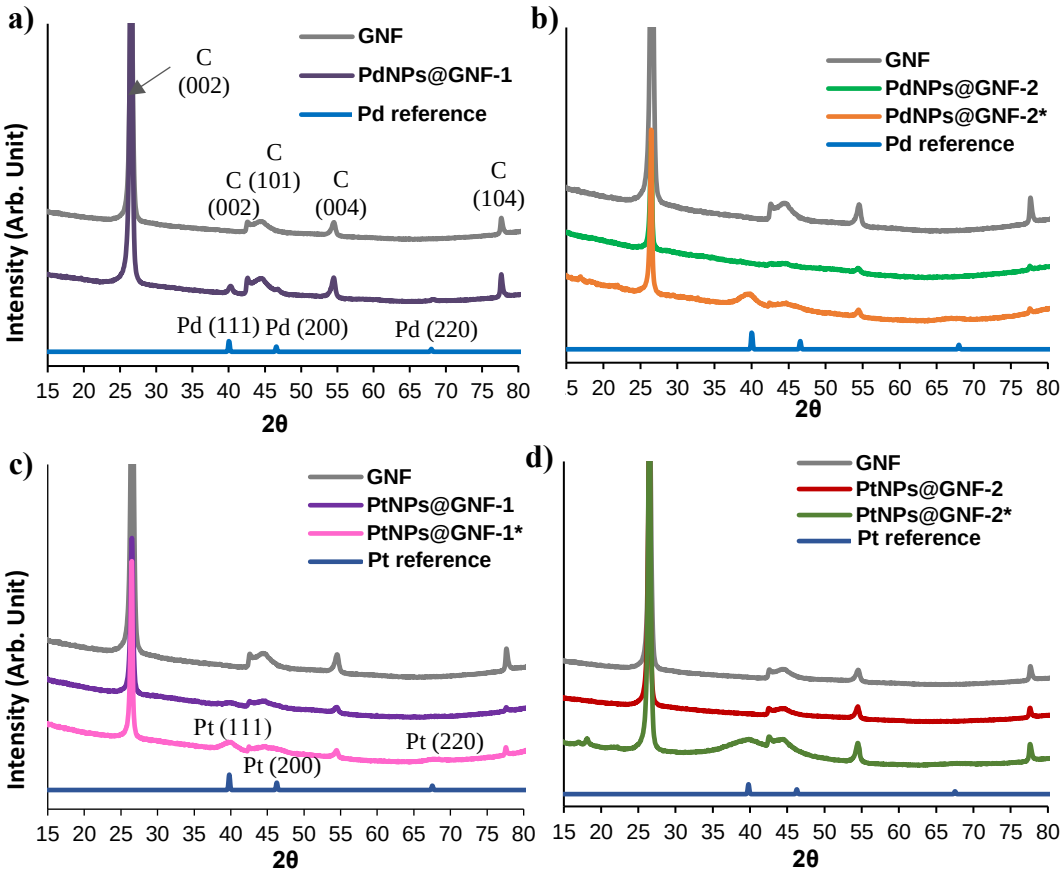

Figure 3.10. Powder XRD patterns of a) PdNPs@GNF-1, b) PdNPs@GNF-2 and PdNPs@GNF-2*, c) PtNPs@GNF-1 and PtNPs@GNF-1* and d) PtNPs@GNF-2 and PtNPs@GNF-2*. Diffractograms for Pd[64] and Pt[65] references and GNF (annealed at 450 °C for 1 h) are shown for comparison. All * composites show 15 % by wt. loading of Pt or Pd respectively for comparison.

PtNPs@GNF-1 and PtNPs@GNF-2 were produced using the $Pt(acac)_2$ and $Ptdba_3$, using similar experimental procedures[66] to those used to make PdNPs@GNF-1 and PdNPs@GNF-2, respectively (Experimental section 3.4.6 and 3.4.7). HRTEM images for PtNPs@GNF-1 showed Pt nanoparticles precisely distributed within the step edges of the nanoreactor with an average particle size of 4.21 ± 1.54 nm (Figure 3.11a-b). HRTEM of PtNPs@GNF-2 revealed very small particles with an average particle size of 1.55 ± 0.48 nm located mostly in the interior of the nanoreactor (Figure 3.11c-d).

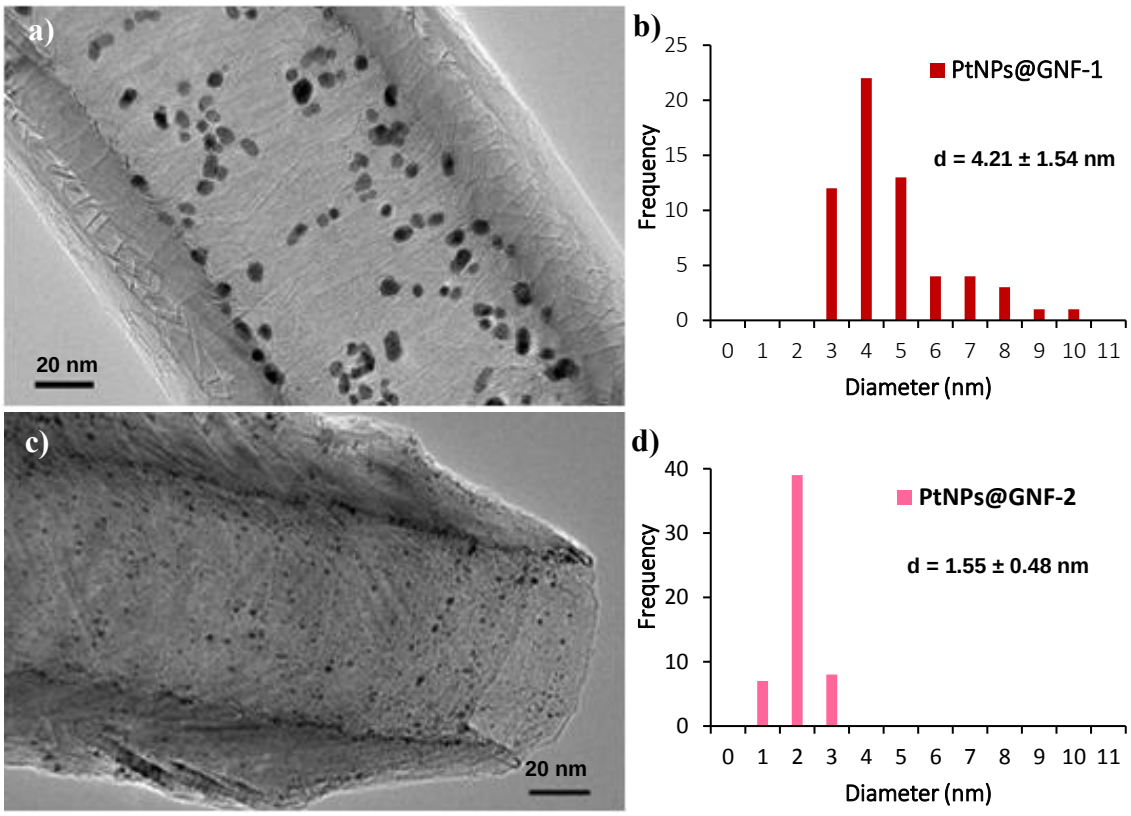

Figure 3.11. Representative HRTEM images of a) PtNPs@GNF-1, and c) PtNPs@GNF-2 loaded with PtNPs (1 % by wt. Pt) and, b) and d) the histograms showing the size distribution of the PtNPs in their respectively composites.

The powder XRD patterns for PtNPs@GNF-1 and PtNPs@GNF-2 were investigated and displayed in Figure 3.10c and 3.10d, respectively. As PtNPs@GNF-1 and PtNPs@GNF-2 did not exhibit clear Pd and Pt diffraction patterns due to the small size of Pt nanoparticles, we re-synthesized all these material with a higher metal loading (15% Pt by weight) resulting in bigger nanoparticle size and therefore allowing clear diffraction patterns for each material which are used to confirm the presence of metallic Pt phases for both materials when compared to the reference Pt metal pattern[65] (Figure 3.10c and 3.10d).

The reduction of nitrobenzene reactions was then tested in the presence of all catalysts using high pressure glass equipment and molecular H_2, and quantified by ^1H NMR (Experimental section 3.4.5). The reaction with empty GNFs displayed no catalytic activity at all. The lower reactivity of PdNP@GNF-1 compared to PdNPs@GNF-2 (containing very small PdNPs) in the reduction of nitrobenzene can be attributed to the larger size, and thus lower catalytic surface area of the PdNPs in PdNPs@GNF-1. In contrast, no reactivity was observed for the smaller PtNPs in PtNPs@GNF-2 compared to the larger PtNPs in PtNPs@GNF-1, which were surprisingly reactive (Table 3.2**)**. Therefore, PdNPs@GNF-2 and PtNPs@GNF-1, which showed a significant activity and better aniline selectivity compared to n-phenylhydroxylamine (the danger of explosion in the accumulation of n-phenylhydroxylamine was considered, however it was reported[67] that it could become if the reaction temperature gets close to 250 °C), were chosen as candidates to couple with the magnetic nanoparticle GNF systems. The reason for the lack of reactivity for the small PtNPs in PtNPs@GNF-2 material is unknown and requires further investigation but it is hypothesised that such small nanoparticles could be quite amorphous and therefore have poorly defined sites for catalysis. Addition to this, the catalyst surface may be less structured and contain some residual dba due to the preparation. This is supported by the lack of observed crystallographic planes in XRD and HRTEM.

Table 3.2. Reduction of nitrobenzene in the presence of the prepared Pd and Pt composite catalyst materials using a high pressure H_2 glass reactor.

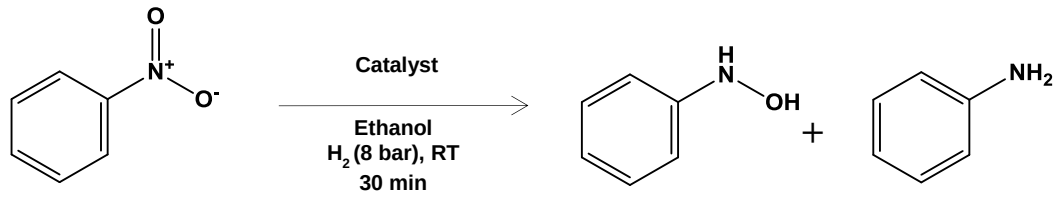

Catalyst	Time	Conversion of Ph-NO_2 (%)	Selectivity (%) Ph-NHOH	Selectivity (%) Ph-NH_2
-	24 h	0	0	0
GNF[a]	24 h	0	0	0
PdNPs@GNF-1	30 min	3.5	71	29
PdNPs@GNF-2	30 min	77	15	85
PdNPs@GNF-2	50 min	100	0	100
PtNPs@GNF-1	30 min	24	36	64
PtNPs@GNF-1	200 min	100	0	100
PtNPs@GNF-2	30 min	0	0	0
PtNPs@GNF-2[b]	24 h	0	0	0

Reaction conditions: Nitrobenzene (0.08 mL, 0.78 mmol), ethanol (0.5 mL), catalyst (0.00047 mmol of metal), H_2 (8 bar), RT. All reactions were performed in duplicate and nitrobenzene conversion was determined by ^{1}H NMR with an error of ± 2 %. [a]GNF were annealed at 450 °C for 1 hour prior to use. [b]PtNPs@GNF-2 was annealed under H_2 flow for 5 h at 150 °C prior to the reaction to get rid of any impurities on the surface of Pt which can cause deactivation of the catalyst.

Due to the lack of reactivity of PdNPs@GNF-1 and PtNPs@GNF-2, we did not further investigate these materials in the reduction of nitrobenzene, continuing only with the PdNPs@GNF-2 and PtNPs@GNF-1.

For a better understanding of the performance of the reaction, the surface area of PdNPs@GNF-2 and PtNPs@GNF-1 was investigated using BET enabling the number of active sites for each catalyst to be approximated. BET surface areas and pore size distributions were studied for GNF, PdNPs@GNF-2 and PtNPs@GNF-1 (Table 3.3 and Figure 3.12).

Table 3.3. BET measurements for GNF, PdNPs@GNF-2 and PtNPs@GNF-1.

	Pore volume, cm^3/g	**Pore sizes, Å**	**BET surface area, m^2/g**
GNF[a]	0.023237	32/54/63/93/252/503	12.08
PdNPs@GNF-2	0.033801	32/54/63/93/252/503	16.06
PtNPs@GNF-1	0.030408	32/54/63/93/252/503	15.67

*GNF were annealed at 450 °C for 1 h prior to use.

As we reported in Chapter 2, GNF have a surface area of 12 m^2/g and contain mesoporous (2-50 nm) and some macroporous (> 50 nm) pores in the carbon structure which is consistent with the size of the step edges (height = 3-5 nm) and the inner channel of the GNF (diameter = 10-100 nm).[61]

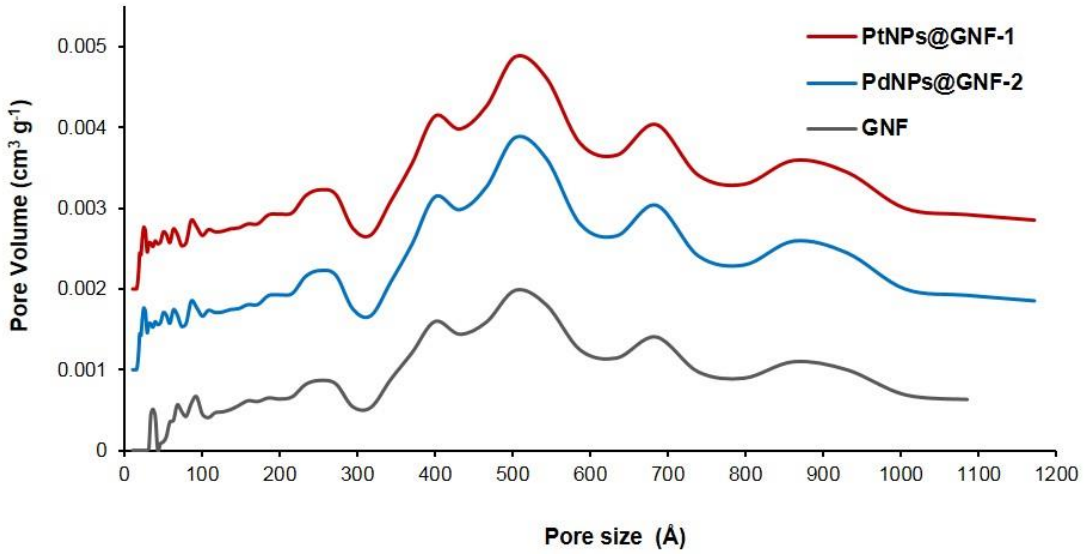

Figure 3.12. Pore size distributions for GNF, PdNPs@GNF-2 and PtNPs@GNF-1.

After adding Pd or Pt nanoparticles to the GNF support, a similar increase in BET surface area is observed for each catalyst, ~16 $m^2\ g^{-1}$ for PdNPs@GNF-2 and ~15.7 $m^2\ g^{-1}$ for PtNPs@GNF-1. This increase in surface area is attributed to the metal nanoparticles in the GNF. This gave surface areas of 3.985 $m^2\ g^{-1}$ for the PdNPs in PdNPs@GNF-2) and 3.596 $m^2\ g^{-1}$ for PtNPs in PtNPs@GNF-1.

3.2.5 Magnetically recoverable metal loaded carbon nanoreactors

Magnetically recoverable carbon nanoreactors were fabricated by developing two different methodologies for the combination of the catalyst and magnetic nanoparticle formation steps. To fabricate magnetic nanoreactors containing catalytic metal nanoparticles using Co@C_n, catalytic Pd or Pt NPs was firstly encapsulated within GNF using the solution method and gas phase filling method respectively and then subsequently combined with commercially available Co@C_n in hexane using the ultrasound conditions previously optimised (see Experimental sections 3.4.4).

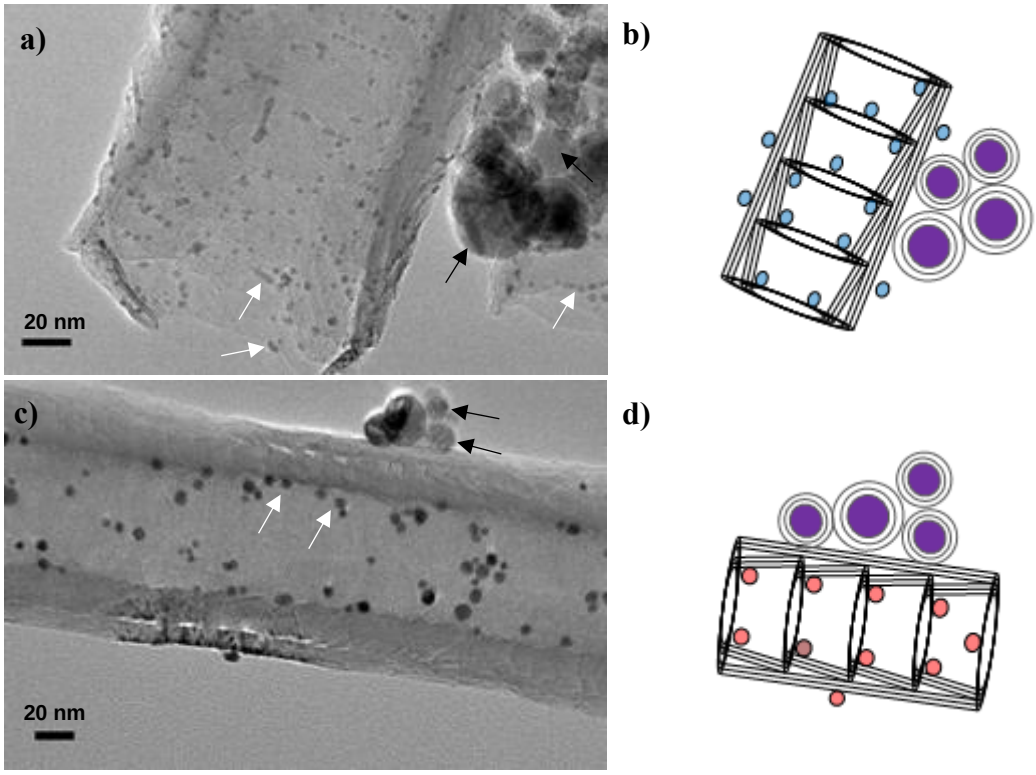

Figure 3.13. a) Representative HRTEM image of PdNPs@((Co@C_n)/GNF), white and black arrows shows PdNPs and Co@C_n attached to the GNF nanoreactor, respectively. b) Schematic diagram depicting the PdNPs@((Co@C_n)/GNF) material with PdNPs (blue) and Co@C_n (purple) both attached to the GNF. c) Representative HRTEM image of PtNPs@((Co@C_n)/GNF), white and black arrows shows PtNPs and Co@C_n both attached to the GNF, respectively. d) Schematic diagram depicting the PtNPs@((Co@C_n)/GNF) material with PtNPs (red) and Co@C_n (purple) both attached to GNF.

HRTEM analysis of both PdNPs@((Co@C_n)/GNF) and PtNPs@((Co@C_n)/GNF), Figure 3.13a and 3.13c respectively, confirmed the successful combination of Co@C_n with PdNPs@GNF and PtNPs@GNF. To fabricate catalytic magnetic nanoreactor using Fe@C_n, the magnetic component was produced initially to give (Fe@C_n)/GNF and then the catalytic Pd or Pt NPs were encapsulated within (Fe@C_n)/GNF using solution and gas phase filling methods, respectively (see Experimental sections 3.4.10 and 3.4.12 for full details). HRTEM images of PdNPs@((Fe@C_n)/GNF) and PtNPs@((Fe@C_n)/GNF) are shown in Figure 3.14a and 3.14b resepctively, confirming successful formation of the two MNPs@(Fe@C_n)/GNF systems.

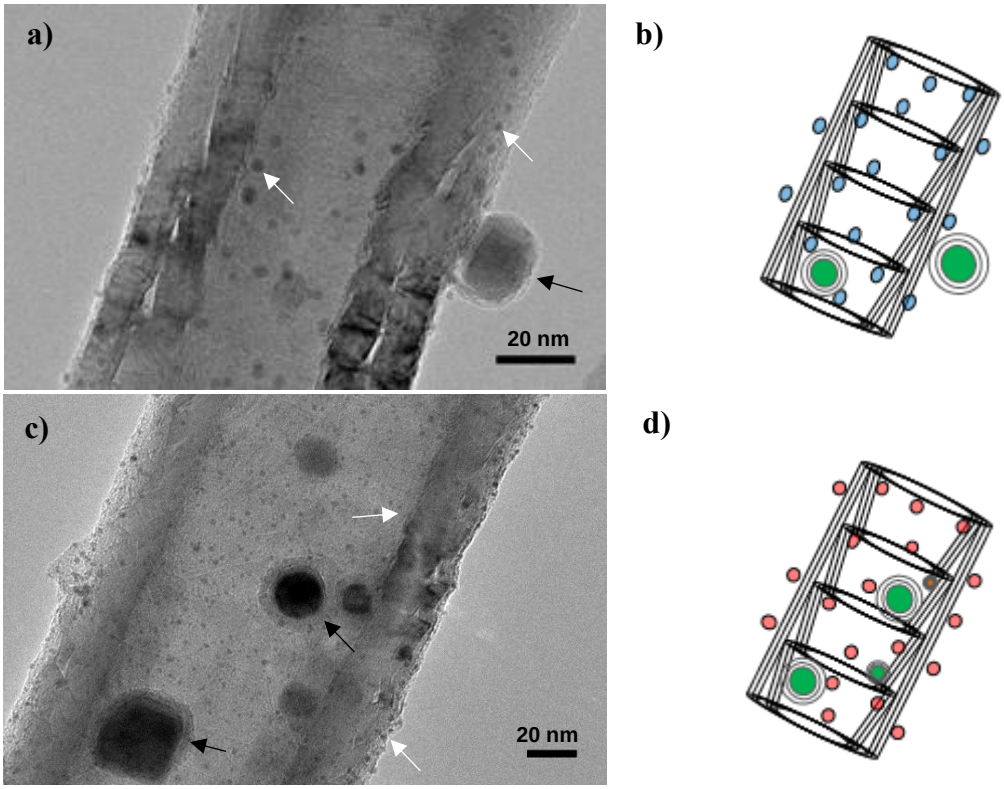

Figure 3.14. a) Representative HRTEM image of PdNPs@((Fe@C_n)/GNF), white and black arrows shows PdNPs and Fe@C_n attached to the GNF nanoreactor, respectively. b) Schematic diagram depicting the PdNPs@((Fe@C_n)/GNF) material with PdNPs (blue) and Fe@C_n (green) both attached to the GNF. c) Representative HRTEM image of PtNPs@((Fe@C_n)/GNF), white and black arrows shows PtNPs and Fe@C_n both attached to the GNF, respectively. d) Schematic diagram depicting the PtNPs@((Fe@C_n)/GNF) material with PtNPs (red) and Co@C_n (green) both attached to GNF.

3.2.6 Catalytic chemical reactions within magnetically recoverable MNPs@((Fe@C_n)/GNF) and MNPs@((Co@C_n)/GNF) catalysts

The catalytic activity of the Pd and Pt catalysts confined within the carbon nanoreactors was also tested using the reduction of the nitrobenzene to give a turnover frequency (TOF) for each catalyst (Table 3.4).

Table 3.4. Reaction data for the reduction of nitrobenzene in the presence of (Co@C_n)/GNF, PdNPs- and PtNPs@((Co@C_n)/GNF), (Fe@C_n)/GNF, and PdNPs- and PtNPs@((Fe@C_n)/GNF)

Catalys	Conversion of Ph-NO_2 (%) / TOF (min^{-1})	Selectivity (%)	
		Ph-NHOH	Ph-NH_2
PdNPs@GNF-2	77 / 72.3	15	85
PtNPs@GNF-1	24 / 25.2	36	64
(Co@C_n)/GNF	0	0	0
PdNPs@((Co@C_n)/GNF)	74 / 69.5	14	86
PtNPs@((Co@C_n)/GNF)	23 / 24.2	43	57
(Fe@C_n)/GNF	0	0	0
PdNPs@((Fe@C_n)/GNF)	72 / 69.1	16	84
PtNPs@((Fe@C_n)/GNF)	22 / 23.2	32	68

Reaction conditions: Nitrobenzene (0.08 mL, 0.78 mmol), ethanol (0.5 mL), catalyst (0.00051 mmol), H_2 (8 bar), RT. All reactions were performed in duplicate and nitrobenzene conversion was determined by ^1H NMR with an error of ± 2 %. The TOFs were calculated as the ratio of the number of molecules of substrate consumed in the reaction per the number of true active catalyst sites calculated by BET measurements per minute.

Pd catalysts functionalised with (Co@C_n)/GNF and (Fe@C_n)/GNF performed very similarly with nitrobenzene TOFs of 69.5 and 69.1, respectively. This is also very similar to the catalytic performance of the PdNPs@GNF-2 in the absence of the magnetic nanomaterials (*c.f.* TOF of 69.1). PtNPs@((Co@C_n)/GNF) and PtNPs@((Fe@C_n)/GNF) also exhibited similar nitrobenzene conversions (TOFs of 24.1 and 23.2, respectively) both to each other and that of the unmodified PtNPs@GNF-1 catalyst (*c.f.* TOF of 25.2). All combined experiments demonstrate that both (Co@C_n)/GNF and (Fe@C_n)/GNF do not contribute to the reaction or change the product selectivity in the absence or presence of the metal nanoparticle catalysts.

Several studies have been reported the reduction of nitro compounds performed under high pressures and temperatures in the presence of Pd and Pt catalyst supported by different materials.[54-62] Karwa *et al*. studied the effect of reaction temperature, hydrogen pressure and solvent on the selectivity of reduction of nitrobenzene in the presence of Pd and Pt catalysts on carbon supports and reported that they observed the formation of phenylhydroxylamine as a by-product to the transformation of aniline at low temperatures and a better selectivity of phenylhydroxylamine in the presence of Pt catalysts compared to Pd catalysts.[54] They also demonstrated that hydrogen pressures between 7-21 atm do not alter the selectivity of the reaction however the solvent used in the reaction significantly affected the selectivity of phenylhydroxylamine, especially solvents with higher dielectric constants such as methanol (32.7) which gave lower selectivity for aniline. This is rationalised as a result of the increased solubility and thus desorption of phenylhydroxylamine into the solvent preventing further hydrogenation to aniline. Takenaka *et al.* studied the catalytic ability of Pt/C and Pt/SiO_2 in the reduction of nitrobenzene at room temperature using molecular hydrogen (1 and 10 bar) and observed very high selectivity for phenylhydroxylamine (>95%).[58] These results are consistent

with our data in which we observed a higher selectivity of phenylhydroxylamine in the presence of PtNPs@GNF compared to PdNPs@GNF while getting higher aniline selectivity overall for each catalyst. Sangeetha *et al*. studied the catalytic activity of Pd supported on hydrotalcite (HT), MgO and γ-Al_2O_3 between 225-300 °C and obtained the best activity in the presence of Pd/HT with a maximum turnover frequency of ~0.8 s^{-1} (48 min^{-1}). [57] Gelder *et al*. investigated the catalytic ability of Pd supported on different active carbon materials in the reduction of nitrobenzene using methanol and isopropyl alcohol as solvents at 50 °C and observed better catalytic activity in methanol with a turnover frequency of 0.27 s^{-1} (16.2 min^{-1}) which is quite low compared to our Pd catalyst supported within a carbon nanoreactor (c.f. our TOF = 72.3 min^{-1}).[55]

The mechanism of the reduction of nitrobenzene is still not been fully understood. However, the Haber mechanism is generally accepted in the literature and proposes two different reaction routes; direct and indirect.[56-62, 68] The direct route is based on the reduction of nitrobenzene to nitrosobenzene (Ph-NO) and consecutive formation to phenylhydroxylamine (Ph-NHOH) and aniline (Ph-NH_2). In the light of the Haber mechanism, several research groups have proposed different additions/alterations to the reduction mechanism.[69-71] Gelder *et al.* has recently proposed a new mechanism which is contrary to the Haber process and showed that nitrosobenzene cannot be an intermediate in the formation of aniline (Scheme 3.5).[64]

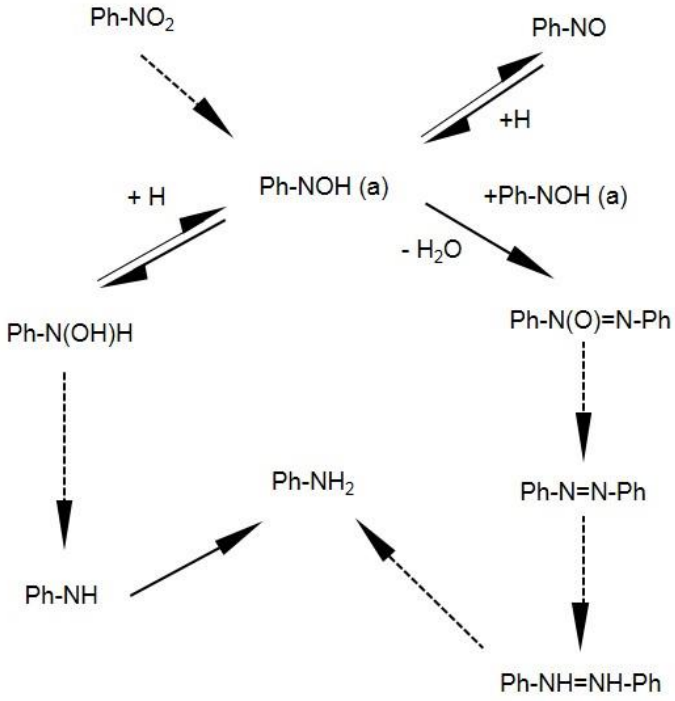

Scheme 3.5. Proposed reaction pathways of the reduction of nitrobenzene by Gelder mechanism.[69]

Our study revealed reduction of nitrobenzene to phenylhydroxylamine to form aniline which is consistent with the direct Haber process, however we did not observe nitrosobenzene or any other side products. We can therefore accept that the Gelder mechanism is also consistent with our results.

3.2.7 Stability tests after the magnetically recovery of MNPs@(Co@C_n)/GNF and MNPs@(Fe@C_n)/GNF

We investigated the reusability and stability of PtNPs- and PdNPs@(Co@C_n)/GNF and @(Fe@C_n)/GNF in the reduction of nitrobenzene, respectively, and compared with a traditional filtration based separation method. In each case the catalyst was separated from the product after each run by applying a magnetic field and reused after washing with ethanol and drying in air without any other treatment and compared to the traditional catalyst recovery of PdNPs and PtNPs @GNF by filtration using a PTFE membrane filter and washing with ethanol (Table 3.5-3.6, Figure 3.15-3.16 and see Experimental 3.4.9-3.4.10).

Recyclability tests showed a significant decrease in nitrobenzene conversion during the five recoveries of each catalyst (Table 3.5-6 6, Figure 3.15-16), however magnetic recovery compared to traditional catalyst recovery by filtration using a PTFE membrane filter demonstrated slightly lower loss in nitrobenzene conversion during the five runs.

Table 3.5. Stability test data showing the activity of PdNPs@GNF-1 in the reduction of nitrobenzene in sequential reactions after conventional recovery based on the filtration using a PTFE membrane paper vs. PdNPs@(Co@C_n)/GNF and PdNPs@(Fe@C_n)/GNF in the reduction of nitrobenzene in sequential reactions after magnetic recovery.

Experiment no.	Catalyst	Conversion of Ph-NO_2 (%) / TOF (min^{-1})	Selectivity (%)	
			Ph-NHOH	Ph-NH_2
1st cycle	PdNPs@GNF-2[a]	77 / 72.3	15	85
	PdNPs@(Co@C_n)/GNF[b]	74 / 69.5	14	86
	PdNPs@(Fe@C_n)/GNF[b]	72 / 69.1	16	84
2nd cycle	PdNPs@GNF-2[a]	57 / 57.3	18	82
	PdNPs@(Co@C_n)/GNF[b]	70 / 65.7	17	83
	PdNPs@(Fe@C_n)/GNF[b]	68 / 64.4	13	87
3rd cycle	PdNPs@GNF-2[a]	48 / 45.1	20	80
	PdNPs@(Co@C_n)/GNF[b]	64 / 60.1	17	83
	PdNPs@(Fe@C_n)/GNF[b]	59 / 55.8	20	80
4th cycle	PdNPs@GNF-2[a]	50 / 46.9	26	74
	PdNPs@(Co@C_n)/GNF[b]	42 / 39.4	28	72
	PdNPs@(Fe@C_n)/GNF[b]	55 / 52.1	22	78
5th cycle	PdNPs@GNF-2[a]	37 / 35.6	29	71
	PdNPs@(Co@C_n)/GNF[b]	46 / 43.2	26	74
	PdNPs@(Fe@C_n)/GNF[b]	47 / 44.5	19	81

Reaction conditions: Nitrobenzene (0.08 mL, 0.78 mmol), ethanol (0.5 mL), catalyst (0.00051 mmol), H_2 (8 bar), RT. All reactions were performed in duplicate and nitrobenzene conversion was determined by ^1H NMR with an error of ± 2 %. The TOFs were calculated as the ratio of the number of molecules of substrate consumed in the reaction per the number of true active catalyst sites calculated by BET measurements per minute. [a]Recovered by filtration. [b]Recovered by magnetic separation.

Table 3.6. Stability test data showing the activity of PtNPs@GNF-1 in the reduction of nitrobenzene in sequential reactions after conventional recovery based on the filtration using a PTFE membrane paper vs. PtNPs@(Co@C_n)/GNF and PtNPs@(Fe@C_n)/GNF in the reduction of nitrobenzene in sequential reactions after magnetic recovery.

Experiment no.	Catalyst	Conversion of Ph-NO_2 (%) / TOF (min^{-1})	Selectivity (%)	
			Ph-NHOH	Ph-NH_2
1st cycle	PtNPs@GNF-1[a]	24 / 25.2	36	64
	PtNPs@(Co@C_n)/GNF[b]	23 / 24.2	43	57
	PtNPs@(Fe@C_n)/GNF[b]	22 / 23.1	32	68
2nd cycle	PtNPs@GNF-1[a]	18 / 21.8	41	59
	PtNPs@(Co@C_n)/GNF[b]	20 / 21	50	50
	PtNPs@(Fe@C_n)/GNF[b]	19 / 19.9	52	48
3rd cycle	PtNPs@GNF-1[a]	15 / 15.6	50	55
	PtNPs@(Co@C_n)/GNF[b]	19 / 19.9	47	53
	PtNPs@(Fe@C_n)/GNF[b]	16 / 16.8	56	44
4th cycle	PtNPs@GNF-1[a]	15 / 15.6	43	57
	PtNPs@(Co@C_n)/GNF[b]	15 / 15.7	47	53
	PtNPs@(Fe@C_n)/GNF[b]	16 / 16.8	53	47
5th cycle	PtNPs@GNF-1[a]	13 / 13.5	48	52
	PtNPs@(Co@C_n)/GNF[b]	15 / 15.7	47	53
	PtNPs@(Fe@C_n)/GNF[b]	15 / 15.7.	53	47

Reaction conditions: Nitrobenzene (0.08 mL, 0.78 mmol), ethanol (0.5 mL), catalyst (0.00051 mmol), H_2 (8 bar), RT. All reactions were performed in duplicate and nitrobenzene conversion was determined by ^1H NMR with an error of ± 2 %. The TOFs were calculated as the ratio of the number of molecules of substrate consumed in the reaction per the number of true active catalyst sites calculated by BET measurements per minute. [a]Recovered by filtration. [b]Recovered by magnetic separation.

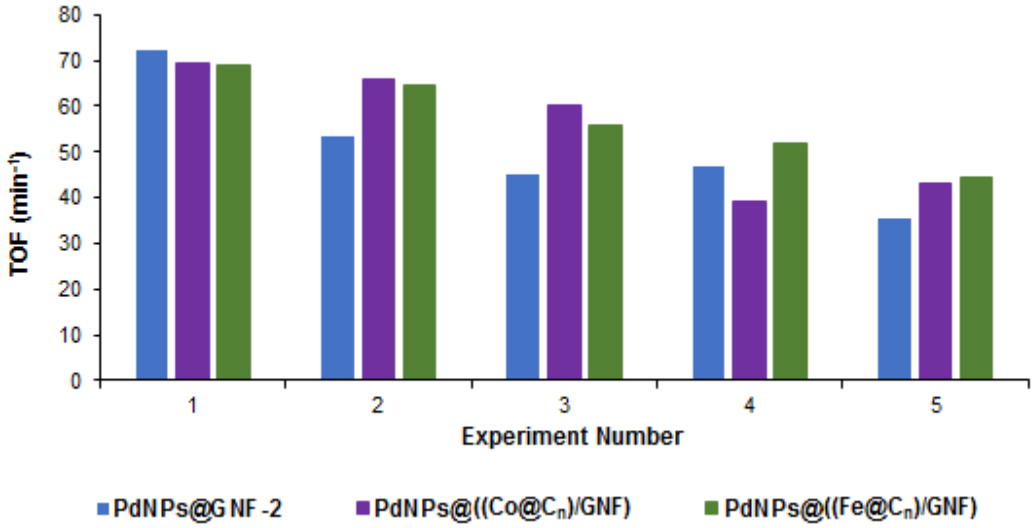

Figure 3.15. Comparison of the nitrobenzene conversion as TOF during the 5 recyclability tests in which PdNPs@GNF-2 was recovered by filtration using a PTFE membrane paper and PdNPs@((Fe@C_n)/GNF) and PtNPs@((Co@C_n)/GNF) by magnetic separation.

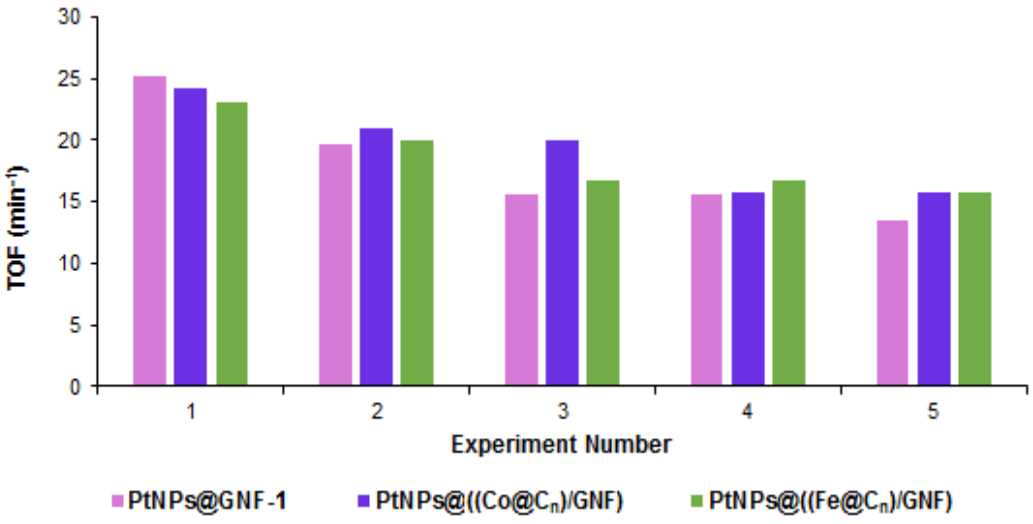

Figure 3.16. Comparison of the nitrobenzene conversion as TOF during the 5 recyclability tests in which PtNPs@GNF-1 was recovered by filtration using a PTFE membrane paper and PtNPs@((Fe@C_n)/GNF) and PtNPs@((Co@C_n)/GNF) by magnetic separation.

To further explore the larger decrease in catalytic activity by traditional recovery compared to magnetic recovery, PdNPs@GNF-2 after traditional recovery and PdNPs@((Co@C_n)/GNF) and PdNPs@((Fe@C_n)/GNF) by magnetic recovery were weighted after each recovery step and an appreciable degree of catalyst loss is observed, *c.f.* 10 % by traditional recovery versus <0.5 % by magnetic recovery during the five recycling (Figure 3.17a). The principle cause of catalyst loss during filtration is that significant materials is irreversibly absorbed onto the PTFE membrane filter (Figure 3.17b).

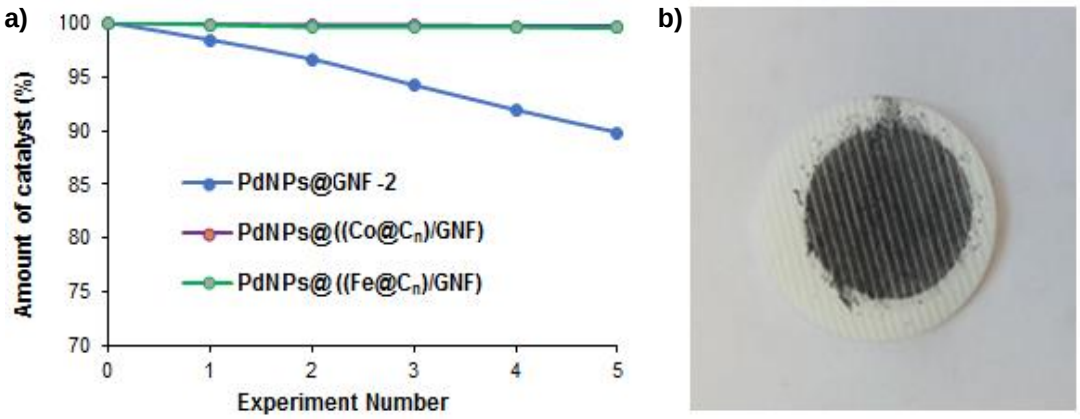

Figure 17. a) Comparison of the loss of PdNPs@GNF-2 catalysts during the five recyclability tests for the reduction of nitrobenzene. The recovery of PdNPs@GNF-2 was achieved by filtration using a PTFE membrane, whilst PdNPs@((Fe@C_n)/GNF) and PdNPs@((Co@C_n)/GNF) were recovered by applying magnetic separation (Experimental sections 3.4.9 and 3.4.10). b) Residual PdNPs@GNF-2 material left on a PTFE membrane after the recovery of PdNPs@GNF-2 via filtration.

The reduced activity of each catalyst during the reaction, using both traditional and magnetic recovery, is most likely to be related to sintering of the migrated nanoparticles during the recyclability process, along with the leaching of Pd and Pt NPs into the reaction medium. To further investigate the reason for the decrease in nitrobenzene conversion after either magnetic or traditional recovery and to probe whether there is loss of active

catalyst nanoparticles from the GNF by leaching during the recyclability tests, the precise metal loading of both PdNPs@GNF-2 and PtNPs@GNF-1 as synthesised and after 5 cycles by filtration were determined by ICP-OES (Table 3.7). ICP-OES results indicated a 3.76 % leaching of PdNPs from GNF compared to a 3.56 % leaching of PtNPs.

Table 3.7. Data showing the precise loading of Pd and Pt metal in PdNPs@GNF-2 and PtNPs@GNF-1, for the catalyst materials as synthesised and after recycling them for 5 times measured by ICP-OES.

	PdNPs (% wt.) in PdNPs@GNF-2 Before the reaction	PdNPs (% wt.) in PdNPs@GNF-2 After the 5.recovery	PtNPs (% wt.) in PtNPs@GNF-1 Before the reaction	PtNPs (% wt.) in PtNPs@GNF-1 After the 5. recovery
% amount of catalyst by ICP-OES	0.532 ±0.04	0.512 ±0.02	0.842 ±0.06	0.813 ±0.02

These results imply that leaching of Pd and Pt nanoparticles from the GNF are negligible and therefore cannot be the reason for the reduction of the catalyst activity during the recycling. However, nanoparticle growth via Ostwald ripening or particle migration and coalescences, as well as the agglomeration of smaller nanoparticles could also be occurring during the recyclability process that would result in a decrease in active catalyst surface area, and thus a reduction of the activity of catalyst. Therefore, further to the ICP-OES, PdNPs@GNF-2 and PtNPs@GNF-1 were studied by HRTEM imaging after 5 reaction cycles (Figure 3.18)

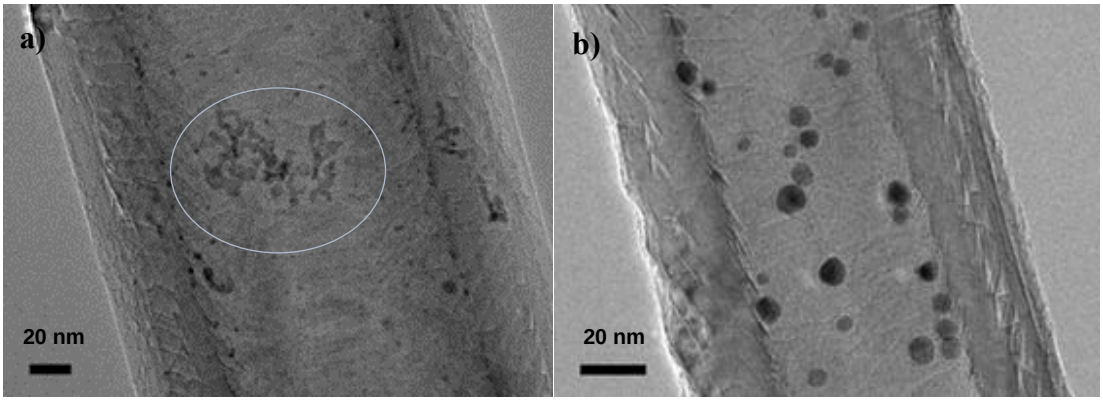

Figure 3.18. HRTEM images of a) PdNPs@ GNF-2, and b) PtNPs@GNF-1 after five recycles of the catalyst tested in the reduction of nitrobenzene.

Some aggregation of the PdNPs was observed whilst the PtNPs seem to remain well-dispersed. However, the average particles size after the fifth cycle measured by HRTEM of 2.4 ± 0.42 nm for PdNPs, and 4.43 ± 0.99 nm for PtNPs, was almost identical to the average size of the nanoparticles before the reaction. Therefore, the reduction in activity must be related to another factor, this could be a number of things, e.g. reordering of the nanoparticle structure or poisoning of the surface, further work is required to understand this fully.

3.3 CONCLUSIONS

This study represents an exciting development in the area of recyclable, catalytically active carbon nanoreactors and shows two different approaches for the magnetic functionalisation of carbon nanoreactors involving the non-covalent attachment of commercial carbon coated Co magnets and the *in situ* formation of carbon coated Fe magnets. Here, we have proven that both methodologies enable the separation of catalytic nanoreactors from the products mixtures in a fast, easy and efficient way by simply applying a magnetic field which has a significant advantages over traditional filtration methods.

These magnetic nanoreactors ((Co@C_n)/GNF and (Fe@C_n)/GNF) have been successfully coupled with catalytic metal nanoparticles (Pd and Pt). The catalytic ability of these catalytic and magnetic nanoreactors were probed in the reduction of nitrobenzene in which both PdNPs@GNF-2 and PtNPs@GNF-1 material exhibited excellent activity, especially PdNPs@GNF-2.

The activity of each catalyst was measured over 5 cycles, separating the catalyst either by magnetic recovery or by traditional filtration using a PTFE membrane. No significant leaching of Pd or Pt was detected, with the change in catalytic activity of the magnetically separated catalyst was comparable to filtration. Retention of the catalyst was more complete in the case of magnetic separation as compared to a loss of of ~10% of the catalyst by PTFE membrane filtration.

Magnetic nanoreactors allow a combination of confinement and recyclability of catalytically active metals offered by the GNF with the magnetic functionality enabling facile re-use of the catalytic system. Overall, this project lays the foundations for generation of magnetically separable carbon nanoreactors and future development of metal-catalysed reactions in magnetic carbon nanoreactors, which in the long term may be scaled up and applied for chemical processes of industrial importance replacing inefficient and energy consuming filtration and centrifugation.

3.4 EXPERIMENTAL

GNF were purchased from Pyrograf Products Inc (PR19, chemical vapor deposition), USA. Co@C_n was purchased from Turbobeads LLC, USA. All other reagents and solvents were purchased from Sigma-Aldrich (UK) and used without further purification. All of the glassware required to perform the experiments was thoroughly cleaned with 'aqua regia' (concentrated hydrochloric and nitric acids (3:1)) and rinsed with deionised

water prior to use.

3.4.1 Characterisation techniques

^{1}H NMR spectra were recorded using a Bruker DPX300 NMR spectrometer. ^{1}H NMR spectra were taken in $CDCl_3$ and were referenced to residual trimethysilane (TMS) (0 ppm) and reported as follows: chemical shift, multiplicity (s = singlet, d = doublet, t = triplet, dd= doublet of doublet, m = multiplet).

HRTEM analysis was performed on a JEOL 2100 Field emission gun microscope with an information limit of 0.12 nm at 100 kV. Samples for HRTEM analysis were prepared by dispersing the materials in HPLC grade iso-propanol using ultra-sonication, then drop casting the resultant suspension onto a lacey carbon film coated copper grid.

TGA analysis was performed on a TA Instruments TGA-SDTQ600 analyser. Samples for TGA analyses were heated in air up to 1000 °C with a heating rate of 10 °C/min.

The powder X-ray diffraction patterns were obtained using a PANanalytical X'Pert PRO diffractometer equipped with a Cu-Ka radiation source (λ= 1.542) operating at 40 kV and 40 mA, with 0.05252° step size and a step time of 5925.18 seconds.

Surface area analysis was performed using the Brunauer–Emmett–Teller (BET) method based on adsorption data in the relative pressure (P/Po) range 0.02 to 0.22 by measuring nitrogen sorption isotherms of the samples (50 mg) at -196 °C on a Micromeritics ASAP 2020 sorptometer. Before analysis, the samples were evacuated for 12 hr at 200 °C under vacuum. The pore size distributions were obtained from a Non-Local Density Functional Theory (NLDFT) method using nitrogen-sorption data.

3.4.2 Synthesis of (Co@C_n)/ GNF

GNF (15 mg, annealed at 450 °C in air for 1 hour prior to use) in hexane (20 mL) and Co@C_n (1.5 mg, corresponding to 10 % by wt. Co in the final (Co@C_n)/GNF material)

in hexane (5 mL) were dispersed separately using ultrasound (10 min). Once dispersed the Co@C_n hexane suspension was slowly added to the GNF dispersion in small portions (0.2 mL) whilst being treated with ultrasonic waves, the resultant dispersion was then sonicated for a further 10 min. Separation of resultant (Co@C_n)/GNF as a black powder was achieved by applying a magnet to the outside of the vial and decanting the hexane solvent.

3.4.3 Synthesis of (Fe@C_n)/ GNF

Ferrocene (5 mg, corresponding to 10 % by wt. Fe in the final (Fe@C_n)/GNF) was combined with GNF (15 mg, annealed at 450 °C for 1 hour prior to use) in a Pyrex tube and sealed under vacuum (10^{-6} bar) using a vacuum pump. The material was then heated at 350 °C for 1 day, and the temperature was then increased to 500 °C for a further day. The sample was the cooled and opened to yield the (Fe@C_n)/GNF material as black powder.

3.4.4 Catalyst Preparation

3.4.4.1 PdNPs@GNF-1

$Pd(acac)_2$ (0.22 mg, corresponding to 0.5 % by wt. Pd in the final PdNPs@GNF-1) was combined with GNF (15 mg, annealed at 450 °C for 1 hour prior to use) in a Pyrex tube and sealed under vacuum (10^{-6} bar) using a vacuum pump and heated at 150 °C for 3 days. After 3 days, the sample inside the Pyrex tube was cooled by immersing in an ice bath. The sample was then removed from the Pyrex tube and sealed in a separate Pyrex tube under argon atmosphere and heated at 550 °C for 3 hours. The final material was then cooled to give PdNPs@GNF-1 as black powder.

3.4.4.2 PdNPs@GNF-2

GNF (15 mg, annealed at 450 °C for 1 hour prior to use) were dispersed in $CHCl_3$ (2 mL) using ultrasound for 10 min. A solution of tris(dibenzylideneacetone)dipalladium(0)-chloroform adduct ($Pd_2(dba)_3.CHCl_3$) (0.375 mg, corresponding to a 0.5 % by wt. of Pd in the final PdNPs@GNF-2 material) in $CHCl_3$ (1 mL) was then slowly added to the GNF dispersion in small portions (0.1 mL) whilst being treated with ultrasonic waves and stirred at 40 °C for 4 hours until the solution became colourless. PdNPs@GNF was then separated from the reaction mixture by filtration and washed repeatedly with acetone (20 mL) using a 0.2 µm PTFE membrane filter to remove free dibenzylideneacetone (dba) to yield the PdNPs@GNF-2 material as black powder.

3.4.4.3 PtNPs@GNF-1

$Pt(acac)_2$ (0.30 mg, corresponding to a 1 % by wt. of Pt in the final PtNPs@GNF-1 material) was combined with GNF (15 mg, annealed at 450 °C for 1 hour prior to use) in a Pyrex tube and sealed under vacuum (10^{-6} bar) using a vacuum pump and heated at 170 °C for 3 days. After 3 days, the sample was cooled by immersing in an ice bath and then removed from the Pyrex tube and sealed in a separate Pyrex tube under an argon atmosphere and heated at 550 °C for 3 hours. The final PtNPs@GNF-1 was then recovered as black powder.

3.4.4.4 PtNPs@GNF-2

GNF (15 mg, annealed at 450 °C for 1 hour prior to use) were dispersed in $CHCl_3$ (2 mL) using ultrasound for 10 min. A solution of tris(dibenzylideneacetone)platinum(0) ($Pt(dba)_3$) (0.69 mg, corresponding to a 1 % by wt. of Pt in the final PtNPs@GNF-2 material) in $CHCl_3$ (1 mL) was then slowly added to the GNF dispersion in small portions

(0.1 mL) whilst being treated with ultrasonic waves and stirred at 70 ° C for 1 day until the solution became colourless. PtNPs@GNF was then separated from the reaction mixture by filtration and washed repeatedly with acetone (20 mL) using a 0.2 μm PTFE membrane filter to remove free dibenzylideneacetone (dba) and obtain the final PtNPs@GNF-2 material as black powder.

3.4.4.5 Magnetic PdNPs@((Co@C_n)/GNF)

PtNPs@GNF-1 (15 mg) in hexane (20 mL) and Co@C_n (1.5 mg) in hexane (5 mL) were dispersed separately using ultrasound for 10 min. The Co@C_n hexane suspension was then added to the GNF dispersion in small portions (0.1 mL) whilst being treated with ultrasonic waves, the resultant dispersion was then sonicated for a further 10 min. The separation of catalyst from the solution was controlled by an external magnet (0.1 T) to give PdNPs@((Co@C_n)/GNF) as black powder.

3.4.4.6 Magnetic PdNPs@((Fe@C_n)/GNF)

(Fe@C_n)/GNF (15 mg) was dispersed in $CHCl_3$ (2 mL) using ultrasound for 10 min. Once GNF was dispersed, $Pd_2(dba)_3.CHCl_3$ (0.34 mg) dissolved in $CHCl_3$ (1 mL) were added to GNF dispersion in small portions (0.1 mL) whilst being treated with ultrasonic waves and stirred at 40 C° for 4 h until the solution became colourless. PdNPs@GNF was then separated from the reaction mixture by filtration using a 0.2 μm PTFE membrane filter and washed repeatedly with acetone (20 mL) to remove the free dibenzylideneacetone and give PdNPs@((Fe@C_n)/GNF) as black powder.

3.4.4.7 Magnetic PtNPs@((Co@C_n)/GNF)

PtNPs@GNF (15 mg) in hexane (20 mL) and Co@C_n (1.5 mg) in hexane (5 mL) were dispersed separately using ultrasound for 10 min. Once dispersed the Co@C_n in hexane

were slowly added to GNF dispersion in small portions whilst being treated with ultrasonic waves, the resultant dispersion was then sonicated for a further 10 min. Separation of the resultant PtNPs@((Co@C_n)/GNF) as black powder was achieved by applying a magnetic field (0.1 T) to the outside of the vial and decanting the hexane solvent.

3.4.4.8 Magnetic PtNPs@((Fe@C_n)/GNF)

$Pt(acac)_2$ (0.3 mg, 1% by wt. Pd) was combined with (Fe@C_n)/GNF (15 mg) in a Pyrex tube, sealed under vacuum (10^{-6} bar) using a vacuum pump and heated at 170 °C for 3 days. The sample inside the Pyrex tube was then cooled by immersing in an ice bath. The sample was removed from the Pyrex tube and sealed in a separate Pyrex tube under an argon atmosphere and heated at 550 °C for 3 hours. PtNPs@((Fe@C_n)/GNF) was then isolated as black powder.

3.4.5 Reduction of nitrobenzene using high pressure H_2 glass reactor

The selected catalyst (10 mg, equivalent to 0.00051 mmol of metal nanoparticles) and an ethanol (0.5 mL) solution of nitrobenzene (0.78 mmol) were stirred in a high-pressure reactor (10 mL volume). The reactor volume was then degassed thoroughly with H_2 for 15 min. The reactor was then sealed and pressurised with H_2 (8 bar) and left for 30 minutes at room temperature. At the end of the reaction, the reactor was slowly depressurized and analysed via ^{1}H NMR spectroscopy using $CDCl_3$ solvent.

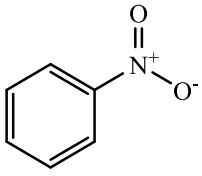

Nitrobenzene (Ph-NO_2): ^{1}H NMR (300 MHz, 297 K, $CDCl_3$, δ, ppm): 8.20-8.17 (m, 2 H), 7.69-7.63 (m, 1H), 7.53-7.48 (m, 2 H).

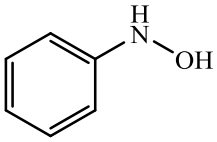

N-phenylhydroxylamine (Ph-NHOH): ^{1}H NMR (300 MHz, 297 K, $CDCl_3$, δ, ppm): 7.23-7.18 (m, 2 H), 6.95-6.93 (d, *J*= 7.54 Hz, 2H), 6.90-6.85 (m, 1 H).

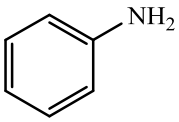

Aniline (Ph-NH_2): ^{1}H NMR (300 MHz, 297 K, $CDCl_3$, δ, ppm): 7.13-7.07 (t, *J*=7.86 Hz, 2H), 6.73-6.69 (m, 1H), 6.68-6.64 (m, 2H).

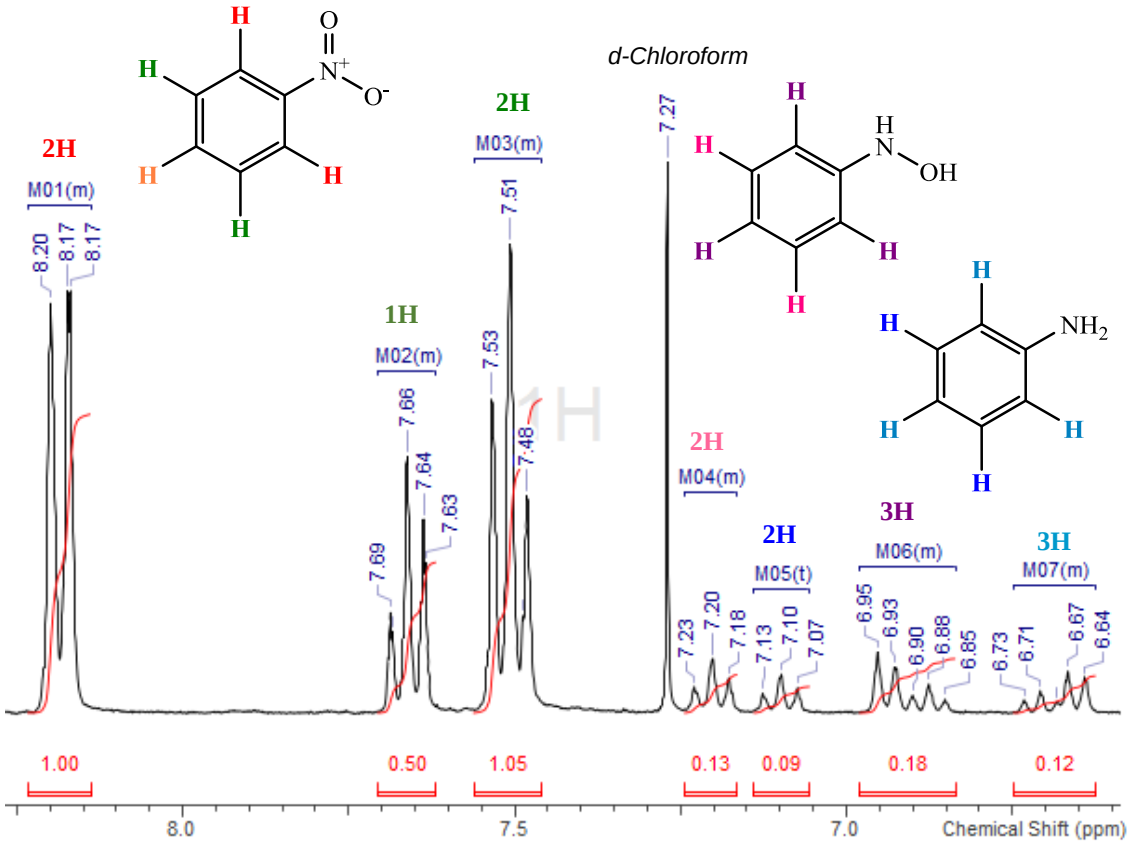

Figure 3.20. ^{1}H NMR of spectrum of the reaction mixture of catalytic reduction of nitrobenzene (Ph-NO_2) to phenylhydroxylamine (Ph-NHOH) and aniline (Ph-NH_2) recorded in $CDCl_3$ at 300 MHz.

3.4.6 UV–Visible spectroscopy measurements

(Co@C_n)/GNF (10 mg) and (Fe@C_n)/GNF (10 mg) were suspended in hexane (10 mL) by stirring at 500 rpm using a magnetic stirrer for 2 min and then a magnetic field was applied for a set periods of time (10, 30, 60 and 90 seconds). For example, after applying a magnetic field for 10 s, 2 mL of solution were taken from the magnetically separated solution using a micro pipette then analysed by UV–Vis spectroscopy between 350–700 nm (wavelength step: 1 nm, scan speed: 240 nm min^{-1}) using a Perkin Elmer Lambda 11 spectrophotometer. The 2 mL solution was then returned to the starting solution and the solution was redispersed and the same procedure was repeated.

3.4.7 Magnetic measurements

Magnetic measurements on (Co@Cn)/GNF and (Fe@Cn)/GNF were carried out in a commercial Quantum Desing MPMS-XL5 Superconducting Quantum Interference Device (SQUID) magnetometer. Samples were carefully prepared using a plastic capsule with a negligible diamagnetic contribution. For both samples variable-temperature (1.8─300 K, with 0.1 T applied field) and field dependent (at 2 K and 300 K with a maximum field of 5 T) magnetisation measurements were carried and compared by dividing the magnetic signal per mass of the measured sample.

3.4.8 ICP-OES measurements

As GNF do not completely digest in strong acids inductively coupled plasma optical emission spectroscopy (ICP-OES) analysis of GNF samples is problematic. To solve this problem PdNPs@GNF-2 and PtNPs@GNF samples (3 x 2 mg), were burned in a boiling tube using a bunsen burner to fully oxidise and hence remove the GNF. The remaining residual metal was then digested in acid (1 mL, aqua regia,) at room temperature using ultra-sonication for 1 h and the resultant solution was diluted with ultrapure water to make

a dilute aqua regia solution (10 % by volume in water). ICP-OES was used to determine the Pd and Pt % loadings of the solutions, respectively using a Perkin Elmer, Optima 2000 DV ICP-OES with S10 autosampler with an axial detection method at wavelengths of 340.458 nm for Pd and 214.423 nm for Pt. Calibration Pd and Pt solutions (0.1, 0.2, 0.5, 1 and 5 mg L^{-1}) were prepared using a Pd standard (Sigma Aldrich) and a Pt standard (VWR Chemicals) and aqua regia (10 % by volume in water), and gave a linear plot with an R coefficient of 0.999999. Blanks showed 0.00 mg L^{-1} of Pd and Pt, respectively. Corrected concentrations of Pd and Pt were then measured as number of mg of Pd and Pt per litre for each sample and correlated to Pd and Pt % loadings.

3.4.9 Catalyst recovery by applying a magnetic field

After each experimental cycle, the catalyst mixed with reaction products were extracted into ethanol (5 mL) and then magnetic field was applied. As the catalyst accumulated on the wall of reaction vessel, the solution mixture was easily separated from the catalyst using a pipette. Ethanol (5 mL) was then added to the catalyst and the same procedure was repeated until no signs of starting materials or products could be observed by ^{1}H NMR. The catalyst was then left to dry at room temperature.

3.4.10 Catalyst recovery by filtration

After each experimental cycle, the catalyst, mixed with reaction products, was extracted into ethanol (5 mL) and then washed with ethanol (20 mL) using a filtration assembly and a PFTE membrane followed by drying at ambient conditions. The washings were repeated until no signs of starting materials or products could be observed by ^{1}H NMR. The catalyst was then collected from the filtration membrane using a spatula.

3.5 REFERENCES

1. S. Iijima, *Nature*, 1991, 354.
2. M. S. Dresselhaus, G. Dresselhaus, A. Jorio, *Annu. Rev. Mater. Res*., *2004*, *34*, *247*-278.
3. S. A. Hodge, M. K. Bayazit, K. S. Coleman, M. Shaffer, *Chem. Soc. Rev.*, 2012, 41, 4409-4429.
4. A. Mamalis, *Precision Engineering*, 2004, 28, 16-30.
5. M. Terrones, *Int. Mater. Rev*., 2004, 49, 325.
6. M. S. Dresselhaus, G. Dresselhaus, P. Avouris, Carbon nanotubes: Synthesis, structure, properties, and applications, Springer, New York, 2001.
7. G. A. Rance, D. H. Marsh, S. J. Bourne, T. J. Reade, A. N. Khlobystov, *ACS Nano*, 2010, 4, 4920-4928.
8. M. Daenen, R. D. De Fouw, B. Hamers, P. G. A. Janssen, K. Schouteden, M. A. J. Veld, The Wondrous World of Carbon Nanotubes 'a review of current carbon nanotube technologies'. Eindhoven University of Technology, 2003, 1-96.
9. H. Chu, L. Wei, R. Cui, J. Wang, Y. Li, *Coord. Chem. Rev.*, 2010, 254, 1117-1134.
10. A. N. Khlobystov, *ACS Nano*, 2011, 5, 9306-9312.
11. P. Serp, J. L. Figueiredo, Carbon materials for catalysis, *Wiley*, 2009, 56.
12. G. G. Wildgoose, C. E. Banks, R. G. Compton, *Small*, 2006, 2, 182-193.
13. W. A. Solomonsz, G. A. Rance, B. J. Harris, A. N. Khlobystov, *Nanoscale*, 2013, 5, 12200-12205.
14. M. J. Ledoux, R. Vieira, C. Pham-Huu, N. Keller, Catalysts. *J. Catal.* 2003, 216, 333.
15. T. W. Chamberlain, J. H. Earley, D. P. Anderson, A. N. Khlobystov, R. A. Bourne, *Chem. Commun.*, 2014, 50, 5200-5202.

16. P. Serp, M. Corrias, P. Kalck, Appl. Catal. A, 2003, 253, 337-358.

17. S. A. Miners, G. A. Rance, A. N. Khlobystov, *Chem. Commun.*, 2013, 49, 5586-5588.

18. W. A. Solomonsz, G. A. Rance, M. Suyetin, A. La Torre, E. Bichoutskaia, A. N. Khlobystov, *Chem. Eur. J.*, 2012, 18, 13180-13187.

19. M. A. Lebedeva, T. W. Chamberlain, A. Thomas, B. E. Thomas, C. T. Stoppiello, E. Volkova, M. Suyetind, A. N. Khlobystov, *Nanoscale*, 2016, 8, 11727-11737.

20. X. Pan, Z. Fan, W. Chen, Y. Ding, H. Luo, X. Bao, *Nat. Mater*., 2007, 6, 507-511.

21. X. Pan, X. Bao, *Chem. Commun*., 2008, 6271-6281.

22. X. Pan, X. Bao, *Acc. Chem. Res.*, 2011, 44, 553-562.

23. A. Hutten, D. Sudfeld, I. Ennen, G. Reiss, W. Hachmann, U. Heinzmann, K. Wojczykowaki, P. Jutzi, W. Saikaly, G.J. Thomas. *Biotechnol.*, 2004, 112, 47.

24. A. H. Lu, W. Schmidt, N. Matoussevitch, H. Bönnemann, B. Spliethoff, B. Tesche, E. Bill, W. Kiefer, F. Schüth, *Angew. Chem.*, 2004, 116, 4403.

25. H. Jia, Y. Lian, M. Ishitsuka, T. Nakahodo, Y. Maeda, T. Tsuchiya, T. Wakahara, T. Akasaka, *Sci. Technol. Adv. Mater.*, 2005, 6, 571-581.

26. L. M. Rossi, N. J. S. Costa, F. P. Silva, R. Gonçalves, *ChemInform*, 2013, 2, 597-614.

27. J. Govan, Y. k. Gun'ko, *Nanomaterials (Basel)*. 2014, 4, 222–241.

28. L. M. Rossi, N. J. S. Costa, F. P. Silva, R. Wojcieszak, *Green Chem.*, 2014, 16 (6), 2906-2933.

29. M. D. Lekgoathi, W.G. Augustyn, J. Heveling, *J Nanosci Nanotechnol.* 2011, 11(8), 7001-5.

30. H. M. Torres Galvis, J. H. Bitter, C. B. Khare, M.Ruitenbeek, A. I. Dugulan, K. P. de Jong, *Science*, 2012, 335, 835.

31. R. N. Grass, W. J. Stark, *J. Mater. Chem.*, 2006, 16, 1825-1830.

32. I.K. Herrmann, R. N. Grass, D. Mazunin, W. J. Stark, *Chem. Mater*., 2009, 21, 3275-3281.

33. Y. Deng, Y. Cai, Z. Sun, J. Liu, J. Wei, W. Li, C. Liu, Y. Wang, D. Zhao, *J Am. Chem. Soc.*, 2010, 132, 8466-8473.

34. L. Zhang, Li. Pinhua, L. Hongji, L. Wang, *Catal. Sci. Technol*., 2012, 2, 1859-1864.

35. A.H. Lu, E. L. Salabas, F. Schüth, *Angew. Chem., Int. Ed.*, 2007, 46, 1222-1244.

36. S. C. Tsang, V. Caps, I. Paraskevas, D. Chadwick and D. Thompsett, *Angew. Chem., Int. Ed.*, 2004, 43, 5649-5649.

37. Z. Xu, H. Li, G. Cao, Z. Cao, Q. Zhang, K. Li, X. Hou, W. Lia, W. Cao, *J. Mater. Chem*., 2010, 20, 8230-8232.

38. M. Rossier, F. M. Koehler, E. K. Athanassiou, R. N. Grass, B. Aeschlimann, D. Günther, W. J. Stark, *Mater. Chem*., 2009, 19, 8239-8243.

39. S. Wittmann, A. Schätz, R. N.Grass, W. J. Stark, O. Reiser, *Angew. Chem. Int. Ed.*, 2010, 49, 1867-1870.

40. G.U. Sumanasekera, B.K. Pradhan, H.E. Romero, K.W. Adu, P.C. Eklund, *Phys. Rev. lett.*, 2002, 89, 166801.

41. I. K. Herrmann, M. Urner, F. M. Koehler, M. Hasler, B. Roth-Z'Graggen, R. N. Grass, U. Ziegler, B. Beck-Schimmer, W. Stark, *Small*, 2010, 6, 1388-1390.

42. A. Schätz, T. R. Long, R. N. Grass, W. J. Stark, P. R. Hanson, O. Reiser, *Chem. Mater.*, 2010, 20, 4323-4328.

43. A. Schätz, R. N. Grass, Q. Kainz, W. J. Stark, O. Reiser, *Chem. Mater.*, 2010, 22, 305-310.

44. B. K. T. Kenneth, C. Singh, M. Chhowalla, W.I. Milne, *Encyclopedia of Nanoscience and Nanotechnology*, 2004, 1, 665-686.

45. R. Saito, G. Dresselhaus, M. S. Dresselhaus, Physical Properties of Carbon Nanotubes, Imperial College Press, 1998.

46. A. Taylor, R.W. Floyd, *Acta Crystallographica* ,1950, 3, 285-289.

47. B. P. Ramesh, W. J. Blau, P. K. Tyagi, D. S. Misra, N. Ali, j. Gracio, G. Cabral, E. Titus, *Thin Solid Films*, 2006, 494, 128-132.

48. P. Hou, C. Liu, Y.Tong, S. Xu, M. Liu, H. Cheng,J. *Mater. Res.*, 2001, 16, 2526.

49. A. W., Hull, *Physical Review*, 1917, 10, 661-696.

50. A. Combessis, C. Mazel, M. Maugin, L. Flandin, *J. Appl. Polym. Sci.* 2013, 130, 1778-1786.

51. S. H. Jeong, K. K. Kim, S. J. Jeong, K. H. An, S. H. Lee, Y. H. Lee, *Synthetic Metals*, 2007, 157, 570–574.

52. I. M. L. Billas, A. Châtelain,W.A. de Heer, *Science*, 1994, 265 (5179), 1682-1684.

53. R. S. Downing, P. J. Kunkeler, H. van Bekkum, *Catal. Today*, 1997, 37, 121-136.

54. S. L. Karwa, K. A. Rajadhyaskha, *Ind. Eng. Chem. Res.* 1987, *26*, 1746-1750.

55. E.A. Gelder, S.D. Jackson, C.M. Lok, *Catal. Letters.*, 2002, 84, 205-208.

56. C. H. Li, Z. X. Yu, K. F. Yao, S. F. Ji, J. Liang, *J. Mol. Catal. A*, 2005, 226, 101-105.

57. P. Sangeetha, K. Shanthi, K.S. Rama Rao, B. Viswanathan, P. Selvam, *Appl. Catal. A Gen.*, 2009, 353, 160-165.

58. Y. Takenaka, T. Kiyosu, J. Choi, T. Sakakuraa, H. Yasuda, *Green Chem.***,** 2009, 11, 1385-1390.

59. F. A. Westerhaus, R. W. Jagadeesh, G. Wienho, M. Pohl, J. Radnik, A. Surkus, J. Rabeah, K. Junge, H. Junge, M. Nielsen, A. Bruckner, M. Beller, *Nature Chemistry*, 2013, 5, 537-543.

60. M. Shokouhimehr, T. Kim, J.S. Woojoo, S. Kwangsoo, Y. Jang, B. H. Kim, J. Kim, T. Hyeon, *Appl. Catal. A Gen.,* 2014, 476, 133-139.

61. M. Turáková, M. Králik, P. Lehocky, P. Pikna, M. Smrcová, D. Remeteiová, A. Hudák, *Appl. Catal. A Gen.,*2014, 476, 103-112.

62. R. B. N. Baig, R. S. Varma, *ACS Sustainable Chem. Eng.,* 2014, 2, 2155-2158.

63. E. O. Pentsak, A. S. Kashin, M. V. Polynski, K. O. Kvashnina, P. Glatzelc, V. P. Ananikov, *Chem. Sci.*, 2015, 6, 3302.

64. A.W. Hull, W.P. Davey, *Phys.l Rev.*, 1921, 17, 571-587.

65. H. E. Swanson, E., Tatge, Standard X-ray diffraction powder patterns I, National Bureau of Standards, U.S., Circular, 1953, 539, 1-95.

66. E. O. Pentsak , V. P. Ananikov, *Russ. Chem. Bull., Int. Ed.,* 2014, 63 (11), 2560.

67. G.V. Smith, F. Notheisz, Heterogeneous Catalysis in Organic Chemistry, Aqcademic Press: San diego, CA, 1999.

68. *Z.* Haber. *Elektrochem*., 1898, 4, 506-513.

69. E.A. Gelder, S.D. Jackson, C.M. Lok, *Chem. Comm.*, 2005, 4, 522-524.

70. A. Corma, P. Concepcion, P. Serna, *Angew. Chem. Int. Ed*., 2007, 467266-467269.

71. M. Turákováa, T. Salmi, K. Eränenc, J. Wärnåc, D. Y. Murzinc, M. Králik, *Appl. Catal. A Gen.,* 2015, 499, 66-76.

4 PALLADIUM NANOPARTICLES IN CARBON NANOREACTORS AS HYBRID ELECTROCATALYST FOR HYDROGEN-EVOLUTION AND HYDROGEN-OXIDATION REACTIONS

4.1 INTRODUCTION

In the last two decades, there has been an increasing interest on clean and renewable energy sources as alternative to fossil fuels.[1-4] For instance, the water-splitting reaction, which consists of the hydrogen and oxygen evolution half-reactions (HER and OER, respectively), has attracted great attention as a sustainable source of hydrogen.[5-7] This gas (H_2) is an attractive energy carrier that can be used to produce clean electricity in fuel cells, where the hydrogen oxidation and oxygen reduction reactions (HOR and ORR, respectively) convert chemical energy into electrical energy.[7-8] Furthermore, driving the HER with renewable sources of energy can lead to a sustainable source of hydrogen fuel that be used in a zero-emission fuel cell of combustion engine.

The hydrogen evolution reaction (HER, $2\ H^+ + 2\ e^- \rightarrow H_2$) that is the cathodic reaction in electrochemical water splitting is a classic example of a two-electron transfer reaction with one catalytic intermediate, H* (where * indicates a site on the electrode surface), and may occur through either the Volmer-Heyrovsky or the Volmer-Tafel mechanism as shown below.

Volmer step: $H^+ + e^- + * \rightarrow H^*$ **Equation 4.1.**

Heyrovsky step: $H^* + H^+ + e^- \rightarrow H_2 + *$ **Equation 4.2.**

Tafel step: $2H^* \rightarrow H_2 + 2*$ **Equation 4.3.**

The hydrogen oxidation reaction (HOR) involves the same reaction steps as the HER except in reverse.

Achieving high energy efficiency for water splitting requires the use of a catalyst to minimize the overpotential necessary to drive the HER. Platinum(Pt)-based catalysts are the best-performing catalyst for HER (and HOR), owing to their negligible overpotential to achieve high reaction rates and durability in acidic solutions.[7-12] However, the high cost and scarcity of this noble metal lead researchers to explore inexpensive alternatives to Pt-based electrocatalyst.[11-18] Among those alternatives, transition metal-based materials have received a lot of attention due to their high abundance and low price. Nevertheless, due to their much higher overpotentials their performances are still inadequate. Palladium (Pd) is considered a cheaper and more abundant alternative to Pt as electrocatalyst, because of its higher electrocatalytic activity and stability than those of transition metal-based materials and their alloys. Recently, different synthetic strategies have been explored to design cost effective Pd-based electrocatalysts aiming to increase the number of active sites and/or their intrinsic activity including nanostructuration, bimetallic alloying and dispersion on carbon.[17-21]

Heydari-Bafrooei *et al.* synthesized a number of MoS_2 composites and studied in HER. They reported that the modification of MoS_2 with palladium provided more active sites for the reactants and improved the HER activity compared to that of MoS_2. They also sythesised Pd-MoS_2 supported on MWNT demonstrated that an excellent HER activity for Pd-MoS_2/MWNT compared to that observed for the free standing Pd-MoS_2 and MoS_2/MWNT.[18] Using MWNT as a support material for Pd-MoS_2 increased the number of free active sites while facilitating the electron transfer alongside the nanotube, and provided an excellent stability in acid media showing a very slight activity loss after a 500 potential-cycling tests.

One of the major drawback of carbon-supported catalysts has been their low durability towards the HOR, as they can be oxidized at cathodic potentials under strongly acidic

conditions.[30-38] Highly graphitized carbon materials such as carbon nanotubes have been put forward due to their unique corrosion resistance. However, the chemical inertness of the perfect basal plane of a multi-walled carbon nanotube (MWNT) results in low dispersion and facile-agglomeration of metallic nanoparticles after potential cycling, leading to a rapid decrease of the electrochemical surface area and activity that detrimentally affect the catalyst durability.

Owing to the catalytic activity of heteroatom-doped graphene materials towards the HER showing overpotentials <200 mV vs RHE to attain 10 mA cm^{-2}, hybridization of Pd nanoparticles (NP) with these carbon nanomaterials represents an appealing strategy for designing highly efficient and cost-effective electrocatalysts.[22-29] Browmik *et al.* studied the HER/HOR activity in acidic media of PdNPs supported on carbon nitride graphene (Pd-CN_x) that shows a large number of active binding sites (triazine units) for NP dispersion.[22] The HER/HOR activity and durability observed is higher than that of commercial Pt/C and Pd/C after 10000 cycles.

The size and coverage of supported Pd clusters seem to play an essential role in promoting the HER/HOR activity. However, no studies have been focused on the confinement effect on the activity and durability of PdNPs, while restricting particle migration and coalescence by providing active binding sites. Previous studies in our group have shown that GNFs have a great potential as electroctalytic nanoreactors where the internal step edges of GNFs can act as effective anchoring points for electrocatalytic nanoparticles and enable the controlled growth of NPs by stabilizing them and restricting their migration during electrochemical cycling.[39-42] In 2016, our group demonstrated the superior electrocatalytic stability of PtNPs supported at the internal step edges of GNFs after 50000 cycles of oxygen reduction reaction compared to a commercial Pt/C catalyst.[42]

In this chapter, a Pd-based electrocatalyst material was designed showing both palladium nanoparticles (PdNPs) supported on (~20% of PdNPs on (/) s-GNF) and encapsulated inside (~80% of PdNPs inside (@) s-GNF) ball-milled graphitised carbon nanofibers through in-situ reduction of Pd_2dba_3 in solution, which was expressed as (PdNPs/-PdNPs@)s-GNF. The electrocatalytic activity and stability of (PdNPs/-PdNPs@)s-GNF were investigated towards the HER/HOR in acidic media using Pd/C and Pt/C commercial catalysts as benchmarks in this study. High-resolution transmission electron microscopy (HRTEM) imaging used here to investigate the structural changes in the (PdNPs/-PdNPs@)s-GNF hybrid under electrocatalytic cycling helps to unravel the observed increased activity after electrochemical cycling. An enhanced activity and stability of (PdNPs/-PdNPs@)s-GNF in HER was discovered compared to Pd/C and Pt/C standards. The initial HER activity of (PdNPs/-PdNPs@)s-GNF was lower than Pd/C and Pt/C reactions with a Tafel slope of 61 mV/dec. However, it exhibited a Pt-like onset potential at -14 mV and an exchange current density of 0.289 mA/cm^2, which was already much better than that of Pd/C. Surprisingly, after stability tests of 30000 HER potential cycles our material exhibited an outstanding stability and an increasing HER activity surpassing Pt/C performance. HRTEM studies after cycling confirmed that the size of the encapsulated PdNPs supported at the step edges remained practically unchanged thanks to the migration barrier imposed by GNF corrugated interiors,while there was significant PtNPs growth due to weak interactions of PtNPs with the carbon support. Further to this, s-GNF support also exhibited an increased HER activity and stability after 5000 HER cycles which can be attributed to electrochemical transformations in graphitic step-edge structure, which also has implications for carbon-palladium bonding in the hybrid material which was revealed by HRTEM.

Overall, the superior HER/HOR activity and stability of (PdNPs/-PdNPs@)s-GNF was attributed to the reactions taking place in a confined nano-environment of s-GNF nanoreactors with highly stabilized and active PdNPs anchored at the step edges. Moreover, structural transformations on step edges, i.e. opening of some step edges promoted the reactions and provided strong interactions improving electron transport, and synergetic effect between the s-GNF and PdNPs.

4.2 RESULT AND DISCUSSION

GNF were shortened by mechanical milling at 10 Hz for 90 min prior to the insertion of PdNPs in which no significant structural nanoscale defects were observed on GNF (Experimental 4.4.1). By shortening GNF, we eliminate the length depended mass transport resistance in HER/HOR (Figure 4.1) and enhance the solubility of these carbon materials in conventional solvent facilitating the film formation on the electrode. The statistical analysis performed using HRTEM confirmed a significant reduction of the mean GNF length from ~0.5-60 μm to 880 ±600 nm by ball milling (Figure 4.1), while maintaining their internal nano-cone structure (step-edges) intact .

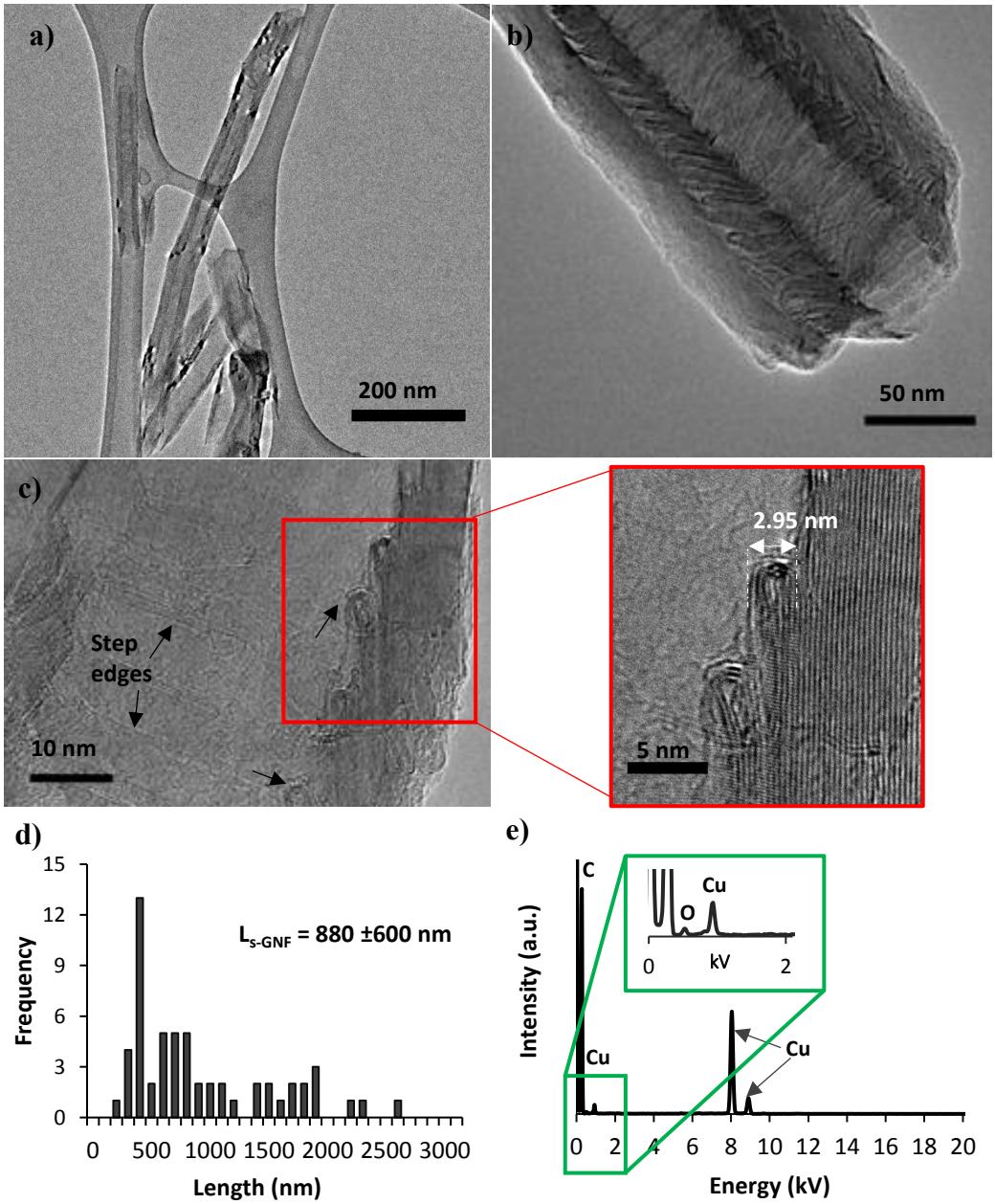

Figure 4.1. (a-c) HRTEM images of S-GNF (c) HRTEM images of S-GNF, red rectangular shape shows the closed step edges with a 2.95 nm high , d) s-GNF length distribution measured by HRTEM (more than 80 nanofibers) and e) EDX of s-GNF after ball milling, green rectangular shapes show the O peaks with an atomic ratio% of C:O as 99.5:0.5 (Cu peaks are due to a copper TEM support grid).

The (PdNPs/-PdNPs@)s-GNF hybrid was prepared using an adapted method from the literature by Pentsak *et al.* in which PdNPs are formed *in-situ* from a chloroform solution of Pd_2dba_3 in the presence of s-GNF (Experimental 4.4.2).[43] The resultant material was imaged by HRTEM confirming the formation of very small and well distributed PdNPs with an average diameter of 4.37 ±1.03 nm, with more than a 80% of PdNPs chemically attached to the s-GNF interiors (Figure 4.2b).

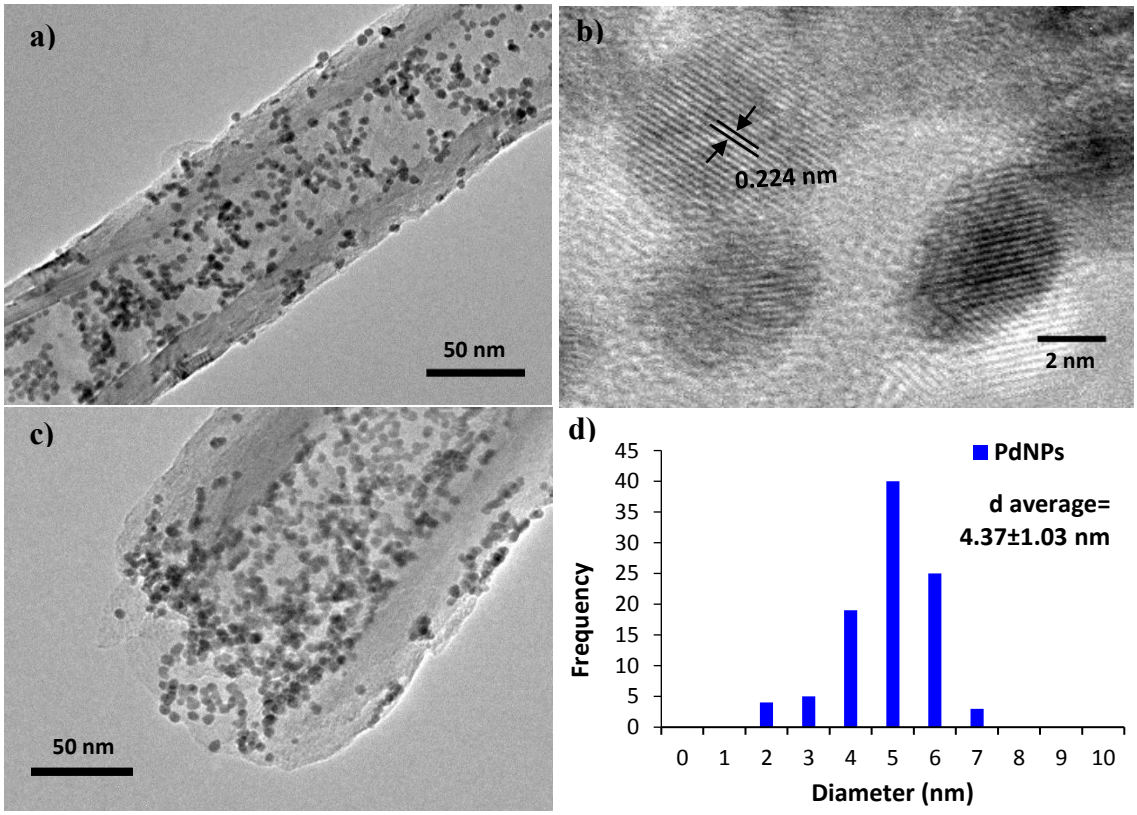

Figure 4.2. (a-c) HRTEM images of (PdNPs/-PdNPs@)s-GNF, b) crystal lattice of PdNPs in GNF with a distance between adjacent planes of 0.224 nm that corresponds to the peak centred at 39.5° (as 2Θ°) from XRD and d) the size distribution of PdNPs inside and outside s-GNF by the measurements of more than 80 nanoparticles via HRTEM.

HRTEM also confirmed the metallic nature of the PdNPs in (PdNPs/-PdNPs@)s-GNF with the metallic lattice fringes of face-centered cubic *Pd* (111) plane with a lattice spacing of 0.224 nm (Figure 4.2d), which corresponds to the diffraction peak centred at 39.5° (2Θ) shown in powder XRD. On the other hand, comparative studies of the powder XRD patterns for (PdNPs/-PdNPs@)s-GNF with s-GNF and a Pd reference were carried out to ascertain the undoubtelly presence of metallic Pd on the hybrid material (Figure 4.3).[44] The small size of the PdNPs is reflecting on the broadening and intensity reduction of all its X-ray diffraction peaks.

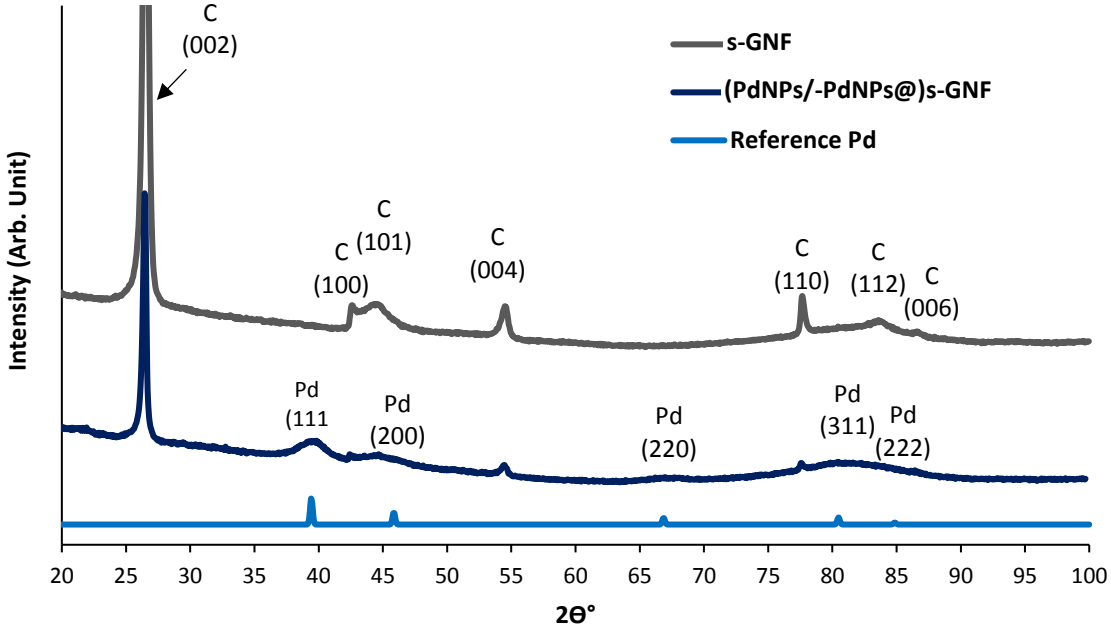

Figure 4.3 Powder XRD patterns of (PdNPs/PdNPs@)s-GNF, Pd reference[44] and s-GNF.

The Pd loading (wt%) in the hybrid was quantified using TGA and shown to be 14.1 ± 0.05 % as the amount of palladium remaining after all carbon of (PdNPs/-PdNPs@)s-GNF being burn out at 1000 °C in air (Figure 4.4). TGA studies of (PdNPs/-PdNPs@)s-GNF showed that there was a small weight loss (~ 2%) starting at ~ 200 C which was possible due to the residual dibenzylideneacetone (dba) left after washing the material with acetone to get rid of (during the formation of PdNPs from $Pd(dba)_3.CHCl_3$, see Experimental 4.2.2). A significant decrease in the oxidation temperature of the GNF from ~700 °C to 550 ° C was also observed due to the Pd content. Carbon content of the material was then burned at ~700 °C. However, another weight loss has been observed between ~800-815 °C which can be due to the non-burned carbon residual. The left material was attributed the residual Pd. The weight gain of left Pd between 815-1000 °C was negligible, therefore we get an average Pd amount showing the material to be 14.1 ± 0.05 % (wt) Pd.

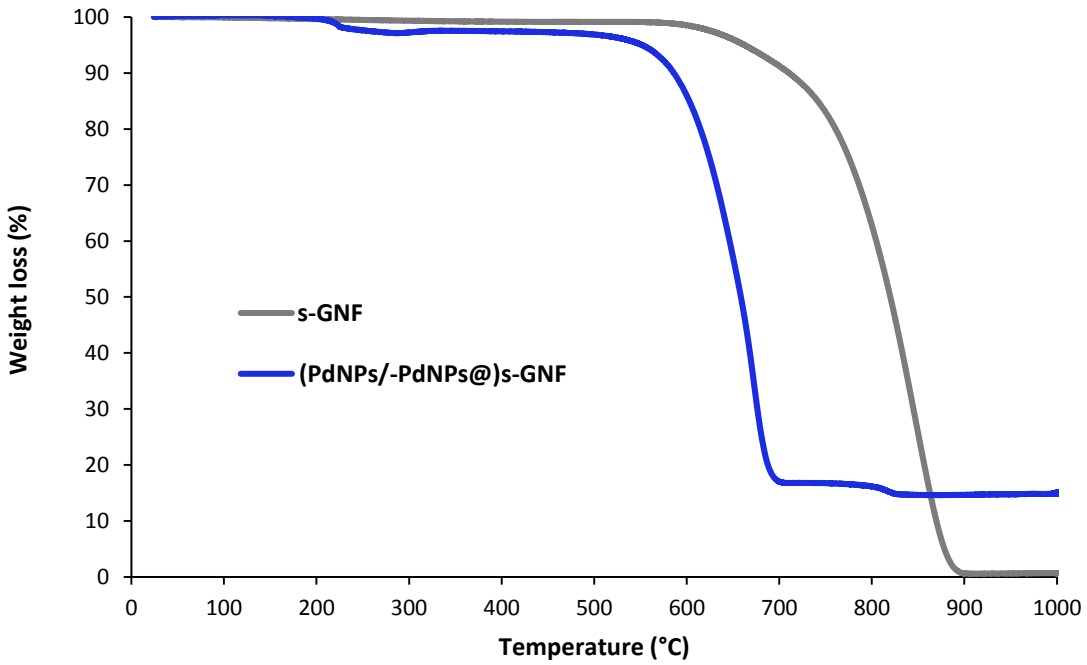

Figure 4.4. TGA measurements of (PdNPs/-PdNPs@)s-GNF (blue) and GNF (green) with 14.1 % ± 0.05 and ~0.5 % residual material by weight, respectively.

Commercially available 20 wt% Pd/C and 20 wt% Pt/C in which both the PdNPs and PtNPs were located on the surface of carbon black were used as benchmark towards the HER/HOR. HRTEM confirmed that both PdNPs and PtNPs were distributed throughout the carbon support in Pd/C and Pt/C, respectively (Figure 4.5).

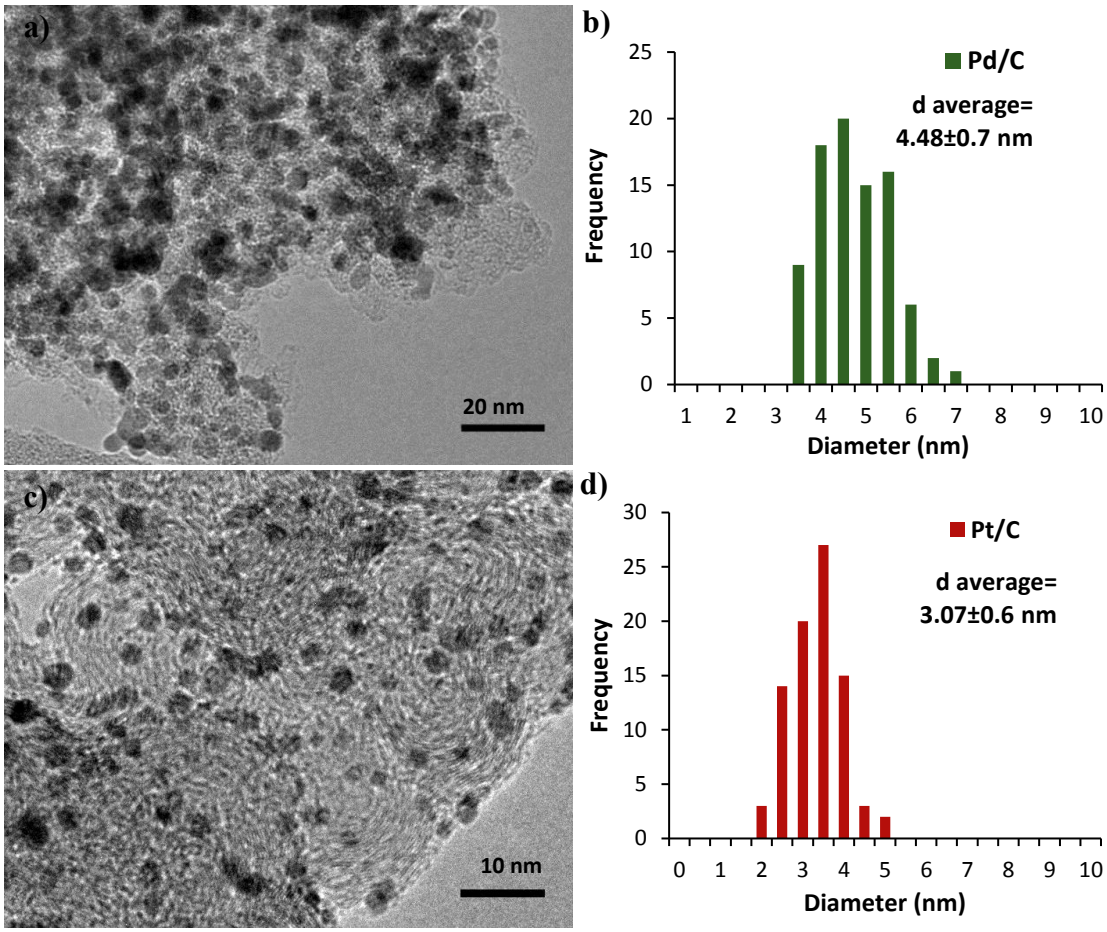

Figure 4.5. HRTEM images and particle size distributions of Pd/C (a-b) and Pt/C (c-d) by the measurements of more than 80 nanoparticles for each catalyst via HRTEM.

Pd/C shows similar NPs size distribution to (PdNPs/PdNPs@)s-GNF, with a mean diameter of 4.48 ± 0.7 nm, while Pt/C has a size distribution of 3.07 ± 0.6 nm. Both commercial catalysts showed very similar or slightly smaller particle size, as in the case of Pt/C, than the size of the PdNPs observed in our hybrid material (Table 4).

Table 4.1. Summary of the average values for nanoparticle size obtained as the mean diameter assuming a spherical shape and metal loading (%) by weight for (PdNPs/PdNPs@)s-GNF, Pd/C and Pt/C.

Catalyst	NPs size (nm)	Metal loading (%wt)
(PdNPs/PdNPs@)s-GNF	4.37 ± 1.03	~14
Pd/C	4.48 ± 0.7	20
Pt/C	3.07 ± 0.6	20

4.2.1 Study of HER on (PdNPs/-PdNPs@)s-GNF hybrid electrocatalyst

Prior to HER measurements, (PdNPs/-PdNPs@)s-GNF electrode was prepared by the dispersion of (PdNPs/-PdNPs@)s-GNF in hexane, followed by the deposition onto a glassy carbon electrode (GCE) by drop casting (Experimental 4.4.3). A three electrode set up system was used for the electrochemical measurements where (PdNPs/PdNPs@)s-GNF, Pt wire and reversible hydrogen electrode (RHE) were used as working, counter and reference electrode, respectively. The electrochemical activity of each catalyst was investigated in HER using linear sweep voltammetry (LSV) measurements between 0.2 and -0.9 V *vs* RHE at a sweep rate of 10 mV/s in a hydrogen saturated 0.1 M perchloric acid solution at room temperature and recorded using NOVA software (Experimental

4.4.3). Polarization curves were obtained by plotting the current density (*j*) vs the potential, where the current density was normalised by dividing the current (*i*) by the geometric surface area of the glassy carbon electrode and the potential was corrected by the ohmic resistance in the solution for each catalyst (Figure 4.6). The accumulation of hydrogen bubbles over time on the surface of the electrode is eliminated after each HER measurement.

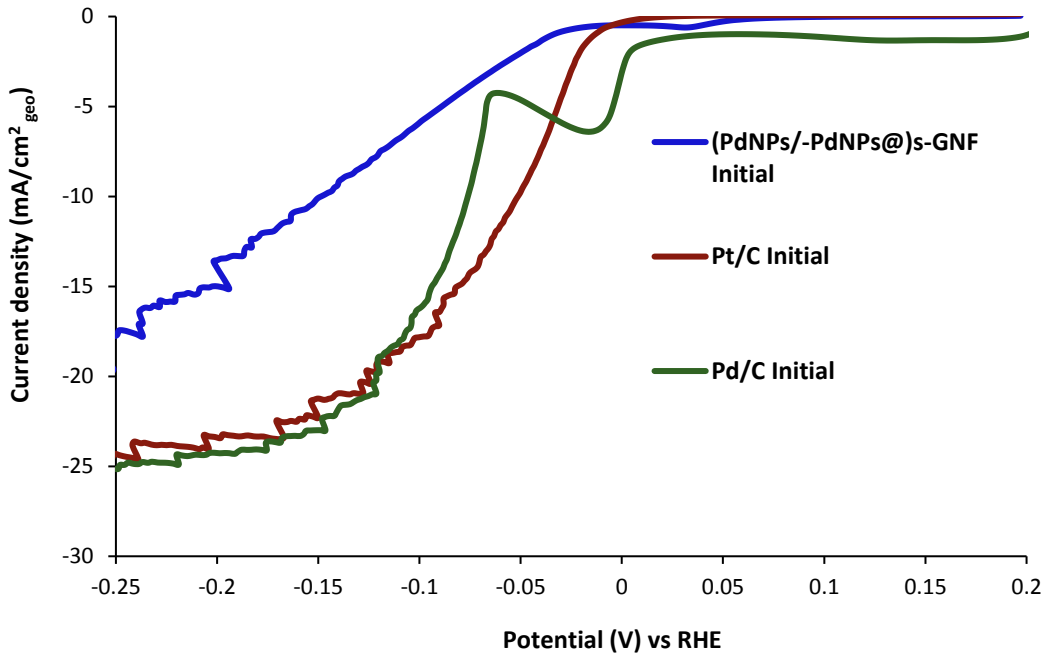

Figure 4.6. Comparison of the ohmic drop corrected HER polarisation curves for (PdNPs/-PdNPs@)s-GNF electrocatalyst with the commercial benchmarks (Pd/C and Pt/C). The small ripples observed in the polarization curves are due to the accumulation of hydrogen bubbles over time on the surface of the electrode.

As expected, Pt/C displayed the smallest onset potential with nearly 0 mV that is in agreement with what is known in the literature as the best active catalyst in HER. Commercial Pd/C and (PdNPs/-PdNPs@)s-GNF exhibited similar characteristic polarization curves where two distinct potential ranges have been observed compared to Pt/C that is consisted with the literature.[22,45] according to our results, the first region from

the Figure 4.6, between 30mV and -60mV, for Pd/C was assigned to the electrochemical hydrogen adsorption and desorption region, while the second region (<-60mV) corresponded to the hydrogen evolution region. (PdNPs/PdNPs@)s-GNF, however, displayed a very small onset potential of ~14 mV compared to that observed for the Pd/C (61mV).

Furthermore, the potential required to achieve a current density of -10 mA/cm^2 is also used to evaluate the electrocatalytic activity of the catalyst material.[46-49] Polarisation curves for the studied electrocatalyst materials showed the next trend for the current density values at -10 mA cm^{-2}_{geo} (normalized by the geometric electrode surface area of the glassy carbon (GC) electrode): Pt/C (52 mV) < Pd/C (74 mV) < (PdNPs/-PdNPs@)s-GNF (148 mV) (Figure 4.6 and Table 4.2).

In addition to the onset potential and the potential required to achieve a current density of -10 mA/cm^2, the Tafel slope is a fundamental parameter to discern the rate determining step in the HER mechanism at the electrode/electrolyte interface and indicates the potential difference required to increase the current density by ten-fold.[50-54] As we mentioned, HER has a three elementary reaction steps in acidic electrolytes which are the Volmer (electrochemical adsorption of H^+ on the electrode), the Heyrovsky (electrochemical desorption of H_2 formed by the reaction of H^+ with the proton from the solution), and the Tafel (chemical combination of the adsorbed H^+ on the electrode to form H_2) steps.[50, 55-56] Tafel slopes for the Volmer, Heyrovsky, or Tafel steps are predicted as about 120, 40, or 30 mV/dec for the rate-determining step, respectively, when Pt is used as an electrocatalyst. Thus, there are two possible reaction mechanisms to evolve H_2, either the Volmer-Heyrovsky or the Volmer-Tafel mechanism.

Tafel slopes can be calculated from the slope of the linear fitting in the polarization curves using the Tafel equation simplified from the Butler-Volmer equation.

$$\eta_a = \frac{0.059}{(1-\alpha_c)n} log(j_0) - \frac{0.059}{(1-\alpha_c)n} log(j) \quad \text{at 25 °C} \qquad \textbf{Equation 4.4}$$

Here η is overpotential (η=E_0-E, i.e. the difference between the potential applied (E) and equilibrium potential (E_0) versus RHE, which is 0 for HER in acid), J_0 is the exchange current density at 0 overpotential. Equation 4.4 can be simplified as

$$\eta = a + b\ log(j) \qquad \textbf{Equation 4.5}$$

This equation indicates a linear relationship between the overpotential and the log (j) and thus a slope b is generated and described as Tafel slope when the overpotential is plotted as a function of $logj$ (Figure 4.7).

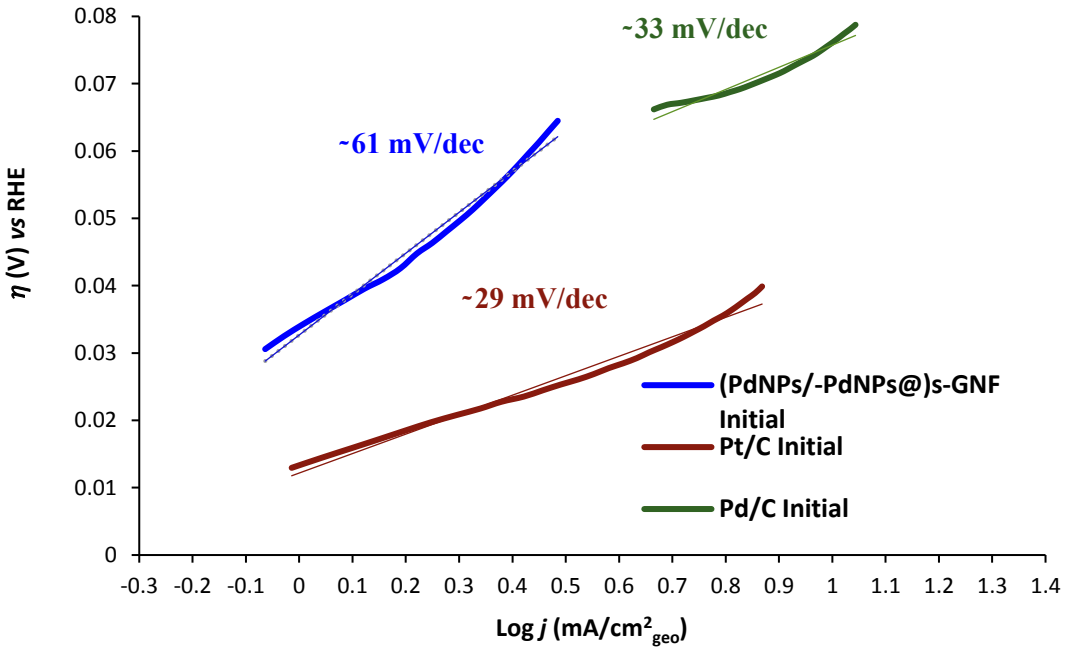

Figure 4.7. Tafel plots for (PdNPs/-PdNPs@)s-GNF electrocatalyst compared to the commercial benchmarks Pd/C and Pt/C.

Here, Pt/C showed the best catalytic activity with a Tafel slope of nearly 29 mV/dec and slightly smaller than Pd/C with a Tafel slope value of nearly 33 mV/dec (Figure 4.7). Tafel slope analysis for both benchmark electrocatalysts suggest the dominant Volmer-Tafel mechanism during the HER process, indicating extremely rapid reaction kinetics,

the recombination of H_{ads} being the rate-determining step. On the contrary, (PdNPs/-PdNPs@)s-GNF showed the highest Tafel slope (61 mV/dec), indicated the Volmer-Heyrowsky mechanism where Heyrowsky step was the rate determining step.

The exchange current density (j_0) indicates the intrinsic activity of the catalyst in HER and can be obtained from the Tafel equation or by extrapolating the linear region to zero overpotential from the Tafel plot.[57-59] A summary of this values together with other electrochemical parameters (including onset potential, overpotential and Tafel slope values) that are required for a better evaluation of the electrocatalyst activity in HER are shown in Table 4.2.

An ideal catalyst is expected to have a low onset potential near to the standard hydrogen reduction potential (0 V_{RHE}) combine with a small Tafel slope, but a large exchange current density value.[11] However, on some occasions a catalyst can exhibit simultaneously a small Tafel slope with a small exchange current density or a high Tafel slope with a high exchange current density. From the Tafel plots, we obtained the highest exchange current density for Pt/C as 0.378 mA/cm^2_{geo}, which is very close to that observed for (PdNPs/-PdNPs@)s-GNF and nearly 7 times larger than that of Pd/C, (Table 4.2). Shao *et al.* recently studied the HER activity of Pt/C (20 wt%) in 0.5 M H_2SO_4 and measured a Tafel slope of 30 mv/dec and an exchange current density of 0.3567 mA/cm^2_{geo} which was consistent with that of the Pt/C in our study (Table 4.2).[13] Although the low HER kinetics associated with (PdNPs/PdNPs@)s-GNF, it had a very small onset potential and higher current density values similar to Pt/C and this can be attributed to active PdNPs supported by the highly conductive s-GNF.

4.2.2 Stability of (PdNPs/-PdNPs@)s-GNF versus Pd/C and Pt/C in HER after 5000 potential cycles.

The long-term stability is a key factor in determining the performance of a electrocatalyst towards HER. The stability of (PdNPs/-PdNPs@)s-GNF after 5000 potential cycles was probed by continuous applied linear potential sweeps between 0.4 and -0.2 V versus RHE at 50mV/s scan rate and compared with Pd/C and Pt/C benchmarks electrocatalysts. During stability tests, the electrode surface was exposed to oxidation and reduction cycles. The electrochemical activity of each catalyst was evaluated as the initial and after the 5000 cycles using the polarization curves and the corresponding Tafel slopes (Figure 4.8 and Figure 4.9).

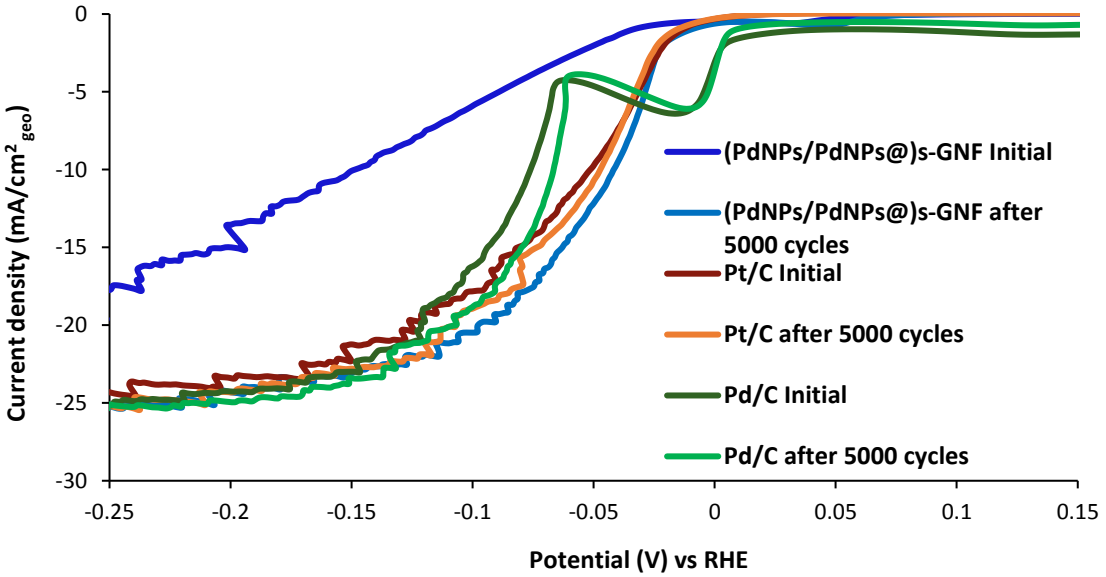

Figure 4.8. HER polarization curves for (PdNPs/-PdNPs@)s-GNF electrocatalyst compared to commercial benchmark Pd/C and Pt/C initial and after 5000 cycles, respectively.

After 5000 HER cycles, (PdNPs/-PdNPs@)s-GNF exhibited an excellent catalytic activity with an onset potential of 0 V and a very low Tafel slope (25.7 mV/dec), which is in contrast with the negligible change on the Tafel slopes observed for Pd/C (31.4 mV/dec) and Pt/C (27.3 mV/dec) (Figure 4.9).

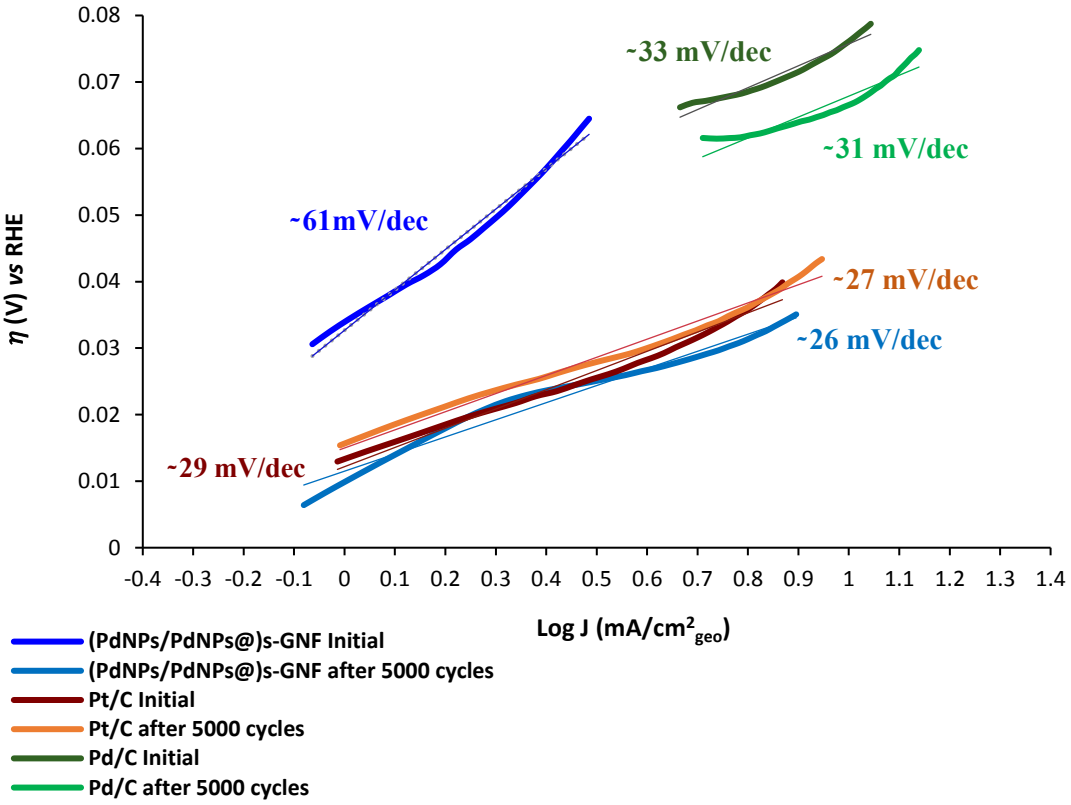

Figure 4.9. HER Tafel plots for (PdNPs/-PdNPs@)s-GNF electrocatalyst compared to commercial benchmark Pd/C and Pt/C initial and after stability test of 5000 cycles, respectively.

Furthermore, the largest exchange current density was obtained for (PdNPs/-PdNPs@)s-GNF that increased from 0.289 to 0.357 mA/cm$^2_{geo}$ after durability tests. However, the exchange current density of Pt/C decreased from 0.378 to 0.272 mA/cm$^2_{geo}$, whilst Pd/C was improved from 0.050 to 0.069 mA/cm$^2_{geo}$, but it was still not comparable to the value of obtained for (PdNPs/-PdNPs@)s-GNF and Pt/C. Moreover the potential value required to obtain a current density of -10 mA/cm^2 was consisting with other parameters following the next trend, (PdNPs/-PdNPs@)s-GNF (41 mV) < Pt/C (47 mV) < Pd/C (66 mV),

which was a significant improvement for our catalyst (Figure 4.8 and Table 4.2). This not only proved the excellent stability but also the improvement on the electrocatalytic activity of (PdNPs/-PdNPs@)s-GNF in HER compared to Pt/C and Pd/C.

Table 4.2. Summary of the onset potential, overpotential at -10 mA/cm^2, Tafel slopes and exchange current density values for the HER measurements initial and after the stability test of 5000 cycles for (PdNPs/-PdNPs@)s-GNF, Pd/C and Pt/C.

	Onset potential (mV)	**Overpotential (mV) at -10 mA/ cm^2**	**Tafel Slope (mV /dec)**	**J_0 (mA/cm$^2_{geo}$)**
(PdNPs/PdNPs@)s-GNF Initial	-14	148	60.7	0.289
(PdNPs/PdNPs@)s-GNF after 5000 cycles	0	41	25.7	0.357
Pd/C Initial	-61	74	32	0.050
Pd/C after 5000 cycles	-56	66	31.4	0.069
Pt/C Initial	0	52	30	0.378
Pt/C after 5000 cycles	0	47	27.3	0.282

To further understand the observed electrochemical performance toward HER after durability test, changes on the structure of the electrocatalyst material ((PdNPs/PdNPs@)s-GNF) was carefully analysed by HRTEM and compared with the commercial electrocatalyst benchmarks (Pd/C and Pt/C) after 5000 cycles (Figure 4.10 and 4.11). Interestingly, PdNPs adsorbed on the atomically flat external surface of s-GNF appears to migrate and grown during potential cycling, in contrast to that observed for PdNPs anchored to the corrugated interiors of s-GNF at the step-edges preventing NP migration. (Figure 4.10 a-c).

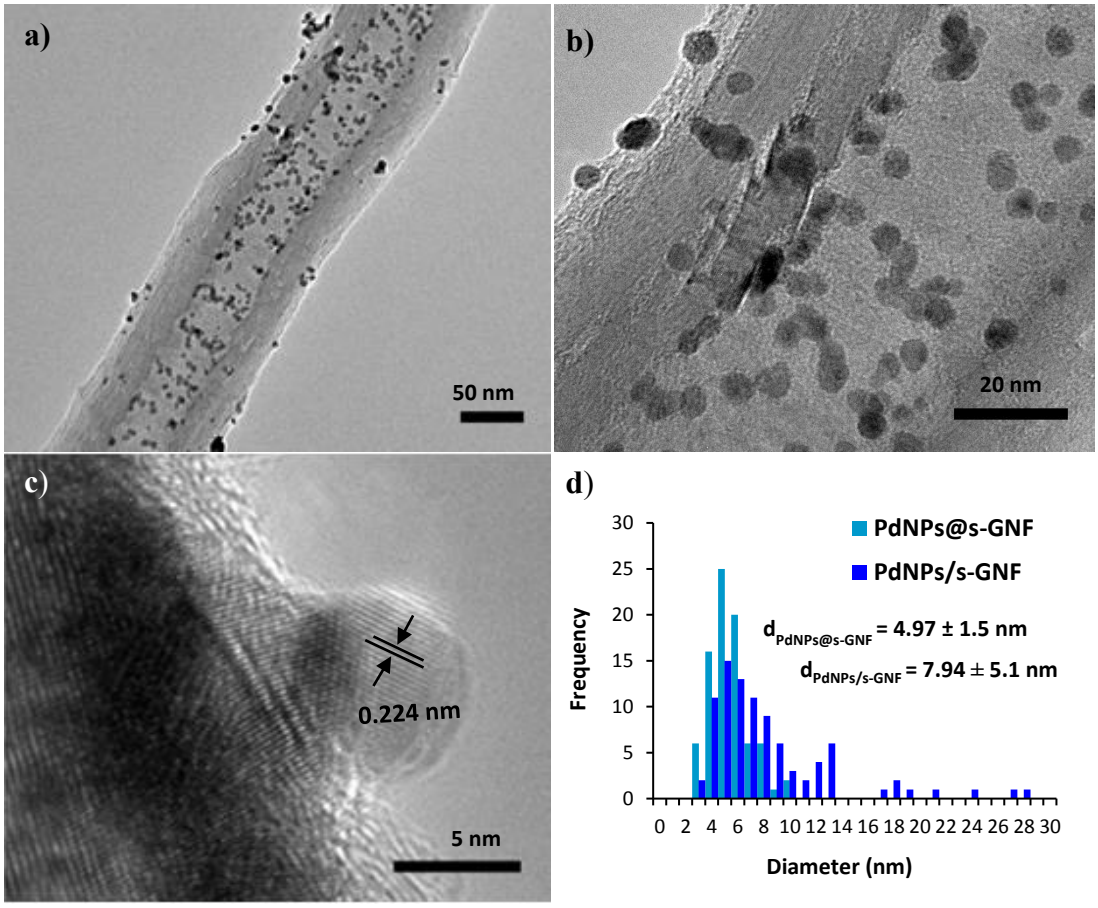

Figure 4.10. (a-c) HRTEM images of (PdNPs/-PdNPs@)s-GNF after the stability test of 5000 cycles **b)** PdNPs on s-GNF as d = 0.224 nm corresponding to the peak centred at 39.5° (as 2Θ°) from XRD and d) the size distribution of PdNPs at the step edges within s-GNF (PdNPs@s-GNF) and on the external of s-GNF (PdNPs/s-GNF), respectively by the measurements of more than 80 nanoparticles for each via HRTEM.

Statistical particle size distribution obtained via HRTEM confirmed the presence of smaller PdNPs at the step edges (4.97 ± 1.5 nm) with an increase of only ~0.5 nm with respect to the PdNPs size observed in (PdNPs/-PdNPs@)s-GNF before cycling (4.49 ± 0.8 nm) (Figure 4.2a and Figure 4.10d), while much bigger PdNPs are found on the external surface of s-GNF (7.94 ± 5.1 nm) confirming their growth during stability tests. A significant particle growth is also observed in Pt/C (6.47 ± 5.2 nm) and Pd/C (8.63 ± 5.3 nm) after 5000 cycles, which is in agreement with the slightly worsening of the electrochemical performance (Figure 4.5 and Figure 4.11).

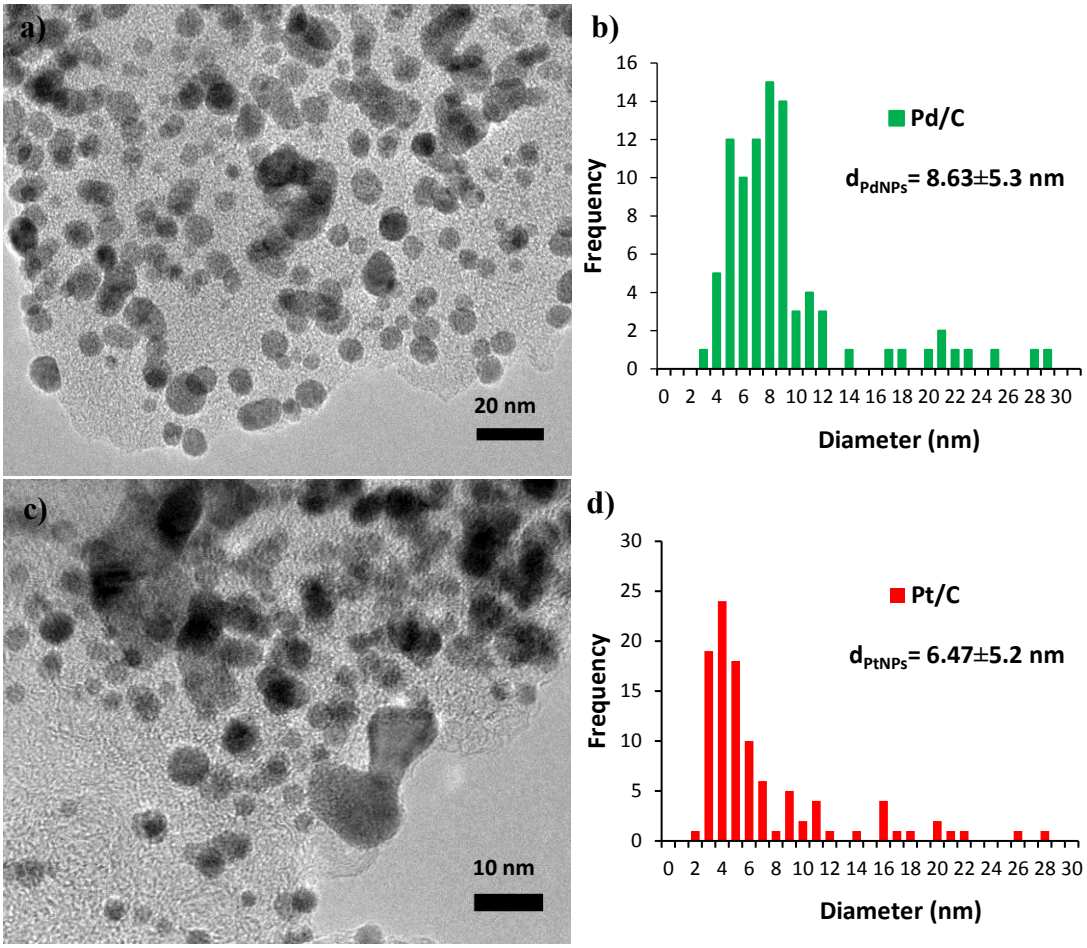

Figure 4.11. a)HRTEM images of Pd/C after 5000 cycles **b)** the size distribution of Pd/C by the measurements of more than 80 nanoparticles via HRTEM **c)**HRTEM images of Pt/C after the stability test of 5000 cycles d**)** the size distribution of Pt/C by the measurements of more than 80 nanoparticles via HRTEM.

Furthermore we examined the CV profiles of PdNPs/PdNPs@)s-GNF, Pd/C and Pt/C before and after the stability test of 5000 cycles, and described the hydrogen adsorption and desorption regions on the CV of Pt/C as it is well understood catalyst in the literature (Figure 4.13.c).[60-62]

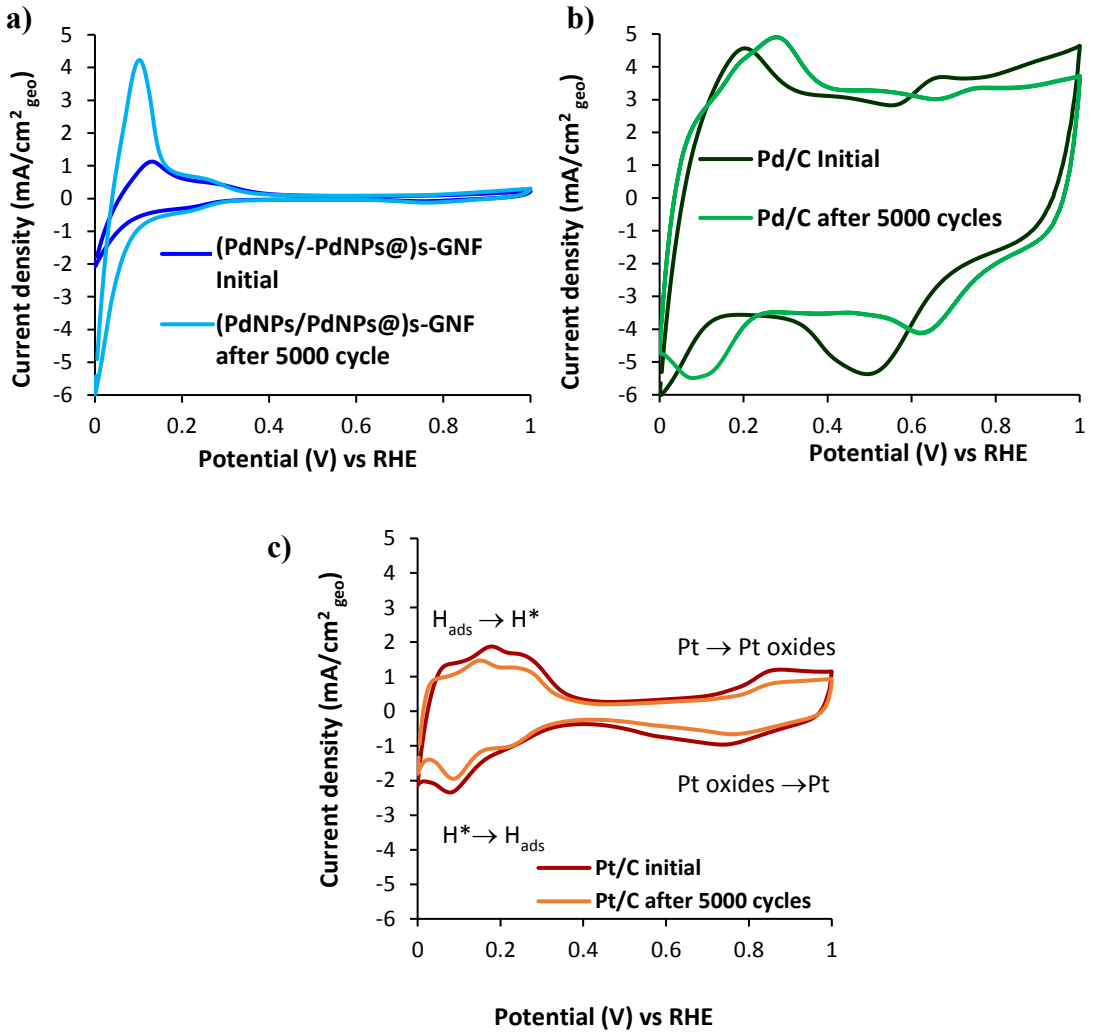

Figure 4.12. CVs of a) (PdNPs/-PdNPs@)s-GNF b) Pd/C and c) Pt/C in the hydrogen adsorption/ desorption potential region at scan rates of 50 mV/s between 0 V and 1 V in N2 saturated 0.1 M $HClO_4$. (Currents was normalized by the geometric electrode surface area of the GC electrode).

In CV profile a cathodic peak below the ~0.4 V versus RDE is considered as underpotential deposition (UPD) region of Pt/C.[61-62] The desorption peak at lower potential between the 0 and 0.2 V corresponds to desorption of weakly bonded H while the desorption peak at higher potential between 0.2 and 0.4 corresponds to desorption of strongly bonded H and described as $H_{UPD\text{-}des}$ for Pt/C (Figure 4.12c). It enables one to calculate the electrochemical surface area (ECSA) of the catalyst from the charge required to form a monolayer of adsorbed hydrogen on the catalyst surface. However, in the case of palladium, it is reported that hydrogen adsoption simultaneously occurs with hydrogen absorption process on Pd surface which confounds the determination of hydrogen monolayer formation by adsorption.[63-65] Therefore, H_{UPD} was not applicable to calculate the ECSA of palladium in our study, ie PdNPs/PdNPs@)s-GNF and Pd/C. For this reason, we optimised the all polarisation curves by dividing to the geometric surface area of the GC electrode assuming that the catalyst spreaded completely over the whole surface of the GC.

4.2.3 Investigating the effect of s-GNF support in HER

Carbon based metal free materials with unique electronic properties such CNTs, graphene sheets, graphite nanoplatelets, carbon nitride, and three-dimensional (3D) carbon architectures have recently been proposed for the development of advanced metal-free catalysts with promising catalytic performances as an alternative to the metal based materials in electrochemical applications.[55, 66-76] In addition to their long term chemical stability in acid, their high electrical conductivity, tunable composition, relatively low cost and abundance of carbon in earth made them exciting candidates for HER. In 2014, pristine MWNTs activated via acid oxidation has been reported for the first time as highly active one dimensional metal free catalyst to generate hydrogen with a very low onset

potentials as -50 mV and -220 mV to achieve a current density of 10 mA/cm2 with a Tafel slope of 71.3 mV/dec and an exchange current density of 0.016 mA/cm^2.[77]

In order to appraise the contribution of s-GNF in the electrochemical performance of (PdNPs/PdNPs@)s-GNF, we investigated the HER activity of s-GNF before and after cycling. The initial HER polarization curves indicated a good catalytic activity for s-GNF with a small onset potential about -27 mV, which means that it starts to generates current near to the HER equilibrium potential (0 V), however a large current density (422 mA) to achieve a current density of -10 mA/cm^2 is observed (Figure 4.13). After 5000 cycles, s-GNF exhibited a significantly increased HER activity similar to (PdNPs/-PdNPs@)s-GNF with a Pt/C like onset potential of 0 V and nearly two fold reduction of the potential required to achieve a current density of -10 mA/cm^2 (261 mV).

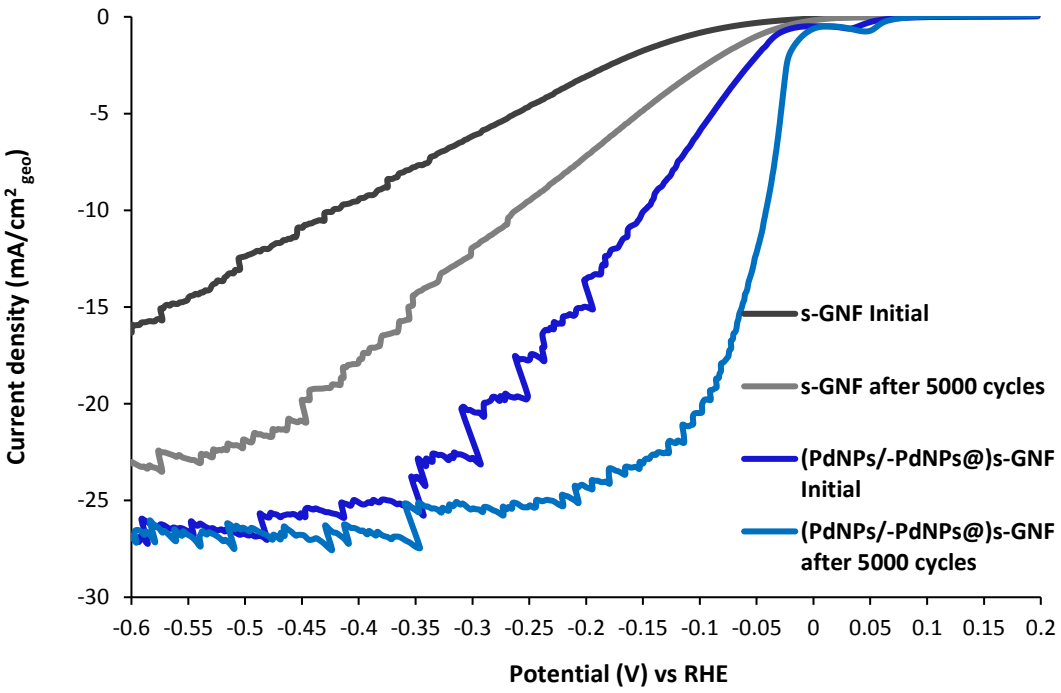

Figure 4.13. HER polarization curves for s-GNF and (PdNPs/-PdNPs@)s-GNF electrocatalyst initial and after stability tests of 5000 cycles , respectively.

The Tafel slope of s-GNF before and after 5000 cycles were 100.6 and 77.3 mV/dec, respectively (Figure 4.14).

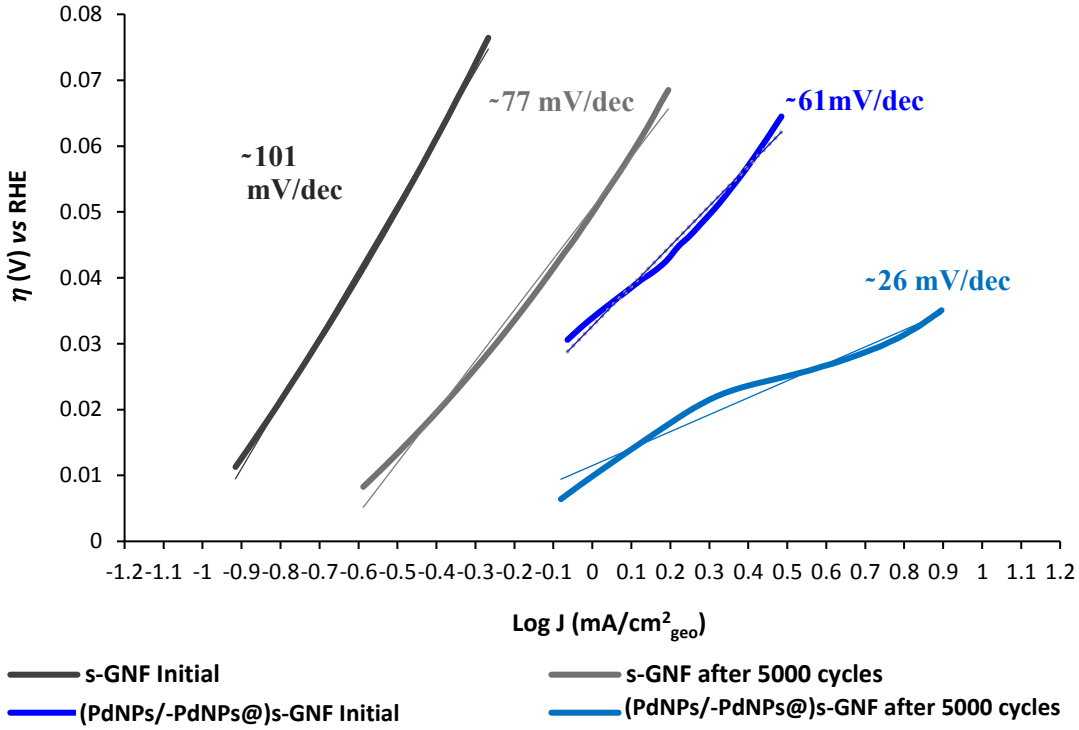

Figure 4.14. HER Tafel plots for s-GNF and (PdNPs/-PdNPs@)s-GNF electrocatalyst initial and after stability test of 5000 cycles, respectively.

The smaller Tafel slope observed after cycling indicates a faster reaction rate but both values indicate that Volmer-Heyrowsky mechanism is involved during HER process where the Volmer step is the rate-determining step. Furthermore, a considerably large exchange current density is observed for s-GNF before cycling (0.0977 mA/cm^2_{geo}), which is two times higher than that of the initial Pd/C (Table 4.2 and 4.3). After stability tests, a further increase of the exchange current density is clearly observed (0.222 mA/cm^2_{geo}) (Table 4.3).

Table 4.3. Indication of the onset potential, overpotential at -10 mA/ cm^2, Tafel slopes and exchange current density values for the initial HER measurements and after the stability tests of 5000 cycles for s-GNF and (PdNPs/PdNPs@)s-GNF.

	Onset potential (mV)	**Overpotential (mV)** at **-10 mA/ cm^2**	**Tafel Slope (mV /dec)**	**J_0 (mA/cm^2_{geo})**
s-GNF Initial	-27	422	100.6	0.0977
s-GNF after 5000 cycles	0	261	77.3	0.222
(PdNPs/-PdNPs@)s-GNF Initial	-14	148	60.7	0.289
(PdNPs/-PdNPs@)s-GNF after 5000 cycles	0	41	25.7	0.357

It is important to find out the significantly improved HER activity and stability of s-GNF during the stability test (5000 cycles). It can be due to the several factors. It is known that the edges of nanotubes and defects promote the electron transfer and the catalytic activity. [55-56,73-76] The shortening process via ball milling which increased the number of nanotubes and thus the number of the open edges increased with some defects on the outer GNF surface. A large number of catalytically active sites containing edge carbon atoms and the residual oxygen functional groups can act as active sites for HER.

However, this process can also generate some residual carbon as a results of some defected tubes which is observed by HRTEM and the presence of these residual carbons with different surface and electronic properties in comparison to GNFs may limit the initial HER activity of s-GNF. It may provide binding sites for HER and the reactants binding to the residual carbon surface may slow the reaction kinetic by the mass transport problems due the pore structure which is unknown. Moreover, the presence of some residual dba (dibenzylacetonate) complex due to the PdNPs formation can also inhibit the activity of PdNPs as it can block the surface of PdNPs leading the limitied access for the reactants. The electrical properties of these residual carbons and presence of residual dba may also reduce the HER activity. Therefore, the improved HER activity of s-GNF and PdNPs/PdNPs@)s-GNF during the stability test can be attributed due to the depletion of residuals resulting in the enhanced interactions of the reactants between the cleaned s-GNF and (PdNPs/-PdNPs@)s-GNF to evolve H_2.

For a better understanding, s-GNF after the stability test was analysed by HRTEM and was observed that some of the graphitic step egdes undergo transformation (opening) during the continuous electrocatalysis compared to the initially closed structure of them in s-GNF (Figure 4.1 and 4.15).

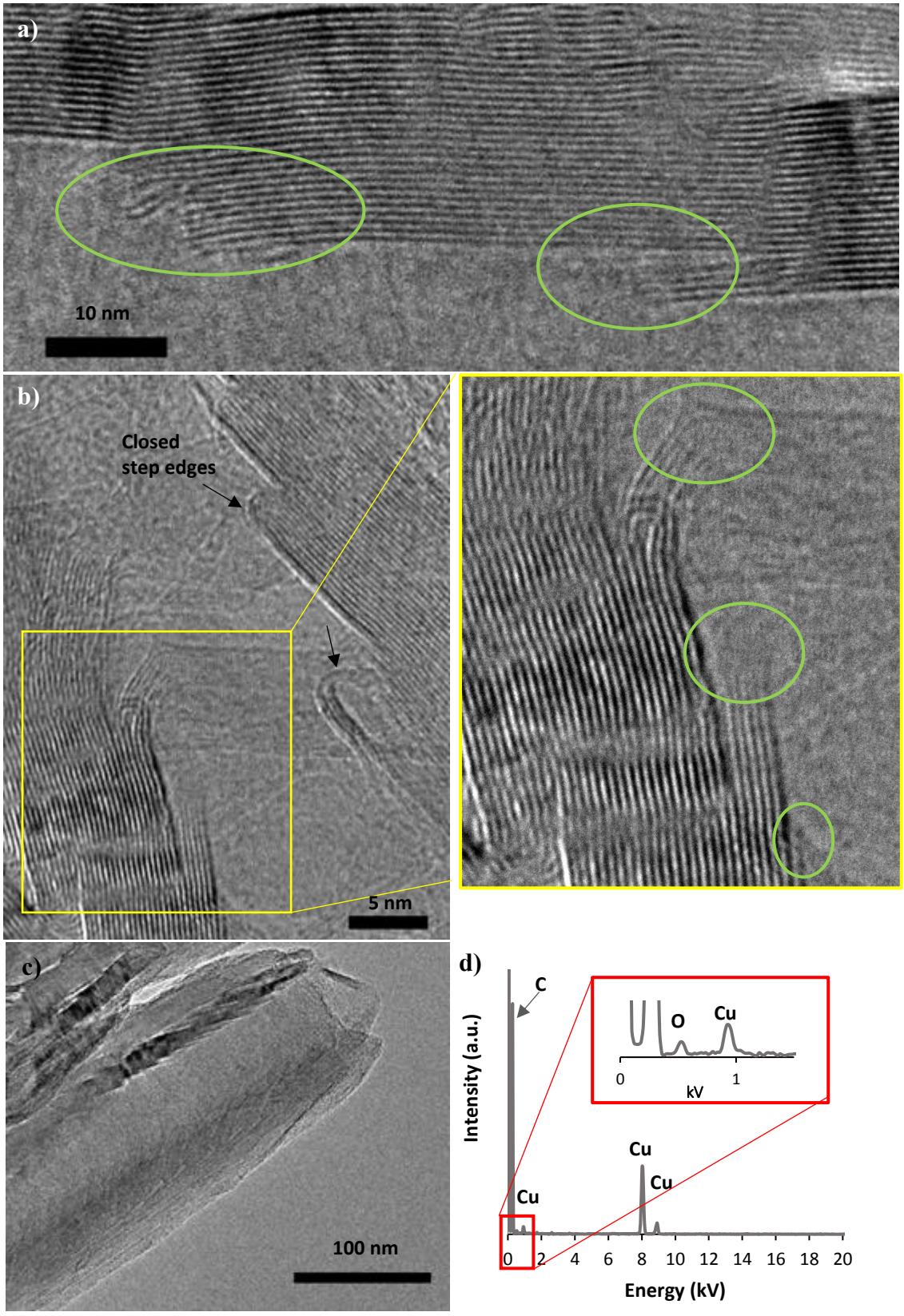

Figure 4.15. (a-c) HRTEM images of s-GNF after the HER stability test of 5000 cycles. Green oval shapes in a) and enlarged region in b) show some opened step edges, d) EDX of s-GNF after ball milling, inset region in the enlarged red rectangular shape shows the oxygen peak with an atomic ratio% of C:O as 99.24:0.76 .

The observed opening of the step edges shown in Figure 4.15 via HRTEM is rationalised to be a result of hydrogen atoms forming covalent bonds with the carbon atoms in the curved part of the graphitic step edges. This is in agreement with previous work which reported the hydrogenation of graphene by free H atoms in the presence of a perpendicular electric field.[78] It is proposed that the C=C bonds in the curved carbon surface at the step edge interact with hydrogen radicals via catalytic hydrogenation to form a chain of C-H bonds assuming along the zigzag direction of the carbon sheet.[79] This results in the conversion of sp^2 hybridised carbons into sp^3 carbon centres. Subsequently, the C-H bonds can then either act as a site to interact with further protons from the solution to form H_2 and reform the initial curved sp^2 hybridised carbon structure, or alternatively the newly formed C-H bonds can undergo further hydrogenation, promoting strain relieving unzipping of the graphitic step edge, rupturing the C-C bonds along line of C-H bonds and forming two planar graphitic layers (Scheme 4.1).

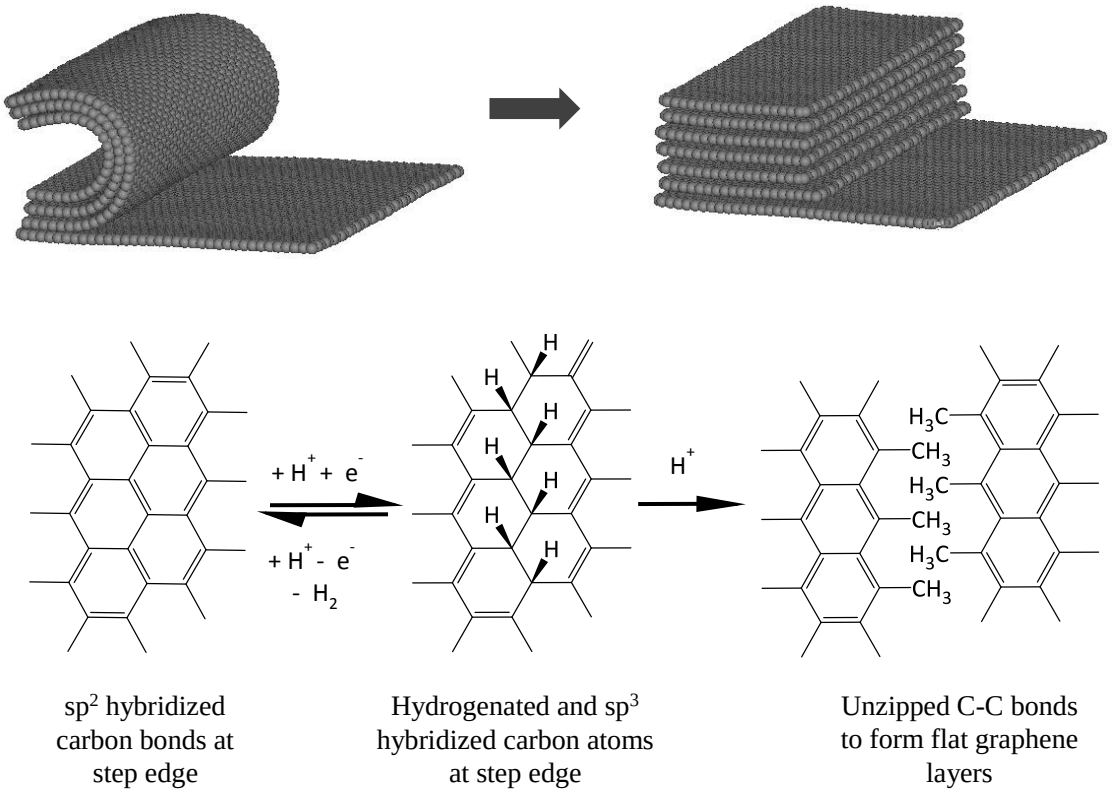

Scheme 4.1. Proposed mechanism showing how protons interact with the C=C bonds of the curved graphtic step edge along the zigzag direction of the carbon sheet. Initially they reversibly forming a line of C-H bonds and then further hydrogentaion leads to rupturing of the curevd carbon sheet and the formation of C-CH_3 teminated flat graphene layers.

The Pd nanoparticles embedded in s-GNF catalyst, (PdNPs/-PdNPs@)s-GNF, exhibited enhanced HER activity during the stability tests (Figure 4.14). This improved activity can be partly explained by considering the analogous improvement in HER activity exhibited by s-GNF alone during identical HER stability tests. This implies that the observed improvement in activity of the (PdNPs/-PdNPs@)s-GNF over time are actually a result of changes in the support during the experiments. However, the HER activity of (PdNPs/-PdNPs@)s-GNF, both initially and after the stability test, was much better than that of s-GNF alone implying that the Pd NPs are also playing an important role in the observed HER activity.

It is proposed that the accessible step edges of the s-GNFs are perfectly structured for selective growth of PdNPs compared to the 'featureless', smooth outer walls of the GNF. The resultant PdNPs/GNF structure at the step edge provides an active binding site for hydrogen ions to produce hydrogen, and the PdNP could conceivably act as a catalyst to lower the energy barrier to hydrogenation and rupturing processes. The PdNPs at the step edges can be bound to the s-GNF in two possible ways: (i) via strong hybridisation between the Pd atoms and carbon π orbitals in the s-GNF forming a π-bond[80] (Scheme 4.2a), and, (ii) via covalent interaction of Pd atoms and the C-CH bonds in the hydrogenated step edges to strong covalent Pd-C bonds[81-83] (Scheme 4.2b). It is proposed that initially the majority of the Pd NPs are bound to the step edges via π-bonds but over time, as hydrogenation occurs and more C-H bonds are formed, more sigma C-Pd bonds are formed which the interactions of Pd cluster with the opened step edges was observed via HRTEM (Figure 4.22d). This leads to more effective conduction from the electrode, through the GNF to the NP and thus higher HER activity over time.

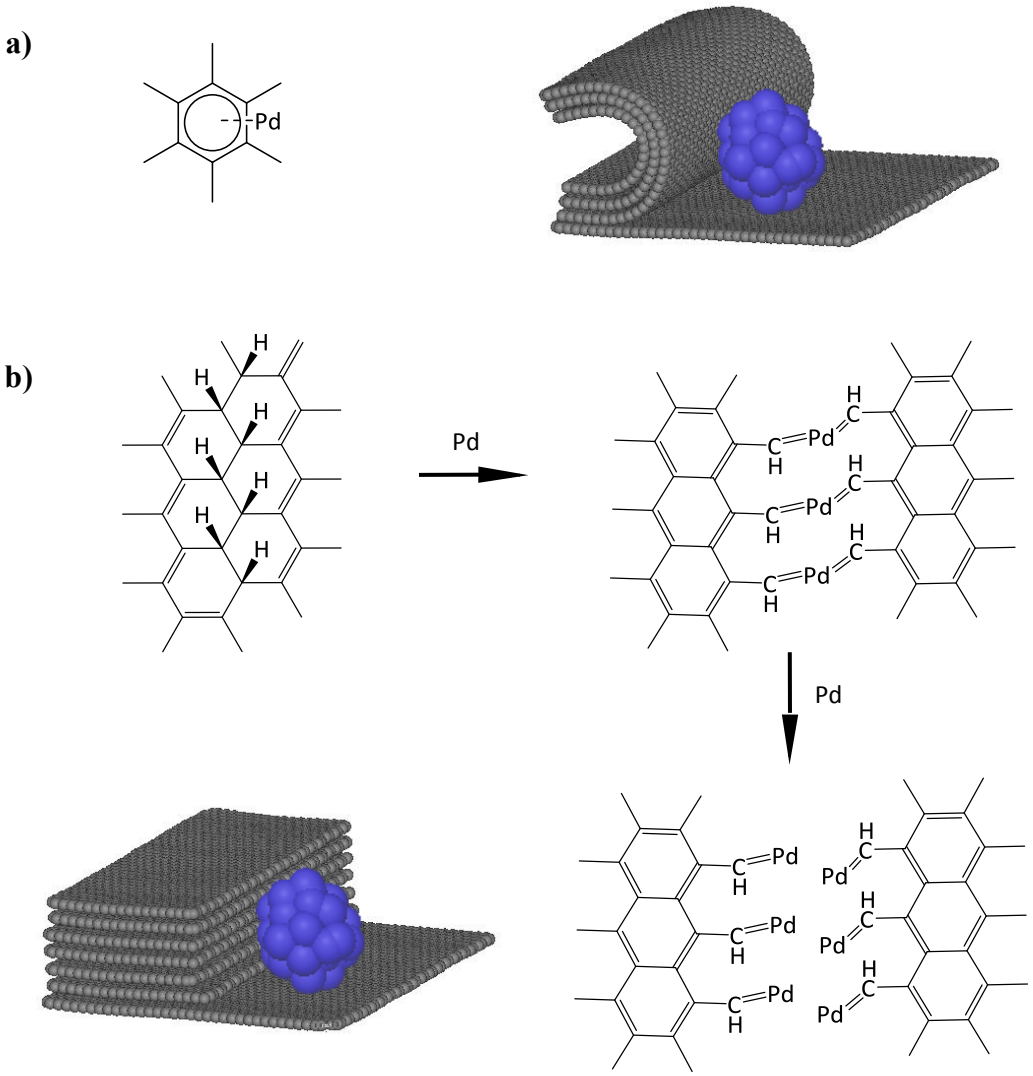

Scheme 4.2. Schematic represantation of **(a)** a Pd atom interacted to the curved carbon sheet of the step edge via π bonding (left) and a model of a Pd cluster (purple) interacted with step edges (dark grey), and, (**b)** the unzipping of the curved carbon sheet of the step edges leading to covalent interactions between the Pd atoms of the NPs and the hydrogenated, planar graphitic sheets and a model of a Pd cluster (purple) interacted with the opened step edges (dark grey) via sigma bond.

These strong interactions of PdNPs at the step edges was also confirmed by HRTEM where the nanoparticle growth and degradation was mostly indicated on the external of s-GNFs due to migration of the nanoparticles on the smooth external of s-GNF in acid, while there was no significant nanoparticles growth due to the highly stabilised nanoparticles at the step edges (Figure 4.22).

In addition to these, the nano-confined space of GNF, in particularly around step edges with ~3 nm high may increase the local concentration of the reactions enabling a faster HER kinetic. As a result, we demonstrated HER activity and stability of PdNPs/PdNPs@)s-GNF was superior that of Pd/C and Pt/C after the stability test of 5000 cycles due to the cleaned surface and improved electron transfer and synergetic effect between the s-GNF and PdNPs.

Furthermore we examined the CV profiles of s-GNF and PdNPs/PdNPs@)s-GNF before and after the stability test of 5000 cycles. In CV profile both $H_{UPD\text{-}des}$ and desorption peaks of s-GNFs and PdNPs/PdNPs@)s-GNF were illustrated in Figure 4. 26, and observed an increase of desorption peak area in current for both s-GNFs and PdNPs/PdNPs@)s-GNF

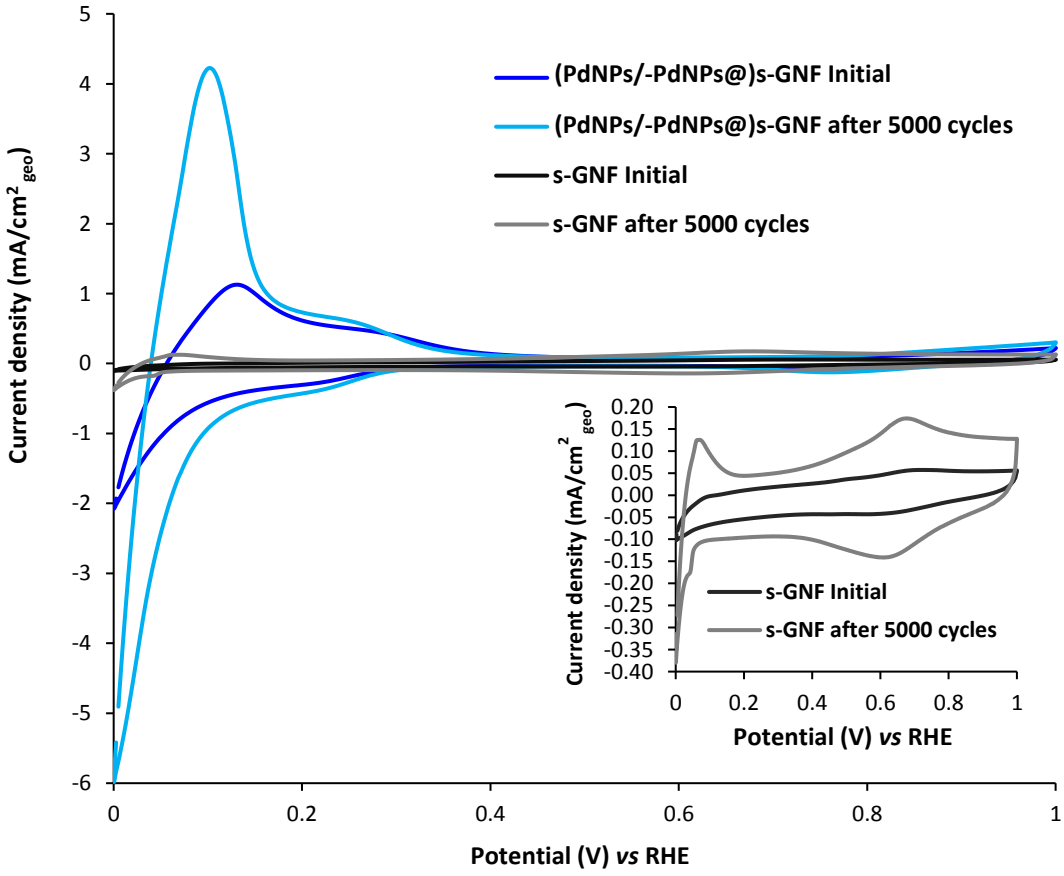

Figure 4.16. CVs of s-GNFs and PdNPs/PdNPs@)s-GNF as initial and after the stability test of 5000 cycles at scan rates of 50 mV/s between 0 V and 1 V in N2 saturated 0.1 M $HClO_4$. (Currents was normalized by the geometric electrode surface area of the GC electrode).

after the stability test which can mean that during the stability the surface of the catalyst was cleaned which enhanced surface area and enabled an efficient mass transport through the both catalysts leading to increase in the HER activity.

4.2.4 Investigating the activity and stability of (PdNPs/-PdNPs@)s-GNF in HER as a function of the cycling number

Electrocatalytic stability of (PdNPs/-PdNPs@)s-GNF were studied as a function of cycling number. The electrochemical activity of (PdNPs/-PdNPs@)s-GNF towards HER were investigated after 2500, 50000, 10000, 20000 and 30000 cycles and compared with Pt/C electrocatlayst benchmark after 5000 and 30000 cycles (Figure 4.20). HER polarization curves at different cycling numbers are shown in Figure 4.17. We observed an enhanced HER activity by the increasing cycling number and summarized all parameters used to evaluate the HER catalyst in Table 4.4.

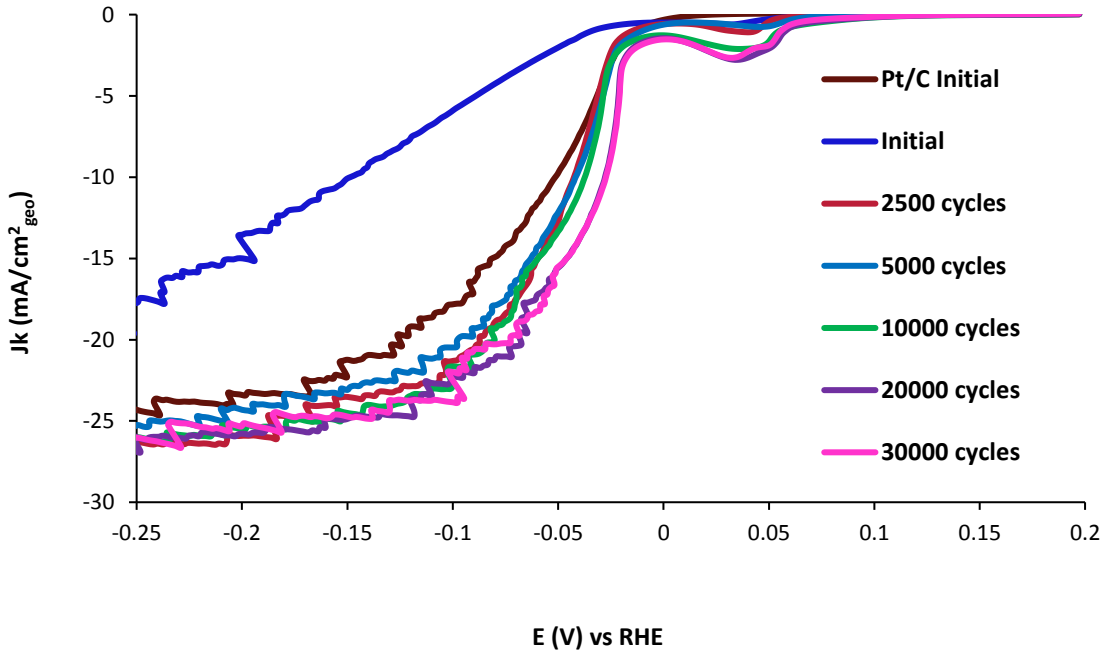

Figure 4.17. HER polarization curves for (PdNPs/-PdNPs@)s-GNF electrocatalyst material as initial and after the stability test at different cycling numbers as, 2500, 5000, 10000 20000 and 30000 with initial Pt/C.

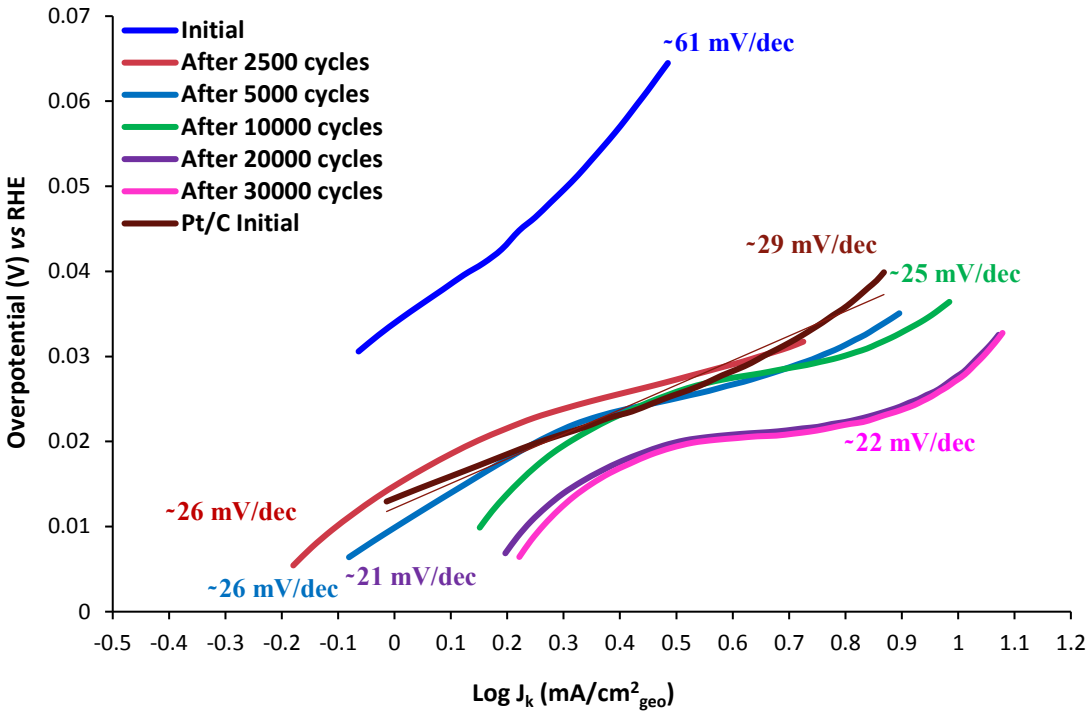

Figure 4.18. Tafel plots for (PdNPs/-PdNPs@)s-GNF electrocatalyst as initial and after the stability test performed at different cycling numbers as 2500, 5000, 10000, 20000 and 30000, respectively.

As can be seen from Figure 4.17, after the initial HER measurement, the onset potential of (PdNPs/-PdNPs@)s-GNF stayed at 0 mV and the Tafel slopes and the potential required to achieve a current density of -10 mA/cm^{2}gradually decreased during to stability cycling up to 30000 cycles, (Figure 4.18 and Table 4.4). Polarisation curves and Tafel slopes of (PdNPs/-PdNPs@)s-GNF after 20000 and 30000 HER cycles showed similar trend; however, the largest exchange current density was obtained for (PdNPs/-PdNPs@)s-GNF as 0.545 mA/cm$^2_{geo}$ after the 30000 cycles (Table 4.4).

Table 4.4. Onset potential, overpotential, Tafel slopes and exchange current density values for the initial HER measurements of (PdNPs/-PdNPs@)s-GNF and after the stability tests at different cycling numbers as 2500, 5000, 10000, 20000 and 30000, respectively.

	Onset potential (mV)	**Overpotential (mV) at -10 mA/ cm^2**	**Tafel Slope (mV /dec)**	**J_0 (mA/cm^2_{geo})**
Initial	-14	148	60.7	0.289
after 2500 cycles	0	42	26.3	0.291
after 5000 cycles	0	41	25.7	0.357
after 10000 cycles	0	37	25.4	0.376
after 20000 cycles	0	28	21.1	0.476
after 30000 cycles	0	27	22	0.545

The CV profiles of PdNPs/PdNPs@)s-GNF as initial and after the stability test with different cycling numbers demonstrated a gradual increase of desorption peak area in current for PdNPs/PdNPs@)s-GNF showing that the surface area of the catalyst was increased during the cycling and enabled a superior HER activity.

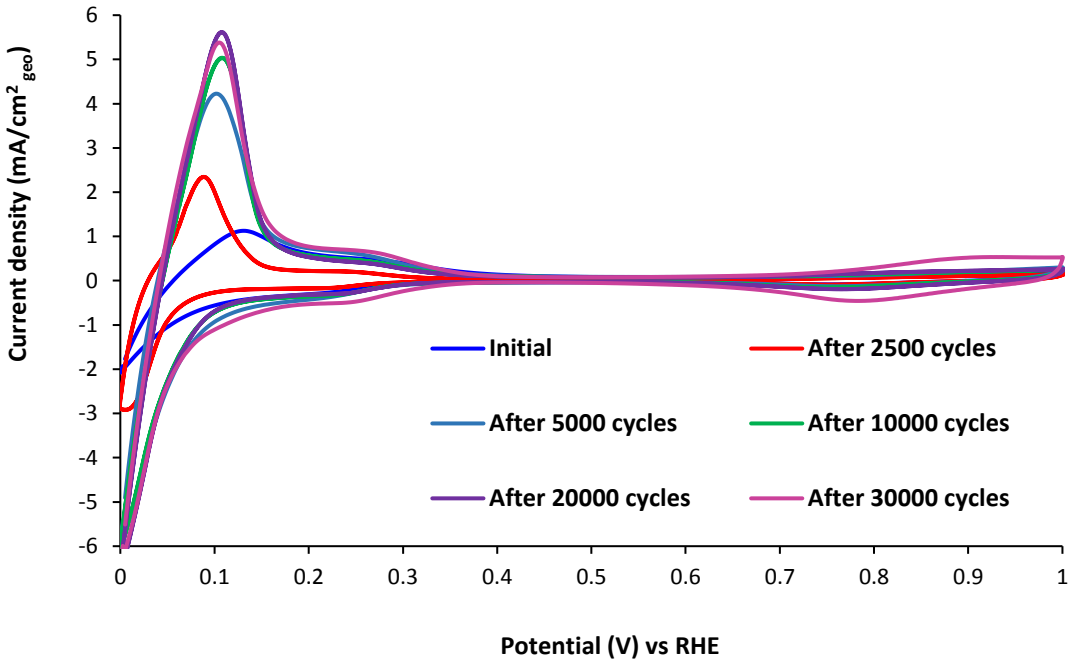

Figure 4.19. CVs of PdNPs/PdNPs@)s-GNF as a function of cycling number at scan rates of 50 mV/s between 0 V and 1 V in N2 saturated 0.1 M $HClO_4$. (Currents was normalized by the geometric electrode surface area of the GC electrode)

Furthermore, we investigated the stability of Pt/C up to 30000 HER cycling and compared with PdNPs/PdNPs@)s-GNF. On the contrary to PdNPs/PdNPs@)s-GNF, HER activity of Pt/C significantly decreased in comparison to its initial activity.

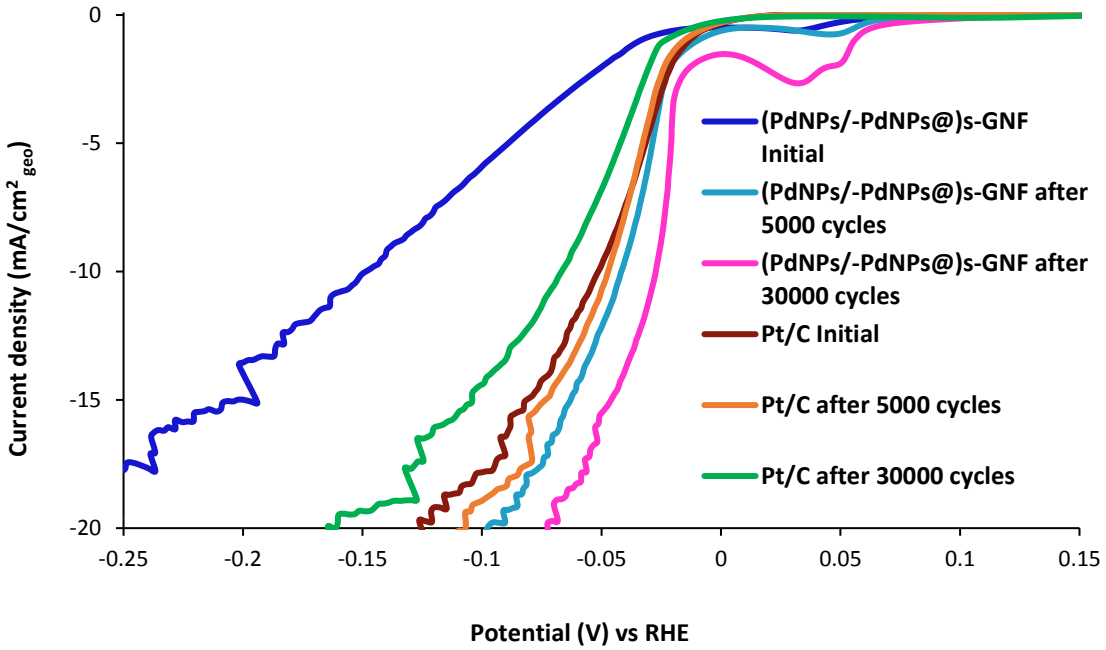

Figure 4.20. HER polarization curves for Pt/C and (PdNPs/-PdNPs@)s-GNF electrocatalyst materials as initial and after the stability test at different cycling numbers as 5000 and 30000.

Although the Tafel slope, i.e. the reaction mechanism remain unchanged, initial onset potential (0 V) changed as -25 mV, the overpotential required to achieve a current density of -10 mA/cm^{2}gradually significantly increased from 52 mV (initial) to 67 mV after stability test of 30000 cycles (Figure 4.21 and Table 4.5).

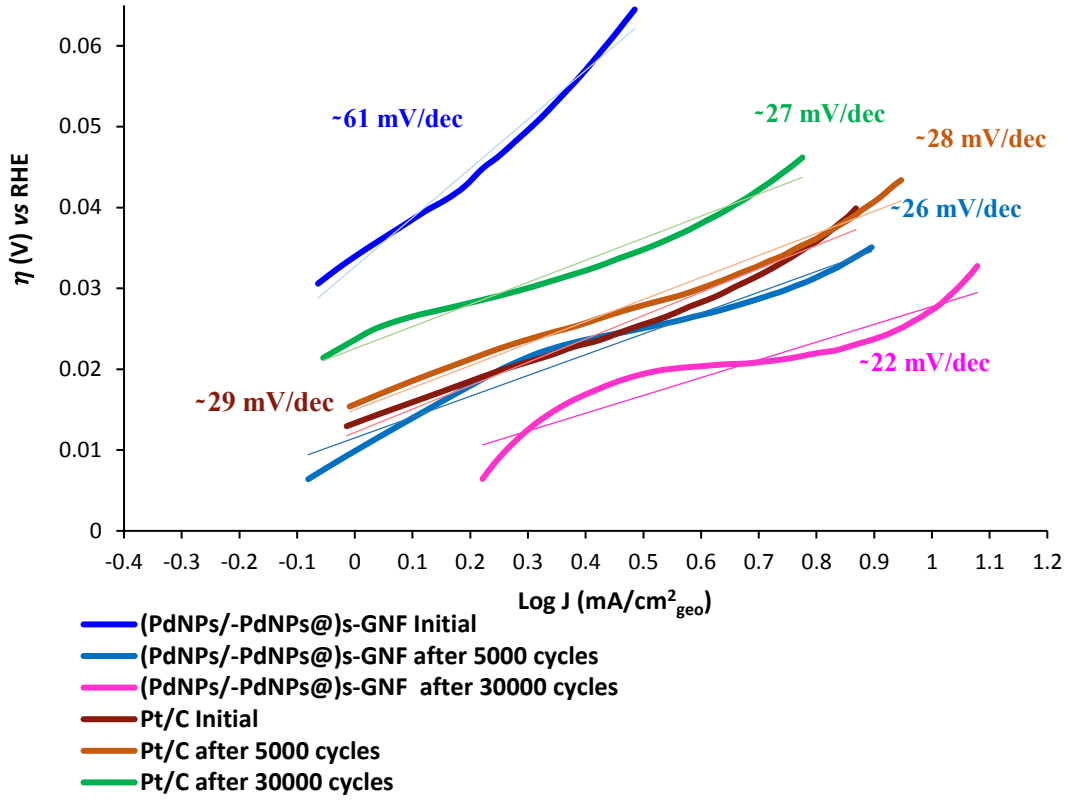

A sharp decrease was also observed in the exchange current density for Pt/C from 0.378 mA/cm$^2_{geo}$ (initial) to 0.149 mA/cm$^2_{geo}$ after the 30000 cycles which was not comparable that of PdNPs/PdNPs@)s-GNF (Table 4). PdNPs/PdNPs@)s-GNF and Pt/C after the stability test of 30000 cycles were analysed by HRTEM (Figure 4.22 and 4.23). PdNPs/PdNPs@)s-GNF indicated that the PdNPs at the step edges was very well stabilised and remained still small in size, 5.2 ± 1.7 nm while the PdNPs on the outer of s-GNFs agglomerated to the bigger NPs, 7.6 ± 3.6 nm and there was comparably less NPs on the outer of s-GNF from the initial sample. It can be explained that some NPs migrated from the s-GNF surface to the solution due to the strong acidic environment

during the reaction. However, it was not applicable to quantify the amount of the PdNPs after the stability test .

Table 4.5. Exhibition of the onset potential, overpotential, Tafel slopes and exchange current density values for the HER measurements as initial and after the stability test of 5000 and 30000 cycles for (PdNPs/-PdNPs@)s-GNF and Pt/C.

	Onset potential (mV)	**Overpotential (mV) at -10 mA/ cm^2**	**Tafel Slope (mV /dec)**	**J_0 (mA/cm^2_{geo})**
(PdNPs/-PdNPs@)s-GNF Initial	-14	148	60.7	0.289
Pt/C Initial	0	52	30	0.378
(PdNPs/-PdNPs@)s-GNF after 5000 cycles	0	41	25.7	0.357
Pt/C after 5000 cycles	0	47	27.3	0.282
(PdNPs/-PdNPs@)s-GNF after 30000 cycles	0	27	22	0.545
Pt/C after 30000 cycles	-25	67	27.3	0.149

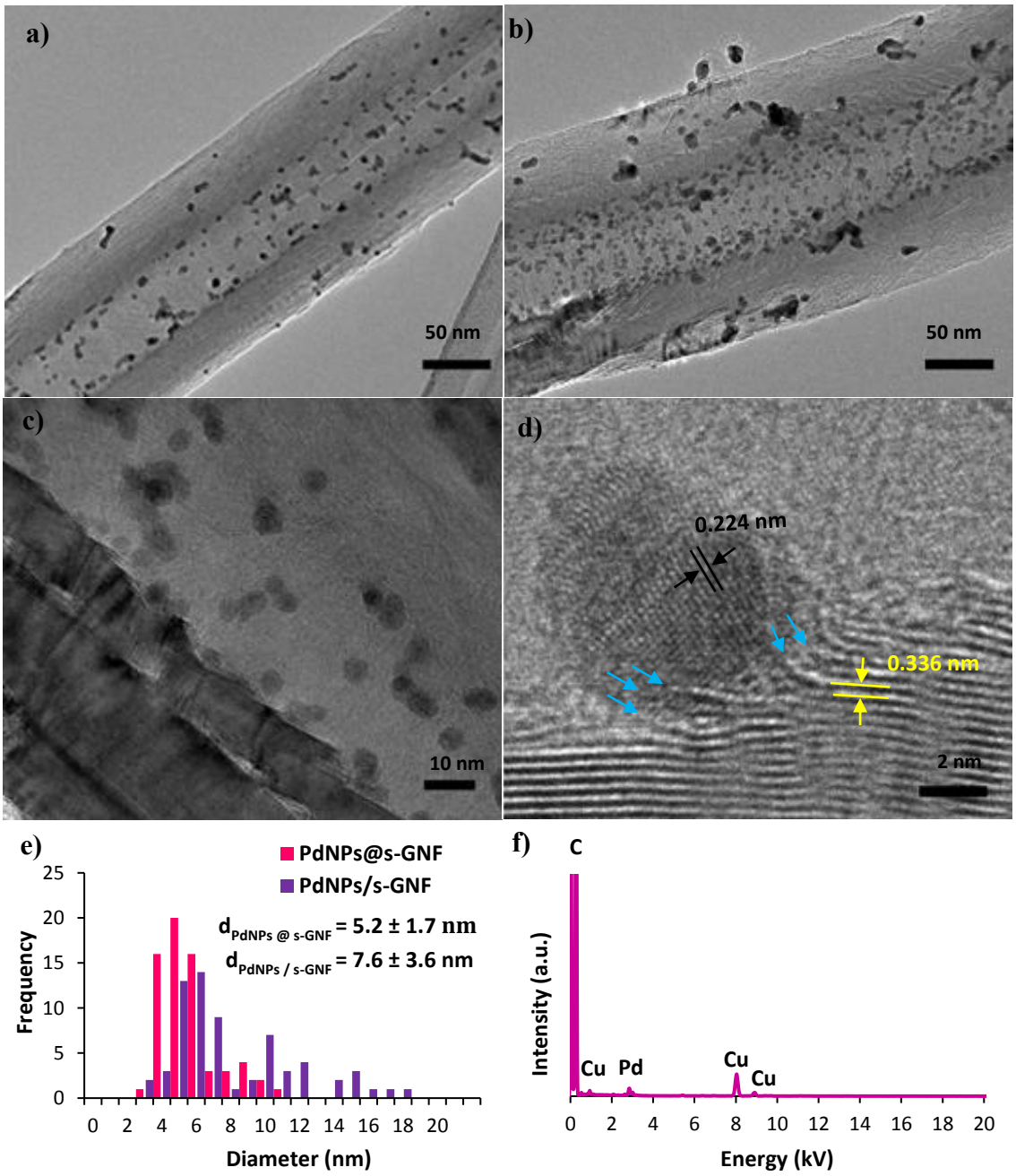

Figure 4.22. (a-d) HRTEM images of (PdNPs/-PdNPs@)s-GNF after 30000 cycles **d)** PdNPs bonded to opened step edges (blue arrows) and d spacing value of PdNPs (black arrows) and graphene layers (yellow arrows) on s-GNF as 0.224 nm and 0.336 nm, respectively, corresponding to Pd (111) and C (002) **e)** particle size distribution (measured using more than 80 NPs **d)** EDX analysis of PdNPs@s-GNF.

HRTEM images of Pt/C exhibited the NPs growth after 30000 cycles, however with similar particle size distribution after the stability test of 5000 cycles (Figure 4.23).

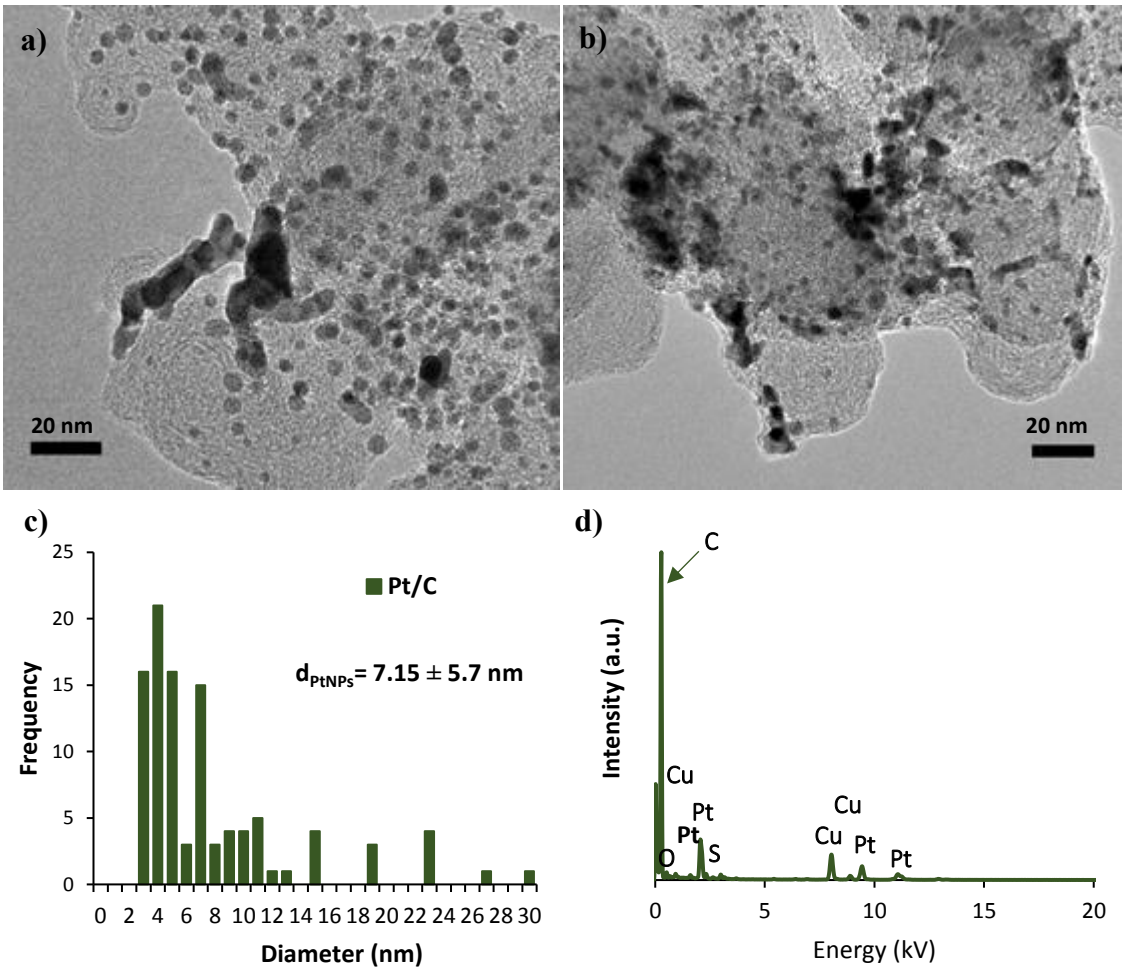

Figure 4.23. (a-b) HRTEM images of Pt/C after 30000 cycles **c)** particle size distribution of Pt (measured using more than 80 NPs **d)** EDX analysis of Pt/C.

These can be attributed to the degradation of Pt/C and oxidising of carbon support during the stability test as the electrode surface was exposed to oxidation and reduction cycles and thus altered electronic properties of the catalyst. However, PdNPs/PdNPs@)s-GNF displayed superior durability and increasing activity in strong acidic media in comparison to Pt/C due to the step edges stabilised the PdNPs and (PdNPs/-PdNPs@)s-GNF enhanced its electronic properties during the stability test.

The CV profiles of PdNPs/PdNPs@)s-GNF and Pt/C as initial and after the stability tests of 5000 and 30000 cycles, respectively were examined (Figure 4.24).

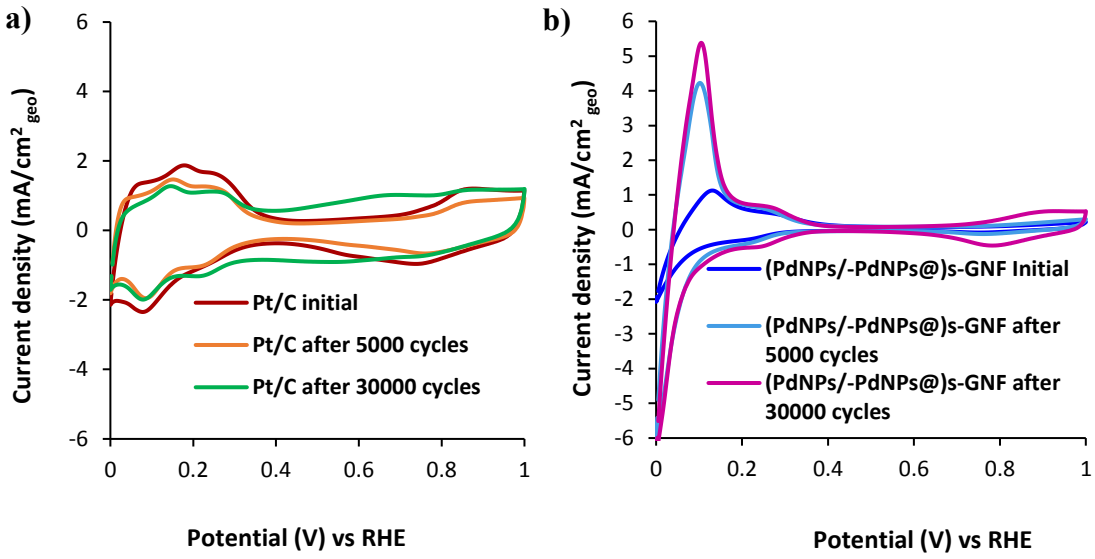

Figure 4.24. CVs of PdNPs/PdNPs@)s-GNF and Pt/C as initial and after the stability test of 5000 and 30000 cycles at scan rates of 50 mV/s between 0 V and 1 V in N2 saturated 0.1 M $HClO_4$. (Currents was normalized by the geometric electrode surface area of the GC electrode).

PdNPs/PdNPs@)s-GNF demonstrated a gradual increase of desorption peak area in current and also bigger oxygen reduction peak between the 0.6-0.9 V however did not affect the HER performance as s-GNF is very stable in acid environment. However, the desorption peak area of Pt/C got smaller compared to the initial CV measurement and the CV profile of Pt/C slightly changed after the 30000 cycles. It also gave a bigger oxygen reduction peak between the 0.6-0.9 V compared to the initial measurement, which is consistent with our evaluation that Pt/C degrades showing that the surface area of the catalyst was increased during the cycling and enabled a superior HER activity.

4.2.5 Study of HOR on (PdNPs/-PdNPs@)s-GNF hybrid electrocatalyst

Hydrogen oxidation reaction (HOR, $H_2 \rightarrow 2H^+ + 2\,e$) that is the consider the reverse of the HER is an important cathode reaction in fuel cell. It is generally accepted that HOR can be limited by the mass transport of H_2 to the electrode surface as evidenced by the plateau in the polarization curves which can be attributed to the limited solubility of H_2. Therefore it is crucial to use the rotating disk electrode (RDE) to eliminate the limited mass transport of H_2 onto the electrode surface.[84]

HOR activity of (PdNPs/-PdNPs@)s-GNF was then studied by applying a potential between -0.2 to 0.9 V versus RHE in H_2 saturated 0.1 M $HClO_4$ solution by rotating the electrocatalyst at 400, 900, 1600 and 2500 rpm rotation speeds at room temperature. HOR polarisation curves were obtained to examine the kinetic of HOR activity of (PdNPs/-PdNPs@)s-GNF by plotting the current density versus potential after the currents were normalized to the geometric area of the glassy carbon electrode and the potentials were corrected by the iR correction. The current density (j) was observed to gradually increase with the increase in the rotation speed applied from 400 to 2500 rpm from the polarisation curves which was consistent with the literature (Figure 4.25a).

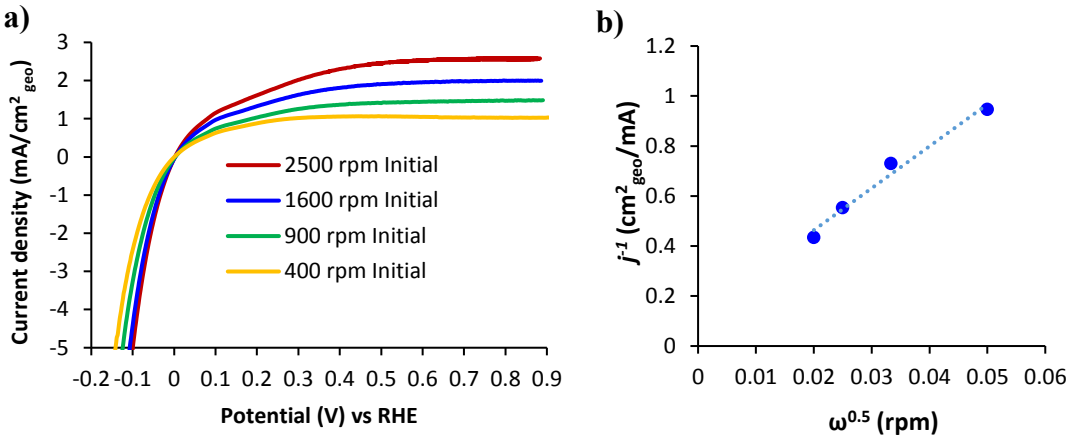

Figure 4.25 a) HOR polarisation curves (positive direction) and b) Koutecky–Levich plot (j^{-1} at 0.4 V versus $\omega^{-1/2)}$) of (PdNPs/-PdNPs@)s-GNF at 400, 900, 1600 and 2500 rpm rotating speeds.

According to the Koutecky-Levich equation, the current density (j) experimentally obtained from RDE measurements depends on two parameters: the kinetic current density (j_k) and the diffusion limiting current density (j_{lim}) (Equation 4.6).

$$\frac{1}{j} = \frac{1}{j_k} + \frac{1}{j_{lim}} \qquad \textbf{Equation 4.6}$$

HOR reaction at 400, 900,1600 and 2500 rpm rotating speed was obtained by plotting j^{-1} versus $\omega^{-1/2}$ at a particular potential (Koutecky-Levich plot). The Koutecky-Levich plot of (PdNPs/-PdNPs@)s-GNF obtained at 0.4 V gave a straight line passing through the origin which confirms that the limiting current at 0.4 V was fully controlled by diffusion of H_2 mass (Figure 4.25b).

There are only a few studies available in the literature on HOR activity of Pd-based catalyst to compare with our results.[84-85] Pronkin *et al.*[86] studied the HOR activity of Pd/C in 0.1 M H_2SO_4 using RDE and reported an exchange current density of ~0.22 mA cm^{-2}_{geo} which was comparable to initial HOR activity of (PdNPs/-PdNPs@)s-GNF (Figure 4.25 and Table 4.6).

We also studied the HOR activity of Pt/C as a benchmark catalyst to compare with that of the (PdNPs/-PdNPs@)s-GNF and observed a similar trend to (PdNPs/-PdNPs@)s-GNF by plotting j^{-1} versus $\omega^{-1/2}$ at 0.4 V where the current density (j) gradually increased with the increase in the rotation speed applied from 400 to 2500 rpm (Figure 4.22a). The Koutecky-Levich plot of Pt/C at 0.4 V gave a straight line passing through the origin similar to that of (PdNPs/-PdNPs@)s-GNF (Figure 4.26b).

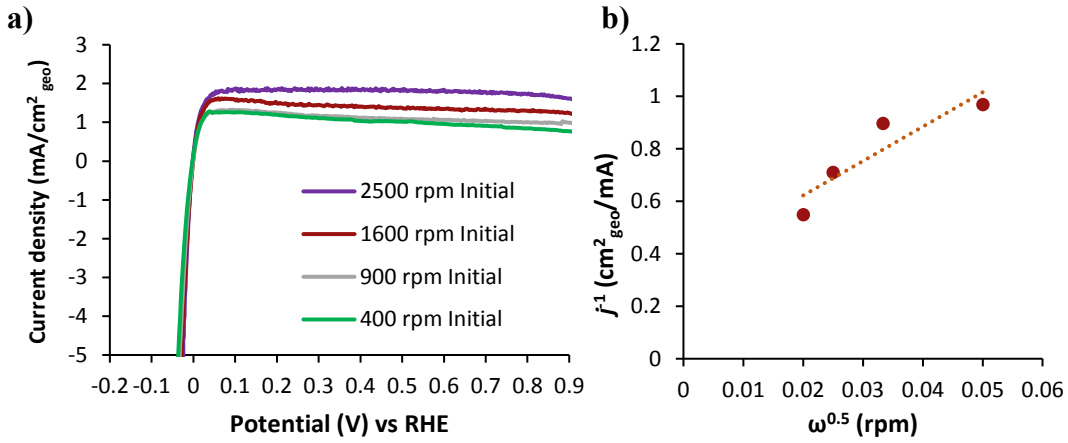

Figure 4.26 a) HOR polarisation curves (positive direction) of Pt/C and b) Koutecky–Levich plot (j^{-1} at 0.4 V versus $\omega^{-0.5}$) of Pt/C at 400, 900, 1600 and 2500 rpm rotating speeds.

To evaluate the HOR activity of (PdNPs/PdNPs@)s-GNF, the kinetic parameters such as Tafel plots and exchange current density were obtained from the plot of the logarithmic kinetic current ($\log j_k$) versus the overpotential (η) using the Butler-Volmer equation. The diffusion limited current density (j_{lim}) can be determined either using the Levich equation:

$$j_{\lim} = 0.62nFD^{2/3}v^{-1/6}C_0\omega^{1/2} \qquad \textbf{Equation 4.7}$$

(where D the diffusion coefficient of the reactant (cm^2/s), F is the Faraday's constant (96,498 C/mol), n the number of electrons in the HOR ($n = 2$), v the kinematic viscosity of the electrolyte (cm^2/s), ω rotation speed (rpm), C_0 is the H_2 concentration in the solution and BC_0 is a constant related to the concentration and diffusivity of the solubility of H_2 gas)

or by extracting the kinetic current density (j_k) from the Koutecky-Levich equation:

$$j_k = (j * j_{lim})/(j_{\lim} - j) \qquad \textbf{Equation 4.8}$$

Here, j is the measured current density (mA/cm^2) at 1600 rpm and j_{lim} is the diffusion limiting current. The diffusion limiting current densities were determined from the polarisation curves, for instance the initial polarisation curves of (PdNPs/-PdNPs@)s-GNF and Pt/C reached the plateau at ~0.3 V and ~0.06 V vs. RHE, respectively and the corresponding currents were used as the diffusion limiting currents to calculate the kinetic current densities for each catalyst using Equation 4.4 (Figure 4.27a). Tafel plots corresponding to the diffusion limited current density for initial (PdNPs/-PdNPs@)s-GNF and Pt/C were then produced by plotting the logarithmic kinetic current ($\log j_k$) versus overpotential (η) for each electro catalyst at 1600 rpm (Figure 4.27b).

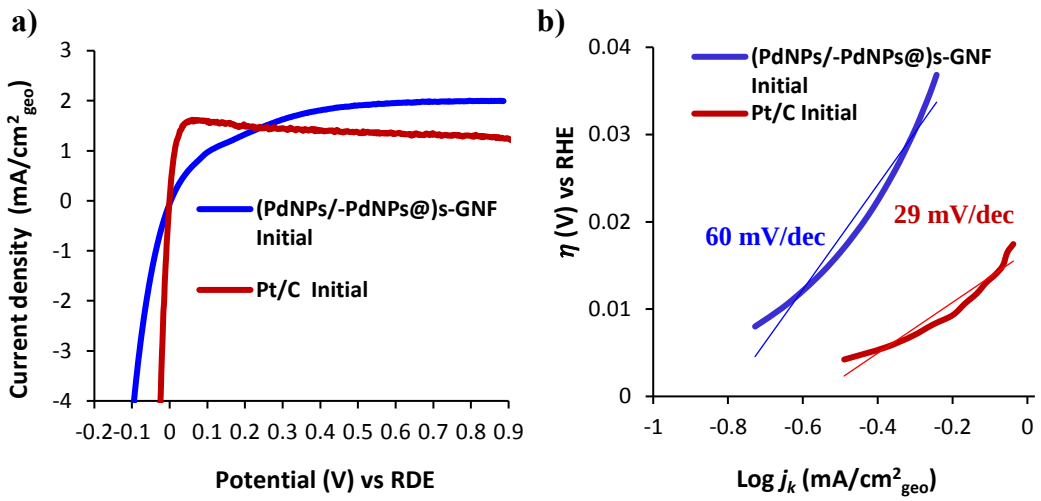

Figure 4.27. a) HOR polarisation curves (positive direction) and (**b**) Tafel plots of (PdNPs/-PdNPs@)s-GNF and Pt/C at 1600 rpm rotating speed.

Table 4.6. Indication of the onset potential, overpotential, Tafel slopes and exchange current density values of (PdNPs/-PdNPs@)s-GNF and Pt/C as initial and after the stability test of 5000 cycles, respectively.

	Tafel Slope (mV /dec)	**J_0 (mA/cm^2_{geo})**
(PdNPs/-PdNPs@)s-GNF Initial	60.1	0.157
(PdNPs/-PdNPs@)s-GNF after 5000 cycles	27	0.278
Pt/C Initial	29.1	0.269
Pt/C after 5000 cycles	28	0.201

The obtained initial HOR Tafel slopes of (PdNPs/-PdNPs@)s-GNF indicated the Volmer-Heyrowsky mechanism where Heyrowsky step was the rate determining step with the Tafel slope of nearly 60 mV/dec, while Pt/C had a Volmer-Tafel mechanism and the desorption of hydrogen atoms was the rate-limiting step.

The HOR stability of (PdNPs/-PdNPs@)s-GNF and Pt/C was also investigated by continuous applied linear potential sweeps between 0.4 and -0.2 V versus RHE at 50 mV/s scan rate by the 5000 potential cycles and the electrochemical activity of the catalyst was evaluated after the 5000 cycles using the HOR polarization and the Koutecky-Levic plots at 400, 900, 1600 and 2500 rpm rotating speeds (Figure 4.28). After the stability test of (PdNPs/PdNPs@)s-GNF, an extra oxidation peak was observed at ~0.06-0.13 V potential range which was consistent for literature in the use of Pd due to the hydrogen adsorption/desorption reaction on the PdNPs (Figure 4.28a).[12,87] (PdNPs/-PdNPs@)s-GNF exhibited dramatically enhanced HOR activity after the stability test with a Tafel slope of 27 mV/dec which suggests that it has a Volmer-Tafel mechanism and the Tafel step is the rate-determining step. We also observed a two magnitude higher exchange current density after the stability test. This is consistent with the HER results of (PdNPs/-PdNPs@)s-GNF before and after the stability test of 500 cycles.

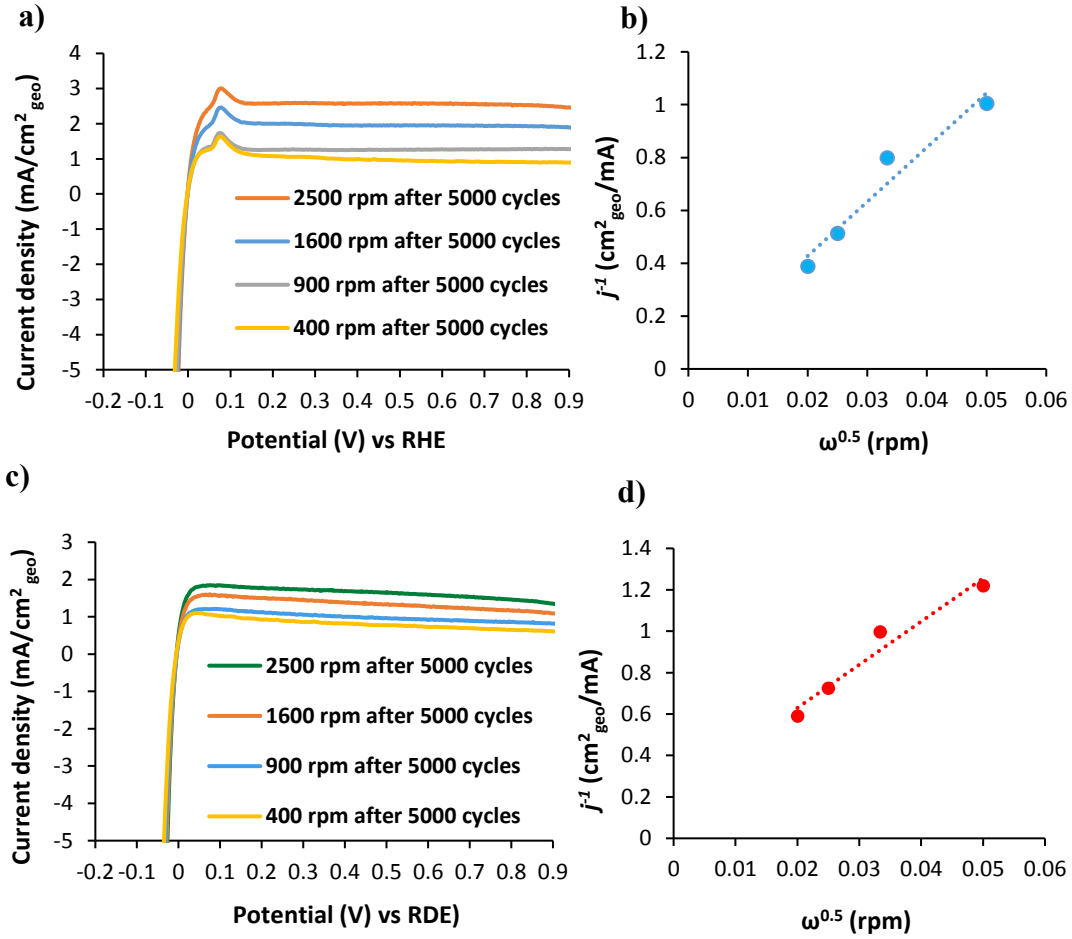

Figure 4.28. a) HOR polarisation curves (positive direction) and b) Koutecky–Levich plot of (PdNPs/-PdNPs@)s-GNF after 5000 HER/HOR cycles at 400, 900, 1600 and 2500 rpm rotating speeds c) HOR polarisation curves (positive direction) and d) Koutecky–Levich plot of Pt/C after 5000 HER/HOR cycles at 400, 900, 1600 and 2500 rpm rotating speeds.

HOR Tafel plots for (PdNPs/-PdNPs@)s-GNF and Pt/C were then produced by plotting the logarithmic kinetic current (log j_k) versus overpotential (η) for each electro catalyst at 1600 rpm after 5000 HOR cycles (Figure 4.2).

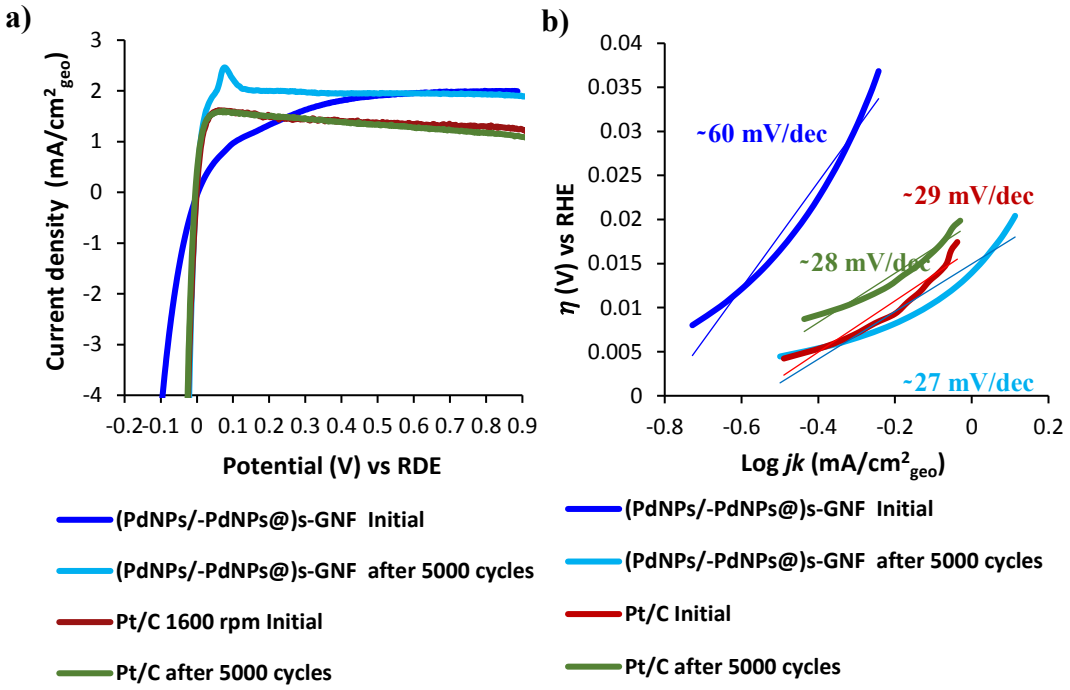

Figure 4.29. a) HOR polarisation curves (positive direction) and (**b**) Tafel plots of (PdNPs/-PdNPs@)s-GNF and Pt/C at 1600 rpm rotating speed.

Overall, the strong interactions of s-GNF support with PdNPs, in particularly the PdNPs interacted with open step edges could provide an efficient electron transport between the s-GNF and PdNPs. These strong interactions of PdNPs at the step edges were also confirmed by HRTEM that the nanoparticle growth and degradation was mostly indicated on the external of s-GNFs due to migration of the nanoparticles on the smooth external of s-GNF in acid, while there was no significant nanoparticles growth due to the highly stabilised nanoparticles at the step edges.

4.3 CONCLUSION

In this chapter, a novel (PdNPs/-PdNPs@)s-GNF hybride material was designed and demonstrated that the superior HER activity of (PdNPs/-PdNPs@)s-GNF in comparison to commercial Pd/C and Pt/C in acidic media. The intitial HER activity of (PdNPs/-PdNPs@)s-GNF was lower than that of the commercial Pt/C and Pd/C catalyst but it was still comparable to them due to its Pt-like HER behavior. However, it indicated an outstanding stability and gradually increased HER activity during the continuous electrochemical HER cycling (up to 30000 cyles). The effect of metal free s-GNF support was studied in HER and observed that an increase in HER activity and stability during the 5000 electrochemical cycling. HRTEM revealed for the first time the presence of some opened step-edges in the s-GNF during the electrochemical cycling. Thefore, the enhanced HER activity of s-GNF after 5000 cycles was accredited to the some opened step edges in s-GNF enabling active sites to form hydrogen and promoting charge transfer. This observation helped to understand the significantly improved HER/HOR activity of (PdNPs/-PdNPs@)s-GNF hydrid during the electrochemical cycling. Overall, superior HER/HOR activity of (PdNPs/-PdNPs@)s-GNF during the electrochemical cycling can be attributed to the several factors. Firstly, reactions taking place in a confined nano-environment of s-GNF could enhance the activity of HER/HOR by increasing the local concentrations of the reactants and enabling better interactons of reactans with the Pd catalyst. Secondly, the enhanced interactions between PdNPs ansd s-GNF promoted the HER/HOR due to the chemical transformations of some step edges, *i.e.* opened step edges, during the electrochemical cyling. The opened step edges enabled stronger interactions between s-GNF and PdNPs, and thus improved the electron transfer and synergetic effects between PdNPs and s-GNF. Thirdly, HRTEM investigation of all catalyst after the stability test proved that the size of PdNPs remained nearly unchanged

due to the strong interactions of PdNPs with step edges, while the migration and growth of PdNPs on the external of s-GNF and PtNPs on carbon support. This can mean that the strong interactions between the step edges and PdNPs prevented the migration of nanoparticles and aggregate to larger clusters leading to some loss in the active surface sites of the catalyst, while there was significant PtNPs growth due to weak interactions of PtNPs with the carbon support. Finally, some residuals formed during the synthesis of (PdNPs/PdNPs@)s-GNF, either on s-GNF such as amorphous carbon or on the PdNPs surface such as dba could have hindered the intial HER/HOR activity of (PdNPs/PdNPs@)s-GNF. Thus, it could be cleaned during the cycling and improved the HER/HOR activity.

In conclusion, this study presents (PdNPs/-PdNPs@)s-GNF hybrid material as promising candidate for fuel cell reactions due to the its outstanding HER/HOR activity and stability It also provides a significant contribution to the field with lack of Pd-based electrocatalyst in HER/HOR. The unique structure and electrochemical properties of s-GNF presents an exciting prospect for the future fuel cell applications to be used as either a metal-free catalyst or support material for other metals catalysts.

4.4 EXPERIMENTAL

GNF were purchased from Pyrograf Products Inc (PR19, chemical vapor deposition), USA. Nafion® (5% solution in a mixture of lower aliphatic alcohols and water) and all other reagents and solvents were purchased from Sigma-Aldrich (UK) and used without further purification. Graphitised nanofibers (GNF) were supplied by Pyrograf® Products Inc. Pt/C (20 wt%, HiSPECTM 3000) and Pd/C commercial catalysts was supplied by Johson Matthey and Alfa Aeser, respectively. Ultra-pure water purified with Millipore Advantage A10 water equipment (resistivity 18.2 MΩ•cm at 25 ˚C) was used in all experiments.

HRTEM analysis was performed on a JEOL 2100 Field emission gun microscope with an information limit of 0.12 nm at 200 kV. Samples for HRTEM analysis were prepared by dispersing the materials in HPLC grade iso-propanol using ultra-sonication, then drop casting the resultant suspension onto a lacey carbon film coated copper grid.

TGA analysis was performed on a TA Instruments TGA-SDTQ600 analyser. Samples for TGA analyses were heated in an inert atmosphere up to 1000 °C with a heating rate of 10 °C/min.

The powder X-ray diffraction patterns were obtained using a PANanalytical X'Pert PRO diffractometer equipped with a Cu-Ka radiation source (λ=1.5418 Å) operating at 40 kV and 40 mA, with 0.05252° step size and 5925.18 second step time.

4.4.1 Shortening the GNF using ball milling

50 mg of GNF (PR19) as received with a length of ~15 ±12 μm as we reported in section 2 were mechanically ground in an ambient atmosphere using a Retsch MM 400 ball mill instrument, containing a steel ball with a diameter of 10 mm. The rolling speed of the milling machine is fixed at 10 Hz for 1.5 hours to obtain the desired s-GNF.

4.4.2 Preparation of (PdNPs/-PdNPs@)s-GNF

s-GNF (15 mg, annealed at 450 °C for 1 hour prior to use) were dispersed in $CHCl_3$ (40 mL) using ultrasound for 10 minutes. A solution of $Pd(dba)_3.CHCl_3$ (11.2 mg, corresponding to a 15 wt %) in $CHCl_3$ (20 mL) was then slowly added to the s-GNF dispersion in small portions (0.5 mL) whilst being treated with ultrasonic waves and stirred at 40 ° C for 1 day until the solution became colorless. PdNPs@GNF was then separated from the reaction mixture by filtration and washed repeatedly with acetone (20 mL) using a 0.2 µm PTFE membrane filter to remove free dba and obtain the final (PdNPs/-PdNPs@)s-GNF material as a black powder.

4.4.3 Electrochemical measurements

The electrochemical experiments were performed by three electrode set up using Autolab potentiostat PGSTAT204 with a glassy carbon electrode (GCE) as the working electrode in a commercial (Pine Instruments), a Pt wire as a counter electrode and a HydroFlex reversible hydrogen electrode (RHE) as the reference electrode, respectively. This system was coupled with a NOVA software. The GCE was cleaned with 0.05µm principal particle size alumina powder solution (Agar Scientific Ltd.) on a polishing paper to remove any impurity which may affect electrochemical measurements. An catalyst ink solution was prepared for each catalyst where catalyst (1 mg) was dispersed in hexane (1 mL) using ultrasonication for 15 mins, respectively. (PdNPs/-PdNPs@)s-GNF ink corresponding of a resultant metal loading of 100 $\mu g/cm^2_{geo}$ were deposited onto the GCE with a 0.196 cm^2 geometric surface area by drop casting and the resultant film was covered by a Nafion solution (5 % Nafion in a mixture of lower aliphatic alcohols and water, 20 µL) and then dried under argon flow at room temperature for 30 min. Pt/C and Pd/C was also prepared using the same procedure but with a resultant metal loading of 100 $\mu g/cm^2_{geo}$.

The potential was cycled at fast scan rates (200 mV/s) for 50 cycles between 0 V and 1.2 V were taken in order to remove any impurities and unwanted species from the surface of the electrode prior to cyclic voltammetry (CV) and HER/HOR measurements. Impedance measurements, the cell resistance was measured immediately after HER/HOR measurements taking the ac impedance spectra from 32 to 0.1 kHz and a voltage perturbation of 10 mV. The real part of the resistance at 1 kHz was taken as the cell resistance and was used to obtain the IR-free potential of the working electrode. All of the I-E curves was corrected by the solution resistance by using $E= E_{experimental}-(I*R)$.

CV measurements were performed in nitrogen saturated 0.1 M $HClO_4$ at scan rates of 50 mV/s between 0 V and 1 V. HER measurement were performed between 0.2V and -0.9 V vs RHE at a sweep rate of 10 mV/s in hydrogen saturated 0.1M $HClO_4$ at room temperature. HOR measurements were performed between 0 V and 1 V vs RHE with a variety of rotating speed at 400, 900, 1600 and 2500 rpm using the rotating disk electrode (RDE). Electrochemical stability test was carried out by continuously applying linear potential sweeps up to 20000 cycles from -0.2 to 0.4 V vs RHE at 50 mV in hydrogen saturated 0.1 M $HClO_4$ at 1600 rpm to get rid of the hydrogen bubbling evolved on the electrode surface during the cycling.

4.5 REFERENCES

1. M. Caban-Acevedo, M. L. Stone, J. Schmidt, J. G. Thomas, Q. Ding, H. C. Chang, M. L. Tsai, J.-H. He, S. Jin, *Nat. Mater.*, 2015, 14, 1245−1251.
2. S. Cobo, J. Heidkamp, P. A. Jacques, J. Fize, V. Fourmond, L. Guetaz, B. Jousselme, V. Ivanova, H. Dau, S. Palacin, M. Fontecave, V. Artero, *Nat. Mater.*, 2012, 11, 802.

3. M. Dresselhaus, I. Thomas, *Nature*, 2001, 414, 332−337.

4. R. M. Navarro, M. A. Pena, J. L. G. Fierro. *Chem Rev*, 2007, 107, 3952-91.

5. Y. Jiao, Y. Zheng, M. Jaroniec. S.Z. Qiao,*Chem. Soc. Rev.*, 2015, 44, 2060–2086.

6. J. D. Benck, T. R. Hellstern, J. Kibsgaard, P. Chakthranont, T. F Jaramillo, *ACS Catal.*, 2014, 4,3957–3971.

7. H. L. Fei, J. C. Dong, M. J. Arellano-Jimenez, G. L. Ye, N. D. Kim, E. L. G. Samuel, Z. W. Peng, Z. Zhu, F. Qin, J. M. Bao, M. J. Yacaman, P. M. Ajayan, D. L. Chen, J. M. Tour, *Nat. Commun.*, 2015, 6, 8668.

8. H. A. Gasteiger, S. S. Kocha, *B.* Sompalli, F. T. Wagner, *Applied* Catalysis *B*: *Environmental, 2005,* 56, 9–35.

9. H. A. Gasteiger, N. M. Marković, Science, 2009, 324, 48–49.

10. S.-K. Park, D. Y. Chung, D. Ko, Y.-E. Sung, Y. Piao, *J. Mater. Chem. A*, 2016, 4, 12720−12725.

11. S. Lu, Z. Zhuang, *Sci China Mater,* 2016, 59, 217–238.

12. J. Durst, C. Simon, F. Hasche, H. A. Gasteiger, *J. Electrochem. Soc.*, 2015, 162, F190-F203.

13. Y. Cheng, S. Lu, F. Liao, L. Liu, Y. Li, M. Shao, *Adv. Funct. Mater.* 2017, *27*, 1700359.

14. N. C. Cheng, N. B. Banis, J. Liu, A. Riese, X. Li, R. Y. Li, S. Y. Ye, S. N. Knights, X. L. Sun, *Adv. Mater.*, 2015, *27*, 277.

15. Y. Xu, M. Kraft, R. Xu, *Chem. Soc. Rev.* 2016, *45*, 3039–3052.

16. D. V. Esposito, S. T. Hunt, A. L. Stottlemyer, K. D. Dobson, B. E. McCandless, R. W. Birkmire, J. G. G. Chen, *Angew. Chem. Int. Ed.*, 2010, *49*, 9859.

17. S. Liu, X. Mu, H. Duan, C. Chen, H. Zhang, *Eur. J. Inorg. Chem.* 2017, 535–539.

18. E. Heydari-Bafrooei, S. Askari, *Int. J. of Hydrogen Energy*, 2017, 42, 2961-2969.

19. L. Zhang, Q. Chang, H. Chen, M. Shao, *Nano Energy*, 2016, 29, 198–219.

20. J. Li, F. Li, S. X. Guo, J. Zhang, J. Ma, *ACS Appl. Mater. Interfaces,* 2017, 9, 8151−8160.

21. S. A. Grigoriev, P. Millet, V. N. Fateev, *J. Power Sources*, 2008, 177, 281-285.

22. T. Bhowmik, M. K. Kundu, S. Barman, *ACS Catal*. 2016, 6, 1929−1941.

23. Y. Zhao, F. Zhao, X. P. Wang, C. Y. Xu, Z. P. Zhang, G. Q. Shi, L. T. Qu, *Angew. Chem. Int. Ed.*, 2014, 53, 13934.

24. M. Shalom, S. Gimenez, F. Schipper, I. Herraiz-Cardona, J. Bisquert, *M.* Antonietti, *Angew. Chem. Int. Ed.* 2014, 53, 3654.

25. J. T. Zhang, L. T. Qu, G. Q. Shi, J. Y. Liu, J. F. Chen, L. M. Dai, *Angew. Chem. Int. Ed.*, 2016, 55, 2230.

26. Y. Ito, W. T. Cong, T. Fujita, Z. Tang, M. W. Chen, *Angew. Chem. Int. Ed*., 2015, 54, 2131.

27. J. J. Duan, S. Chen, M. Jaroniec, S. Z. Qiao, *ACS Nano*, 2015, 9, 931.

28. Y. Jiao, Y. Zheng, K. Davey, S. Z. Qiao, *Nat. Energy*, 2016, 1, 16130.

29. D.-W. Wang, D.Su , *Energy Environ. Sci.*, 2014 ,7 , 576 .

30. W. Sheng, H. A. Gasteiger, Y. Shao-Horn, *J. Electrochem. Soc.*, 2010, 157, B1529-B1536.

31. W. Zhou , J. Jin , L. Yang, D. Hou, G. Li, S. Chen, *Nano Energy*, 2016, 28, 29.

32. Y. Shao , G. Yin , Z. Y. Gao , *Electrochim. Acta*, 2006 , 51 , 5853

33. X. Wang , W. Li , Z. Chen , M. Waje , Y. Yan , *J. Power Sources*, 2006 , 158 , 154.

34. Y. Li, H. Wang, L. Xie, Y. Liang, G. Hong, H. Dai, *J Am. Chem. Soc*, 2011, 133, 7296-7299.

35. T. Lin, C. Liu, J. Lin, *Appl Catal B Environmental*, 2013, 134, 75-82.

36. Y. Cai, X. Yang, T. Liang, L. Dai, L. Ma, G.W. Huang, W. Chen, H. Chen, H. Su, M. Xu, *Nanotechnology*, 2014, 25, 465401-465406.

37. X. Ren, X. Ren, L. Pang, Y. Zhang, Q. Ma, H. Fan, S. Liu, *Int. J. Hydrogen Energy*, 2016, 41, 916-923.

38. S. Ghasemi, S. R. Hosseini, S. Nabipour, P. Asen, *Int. J. Hydrogen Energy*, 2015 40, 16184 -16191.

39. M. C. Gimenez-Lopez , A. La Torre , M. W. Fay , P. D. Brown , A. N. Khlobystov , *Angew. Chem. Int. Ed.* 2013, *52*, 2051.

40. A. La Torre , M. C. Gimenez-Lopez , M. W. Fay , G. A. Rance , W. A. Solomonsz , T. W. Chamberlain , P. D. Brown , A. N. Khlobystov , *ACS Nano* 2012, *6*, 2000.

41. A. La Torre , M. C. Gimenez-Lopez , M. W. Fay , C. H. Lucas , P. D. Brown, A. N. Khlobystov, *Small*, 2015, *11*, 2756 .

42. M. del Carmen Gimenez-Lopez, A. Kurtoglu, D. A. Walsh, A. N. Khlobystov, *Advanced Materials*, 2016, 28, 9103-9108.

43. E. O. Pentsak, A. S. Kashin, M. V. Polynski, K. O. Kvashnina, P. Glatzelc, V. P. Ananikov, *Chem. Sci.*, 2015, 6, 3302.

44. H. E. Swanson, E., Tatge, Standard X-ray diffraction powder patterns I, National Bureau of Standards (U.S.), Circular, 1953, 539 (1), 1-95.

45. A. Zalineeva, S. Baranton, C. Coutanceau, G. Jerkiewicz, *Langmuir*, 2015, 31, 1605−1609.

46. J. D. Benck, T. R. Hellstern, J. Kibsgaard, P. Chakthranont, T. F. Jaramillo, *ACS Catal*. 2014, 4, 3957–3971

47. J. Li, G., Zheng, *Adv Sci*, 2017, 4,1600380. http://dx.doi.org/10.1002/advs.201600380.

48. Y. J. Tang, Y, Wang, X. L. Wang, S. L. Li, W. Huang, L. Z. Dong, *Adv Energy Mater*, 2016, 6 :1600116.

49. C. G. Morales-Guio, L. A. Stern, X. Hu, *Chem. Soc. Rev*., 2014, 43, 6555—6569.

50. J. O. M. Bockris, E. C. Potter, *J. Electrochem. Soc*., 1952, 99, 169.

51. A. J. Bard and L. R. Faulkner, Electrochemical Methods: Fundamentals and Applications, John Wiley, New York, 2000.

52. G. Eliezer, Physical Electrochemistry, John Wiley, New York, 2011.

53. D. K. Singh, R. N. Jenjeti, S. Sampath, M. Eswaramoorthy, *J Mater Chem A*, 2017,5.

54. Y. Liu, H. Yu, X. Quan, S. Chen, H. Zhao, Y. Zhang, *Sci Rep*, 2014, 4, http://dx.doi.org/10.1038/srep06843. Article number: 6843.

55. B. Conway, B. Tilak, *Electrochim Acta*, 2002, 47, 3571−3594.

56. M. Gong, W. Zhou, M. C. Tsai, J. Zhou, M. Guan, M. C. Lin, B. Zhang, Y. Hu, D. Y. Wang, J. Yang, S. J. Pennycook, B. J. Hwang, H. Dai, *Nat. Commun*. 2014, 5, 4695.

57. Kucernak, A.R., Zalitis, C., *J. Phys. Chem. C*, 2016, 120, 10721−10745

58. M. R. Gao, J. X. Liang, Y. R. Zheng, Y. F. Xu, J. Jiang, Q. Gao, J. Li, S. H. Yu, *Nat. Commun*. 2015, 6, 5982.

59. Q. Lu, G. S. Hutchings, W. Yu, Y. Zhou, R. V. Forest, R. Tao, J. Rosen, B. T. Yonemoto, Z. Cao, H. Zheng, J. Q. Xiao, F. Jiao, J. G. Chen, *Nat. Commun.* 2015, *6*, 6567.

60. A. R. Kucernak and G. J. Offer, *Phys. Chem. Chem. Phys.*, 2008, 10, 3699-3711.

61. M. Łukaszewski, M. Soszko, A. Czerwiński, Int. J. Electrochem. Sci., Vol. 11, 2016.

62. K.J.J. Mayrhofer, D. Strmcnik, B.B. Blizanac, V. Stamenkovic, M. Arenz, N.M. Markovic, *Electrochim. Acta.,* 2008, 53, 3181–3188.

63. M. Łukaszewski, M. Soszko, A. Czerwiński, *Int. J. Electrochem. Sci.*, 11, 2016.

64. S. Henning, J. Herranz, H. A. Gasteiges, *Int. J. Hydrogen Energy*, 2015, 162, F178-F189.

65. M. Shao, J. H. Odell, S-I. Choi, Y. Xia, *Electrochem. Commun*., 2013, 31, 46–48.

66. C. Hu, L. Dai, *Angew. Chem. Int. Ed.,* 2016, 55, 11736 – 11758.

67. W. Cui, Q. Liu, N. Cheng, A. M. Asiri, X. Sun, *Chem. Comm.* 2014, *50*, 9340.

68. Y. Zheng, Y. Jiao, M. Jaroniec and S. Z. Qiao, *Angew. Chem., Int. Ed.*, 2015, 54, 52–65.

69. J. Zhang, L. Qu, G. Shi, J. Liu, J. Chen and L. Dai, *Angew. Chem., Int. Ed.*, 2016, 55, 2230–2234.

70. T. N. J. I. Edison, R. Atchudan, N. Karthik, Y. R. Lee, *Int. J. Electrochem. Sci.,* 2017, 42, 14390 - 14399.

71. S. Li, Z. Lu, Y. Yang, Y. Liu, H. Zou, H. Yang, J. Jin, J. Ma, *J. Mater. Chem. A*, 2017, 5, 6405–6410

72. Y. P. Zhu, Y. Jing, A. Vasileff, T. Heine, S. Z. Qiao, *Adv. Energy Mater*. 2017, 1602928

73. D. Deng, K. S. Novoselov, Q. Fu, N. Zheng, Z. Tian and X. Bao, *Nat. Nanotechnol*., 2016, 11, 218–230.

74. Y. Tian, Y. Ye, X. Wang, S. Peng, Z. Wei, X. Zhang, *Applied Catalysis A: General*, 2017, 529, 127–133.

75. M. Wang, Z. Wang, X. Gong and Z. Guo, *Renew. Sust. Energ. Rev.*, 2014, 29, 573–588

76. S. Pal, M. Sahoo, V. T. Veettil, K. K. Tadi, A. Ghosh, P. Satyam, R. K. Biroju, P. M. Ajayan, S. K. Nayak, T. N. Narayanan, *ACS Catal.,* 2017, 7, 2676−2684.

77. M. Harada, N. Tamura, M. Takenaka, *J. Phys. Chem. C*, 2011, 115, 14081−14092.

78. Z. Ao, S. Li, Hydrogenation of Graphene and Hydrogen Diffusion Behavior on Graphene/Graphane Interface, Graphene Simulation, Prof. Jian Gong (Ed.), InTech, 2011. DOI: 10.5772/20676.

79. J. Berashevich, T. Chakraborty, Phys. Rev. B., 2011, 83, 195442.

80. C. Gong, D. Hijonos, W. Wang, N. Nijem, B. Shan, R. M. Wallace, K. Cho, Y. J. Chabal, *ACS Nano*, 2012, 6, 5381-5387.

81. G. M. Psofogiannakis, G. E. Froudakis, *Chem. Commun*., 2011, 47, 7933-7943.

82. V. B. Parambhath, R. Nagar, K. Sethupathy, S. Ramaprabhu, *J. Phys. Chem. C*, 2011, 115, 15679-15685.

83. C. I. Contescu, C. M. Brown,Y. Liu, V. V. Bhat, N. C. Gallego, *J. Phys. Chem. C*, 2009, 113, 5886-5890.

84. J. Zheng, Y. Yan, B. Xu, J. *Electrochem. Soc.*, 2015, 162, F1470-F1481.

85. M. Shao, *J. Power Sources*, 2011,196,2433–2444.

86. S. N. Pronkin, A. Bonnefont, P. S. Ruvinskiy, E. R. Savinova, *Electrochim. Acta.*, 2010, 55. 3312–3323.

87. J. Zheng, S. Zhou, S. Gu, B. Xu, Y. Yan, *J. Electrochem. Soc*., 2016, 163, F499-F506.

5 CONCLUDING REMARKS

Carbon nanoreactors have the potential to provide materials which will revolutionise many areas such catalysis, electro-catalysis and electronic devices due to their unique physicochemical properties. However, the fundamental relationship between how the structure of carbon nanoreactors, e.g. size, shape, atomic bonding, number of defects etc. affects the fabrication of metal nanoparticles and subsequent chemical reactions within the confined space they possess is still remarkably underdeveloped and poorly understood. In particular, SWNTs as the narrowest nanoreactors with the most extreme spatial confinement are least extensively studied compared to wider carbon nanoreactors, such as MWNTs. In Chapter 2, SWNTs were investigated as active supports for RuNPs and compared with other carbon nanostructures, which impose different degrees of confinement, using exploratory hydrogenation reactions. The catalytic activity of RuNPs encapsulated into the extremely confined space of SWNT (d_{SWNT} ~1.5 nm) was compared with that of RuNPs confined inside wider, hollow GNFs (d_{GNF} ~50 nm) and, RuNPs supported on commercial Ru/C, which represented a 'confinementless' control. The carbon nanoreactor supported RuNPs were then probed in both single and competitive hydrogenation both with small, norbornene, and relatively larger aromatic group containing, benzonorbornadiene, reactants. This study revealed that controlling the nanoscale environment around catalysts can efficiently enhance the efficiency of chemical reactions due to the stabilised nanoparticles and heightened interactions of the catalyst with the reactants. RuNPs@GNF exhibited TONs of 11216 for norbornene and 4145 for benzonorbornadiene which were dramatically higher than that of unconfined RuNPs in commercial Ru/C (cf. TONs of 7428 for norbornene and 3058 for benzonorbornadiene). In addition to this, with competitive hydrogenation reactions, the

conversion of aromatic reactants was observed to increase for the confined catalyst due to an increased affinity of the aromatic groups to the interior of nanoreactors resulting in a change in the ratio of products formed, e.g. RuNPs@GNF and RuNPs@SWNT both exhibited higher benzonorbornadiene conversion and selectivity compared to norbornene, with benzonorbornadiene:norbornene ratios of 1:0.5 and 1:0.79, respectively. This is in stark contrast to the complete absence of product selectivity in the presence of Ru/C. However, the presence of RuNPs in the narrow SWNT also blocked some of SWNT channels resulting in lower accessible surface areas and thus lower turnover numbers than predicted. Surprisingly, RuNPs confined in the much wider GNFs resulted in the most significant enhancements, demonstrating remarkable activity and product selectivity compared to unconfined RuNPs on the outer surface of SWNTs or carbon black. This was attributed to the fact that nanoscale graphitic step-edges within the GNF are completely accessible and possess the correct shape to interact favourably with the reactant molecules resulting in high local concentrations of reagents at the step-edges. As the step-edges are also the correct shape to act as anchoring points for the RuNPs this leads to high local concentrations of reactant molecules at the catalytically active RuNPs. This results in accelerated reaction kinetics and therefore the highest observed activity. Therefore, GNFs can be an attractive alternative to the extremely narrow SWNT nanoreactors for preparative catalysis.

Carbon nanoreactors are excellent supports for heterogeneous catalyst systems, however, the low density and hydrophobicity of carbon nanoreactors makes using them in liquid phase reactions problematic. Issues with the separation of them from the reaction solution is challenging using conventional separation techniques such as filtration and centrifugation resulting in the need for expensive equipment and secondary processes. Therefore, creating recoverable and recyclable nanoreactor catalyst systems in an easy,

cheap and efficient way for liquid phase reactions, and hence reducing the negative economic and environmental impact of multiple stage separations, is essential if they are to be exploited fully in preparative chemistry. Chapter 3 outlines the development of a methodology to combine catalyst formation and magnetic functionalisation steps to produce catalytically active, magnetically separable carbon nanoreactors. The work focussed on creating magnetically recyclable and catalytic carbon nanoreactors: by firstly attaching commercial graphene-like carbon coated magnetic Co nanomagnets to the GNF sidewalls using non-covalent interactions (van der Waals forces). Secondly, by the in situ formation of carbon coated iron nanomagnets (Fe@C_n) on the GNF. UV-Vis measurements demonstrated the excellent separation of both (Co@C_n)/GNF and (Fe@C_n)/GNF with a low magnetic nanoparticle loading (~8-9 wt%) from the solution, which was achieved in a short period of time (~90s) by applying a magnetic field. Additionally, Pd and Pt nanoparticles supported by GNF nanoreactors were synthesised and initially tested in the reduction of nitrobenzene using a high pressure H_2 glass vessel in the absence of magnetic nanoparticles to explore suitable reaction conditions. Overall PdNPs@GNF-2 demonstrated the highest activity with a TOF of 72.3 min^{-1}, and high aniline selectivity (85%) at room temperature. Finally, active metallic catalyst formation and magnetic functionalisation steps were combined and the sustained activity of the hybrid PtNPs- and PdNPs@(Co@C_n)/GNF and @(Fe@C_n)/GNF materials was probed using magnetic recovery cycles in heterogeneous nitrobenzene reduction reactions. These experiments indicated that both (Co@C_n)/GNF and (Fe@C_n)/GNF supports do not contribute to the reaction and the product selectivity in the absence or presence of the metal nanoparticle catalysts remained essentially the same. Moreover, the recyclability and stability of these magnetic and catalytic nanoreactors in the reduction of nitrobenzene were measured over 5 reaction/separation cycles using magnetic separation and

compared with a traditional filtration based separation method. A significant amount of catalyst loss (>10% by wt.) was observed during traditional filtration separations, while negligible catalyst loss (< 0.5% by wt.) was observed by magnetic recovery.

All of these steps were successfully performed, and as a result novel magnetically separable and catalytic carbon nanoreactor systems were created allowing an easy and efficient combination of different metal catalyst and nanoreactors to investigate the confinement and recyclability of catalytic nanoreactors. This work represents an exciting development in the area of recyclable, catalytically active carbon nanoreactors. It may open a new door for the future developments of this field which in the long term may be scaled up and applied for chemical processes of industrial importance replacing inefficient and energy consuming conventional separation techniques.

Carbon nanoreactors are also interesting as materials for energy related applications such as the hydrogen fuel cells and water splitting reactions where they can act as electrocatalysts due to their unique properties such as high electrochemical conductivity and surface area. However, there is a gap in the literature with respect to the role that confinement affects the activity and durability of metal catalyst such as palladium in hydrogen evolution and hydrogen oxidation reactions (HER/HOR). In Chapter 4, the GNFs were shortened using a newly developed ball milling procedure, and combined with PdNPs to form ((PdNPs/PdNPs@)s-GNF. HRTEM revealed that some PdNPs were located within the s-GNF while some of them immobilised on the external of s-GNF. The s-GNF supported PdNPs were probed in HER/HOR and compared to commercial Pd/C and Pt/C materials in acid media. A significant enhancement in the activity and stability of (PdNPs/-PdNPs@)s-GNF (studied over 30000 cycles) was observed under electro-catalytic cycling in HER/HOR compared to that of commercial Pt/C, which exhibited a lower activity and durability. The initial HER activity of (PdNPs/-PdNPs@)s-GNF was

lower compared to commercial Pd and Pt nanoparticles supported by carbon black. Initially, it exhibited a Tafel slope of 61 mV/dec; however, a Pt-like onset potential at -14 mV and exchange current density of 0.289 mA/cm^2 were observed, which was much higher than that of Pd/C. After 5000 cycles, (PdNPs/-PdNPs@)s-GNF showed an onset potential at 0 mV, a Tafel slope of 25.7 mV/dec, an exchange current density of 0.357 mA/cm^2 and an overpotential of -41 mV which achieved a current density of -10 mA/cm^2 in HER. After 30000 cycles, (PdNPs/-PdNPs@)s-GNF exhibited an onset HER potential of 0 mV, a current density of 10 mA/cm^2 at a very small overpotential of 27 mV, a Tafel slope of 22 mV/dec and an exchange current density of 0.545 mA/cm^2, and most importantly, revealed better stability than that of Pt/C and any other catalysts reported previously. Furthermore, s-GNF nanoreactors were explored for the first time as a metal free electrocatalyst and support in HER, showing enhanced HER activity and stability during the 5000 electrochemical cycling preformed. In similar fashion to (PdNPs/-PdNPs@)s-GNF, the s-GNF showed an onset potential of 0 mV, a current density of 10 mA/cm^2 at an overpotential of 261 mV, a Tafel slope of 77.3 mV/dec and an exchange current density of 0.222 mA/cm$^2_{geo}$ after 5000 cycles, which was much higher than that of the initial HER values of s-GNF and other metal free HER catalysts. HRTEM imaging enabled the investigation of structural changes in the s-GNF and (PdNPs/-PdNPs@)s-GNF hybrid material and was used to rationalise the increase in activity after electrochemical cycling. TEM revealed chemical transformation of the step edges (the presence of some opened step edges, formed during the electrochemical cycling, were observed) which are believed to enhance the activity of the nanoreactor. Furthermore, HRTEM confirmed stronger interaction between PdNPs and the open step edges after electrochemical cycling. Therefore, the size of the PdNPs remained nearly unchanged due to stabilisation at the step edges, while there was a significant growth of Pd and Pt

nanoparticles on the control, carbon black support. HOR activity of (PdNPs/-PdNPs@)s-GNF was also studied using a rotating disc electrode (RDE) and demonstrated that the current density gradually increased at increasing rotation speeds as a result of reduced mass transport limitations. Initially, (PdNPs/-PdNPs@)s-GNF exhibited a slow HOR kinetic at 1600 rom rotation speed with a Tafel slope of 60 mV/dec and exchange current density of 0.157 mA/cm^2_{geo} compared to that of Pt/C with a Tafel slope of 29 mV/dec and exchange current density of 0.269 $mA/cm^2_{geo.}$ However, (PdNPs/-PdNPs@)s-GNF exhibited enhanced HOR activity with a Tafel slope of 27 mV/dec and exchange current density of 0.278 mA/cm^2_{geo} after 5000 cycles, while Pt/C indicated a decreased activity and stability with an exchange current density of 0.201 mA/cm^2_{geo}. In conclusion, it was demonstrated that HER/HOR catalysed by PdNPs in the confined nano-environment of s-GNF nanoreactors exhibited an excellent electro-activity and stability up to 30000 cycles due to improved charge transfer and a synergetic effect between the PdNPs and s-GNF. This may be a significant contribution to the future studies on Pd-based carbon nanoreactors in the use of fuel cell reactions. It has the potential to be developed for industrial applications and provides an insight for the development of new hybrid materials using different metals and s-GNF carbon nanoreactors.

In summary, the work presented in this thesis provides a significant contribution to the development of metal-nanoreactor based hybrid materials, providing essential fundamental understanding, which is vital if the materials are to find application in as catalysts in industrial catalytic reactions and act as efficient, magnetism based, catalyst recovery systems. More specifically, this study advances the use of carbon nanomaterials in relatively underdeveloped electrochemical fuel cell applications exploiting the nanoconfinement effects of carbon nanoreactors to increase the stability and activity of the catalytic nanoparticles. Therefore, this work paves the way for further research into

the development of GNF based carbon nanoreactors as electro-catalysts and supports in a variety of electrochemical applications.